

ALMA MATER STUDIORUM - UNIVERSITÀ DI BOLOGNA

DEI - Dipartimento di Ingegneria dell'Energia Elettrica
e dell'Informazione "Guglielmo Marconi"

Dottorato in Bioingegneria
Ciclo XXIX
09/G2 - Bioingegneria; ING-INF/06

**AUTOMATIC COMPUTATION OF LIVER AND
LUNG PERFUSION PARAMETERS THROUGH
THE ANALYSIS OF CT IMAGE SEQUENCES**

Silvia Malavasi

Coordinatore del corso di Dottorato

Prof. Elisa Magosso

Relatore

Prof. Alessandro Bevilacqua

Co-Relatore

Prof. Giampaolo Gavelli

Esame finale: 12 Maggio 2017

ALMA MATER STUDIORUM - UNIVERSITY OF BOLOGNA

DEI - Department of Electrical, Electronic and Information
Engineering "Guglielmo Marconi"

Doctorate in Bioengineering
Cycle XXIX
09/G2 - Bioengineering; ING-INF/06

**AUTOMATIC COMPUTATION OF HEPATIC AND
LUNG PERFUSION PARAMETERS THROUGH
THE ANALYSIS OF CT IMAGE SEQUENCES**

Silvia Malvasi

Coordinator

Prof. Elisa Magosso

Tutor

Prof. Alessandro Bevilacqua

Co-Tutor

Prof. Giampaolo Gavelli

PhD course: January 1, 2014 - December 31, 2016

Final exam: May 12, 2017

To my family and to myself

*Ever aim at the top, however badly things go
you'll have walked among stars.*

*Punta sempre in alto, male che vada
avrà camminato tra le stelle.*

(Maria Battistello)

Internal reviewer:

Prof. **Claudio Lamberti**,
University of Bologna, Italy,
email: claudio.lamberti@unibo.it

External reviewer:

Prof. **Valérie Vilgrain**,
Beaujon Hospital, Clichy, France,
Paris 7 University, France,
email: valerie.vilgrain@aphp.fr

Keywords

IMAGE PROCESSING

SIGNAL ANALYSIS

QUANTITATIVE IMAGING

BIOMEDICAL IMAGING

MULTI-CENTRE STUDY

CANCER

Abstract (English version)

Computed Tomography perfusion (CTp) is a functional imaging technique that has aroused a lively interest in oncology in the recent years mainly because it is a very promising approach for early assessment of the effectiveness of the new anti-angiogenic therapies for cancer treatment. Nonetheless, some difficulties to achieve standardized, repeatable and reproducible results have slowed down its application in the daily clinical practice. This Thesis work addresses three important issues that needed to be faced to advance CTp towards standardization: the lack of methods to measure the reliability of results, the clinical relevance of the global perfusion parameter values commonly utilised, a critical revision of protocols of the multi-centre studies, essential to assess CTp reproducibility. In this work, lung and liver CTp examinations have been considered, since they are among the most studied sites in oncology.

First, through a voxel-based spatio-temporal signal analysis, I set up an error index capable to measure the quality of perfusion results and validated it using examinations whose signals was degraded by different patient motion degrees. After proving the effectiveness of the index to detect unreliable perfusion values on single voxels, structured regions affected by noise (*e.g.* artefacts) or representing semantic patterns undesirable in CTp studies (*e.g.* vessels or bronchi) have been looked for on whole slices. Exploiting the voxel-based analysis and the same error index, an adaptive algorithm developed on purpose has allowed detecting all those regions automatically, and to exclude their perfusion values from either any subsequent processing or clinical consideration.

The common practice in CTp perfusion studies is providing one averaged value only for each perfusion parameter, computed on the whole tumour, with the main purpose of reducing the effects of data variability, but at the expense of tumour heterogeneity, a key feature that is neglected. Accordingly, whole lung lesions were considered to inquire into the clinical representativeness of global perfusion values. After removing all perfusion errors, and proposing a statistical index to quantify tumour functional heterogeneity, the use of one

global value has been proved to even mislead clinical considerations.

The last part of the Thesis regards the activities carried out in the widest European liver CTP multi-centre study. Some algorithms for signal enhancement to improve the accuracy of perfusion results were developed so as to make CTP examinations of different Centres more comparable. Some meaningful results regarding baseline and blood flow values of liver are reported and discussed, highlighting whether and to what extent different CT scanners affect CTP outcomes. Starting from an extensive analysis regarding the great number of differences in the actual execution protocols, acquisition parameters and information storing, tentative guidelines are provided to help considering all the concealable sources of heterogeneity in advance, before planning the multi-centre protocols.

Abstract (Italian version)

La Tomografia Computerizzata perfusionale (TCp) è una tecnica di *imaging* funzionale che negli ultimi anni ha suscitato un crescente interesse nel campo oncologico, in quanto ha dimostrato di essere una tecnica molto promettente per la valutazione precoce dell'efficacia delle nuove terapie anti-angiogeniche per il trattamento dei tumori. Ciò nonostante, la sua applicazione nella pratica clinica è stata rallentata a causa della difficoltà nel conseguire risultati standardizzati, ripetibili e riproducibili. Questa Tesi tratta tre importanti aspetti che dovevano essere affrontati per far avvicinare la TCp alla standardizzazione: la mancanza di metodi per misurare l'affidabilità dei risultati, la rilevanza clinica dei parametri perfusionali globali comunemente utilizzati in letteratura ed una revisione critica dei protocolli degli studi multicentrici, essenziali per la valutazione della riproducibilità della tecnica. Questo lavoro tratta esami TCp polmonari ed epatici in quanto fegato e polmone sono tra gli organi maggiormente esposti all'insorgenza dei tumori.

Innanzitutto, attraverso un'analisi spazio temporale del segnale basata su singolo *voxel*, è stato messo a punto un indice di errore in grado di misurare la qualità dei risultati perfusionali. Tale indice è stato inoltre validato utilizzando esami i cui segnali apparivano alterati da differenti gradi di movimento del paziente. Dopo aver provato l'efficacia dell'indice nel rilevare singoli *voxel* associati a valori perfusionali non affidabili, sono state cercate su intere *slice* regioni affette da rumore strutturato, quali artefatti, o rappresentanti strutture fisiologiche, quali vasi e bronchi, normalmente escluse negli studi perfusionali. Sfruttando l'analisi orientata al *voxel* ed il medesimo indice di errore, è stato sviluppato un algoritmo adattativo specifico che ha consentito di rilevare tutte quelle regioni in modo automatico e di escludere i loro valori perfusionali da qualsiasi successiva elaborazione o considerazione clinica.

È pratica comune negli studi TCp fornire un unico valore mediato calcolato sull'intero tumore per ogni parametro perfusionale con lo scopo principale di ridurre l'incertezza dei dati ma con l'effetto secondario di trascurare la

variabilità dovuta all'eterogeneità tumorale, che rappresenta un'importante caratteristica per ogni valutazione clinica. Quindi, allo scopo di indagare la rappresentatività clinica dei valori perfusionali globali, sono state considerate lesioni tumorali complete ed è stato proposto un indice statistico in grado di identificare l'eterogeneità funzionale. Dopo aver rimosso tutti i valori perfusionali non affidabili, è stato dimostrato come un unico valore globale non possa essere rappresentativo ed anzi, possa fuorviare le conclusioni cliniche.

Infine, l'ultima parte della Tesi riguarda le attività portate avanti nel contesto del più ampio studio multicentrico europeo di TCp epatica. Innanzitutto vengono proposti diversi algoritmi sviluppati per il miglioramento del segnale e dell'accuratezza dei risultati perfusionali, così da rendere maggiormente comparabili gli esami TCp effettuati in Centri differenti. In seguito, vengono riportati e presentati alcuni interessanti risultati riguardanti i valori epatici di *baseline* e di *blood flow*, discutendo quanto diversi scanner TC possano eventualmente influenzare la riproducibilità dei risultati perfusionali. A partire da un'analisi approfondita riguardante l'elevato numero di differenze riscontrate nei protocolli effettivi di esecuzione degli esami TCp nei parametri di acquisizione e nella memorizzazione dell'informazione sono state infine fornite delle linee guida preliminari con lo scopo di aiutare a considerare in anticipo, prima della pianificazione dei protocolli multicentrici, tutte le possibili fonti di eterogeneità, comprese quelle implicite.

Contents

Abstract (English version)	xiii
Abstract (Italian version)	xv
Contents	xvii
1 Introduction and Thesis overview	1
2 Background and state of the art	7
2.1 Tumour angiogenesis and imaging biomarkers	7
2.2 Perfusion parameters in CTP	11
2.2.1 The perfusion parameters	15
2.2.2 Methods based on IDT	17
2.2.3 Methods based on the PCM	23
2.3 Clinical Application of CT perfusion in oncology	30
2.3.1 Correlation of CTP parameters with tissue angiogenesis .	31
2.3.2 The use of CTP parameters in diagnosis	31
2.3.3 The use of CTP in therapy monitoring and survival pre- dicting	34
2.4 Open issues in CTP	36
2.4.1 Lack of standardization	36
2.4.2 Radiation dose and Acquisition parameters	37
2.4.3 Repeatability and reproducibility	38
2.4.4 The problem of motion	40
2.4.5 Signal post-processing	40
2.4.6 Methods and models to compute perfusion parameters .	41
2.4.7 The analysis of results	43
3 Computation of CTP parameters	45
3.1 From image sequence to TCC	45

3.1.1	Denoising methods	46
3.1.2	Perfusion values computation	47
3.1.3	The fitting model	47
3.2	Goodness of fit: some error indexes	51
3.2.1	Temporal error indexes	52
3.2.2	Spatio-temporal error indexes	57
3.3	Automatic error thresholding	59
3.4	Quantitative assessment of perfusion local spatial coherence	65
3.5	Quantitative measurement of functional heterogeneity	67
4	A method to assess perfusion values reliability	71
4.1	Background	71
4.2	Validation of the temporal error index μ_ϵ	77
4.2.1	CTp examinations	78
4.2.2	Acquisition protocol	79
4.2.3	Image alignment	80
4.2.4	Validation procedure	81
4.2.5	Statistical analysis	83
4.2.6	Experimental results	84
4.2.7	Concluding remarks	91
4.3	An automatic method to detect unreliable perfusion values	92
4.3.1	CTp examinations	93
4.3.2	Acquisition protocol and data processing	93
4.3.3	Manual annotation	93
4.3.4	Comparison between annotated slices and thresholded error masks	94
4.3.5	Statistical analysis	95
4.3.6	Experimental results	96
4.3.7	Concluding remarks	101
5	Multi-slice analysis of <i>BF</i> values	103
5.1	Background	103
5.2	CTp examinations	105
5.3	Acquisition protocol and data processing	105
5.4	Statistical analysis	106
5.5	Experimental results	107
5.5.1	Baseline CTp	107
5.5.2	Follow-ups CTp	107

5.5.3	Baseline and FU CTp	111
5.6	Concluding remarks	114
6	PIXEL: a multi-centre study	115
6.1	The need for multi-centre studies	115
6.2	Technical issues in multi-centre studies	120
6.3	PIXEL data: early analysis	123
6.3.1	The DICOM files	124
6.3.2	The dataset	125
6.3.3	Volume slices: number and thickness	125
6.3.4	Pixel size	126
6.3.5	Acquisition protocol and time information	127
6.3.6	Tube current and voltage	130
6.3.7	Radiation dose	130
6.3.8	Administration of the contrast agent	131
6.3.9	CT scanners	132
6.3.10	Resuming of the acquisition parameters used in the dif- ferent Centres	132
6.4	Assessment of image quality	134
6.4.1	Frequency domain	135
6.4.2	Temporal domain	137
6.5	Some hints to set up of a CTp multi-centre study	146
6.5.1	Planning phase	147
6.5.2	Calibration phase	148
6.5.3	Training of medical and technical staff	148
6.5.4	Check of CTp examinations	148
6.5.5	Data analysis	149
7	PIXEL: a multi-centre study	151
7.1	Summary	151
7.2	Early prototype of rigid registration algorithm	157
7.3	Baseline	170
7.3.1	TACs computing methods	171
7.3.2	Baseline value computation	172
7.3.3	Baseline algorithm: preliminary test	177
7.3.4	Baseline values in a single Centre	184
7.3.5	Multi-centre study of baseline values	186
7.3.6	Concluding remarks	189

7.4	Computation of perfusion values	189
7.4.1	Single input <i>BF</i> values in normal liver	190
7.4.2	Dual input <i>BF</i> values in normal liver	197
7.4.3	Multi-centre study on single-input <i>BF</i> values	204
7.4.4	Multi-centre study on dual-input <i>BF</i> values	207
7.4.5	Concluding remarks	213
8	Conclusions	215
	Appendix	219
	List of Abbreviations	223
	List of figures	227
	List of tables	233
	Bibliography	235

Chapter 1

Introduction and Thesis overview

Cancer is among the leading causes of death worldwide [1]. Only in Italy, the Italian Association of Cancer Registries (AIRTUM) has forecasted 365000 new tumour diagnoses in 2016 alone (*i.e.*, about 1000 subjects per day) [2]. In particular, over the world the most common site of diagnosed cancer is lung, followed by breast and colonrectum [3]. Lung cancer is also the most common cause of tumour death [4], followed by liver cancer [3]. A peculiarity of this last kind of tumour is that, in the liver, metastatic cancers are more common than primary cancers. For instance, the liver is the most common site of metastasis from colorectal cancer (CRC) [5].

In the last few years, the worldwide risk of dying from cancer is globally decreased [6]. This improvement is also attributable to the introduction of the new anti-angiogenic therapies that, administered in combination with conventional chemotherapy (*i.e.*, cytostatic drugs) and radiotherapy, have shown to increase patients survival in several cancer types [7]. Differently from conventional anti-cancer therapies, the effects of anti-angiogenic treatments are visible earlier on tissue functional behaviour (*i.e.*, the vascular network of the tumour) and only later in time on morphology [8]. As a result, a lively interest has aroused around new perspective biomarkers, useful to monitor the status of tissue neovascularization and to evaluate the effects of anti-angiogenic therapies.

Computed Tomography perfusion (CTp) is an imaging technique that thanks to its wide availability, low invasivity, and capability to provide images with a high spatio-temporal resolution, results to be one of the most promising methodologies for the earlier assessment of the efficacy of the anti-angiogenic

therapies [9]. Through the analysis of the CTP sequences acquired, it is possible to compute perfusion parameters owing information regarding tissue vascularization. In particular, these perfusion parameters have shown to be useful to evaluate tumour neovascularization, characterize and differentiate tissues, monitor anti-angiogenic therapies, and predict patient survival in several cancer types [8, 10].

Despite the high potential shown by CTP in both cancer diagnosis and prognosis, there are still some open issues that have prevented the use of this technique in the standard clinical practice [8]. In this Thesis, I focus my attention on three topics related to the keywords reliability, standardization, and reproducibility of perfusion results. The first issue regards the lack of methods to evaluate perfusion results' accuracy and to detect the presence of non-systematic errors. In the literature, all the perfusion values achieved have always been considered reliable, even when affected by errors (*e.g.* caused by the presence of noise or artefacts), this constituting an obstacle for the achievement of repeatable perfusion results. The second issue is related to the low reproducibility of perfusion values, mainly caused by the huge amount of variability sources affecting CTP data and results. To face this problem, many authors have used global perfusion parameters, often computed as the average of voxel-based perfusion values found on a single tumour section or on the whole tumour. However, the higher reproducibility achieved by global values with respect to voxel-based ones is due to the averaging operation, that reduces sensibility of results to all the variability sources, tissue heterogeneity included, this weakening, if not jeopardizing the clinical relevance of results. The third and last issue regards the lack of standardization in both the acquisition and data processing protocols. This problem has been an obstacle to the set-up of multi-centre studies which are fundamental to introduce an imaging technique as a standard to be used in the clinical routine. Actually, the huge amount of inhomogeneities between data has even prevented the evaluation of perfusion values reproducibility computed on examinations acquired by using different Computed Tomography (CT) scanners.

The goal of my PhD activities was to face these issues to allow improving the CTP techniques to come to a more and more quantitative imaging (Chapter 3). In particular, the first issue has been faced by developing an automatic method to identify and exclude from the analysis those perfusion values computed on data particularly affected by noise or artefacts and thus considered to be unreliable. To this purpose, a fine-to-coarse strategy has been developed, which starting from the quantitative analysis of the signal coming

from the single voxel, was extended first to the single tumour section (Chapter 4) and finally to the whole lesion (Chapter 5). This technique, that has been applied to CTP examinations acquired in the same Centre and pertaining to patients with liver and lung cancer, permitted to obtain better perfusion results (*i.e.*, more reliable and repeatable) on which drawing clinical evaluations. The second issue has been faced by carrying out a deep analysis about the representativeness of global perfusion values used in the literature. To this purpose, a three step statistical analysis has been carried out to evaluate the representativeness of tumour and single section global perfusion values. In addition, an indicator of tumour functional heterogeneity has been proposed to evaluate whether perfusion values equivalences found out with statistical tests were numerical only or also owned a clinical significance (Chapter 5). The third issue was faced by deeply analysing data coming from the first CTP multi-centre study on liver and by carrying out a preliminary perfusion analysis. Through the analysis of the almost 400 examinations acquired in 15 different Centres, it was possible to identify all the intra- and inter-centre sources of variability affecting CTP data (and outcomes, accordingly) and to provide a sort of guidelines to correctly set-up this kind of studies (Chapter 6). In addition, data of different Centres acquired by using the same acquisition protocol were analysed to evaluate whether the use of different CT scanners could affect perfusion results (Chapter 7).

Besides the present introductory Chapter, this Thesis is organized in seven Chapters, all treating different aspects of the same matter. Accordingly, the experimental results are presented in Chapters 4, 5, 6, 7, pertaining to the specific topic of the related Section. The content of this Thesis is organized as follows:

- Chapter 2 contains the background and the state of the art regarding the use of CTP in oncology. Starting from the description of angiogenesis (*i.e.*, the key process driving tumour growth), it is possible to understand the increasing need for the assessment of anti-angiogenic therapies efficacy and why dynamic contrast enhanced (DCE) imaging techniques have become so important in oncology. A comparison between different DCE techniques is carried out to motivate why CTP represents one of the most suitable techniques for the evaluation of therapies' efficacy and of cancer's diagnosis and prognosis. Then, a summary of the main clinical results achieved through the analysis of CTP perfusion parameters is reported, with particular attention to lung cancers and liver tumours.

Finally, the most relevant open issues still delaying the use of CTP in the clinical practice are discussed.

- Chapter 3 starts going into the matter of this Thesis work and presents the main methods used to process and analyse temporal tissue signals. First of all, a discussion about the strategies selected to post-process CTP images and the extracted voxel-based signal which perfusion parameters are computed on is reported. Four temporal error indexes to evaluate the signal quality are then proposed and compared, motivating the reasons standing behind the choice of the error index selected for our studies. After that, two different methods to automatically find out a cut-off value between “good” signals and “bad” signals are presented. Finally, an index to assess tumour functional heterogeneity is proposed.
- Chapter 4 describes the analysis that has been carried out first on the signal of single voxels and, subsequently, on tumour sections. In particular, the temporal error index selected in Chapter 3 is validated as a marker of perfusion values unreliability. This has been done by exploiting signals of a different known quality that were achieved by building four different sequences for each patient, according to as many alignment methods for motion correction. Therefore, the analysis of CTP voxel-based signals has been shifted to slice level. The two automatic thresholding methods presented in Chapter 3 have been applied to the error values computed on the signals of whole tumour sections so as to find out the unreliable voxels to be excluded from the analysis. In particular, this procedure has shown to be able to automatically detect and exclude all those structures (*e.g.* bronchi, vessels, and artefacts) usually jeopardizing qualitative and quantitative perfusion analysis.
- In Chapter 5, the analysis carried out on the single tumour section has been extended to the whole lesion. A deep study regarding tumour heterogeneity representativeness of global and single-slice perfusion values used in the literature is carried out. In particular, the error and perfusion parameters are computed on each slice of the tumour, as well as the index presented in Chapter 3 and representing the tumour functional heterogeneity. Then, a three step analysis is carried out. First of all, the representativeness of the global perfusion values computed on the whole lesion with respect to those computed on the single slices was evaluated to verify whether and to what extent, the use of global perfusion values

could be representative of tumour single section. After that, the equivalence between perfusion of different sections of the same tumour was evaluated to verify to what extent single tumour sections could be representative of the whole tumour. Finally, spatial perfusion distribution is compared in tumours having the same global perfusion value to assess whether the use of one perfusion value computed over the whole tumour could be effective in clinical decision making.

- Chapter 6 deals with the analysis of data collected in the first CTP multi-centre study on liver. All the standardization issues related to the acquisition protocol are analysed as well as the intra- and inter-centre variability sources that could affect perfusion analysis. In particular, the implication of using different CT scanners or the variability introduced by different operators are discussed. Besides that, a quality image analysis of the CTP sequences acquired in different Centres is carried out for an early assessment of the possible inhomogeneities introduced by different CT scanners or acquisition parameters. Finally, a draft of possible guidelines regarding how a CTP multi-centre study should be carried out is presented.
- Chapter 7 describes all the methods that have been implemented to improve data and perfusion computation of multi-centre examinations to evaluate how the use of different CT scanners affect perfusion results. In particular, the algorithm to compute perfusion has been improved and adapted to the analysis of CT examinations of normal liver. An algorithm for liver ROIs registration on CT images has been implemented in its early stage. In addition, a method to correctly compute baseline values (*i.e.*, the tissue density value before the arrival of contrast agent), which are of a fundamental importance to achieve accurate perfusion values has been developed and tested against the most common methods used in the literature. After that, baseline values of examinations acquired in different Centres have been computed and compared to evaluate whether and to what extent the use of different CT scanners affects baseline values. Finally, tests on perfusion values computed on patients of a single Centre and of different Centres have been carried out to assess and analyse single and dual-input hepatic perfusion values in patients with CRC and to evaluate whether the use of different CT scanners affects the computed results.

- Concluding remarks and hints for possible future works are reported and discussed in Chapter 8.

The work developed in this Thesis has been carried out within the:

- Computer Vision Group (CVG), Advanced Research Center on Electronic Systems (ARCES), University of Bologna, Italy. Director: Prof. Alessandro Bevilacqua

in partnership with the following institutions:

- Diagnostic Imaging Unit, Istituto Romagnolo per lo Studio e la cura dei Tumori (IRCCS-IRST), Meldola (Forlì-Cesena), Italy. Director: Dr. Domenico Barone
- Department of Radiology, Beaujon Hospital, Clichy, France, Director: Prof. Valérie Vilgrain

The activities discussed in this Thesis pertain to two projects:

- PERFECT - Automatic analysis of hepatic and lung PERFusion through the use of CT-4D image reconstruction
- PIXEL - Perfusion IndeX: Evaluation for Liver metastases

In particular, I spent the first two years to implement and validate the error indexes and the thresholding methods presented in Chapter 3 and discussed in Chapter 4 that permitted to achieve reliable perfusion values. During the second year I also started working on the analysis regarding the representativeness of global perfusion values often adopted in the literature with respect to tumour heterogeneity. Instead, during the last year I mainly focused my attention on data regarding the multi-centre study and carried out analyses and experiments presented in Chapters 6 and 7 to evaluate whether the use of different CT scanners affects the outcomes of perfusion examinations. The methods developed and the results obtained have been partly published in four scientific journals, five international and four national conference proceedings. In addition, they have been also presented in three oral communications.

My 3-year PhD programme in Bioengineering was granted by the Italian Minister of Education, Universities and Research (in Italian, MIUR).

Chapter 2

Background and state of the art

Tumour angiogenesis is the hallmark of cancer capability to develop and metastasize. In the last few years, several tumour anti-angiogenic drugs have been developed, arousing interest around minimally invasive imaging techniques that have shown promising capability to assess the effects of these new therapies. CTP is one of the imaging techniques mostly investigated to this purpose. The analysis of the signal that can be extracted from each tissue voxel of the CT image sequence allows the computation of perfusion parameters connected to tissue angiogenesis. Despite the clinical usefulness of CTP has been demonstrated in several studies, some open issues prevent its application in the clinical practice.

In the next paragraphs of this Chapter, all these aspects will be taken into account and discussed to allow a better understanding of this PhD Thesis work.

2.1 Tumour angiogenesis and imaging biomarkers

The term “angiogenesis” is used to describe the process of new vessels formation that is essential for the embryologic development, the normal tissue growth, and tissue reparation [11]. Angiogenesis regularization happens at a molecular level and is driven by several factors, the principal of which is the vascular endothelial growth factor (VEGF) [12].

Some pathologies, such as cancer, are able to interfere with the cellular angiogenesis regularization factors giving origin to abnormal vascular networks. Gene mutations inside tumour cells indeed, cause the release of new regular-

ization factors that perturb the regular angiogenesis process [13] entailing the creation of new vessels that are more dilated, tortuous, and permeable than the normal ones [14]. Moreover, the coexistence of multiple cancer genetic subpopulations provokes variable degrees of neovascularization in different tumour types [15]. All these features contribute to improve the degree of tumours heterogeneity that has a deep influence on lesion's growth and response to anti-cancer therapies (*i.e.*, chemotherapy, radiotherapy, and immunotherapy) [14, 16].

Angiogenesis has become the hallmark of tumour capability to develop and metastasize and the target for the production of new anti-cancer therapies [17]. Anti-angiogenic drugs able to inhibit vascular tumour growth (*i.e.*, anti-VEGF) have been then widely developed in the last few decades [7]. The administration of these therapies also in combination with conventional chemotherapy and radiotherapy have shown to increase patients survival for several cancer types. A positive impact on patients overall survival (OS) and progression-free survival (PFS) has indeed been found in cancer of the lung [18, 19], liver [20, 21], colon-rectum [22, 23], kidney [24, 25], breast [12, 26], and ovary [27, 28]. Despite these encouraging results, there are also some studies that did not observe any significant improvement in survival due to anti-angiogenic drugs administration. This is the case of breast cancer [29] and CRC [30, 31]. Moreover, there are some tumour sites such as pancreas, prostate, and skin in which anti-angiogenic therapies have only a limited impact on OS [32]. Several studies have thus been carried out to try understanding the mechanism which anti-angiogenic drugs are based on and improving their efficacy accordingly [33, 34]. At the beginning, it was hypothesized that anti-angiogenic agents would have destroyed tumour vessels, depriving cancer from oxygen and nutrient necessary to its growth [35, 36]. However, this would have also prevented drugs to reach the tissue, this yielding an increasing tumour hypoxia, a well-known marker of poor response to therapies [37] and patient OS [38]. Further on, it was found that anti-angiogenic drugs act as a vascular normalization factor, remodelling the network of vessels to a normal vasculature, hence permitting a higher drug delivery [33]. Anyway, the mechanism by which the anti-angiogenic therapies are able to improve survival over chemotherapy alone is still not fully clear [39].

The development of anti-angiogenic drugs brings about the need for biomarkers able to evaluating the status of the tissue neovascularization process and to monitoring the effects of anti-angiogenic therapies. The most widely used methods to assess the efficacy of chemoterapeutic agents are the Response

Evaluation Criteria in Solid Tumour (RECIST) [40] and RECIST 1.1 [41], besides the World Health Organization (WHO) criteria [42]. All these criteria are uniquely based on the evaluation of changes on lesions number and size, by measuring the long-axis of the lesion in one (in case of RECIST or RECIST 1.1) or two (in case of WHO) dimension. Anyway, due to their non-cytotoxicity, the anti-angiogenic drugs aim at normalizing the vascular network of cancers without necessarily influencing tumour size and affect morphology quite a long time after functional changes happened [8]. This is the reason why the conventional criteria characterizing treatment response may not be effective and there is a need for new and more effective biomarkers [15, 43].

The *in vivo* biomarkers that can be used to evaluate angiogenesis can be of two types: direct or indirect ones [44, 45]. An ideal direct biomarker would be the microvessel density (MVD) that has shown a good correlation with poor prognosis and tumour metastases [46]. However, biopsy requires taking a tissue sample, an invasive procedure of limited applicability and effectiveness to provide a direct measure of biomarkers. In fact, due to its invasiveness, biopsy cannot be used with the frequency needed to monitor angiogenesis and to assess therapies effects [47]. In addition, only a very small portion of tissue is analysed, thus making biopsy prone to error sampling and inter-observer variability and not suitable for the analysis of highly heterogeneous tissues, accordingly [48]. The need of more appropriate and accurate biomarkers aroused interest towards indirect biomarkers, in particular derived from DCE imaging techniques, which are able to provide perfusion parameters correlated to the tissue vascular characteristics. DCE imaging techniques are indeed non-invasive methods able to assess the microcirculatory function of the investigated tissues [49, 50] and the tumour response to therapies, earlier than permitted with techniques based on morphological changes only [8]. All the DCE imaging techniques are based on the same principle, that is the measurement of tissue and vascular enhancement over time obtained by acquiring images of the same sample before, during, and after the administration of a contrast agent (CA). Finally, the application of apposite kinetic models, and methods, on the signal extracted from the images allows computing perfusion parameters [51]. More details regarding the perfusion parameters and the methods used for their computation are provided in Sects. 2.2.1 and 2.2.2, respectively.

The main DCE imaging techniques that have been used in the characterization and assessment of tumour angiogenesis are:

- DCE CT
- DCE magnetic resonance imaging (MRI)
- DCE ultrasound (US)
- Positron-emission tomography (PET)

The main features of these imaging techniques are resumed in Table 2.1.

Dynamic imaging techniques					
Technique	Morphologic information	Functional information	Availability	Cost	Other features
DCE-CT	Very good	Very good	High	Medium	Exposure to ionizing radiation Toxicity of CA Attenuation proportional to CA concentration
DCE-MRI	Very good	Very good	Low	High	Versatility in pulse sequences
DCE-US	Medium	Good	Very high	Low	Highly operator dependent Limited depth of penetration
PET	Very bad	Good	Very low	High	Radiation exposure High toxicity of CA Emission proportional to CA concentration

Tab. 2.1: Main features characterizing the most used functional imaging techniques.

DCE-CT is undoubtedly one of the most used imaging techniques for angiogenesis evaluation. The main strong point of this technique is its capability of providing high spatial-temporal resolution data, this favouring the achievement of high quality morphological and functional information [9]. Moreover, the wide availability and the low-cost of this technique has fostered its spread and use [49]. Despite its lower availability and higher costs, DCE-MRI is another widely used technique. Similarly to DCE-CT, DCE-MRI provides very high spatial-temporal data, but without exposing patients to ionizing radiations [52]. Nonetheless, DCE-MRI is a highly versatile technique since it allows choosing between several pulse sequences. As drawbacks, this methodology results to be very complex and the signal provided is not directly proportional to CA concentration inside tissue [9]. Another used imaging technique is the DCE-US. This low-cost and widely available technique also provides functional information without releasing any ionizing radiations [52]. However, besides suffering from intra- and inter-observer variability, DCE-US suffers from technical limitations such as the low depth of tissue penetration and a lower quality

of the morphologic information provided [53]. As regards nuclear medicine, one technique used is PET, that is high sensitive to signal variations even with very low quantities of CA, is capable to provide metabolic information and provides a signal that is directly proportional to the concentration of CA inside tissue. Nevertheless, this technique has many drawbacks such as high cost, radiation exposure, technical complexity, and lack of morphological information [9]. In addition, differently from the imaging techniques previously discussed, PET does not directly investigate the vascular system. This causes in some cases apparent divergent assessments of tumour physiology with respect to perfusion parameters obtained using DCE-CT, DCE-MRI, or DCE-US [54]. To overcome some of the above mentioned drawbacks, the use of combined PET and DCE-CT is discussed in the literature more and more frequently. In fact, joining together morphological and functional information of DCE-CT with metabolic one provided by PET, it is possible to gather these complementary information in one, very effective, tool [55]. However, the very long time needed for examinations and the extremely high costs [16] limit its use.

2.2 Perfusion parameters in CTP

Perfusion has been defined as the transport of blood to a unit volume of tissue per unit of time [56]. The first publication regarding the use of DCE-CT to quantify perfusion (*i.e.*, CTP) dates back to 1980 [57]. In that study, the author proposed for the first time a method to compute the blood flow (BF) of the brain in healthy patients. However, in those years both image acquisition and data processing were too slow to allow the technique to become widely accepted. At the beginning, CTP has been used only in perfusion studies of the myocardial and the kidney [51]. The turning point arrived with the introduction of two technical innovations: the use of multiple detector rows and of slip rings. The former allowed improving the z -coverage of the analysed tissue for each gantry rotation [58], while the latter allowed continuous rotation of the x-ray tube by removing all the fixed connections of the rotating components. These innovations permitted faster image acquisitions and the introduction of the helical (or spiral) scan mode. Differently from the “classic” acquisition modality (the axial mode), where the image acquisition occurs in static conditions, in the helical scan mode the patient table is continuously moved while the image acquisition goes on, allowing the acquisition of a tissue volume rather than separate tissue slices [59]. The spread of CT systems

equipped with multiple detector rows and slip rings allowed the diffusion and the use of CTP in several diseases with particular success in acute stroke and oncology [54].

To enable the computation of perfusion parameters, CTP relies on four principles:

- the repetition of image acquisition of the same tissue portion
- the administration of a “short and sharp” bolus of iodinated CA
- the selection of at least one vessel supplying the analysed input
- the application of proper methods and kinetic models to extract signal and compute perfusion parameters

The repetition of image acquisition of the same tissue portion before, during, and after the administration of CA shows the attenuation changes caused by CA arrival which are related to tissue perfusion [60]. In particular, by using a iodinated CA the tissue attenuation changes are directly proportional to CA concentration inside tissue that are thus easily measurable [61]. At the beginning, tissue contrast enhancement is mainly due to the arrival of CA in the intravascular (IV) space. As time goes on, CA gradually moves by passive diffusion from the IV to the extravascular (EV) and the extracellular spaces, and the tissue contrast enhancement is due to the presence of CA within both the blood vessels and the interstitial space [13]. These two phases can be observed in the tissue signal that can be extracted from the CTP image sequences. By placing a region of interest (ROI) on the analysed tissue, it is then possible to extract a time concentration curve (TCC) from each voxel of the ROI. Therefore, this time signal is composed by the density values, expressed in Hounsfield Units (HU), assumed by a specific voxel of the ROI in different time instants. Since the HU values are directly proportional to the quantity of CA within the IV and the EV space of a voxel in a specific time instant, the shape of the TCCs reflects the passage of CA inside tissue [62].

CA has to be administrated in a small quantity and at a high flow rate in order to obtain a “short and sharp” bolus [63], needed to allow a more accurate computation of perfusion parameters [61]. Moreover, the increase of the iodine delivery rate helps reducing the dose and, in case of organs with a dual blood supply (*e.g* liver and lung), permits to better identify the two tissue enhancement portions of the signal caused by CA bolus coming from the two different vascular input [64].

The third requirement of CTP is the selection of at least one vessel nourishing the analysed tissue. By placing a ROI inside the selected input vessel (usually an artery such as the aorta), and by averaging the density values inside the ROI of each acquisition time instant, it is possible to obtain a single TCC that will be “compared” with the tissue TCCs in order to compute perfusion parameters [8]. Several recommendations about the correct choice of the input vessel and the positioning of the ROI have been made in the literature. The selection of a feeding vessel big enough to prevent partial volume effects causing the underestimation of the input signal, is highly recommended [63]. Moreover, originally it was suggested to place the arterial ROI as close as possible to the analysed tissue in order to reduce time delay effects and achieve more accurate perfusion parameters. However, recently several algorithms have been developed in order to correct for this delay and this requirement is thus not so mandatory [65]. In organs characterized by a dual-input blood supply such as liver and lung, it is possible to place a ROI on each vascular input. This means that in the liver it is possible to draw a ROI on the aorta (or on an hepatic artery) and one on the portal vein [8], while in the lung it is possible to place one ROI on the aorta and a second one on a pulmonary artery [66]). In Figure 2.1, there is an example of the ROIs that can be drawn

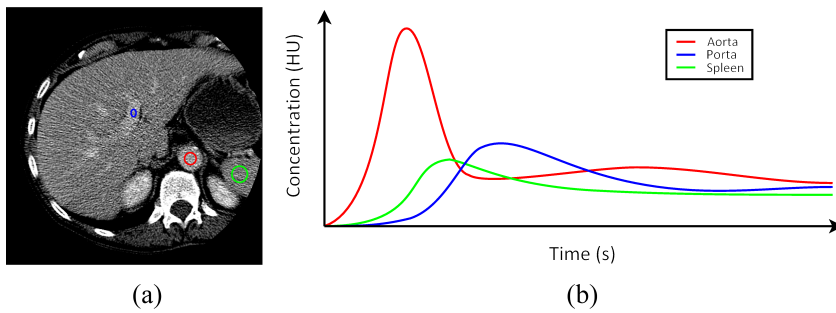


Fig. 2.1: A liver CTP image with ROIs placed on aorta (in the red colour), portal vein (in the blue colour), and spleen (in the green colour) (a) and the averaged TCCs extracted from each ROI (in the same colours) (b).

in the liver in order to consider a dual vascular supply. In these organs, the use of a single input instead of two means assuming that the tissue vascular supply is predominantly arterial and accepting that a systematic underestimation of perfusion values occurs (as it is reported in [67] for the lung and in [68] for the liver). The use of two input allows improving the reproducibil-

ity of perfusion results, the characterization of tissues, and the assessment of treatment response. Indeed, in a study of 7 patients with liver tumours it was observed that perfusion results obtained by using two input were more reproducible than those computed by considering a single input only [68]. Moreover, the computation of perfusion parameters achievable only by considering two vascular input allowed to differentiate malignant and benign lung lesions [69] and to distinguish hepatic tumour from normal liver tissue [70, 71]. Perfusion parameters achieved with dual-input were also used by Ohno *et al.* in order to predict response to chemio and radiotherapeutic treatments and the OS of 53 [72] and 66 [73] patients with non-small cell lung cancer (NSCLC). Or else, by analysing these parameters, Wei-Fu *et al.* [74] found a threshold value able to predict patient survival after therapies administration. However, the possibility to consider a dual-input blood supply in the perfusion analysis strictly depends on the z -coverage of the CT system and on the acquisition protocol adopted. Indeed, as reported in [75] for liver and in [76] for lung, by using a narrow volume coverage or an inappropriate field of view (FOV), it is not always possible to acquire in the same image both the tissue being studied and the two vascular input. If the two input vessels are not present in the CT images, one input only has to be considered.

The last principle which CTP is based on is the application of apposite kinetic models and methods to the arterial and the tissue TCCs in order to compute perfusion parameters [52]. All the models applied assume that the tissue behaves as a linear and time-invariant system. This means that the output of the system (*i.e.*, the tissue) to multiple stimuli (*i.e.*, the arrival of CA bolus from different input) is equal to the sum of the tissue response to the single stimuli separated. Moreover the response of the system is considered constant in time, independently from the time instant in which the stimulus is applied. On the base of these assumptions, two different theoretical concepts on which the models and the methods to compute perfusion parameters are based, have been developed [61]: the indicator dilution theory (IDT) and the pharmacokinetics compartment models (PCM).

In the next paragraph (Sect. 2.2.1), a summary of the physical and biological meaning of the main used perfusion parameters is reported. Instead, Sects. 2.2.2 and 2.2.3 report the principal methods and models used to compute perfusion parameters on the base of IDT and of PCM principles.

2.2.1 The perfusion parameters

CTp permits the calculation of several perfusion parameters, depending on the kinetic model or method applied to the signal. By assuming that CA does not diffuse from the IV space (*i.e.*, modelling tissue as a single-compartmental model) it is possible to measure the BF , the blood volume (BV), and the mean transit time (MTT). On the contrary, by assuming that CA can join the EV space (*i.e.*, apply a model with more than one compartment) it is also possible to assess the permeability surface (PS), the extraction fraction (EF), and the k^{trans} . The way by which each of these parameters is related to the pathology features of tumour angiogenesis and to the effects that the anti-angiogenic drugs have on the vascular network is complex [8]. In this paragraph, the main quantitative perfusion parameters used in literature are summarized as well as their physical meaning and how they are supposed to enable the assessment of tumour angiogenesis and the evaluation of tumour response to therapies.

BF has been defined as the transport of blood to a unit volume of tissue per unit of time and is expressed in $ml/min/100ml$ or in $ml/min/100g$ [52]. Its value tends to increase with the increase of MVD [60]. In organs characterized by a dual vascular supply, it is possible to compute BF values separately for the two contributions. For instance, in the liver there are the arterial BF (aBF) and the portal BF (pBF) while in the lung there are the bronchial BF and the arterial BF . The total BF value can then be achieved as the sum of the two partial BF values and a perfusion index (PI) can be computed to quantify the influence of the two blood supplies over the total BF [77].

BV measures the volume of blood flowing in the tissue, including blood inside arteries, arterioles, capillaries, venules and veins. BV is usually measured in $ml/100ml$ or $ml/100g$ [52]. As BF , the BV value increases with higher MVD [60].

MTT represents the mean time taken by the blood to transit through the tissue vascular network (from arteries to veins) and it is expressed in seconds (s) [60]. This parameter is not directly extracted from the kinetic models, but it is derived from BF and BV values (see Sect. 2.2.2).

PS measures the product between the permeability and the total surface of the capillary endothelium in a unit mass of the tumour and is expressed in $ml/min/100 ml$ [78, 79]. As reported in Sect. 2.1, abnormal vessels generated after a gene mutation show a poorly formed vascular basement membrane characterized by a high permeability [14].

EF has the same unit of measure as PS , but it represents the fraction of CA arriving at the tissue that leaks into EV space in a single passage through the vasculature. Like PS , EF is directly related to the permeability of the analysed vessels to CA [78, 79].

Finally, k^{trans} is the constant flow rate of CA from IV to EV space and is expressed in min^{-1} [78, 80].

The combination of these parameters allows making important evaluations about the analysed tissues. For instance, the increase of BF and BV values can point out the presence of newly formed vessels if PS assumes high values, or the presence of mature vasculature if PS value is normal or low. On the contrary, low BF and BV values can indicate the presence of necrosis or inflammation, whether they are coupled with low or high PS values, respectively [81].

All these parameters are usually represented through the use of colorimetric perfusion maps, such as that reported in Figure 2.2 (c) together with a full

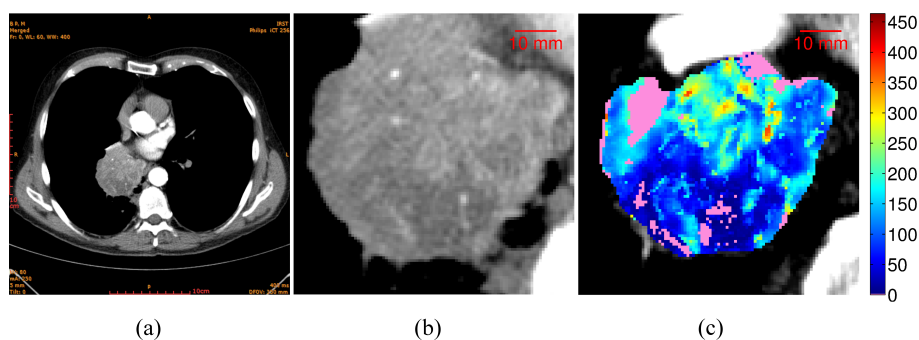


Fig. 2.2: Lung CTP image (a), the lesion magnified (b), and relative BF colorimetric map (c).

slice (a) and the magnified lung lesion (b). Here, blue colours are used to highlight the regions with the lowest perfusion while red colours indicate the highest perfused areas. Instead, the pink colour is used to point out unreliable BF values (Sect 4.2). This way of visualizing results is particularly useful since it permits a first visual analysis of the perfusion parameters and the assessment of spatial correlation and functional heterogeneity.

Another category of perfusion parameters providing semi-quantitative measures exists and are sometimes adopted in perfusion studies. For instance, the “area under the curve” (AUC) is related to BF and the quantity of CA administered, and it is computed as the integral of the tissue TCC. Also, the “peak enhancement” is connected to BV and corresponds to the peak of the tissue

TCC, while the “time to peak” is related to BF and represents the lag between CA administration and the peak enhancement [82]. However, these measurements are very sensible to differences in iodine sensitivity of CT systems and depends upon several factors such as the arterial input function, patient’s central hemodynamics, and their weight [83]. Quantitative measurements such as those discussed above are consequently often preferred.

2.2.2 Methods based on IDT

IDT considers tissue as a “black box” and consequently analyse the system without making any morphological or physiological assumption [84, 85]. In general, the output of a system can be described by the convolution between the input function and the impulse response function of that system. By considering the organ or the tissue investigated as the system, its input and output functions correspond to the concentration of CA in the arterial inflow $C_a(t)$ (in mg/ml) and the venous outflow $C_v(t)$ (in mg/ml), respectively. Instead, $h(t)$ is the probability density function of CA particles and, in practice, represents the distribution of transit times required by the molecules of CA to move from the entrance to the exit of the system, by whatever path. The relation between $C_v(t)$ and $C_a(t)$ can thus be described as in Eq. 2.1:

$$C_v(t) = h(t) \otimes C_a(t) = \int_0^\infty h(t - \tau) C_a(\tau) d\tau \quad (2.1)$$

Since, for the principle of mass conservation, all tracer particles entering the system sooner or later leave it, the AUC of $h(t)$ is unitary, as reported in Eq. 2.2:

$$\int_0^\infty h(t) dt = 1 \quad (2.2)$$

Moreover, since $h(t)$ is the frequency function of transit times, by definition, MTT is given as its first moment, as described in Eq. 2.3 [61]:

$$MTT = \int_0^\infty th(t) dt \quad (2.3)$$

However, since usually there are no a-priori information about the vascular network, $h(t)$ is unknown and MTT cannot be computed directly from Eq. 2.3.

In the particular case of a system with a single input and a single output, as that depicted in Figure 2.3, it is possible to apply the Fick principle, describing the law of mass conservation. In particular, the Fick principle states that $Q(t)$,



Fig. 2.3: Outline of a single input and single output mono-compartmental model.

the rate at which the quantity of CA (expressed in mg) accumulating in an organ at any time t , depends on the organ BF , $C_a(t)$ and $C_v(t)$ [47], and it is described by Eq 2.4:

$$\frac{dQ(t)}{dt} = BF \cdot C_a(t) - BF \cdot C_v(t) \quad (2.4)$$

However, venous outflow cannot be correctly measured by DCE imaging techniques since the outflow vessels are too small if compared with the spatial resolution of CT scanners. The measurement of $C_v(t)$ would then be an underestimation of its true value, due to partial volume effect [61, 86]. Therefore, since the use of DCE imaging techniques only permits to measure regional BF within a tissue or an organ, the Fick principle has to be reinterpreted. In particular, $Q(t)$ is the mass concentration of CA in tissue (expressed as percentage in mg/g) and BF is the specific BF of that tissue (in $ml/min/g$).

In order to compute BF parameters, two methods exist. While the first one is based on the use of an additional assumption, the second one directly faces the convolution problem through the use of Eq. 2.1. Both these methods are presented below.

After the injection of CA, there is a period of time during which CA remains inside tissue. During this period, it is possible to make the assumption of no venous outflow (*i.e.*, $C_v(t) = 0$), and this is the assumption which the first method is based on to compute perfusion parameters. Hence, Eq. 2.4 can be rewritten as follows:

$$\frac{dQ(t)}{dt} = BF \cdot C_a(t) \quad (2.5)$$

and consequently, assuming that the rate of tracer accumulation is maximal when the arterial concentration is maximal, we can write Eq. 2.6:

$$\left[\frac{dQ(t)}{dt} \right]_{Max} = BF \cdot [C_a(t)]_{Max} \quad (2.6)$$

With the acquisition of rapid series of CT images, it is possible to extract BF from Eq. 2.6 and compute it as the rate between the maximum slope of the tissue TCC (computed on the increasing portion of the TCC identified during the first pass phase) and the peak height of the arterial TCC as shown in Eq. 2.7 [61]:

$$BF = \frac{\left[\frac{dQ(t)}{dt} \right]_{Max}}{[C_a(t)]_{Max}} \quad (2.7)$$

This method to compute BF is known as the **maximum slope method** (MSM) or simply **slope method** and has been validated in liver [87, 88], kidney [89], pancreas [90], and brain [91, 92]. Figure 2.4 shows ideal aortic

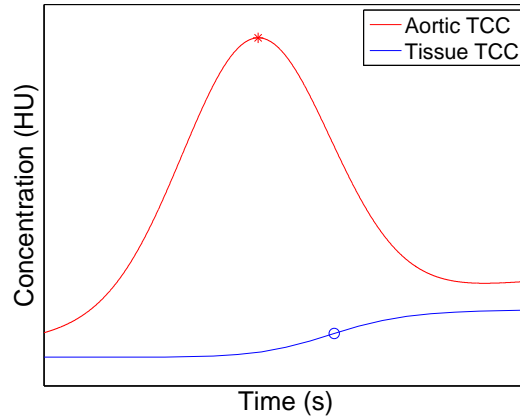


Fig. 2.4: Representation of the aortic TCC (in the red colour) and of a tissue TCC (in the blue colour). The red star indicates the aortic peak while the blue circle highlights the point of maximum slope of the tissue TCC.

and tissue TCCs with two markers in correspondence of the time points where the parameters needed by the MSM (*i.e.*, the aortic peak and the maximum slope) have to be computed. The MSM can be applied also in biological systems with a dual-input supply as the one schematized in Figure 2.5. In these cases, the MSM is applied two times, by considering the contribution of the two input functions separately. For instance, as regards the hepatic district, while CA brought by the arterial input directly flows into the liver, CA arriving through the portal vein arrives later, since it passes through the spleen first. Therefore, usually the peak time of the splenic TCC is considered as the separating time threshold between the two different TCC portions. Indeed, while the enhancement of the tissue TCC before the splenic peak is

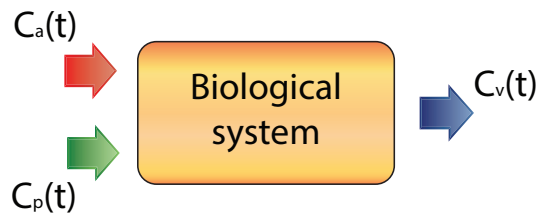


Fig. 2.5: Representation of a dual-input and a single-output mono-compartmental model.

considered to be caused predominantly by the arterial input, the part after is mainly attributed to the portal vein. MSM is then applied twice according to what depict in Figure 2.6. The first time, it is carried out on the first part of

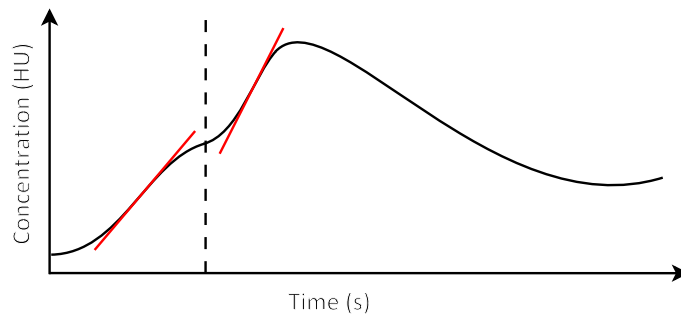


Fig. 2.6: Typical tissue TCC of a dual-input system with the two portions separated by the dotted vertical line and the two maximum slopes highlighted by the red lines.

the tissue TCC by using the aorta or an hepatic artery as the vascular input, and the second time on the second part of the tissue TCC using the portal vein as the vascular input [8]. The same procedure can be used in the lung by considering the left atrium peak as the time separator of the two tissue TCC portions: the pulmonary portion before the peak, and the bronchial portion after [76].

The main strong points of MSM are the mathematical, numerical and conceptual simplicity. Nevertheless, the assumption of no venous washout does not hold any more at the time instant when the tissue maximum slope is computed. In fact, in some cases where the tissue is highly perfused and lowly vascularized or the administered bolus of CA is not “short and sharp”, it may

happen that part of CA starts leaking from the tissue *before* the maximum slope time instant. In these cases, if the venous outflow is relevant, BF will be underestimated [61, 86]. However, thanks to its easy implementation and to its versatility, this method has been implemented in several commercial software [52] and it is currently widely applied to several body districts such as lung [73], liver [93], kidney [94], and pancreas [95].

The second method based on IDT and known as **deconvolution** method, avoids the assumption of no venous outflow by solving the inverse process of convolution. To well understand this method, the impulse residual function $R(t)$ has to be introduced. $R(t)$ (represented in Figure 2.7) is a function

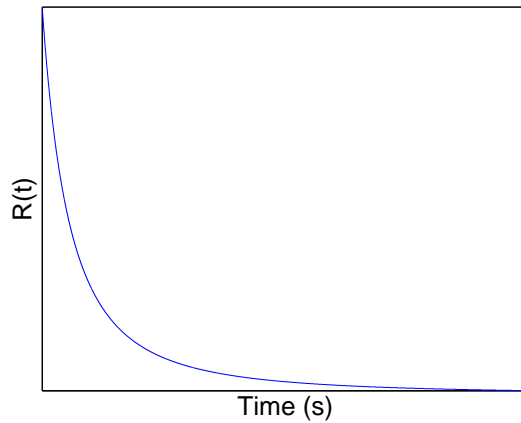


Fig. 2.7: Input residual function $R(t)$.

describing the quantity of CA still inside tissue at time t and can be written through Eq. 2.8:

$$R(t) = 1 - \int_0^t h(\tau) d\tau \quad (2.8)$$

By considering Eqs. 2.1 and 2.4 and thanks to $R(t)$, it is possible to express the relation between $C_a(t)$ and the tissue concentration $C_t(t)$ through Eq. 2.9 (see Appendix 8 for more details):

$$C_t(t) = BF \cdot R(t) \otimes C_a(t) \quad (2.9)$$

When CA is still in the IV network it is possible to solve the deconvolution problem and extract the flow-scaled $R(t)$, that is the product $BF \cdot R(t)$ [47]. The value of BV and BF can be extracted as the area and the maximum height of the kernel $BF \cdot R(t)$, respectively [61, 86]. By applying the central volume

principle [84], it is finally possible to compute MTT as the rate between the area and the maximum height of the flow scaled $R(t)$:

$$MTT = \frac{BV}{BF} \quad (2.10)$$

Like MSM, the deconvolution technique allows considering the dual vascular input. This can be done by describing the vascular input as the combination between the two blood supplies. In particular, by introducing PI , the total input of the system $BF \cdot C_a(t)$ can be written as described in Eq. 2.11:

$$BF \cdot C_a(t) = PI \cdot C_a(t) + (1 - PI) \cdot C_p(t) \quad (2.11)$$

Therefore, Eq. 2.9 can be rewritten as in Eq. 2.12:

$$C_t(t) = [PI \cdot C_a(t) + (1 - PI) \cdot C_p(t)] \otimes R(t) \quad (2.12)$$

where $C_p(t)$ is the concentration of the second vascular input [77].

Although the deconvolution method has been validated in cerebral studies both against microspheres [96] and stable xenon [96, 97], it presents several drawbacks due to its numerical properties. Indeed, while the convolution operation gives a unique result, the inverse problem is ill-posed and returns multiple solutions, all mathematically approximating the result of the convolution between $C_t(t)$ and $C_a(t)$, but with some of them having no physiological meaning and without knowing the right one [86]. To solve this problem, additional assumptions on the shape of $R(t)$ or correction methods have to be applied. Several methods have indeed been proposed to achieve more correct results [98, 99]. The most spread in literature include the use of Wiener filter on the Fourier transform of the deconvolution problem [100] and the application of regularization methods such as the truncated singular value decomposition [101, 102] and the Tikhonov regularization method [102, 103]. A further problem of deconvolution is due to its sensitivity to bolus dispersion and delay. Indeed, to reach the tissue analysed, CA has to pass through vessels and microvessels of different dimension and length, this causing a delay and a dispersion of the bolus measured inside the arterial input. Therefore, since the shape of the function $R(t)$ extracted from deconvolution reflects properties of both vasculature and tissue, CA delay and dispersion will affect $R(t)$ shape and in turn the obtained perfusion values [104, 105]. Many studies have thus been conducted in order to reduce the side effects of this issue and to permit

a more accurate estimation of perfusion parameters [106, 107]. Despite deconvolution approach is complex and still shows some limitations, this technique has been widely implemented and it is currently adopted in several perfusion studies [108, 109, 110].

2.2.3 Methods based on the PCM

The alternative method to IDT to analyse the tracer kinetic is PCM. While in IDT the tissue is considered as a black box, in PCM, some assumptions about the physiology of the analysed tissues are taken into account.

To better understand this part and the terminology used, it is important to have clear in one's mind the tissue physiological fluids and their classification, represented in Figure 2.8. Indeed, fluids can be subdivided in the two macro-

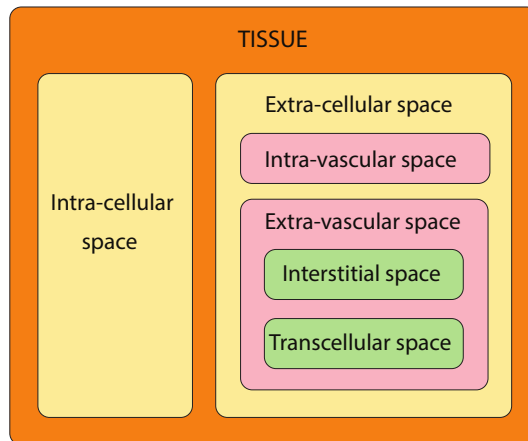


Fig. 2.8: Classification of the fluids inside a physiological tissue.

categories of intra- and extra-cellular fluids. Moreover, the extra-cellular fluids in their turn can be subdivided in IV and EV fluids. IV fluid is constituted by blood plasma, while EV fluid is made of the interstitial and the transcellular fluids. However, since the volume of the transcellular fluid is very low and often negligible, EV space can be considered as made by the interstitial fluid only. For this reason, EV is often called interstitial space.

Differently from IDT, in PCM tissue is described by several interacting compartments, each reflecting a different state of the administered CA. Each compartment is characterized by the same kinetic status as CA [105] and it can be assumed as being either *well-mixed* or *plug-flow*. In the first case, the

concentration within the compartment is assumed to be spatially uniform at any given time (Figure 2.9 (a)), meaning that CA spreads and diffuses inside

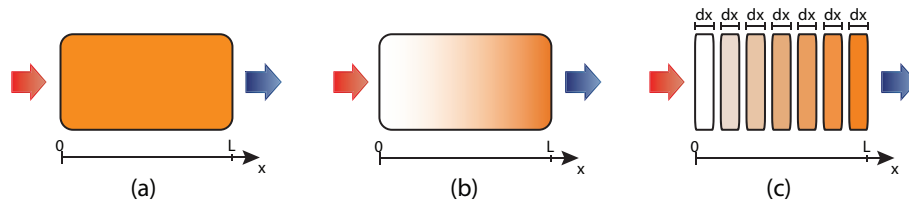


Fig. 2.9: Example of a well-mixed (a) and a plug-flow (b) compartment, referred to a generic time instant t_i where CA is distributed uniformly and following a gradient (from $x = 0$ to $x = L$), respectively. Finally, the plug-flow compartment in (b) has been further subdivided in infinite single compartments, each having a different constant spatial concentration (c).

the compartment instantaneously. On the contrary, in case of a plug-flow compartment, the concentration of CA is considered to be spatio-temporally variant, following a gradient (Figure 2.9 (b)). In particular, it is assumed that CA is carried on through a tube, whose length is parametrised by x (*i.e.*, ranging from $x = 0$ to $x = L$). For instance, this assumption may hold when describing the status of CA inside the capillary bed, whose diffusion from arteriole to venule takes a finite time and is not uniform immediately along the whole vessels path [62, 111]. The concentration inside the compartment is both temporally and spatially-dependent. Therefore, in order to mathematically describe the system, the tube is subdivided into a series of small cylindrical sections discs with infinitesimal height $dx \rightarrow 0$, that are rings with an inner constant spatial concentration (*i.e.*, practically discs), so as that each disc can be considered as a single compartment (Figure 2.9 (c)) [111].

In the following paragraphs, the main PCM used in the literature to evaluate perfusion parameters are briefly described. Starting from the single-compartment model, the next paragraphs consider models composed by even more compartments, up to four. However, this section is mainly focused on the single- and two-compartment models which are those mostly used in the literature.

The **dual-input single-compartment model** (2I1CM) is characterized by one well-mixed compartment, two vascular input and a single output (Fig-

ure 2.5). This model can be described by the following differential equation:

$$\frac{dC_t(t)}{dt} = k_{1a} \cdot C_a(t) + k_{1p} \cdot C_p(t) - k_2 \cdot C_t(t) \quad (2.13)$$

where the parameters k_{1a} and k_{1p} represent the arterial and the portal inflow rate constant, respectively, and k_2 is the outflow rate constant of the system. By solving Eq. 2.13 for $C_t(t)$, it is possible to write Eq. 2.14:

$$C_t(t) = \int_0^t [k_{1a} \cdot C_a(T - \tau_a) + k_{1p} \cdot C_p(T - \tau_p)] \cdot e^{-k_2 \cdot C_t(t-T)} dT \quad (2.14)$$

where τ_a and τ_p are the delay parameters representing the transit time of CA from aorta and portal vein to the tissue, respectively. By fitting tissue TCCs with the model described in Eq. 2.14 and exploiting a minimization of the fitting errors to achieve the best fitting, it is possible to compute the values of the parameters k_{1a} , k_{1p} and k_2 for that fitting curve. aBF , pBF , and MTT can thus be achieved according to Eqs. 2.15, 2.16, and 2.17:

$$aBF = \frac{k_{1a}}{EF} \quad (2.15)$$

$$pBF = \frac{k_{1p}}{EF} \quad (2.16)$$

$$MTT = \frac{1}{MTT} \quad (2.17)$$

Since EF in the liver can be assumed as being unitary [112], aBF and pBF correspond to k_{1a} and k_{1p} , respectively. This model has been validated against microspheres by Materne *et al.* [112] in the liver and has been used in several hepatic perfusion studies, such as [113, 114]. However, 2I1CM could be used also in case of a single vascular input, by assuming $k_{1p} = 0$. Therefore, starting from Eq. 2.14, it is possible to obtain the following model:

$$C_t(t) = \int_0^t k_{1a} \cdot C_a(T - \tau_a) \cdot e^{-k_2 \cdot C_t(t-T)} dT \quad (2.18)$$

Therefore, in this case, aBF represents the total BF value of the organ and corresponds is equal to k_{1a} . Nevertheless, this model has been mainly applied to dual input systems.

The **two-compartment exchange model** (2CXM) describes the plasma and the interstitial spaces as two well-mixed compartments (Figure 2.10). Since it is assumed that EV exchanges CA with IV only, to fulfil the mass

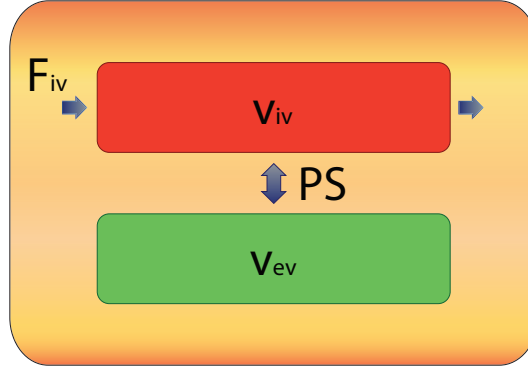


Fig. 2.10: Schematic representation of 2CXM, where F_{iv} is the plasma flow, v_{iv} and v_{ev} are the volume of the plasma and the interstitial space, respectively and PS is the permeability surface between the two compartments.

conservation principle (stating that no CA accumulates in the system), the exchange of CA between the two compartments is the same in both directions. The equation of the model can be then written according to Eq. 2.19:

$$v_{ev} \cdot \frac{dC_{ev}(t)}{dt} = PS \cdot C_{iv}(t) - PS \cdot C_{ev}(t) \quad (2.19)$$

where C_{ev} and C_{iv} represent CA concentration in EV and IV, respectively, and v_{ev} is the EV volume. This model has been first applied to CT perfusion studies [115], but recently its application has been extended to MRI perfusion studies [116, 117].

The **tissue homogeneity model** (THM) is similar to 2CXM, but it describes the plasma space as a plug-flow system (Figure 2.11). However, this model has not been widely adopted since the differential equations defining the model does not have a time-domain solution [111]. To solve this problem, the **adiabatic approximation to the tissue homogeneity model** (AATHM) has been proposed by Lee [118]. The only difference between this model and THM is the assumption that CA cannot pass through the capillary walls (*i.e.*, $PS = 0$) in all spatial points other than $x = L$ (as shown in Figure 2.12). IV and EV can thus be respectively described by the two following differential equations (Eq. 2.20 and Eq. 2.21):

$$\frac{v_{iv}}{L} \frac{\partial C_{iv}(x, t)}{\partial t} = -F_{iv} \cdot \frac{\partial C_{iv}(x, t)}{\partial x} \quad (2.20)$$

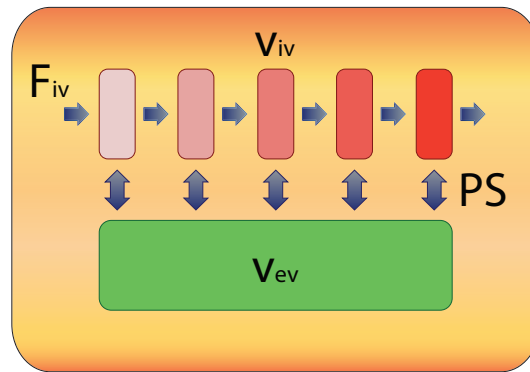


Fig. 2.11: Schematic representation of THM. Here, the plasma compartment is represented as a plug-flow system.

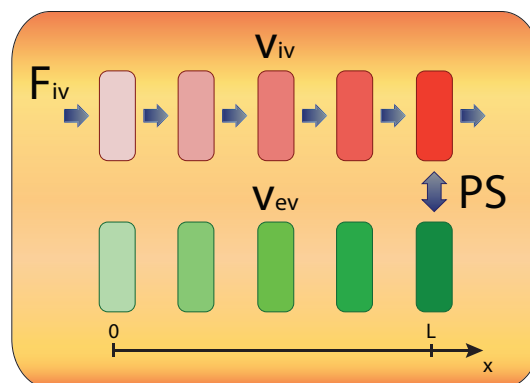


Fig. 2.12: Schematic representation of AATHM. The plasma compartment is represented as a plug-flow system and CA exchange occurs only at $x = L$.

$$v_{ev} \frac{dC_{ev}(t)}{dt} = PS \cdot C_v(t) - PS \cdot C_{ev}(t) \quad (2.21)$$

where v_{iv} is the IV volume, $C_v(t)$ is the plasma concentration at the venous outlet, supposed to be equal to $C_{iv}(L, t)$, and F_{iv} is the plasma flow (*i.e.*, the volume of plasma entering a unit of tissue volume per unit of time, expressed in $ml/min/ml$). AATHM has been implemented in commercial software [52] and, as such, it has been widely used [119, 120].

The **distributed parameter model** (DPM) assumes that both the compartments are plug-flow (Figure 2.13). The interstitial space is thus modelled

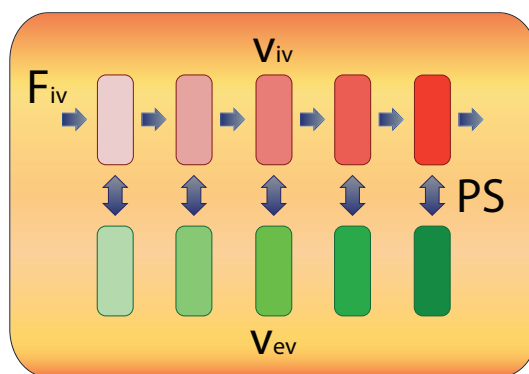


Fig. 2.13: Schematic representation of DPM. Here, both plasma and interstitial compartment are represented as plug-flow systems.

as a series of infinitesimal compartments which interact only with the neighbouring capillary walls. Consequently, in this model both C_{iv} and C_{ev} depend on the spatial position where they are measured. DPM is described by Eq. 2.22:

$$v_{ev} \frac{dC_e(x,t)}{dt} = PS \cdot C_{iv}(x,t) - PS \cdot C_{ev}(x,t) \quad (2.22)$$

DPM has been validated with microspheres [121] and it has been recently applied mainly for the evaluation of liver perfusion [122, 123].

The two-compartment models presented above permit to evaluate the value of four parameters: F_{iv} , PS , v_{iv} , and v_{ev} . However, due to their complexity, the use of simpler models with two- or three-parameters has been often preferred. These simpler models are derived from the four-parameter two-compartmental models described above through the formulation of further assumptions on at least one of the four parameters [82]. The three simplified two-compartment models mainly used in the literature are presented below.

The **Tofts Model** (TM) [124] assumes that the IV space is negligible (*i.e.*, $v_{iv} = 0$) and can be described as in Eq. 2.23:

$$C_t(t) = k^{trans} \cdot e^{-\frac{k^{trans}}{v_{ev}t}} \otimes C_a(t) \quad (2.23)$$

An extension of TM is the **extended Tofts Model** (eTM) that can be derived by the compartmental model discussed above, through the assumption of infinite F_{iv} (*i.e.*, highly perfused tissues). This assumption allows considering $C_a(t)$ equals to $C_{iv}(t)$ and k^{trans} equals to PS . The eTM can be described by Eq. 2.24 :

$$C_t(t) = v_{iv} \cdot C_{iv}(t) + k^{trans} \cdot e^{-\frac{k^{trans}}{v_{ev}t}} \otimes C_a(t) \quad (2.24)$$

In TM, only k^{trans} and v_{ev} can be assessed, while in eTM it is also possible to evaluate the v_{iv} value. Despite the accuracy of these parameters highly depend on the tissue hemodynamic status, that is often unknown in advance [125], both these two- and three-parameter models are often currently applied [116, 126, 127, 128].

On the contrary, the **uptake model** is based on the assumption that due to high v_{ev} or low PS , $C_{ev}(t)$ is much lower than $C_{iv}(t)$ and hence the outflow from the interstitial space is negligible. This model can be derived from any of the four-parameter models previously discussed by imposing the condition $C_{ev} = 0$. This three-parameter model allowing to evaluate F_{iv} , PS , and v_{iv} [82] is not so diffused in CTP. However, the **Patlak model** that can be derived by the uptake model, assuming F_{iv} as an infinity quantity, has been widely adopted. In Patlak model, $C_{iv}(t)$ is considered equal to $C_a(t)$, while k^{trans} is equal to PS . From Eq. 2.25:

$$C_t(t) = v_{iv} \cdot C_{iv}(t) + k^{trans} \otimes C_a(t) \quad (2.25)$$

it is thus possible to extract v_{iv} and k^{trans} [129, 130]. By imposing $X(t) = \frac{\int_0^\infty C_a(\tau) d\tau}{C_a(t)}$, and $Y(t) = \frac{C_t(t)}{C_a(t)}$ it is possible to rewrite Eq. 2.25 in the simpler form:

$$Y(t) = v_{iv} + k^{trans} \cdot X(t) \quad (2.26)$$

Thanks to the possibility of linearise Eq. 2.25 and thus to solve the problem graphically [129, 130], Patlak model is highly attractive. Indeed, this model has been implemented both in in-house and commercial software and widely adopted in several perfusion studies [131, 132, 133].

Some few perfusion studies using three [134, 135] and four [135] compart-

mental model have been proposed in the literature. However, due to their complexity caused by the high number of compartments and of parameters considered, the use of these models have still not gain a wide success in CTp perfusion studies.

Table 2.2 presents a brief summary of the main features regarding the discussed methods to compute perfusion parameters.

Kinetic models and methods used to compute perfusion parameters					
Principle	Method/Model	NC	Parameters	Assumptions	Complexity
IDT	MSM	1	BF	No venous outflow	Low
	Deconvolution	1	BF, BV, MTT	Assumptions about the shape of $R(t)$	High
	2IICM	1	aBF and pBF	well-mixed compartment	Medium
	2CXM	2	$F_{iv}, PS, v_{iv}, v_{ev}$	IV and EV are well-mixed	Medium
	THM	2	$F_{iv}, PS, v_{iv}, v_{ev}$	IV is plug-flow and EV is well-mixed	High
PCM	AATHM	2	$F_{iv}, PS, v_{iv}, v_{ev}$	IV is plug-flow, EV is well-mixed, and the exchange of CA occurs only at venous end	High
	DPM	2	$F_{iv}, PS, v_{iv}, v_{ev}$	IV and EV are plug-flow	High
	TM	2	$k^{trans}, v_{iv}, v_{ev}$	$F_{iv} \approx \infty$ and $v_{iv} \approx 0$	Low
	eTM	2	k^{trans}, v_{ev}	$F_{iv} \approx \infty$ or $v_{iv} \approx 0$	Medium
	Patlak model	2	k^{trans}, v_{iv}	$C_{ev} < C_{iv}$	Low

Tab. 2.2: Main features of the most commonly used methods and models: the principle on which they are based on, the number of compartments (NC) they consider, the perfusion parameters they yield, the assumptions which they are based on, and their complexity level.

2.3 Clinical Application of CT perfusion in oncology

CTp has proved to be a very useful tool in several clinical applications. Several very recent reviews [10, 136, 137, 138, 139, 140, 141], have been indeed published gathering clinical results obtained through the use of CTp. This paragraph resumes the main clinical results achieved by exploiting CTp parameters in several body districts, with a special focus on lung and liver, which are the two organs dealt with in this Thesis.

2.3.1 Correlation of CTP parameters with tissue angiogenesis

One of the main reasons for which DCE imaging techniques were introduced in the oncology research is the needs for tools able to assess tumour angiogenesis. To this purpose, CTP parameters showed to be well correlate with several angiogenesis biomarkers (*e.g.* MVD or VEGF) in cancer of lung [142], liver [143], prostate [144], kidney [145], head and neck [146], and soft tissues [147]. In particular, in the lung cancer a significant correlation between MVD and BV [142, 148] and also between MVD and BV [149] was found in patients with several tumour subtypes. In two more studies on the lung cancer carried out by Ma *et al.*, a correlation between MVD and the perfusion parameters was found also for PS [150] and MTT [151]. Moreover, in this last work a great correlation between VEGF and BF , BV , PS , and MTT was also reported [151]. As regards liver tumours, a significant correlation was observed between VEGF receptor 2 and BF , BV , and the hepatic PI (HPI) [143]. The arterial and the total BF instead, resulted to be correlated with both MVD [71] and the level of circulating IL-8 [152]. However, discrepancies between results were found in CRC. Indeed, while Goh *et al.* [153] found correlation between PS , BV , and MVD, in two more recent works [154, 155] no significant correlations could be found between MVD and BF , BV , MTT , PS , and k^{trans} . A possible reason why these results do not agree can be found in [155]. In this work, Dighe *et al.* suggest that while CTP parameters aim at measuring tumour functional characteristics, the MVD is based on the morphological count of all vessels, some of which could not even be perfused.

2.3.2 The use of CTP parameters in diagnosis

Cancer diagnosis and therapeutic decision making strictly depend on the information that a clinician is able to achieve as regards extension, stage, grade, and stratification of tumours. By using conventional imaging techniques, cancer tissue often does not show features allowing distinguishing it from healthy tissues. Detection and assessment of tumour extension is consequently rarely possible with conventional imaging techniques and, when so, it is often not possible to characterize the tissue as benign or malign. Of course, assessing both tumour grade and stage that have shown to be correlated with tumour aggressiveness and prognosis, and that are therefore fundamental for the choice of the therapy on the decision making process, is quite impossible with the use

of conventional imaging [82]. On the contrary, CTP has shown to be effective in characterization, differentiation, and estimation of tumour grade and stage. Several perfusion parameters have indeed shown to be significantly different if measured in the tumour or in the normal tissue. For instance, BF and PS in the prostate [156] and BF , BV , and PS in the kidney [157] showed to be significantly higher in tumour than in the surrounding tissue. Moreover, BF , BV , PS , and MTT were found to be significantly different in the pancreas [133] and in the colon-rectum [158]. In the liver, things are more complicated due to the effects that tumour progression has on liver blood supply. It is well-known indeed that the evolution of hepatocellular nodules in hepatocellular cancer (HCC) cause a decrease in the pBF and an increase in the aBF and in the HPI [8]. This was observed in several studies comparing normal liver with metastases from CRC [70] and normal liver with HCC [71, 159]. Opposite results were obtained for the global BF value in the comparison between HCC and normal tissue. Indeed, while Yang *et al.* [71] found global BF value lower in HCC than in normal liver, Ippolito *et al.* [159] found the global BF value higher. Anyway, BF value is not the only marker that have been identified to characterize liver tumours. Indeed, by analysing liver metastases from endocrine tumours, Lefort *et al.* [160] found that BF was significantly higher and MTT was significantly lower in metastatic tissue than in normal liver. Also Frampas *et al.* [161] observed a significant difference between MTT values computed in HCC and in the surrounding normal parenchyma. Wang *et al.* [123] instead, found as a characterization marker the PS value that resulted to be significantly higher in the metastases from neuroendocrine tumours than in the normal liver.

Completely different is the case of lung nodules detection. Thanks to the high density difference between lung normal tissue (that typically ranges between -700 and $-900HU$ [162]) and lung nodules (usually between -200 and $200HU$ [163]) it is not so difficult to detect the presence of abnormal tissue mass even with conventional imaging techniques. However, density alone cannot allow differentiating between benign and malignant lung nodules [164]. To this purpose, CTP has shown to be very useful by proving that benign and malignant nodules are characterized by significantly different perfusion values. This was demonstrated for BF , BV , EF in [165, 166], for BF , BV , PS in [167], and for the pulmonary PI in [76]. Further studies also taken into account the inflamed tissue were carried out by Li *et al.* [168] and Ma *et al.* [151]. Both the authors found that BF and BV were able to discriminate benign nodules from inflamed tissue and malignant nodules. However, none of these two

parameters was significantly different to enable a differentiation between the inflamed tissue and the malignant nodules. A solution to this issue was proposed by Li [168], that also investigated PS . This last perfusion parameter indeed, showed significant differences between inflamed tissue and malignant nodules, thus enabling their discrimination. The combined use of BF and PS , or of BV and PS can thus yielding a complete discrimination between inflamed tissue, benign and malignant solitary lung nodules. CTP parameters have also shown a great differentiation capability in the colon-rectum to distinguish between cancer and diverticulitis [158] and in pancreas to differentiate adenocarcinomas and masses forming pancreatitis [133].

Another important feature necessary to make a correct diagnosis is the knowledge of tumour subtypes. In this way, CTP has also shown good performance in kidney to identify papillary renal cell carcinoma, chromophobe renal cell carcinoma and angiomyolipoma [157], and in the liver to discriminating between HCC, hypo-vascularized, and hyper-vascularized metastases [169]. Heterogeneous results were instead found as far as the differentiation of lung cancer subtypes was concerned. Li *et al.* [148] did not find any significant differences between BV values computed in adenocarcinomas, squamous cell carcinomas, large cell carcinomas and small cell carcinomas. Similar results were obtained by Spira *et al.* [149], that analysed BF and BV in adenocarcinomas, squamous cell, and small cell lung cancers. On the contrary, a more recent research of Nguyen-Kim *et al.* [170] addressing dual vascular supply pointed out a significant difference of BF values in some tumour subtypes. In particular, BF was found to be lower in adenocarcinomas than in squamous cell carcinomas and large-cell carcinomas, while in large-cell carcinomas the bronchial BF resulted to be significantly higher than in adenocarcinomas. Instead, Fraioli *et al.* [171] by using a single vascular input, found significant differences in BV values of large cell carcinoma, adenocarcinoma and squamous cell carcinoma.

Other two information needed to make a correct and accurate diagnosis are tumour staging and grading. Capability of CTP to assess tumour staging has been drawn in prostate [172] and in head and neck [173] cancer. On the contrary, the study by Reiner *et al.* [145] on renal cell carcinoma did not show any correlation between tumour stage and BF , BV , and k^{trans} . As regards tumour grading, a good efficacy of CTP was observed in colorectal [154], prostate [172], brain [174], and pancreas [175] cancer. Worse results were instead obtained for kidney, liver, and lung cancer. In particular, the results obtained in kidney varied based on tumour types. In the same year, Reiner *et al.* [145] did not obtain any correlation between renal cell carcinoma grade and BF , BV , and

k^{trans} , while Zhang *et al.* [176] shown the capability of BV to differentiate between high and low grade of clear cell carcinoma. In the liver, a study enrolling 52 patients with HCC did not found any correlation between tumour grading and aBF , pBF , total BF , HPI , and BV . In lung, both Nguyen-Kim *et al.* [170] and Li *et al.* [148] did not found any correlation between tumour grading and the perfusion parameters being tested (*i.e.*, PI in [170], and BF , BV , MTT in [148]). However, opposite results were achieved in a larger study carried out by Spira *et al.* [149] that observed a correlation between lung cancer grade and BF values in 72 patients with several different subtypes of lung cancer. In this study indeed, lower values of BF corresponded to a higher tumour grade.

2.3.3 The use of CTP in therapy monitoring and survival predicting

Another important issue for which DCE imaging techniques have been introduced is the assessment of anti-angiogenic drugs efficacy and the early prediction of their outcome. In a recent work, Prezzi *et al.* [177] report how the effects of anti-cancer therapies can be evaluated by using BF , BV , PS , and EF . Indeed, the standard chemotherapy and the vascular disrupting agents, provoke the reduction of BF , BV , PS , and EF values, while the administration of radiotherapy produces their reduction only after an initial increase. The administration of angiogenesis inhibitor only affects the values of PS and BF , which first increase and then diminish. All these effects have been observed in several studies regarding different body districts. For instance, the administration of Bevacizumab and radiotherapy has been found to cause a reduction in BF , BV , and PS values of the soft tissues sarcomas [147]. A decrease of BF values was observed in neuroendocrine tumours after the administration of Bevacizumab and Everolimus [178], in esophageal cancer after chemoradiation therapy [179] and in chest and abdomen after the administration of a combination of AZD2171 and gefitinib [180]. In a study regarding advanced HCC a decrease of BF , BV , and PS was observed after the administration of bevacizumab in combination with gemcitabine and oxaliplatin [181]. In NSCLC, the administration of sorafenib and erlotinib caused a decrease of BF value [182], while the use of chemotherapy combined with anti-angiogenic drugs (*e.g.* paclitaxel and bevacizumab) caused a significant reduction of BF and PS values in advanced lung adenocarcinoma [183], large cell carcinoma, adenocarcinoma, and squamous cell carcinoma [171].

CTp has also shown to have a great prediction capability of patient survival

with cancer in several body districts. Perfusion parameters have been capable of discerning the patients responding to therapy from those who did not in soft tissues sarcomas [147], in esophageal [179, 184], oropharynx [185], and lung cancer. In particular, in NSCLC BF was significantly different between responders and non responders in [73, 182, 186], while the total tumour BV was identified as the most effective indicator in [187]. Instead, significant differences in both BF , BV , and PS values were found in the advanced lung adenocarcinoma between responders and non-responders patients [183]. As regards the liver, different results were achieved by Frampas *et al.* [161] and Jiang *et al.* [181] through the analysis of different perfusion parameters. In 11 patients with advanced HCC, treated with sorafenib and suritinib, Frampas did not find any significant differences at baseline between BF , BV , MTT , and PS values between RECIST progressors and non-progressors (measured at month one and two). On the contrary, Jiang *et al.* [181] found that the k^{trans} value measured in 23 patients with HCC and treated with bevacizumab and GEMOX-B was significantly different in responders and non-responders. In that case, k^{trans} could be considered as a biomarker predicting patients response.

CTp parameters also showed to correlate with OS in cancer of esophagus [179, 184], colon-rectum [188], rectum [189], pancreas [190], brain [191], liver [74], and lung [39, 72]. The relation between CTp parameters and PFS was demonstrated in oropharynx [185], liver [181] and lung [182] cancer. As regards the lung, in a recent study Hayano *et al.* [192] did not notice any correlation between OS or PFS and BF , BV , and MTT values computed in 35 patients with NSCLC. These results are at the opposite of those obtained in the two studies on NSCLC found in by Wang *et al.* [186] and Li *et al.* [193], which confirmed the capability of CTp parameters to predict both patient OS and PFS. The main difference between these studies is in the perfusion parameters considered. In the work of Wang *et al.*, PS was the marker of survival, which was not computed by Hayano *et al.*. Differently, Li *et al.* considered a dual vascular supply and identified the marker of survival in the bronchial BF , while Hayano computed perfusion values by using a single input only.

A further final improvement brought by the use of CTp is the assessment of perfusion parameters' capability to predict the development of metastases, as it was shown in two studies on CRC [194] and rectal cancer [189].

2.4 Open issues in CTP

Despite CTP has shown to be a very promising technique in the oncological field for its capability to assess angiogenesis, characterizing and differentiating tissues, monitoring therapies, and predicting survival of tumours in several body districts (Sect. 2.3), it has not been applied in the clinical practice yet. Several issues concerning the CTP examinations are still open and needs to be dealt with. These issues regard different phases of the process involved in the achievement of correct perfusion results, from CT images acquisition till the computation of perfusion parameters. Some of the steps have already been faced in literature, some at last partially, while some others have still to be addressed. The main ones are:

- the lack of standardization in both acquisition and data analysis protocols
- the definition of the acquisition parameters in function of the radiation dose
- the lack of repeatability and reproducibility of perfusion results
- the presence of patient motion
- the application of the most correct post-processing procedure
- the selection of methods and models to compute perfusion parameters
- the way to analyse the reliability of perfusion results

All these issues are discussed in the following subsections.

2.4.1 Lack of standardization

One of the most critical issues of CTP is the lack of standardization in both acquisition and data analysis protocols. In fact, this issue prevents the widespread use of CTP [8], the comparison of results obtained in different clinical studies [111], and the implementation of multi-centre studies [111, 195].

The problem of the lack of standardization has been addressed by Miles *et al.* in [83]. The Delphi process involving several DCE-CT experts allowed the development of guidelines addressing various aspects of the acquisition and the data analysis protocols. The first issue that has been faced regards CT scanner requirements. Indeed, the limited z -coverage has been one of the many

limitations of CTP up to the recent advances of CT systems. In fact, until a few years ago the need of examinations with a high temporal resolution limited the width of the studied volume, that had to be limited to a single section, or a few sections, only [63, 54]. The introduction of CT machines endowed with 256 or 320 detector rows and capable to acquire images at a high temporal resolution in both axial and helical modalities, allowed achieving a wider z -coverage and performing the analysis of the whole tumour or of multiple lesions present inside an organ [81]. In addition to the indications on CT scanner requirements, the work in [83] also returns recommendations regarding the acquisition protocol to be followed, the CT system quality assurance (that should be carried out on phantoms before beginning each clinical trial), and the results that should be presented in a CTP study.

Despite the useful recommendation given in [83], several aspects of CTP acquisition and processing protocols still needs to be faced. Indeed, without knowing exactly the effects that a variation of acquisition parameters would cause on results, the use of different acquisition protocols would prevent the comparison of results obtained in different CTP studies and the set-up of multi-centre studies. In particular, multi-centre studies are essential before introducing an imaging technique as a standard to be used in the clinical routine. This issue is addressed in Chapter 6, where through the analysis of data coming from a CTP multi-centre study on liver, it has been possible to draw some preliminary guidelines about the set-up of multi-centre studies.

2.4.2 Radiation dose and Acquisition parameters

The reduction of radiation dose is one of the main challenges of CTP. Due to the cancer risk associated to radiation exposure, the dose delivered to patients should be decreased as much as possible, without compromising the quality of the achieved perfusion results [83]. The radiation burden is associated to the CT tube current and voltage (and finally to mAs), and to the number of “volumes” acquired. The decrease of tube current and voltage allows reducing the radiation dose administered to the patient [131] at the expense of the quality of results [8]. The reduction of detected signal results in increased noise levels [64] and in artefacts from beam hardening [8] that can significantly affect the quality of the computed perfusion values. A possibility to face this problem and reduce image noise is increasing the slice thickness and lowering the resolution of the reconstruction filters. However, this would lower the image spatial resolution [196]. Another possible solution to reduce the overall

radiation dose is to diminish the number of images acquired by shortening the duration of the examination or by decreasing the sampling frequency. However, the diffusion of CA inside tissue and its spread out of the IV space take a finite time and the use of too short duration acquisition sequences could not allow monitoring these events, hence yielding possibly misleading perfusion values. This is yet more true for those perfusion parameters such as PS and EF describing CA exchange between two or more compartments [54]. On the other hand, the radiation dose reduction by decreasing the sampling frequency leads to a poorer image temporal resolution, this affecting the accuracy of the computed perfusion parameters. This is particularly true for those perfusion parameters computed by using methods based on the IDT, such as MSM, for which having a high temporal resolution is of fundamental importance [197]. However, independently from the method adopted, the exposure reduction has unavoidable consequences on the acquired image quality and on the accuracy of perfusion results computed on those data. A trade off between heavily side effects associated to the received radiation dose and benefits deriving from the clinical information coming from CTP thus needs to be found [81]. Actually, several perfusion studies have been carried out in order to estimate perfusion parameters quality achieved by using low-dose acquisition protocols [131, 198, 199]. However, at present there are no precise guidelines about the exact method to adjust acquisition parameters in order to guarantee a satisfying image quality and a “low” radiation dose for each patient [83].

2.4.3 Repeatability and reproducibility

Repeatability and reproducibility of perfusion parameters are mandatory prerequisites of CTP technique to enable its use in the clinical practice. In the last few years, some studies have been carried out to this purpose. For instance, Sahani *et al.* [200] found a high correlation and a low variability between BF , BV , MTT , and PS values computed on two consecutive CTP image sequences acquired at 30 hours time distance in 4 patients with HCC. Low differences between BF , BV , MTT , and PS values were also found by Goh *et al.* [201] in two consecutive CTP examinations performed in 48 hours on ten patients with CRC. Two different studies were instead carried out on lung to assess perfusion parameters reproducibility by using different z -coverage [202, 203]. In both these works, ten patients with lung cancer underwent two consecutive CTP scans (repeated within 24 hours) and the median BF and PS values were computed on both a single slice and four adjacent tumour sections. A greater

reproducibility of perfusion parameters was achieved by computing them on analysing a wider volume coverage. Two more studies [204, 205] were finally performed to assess reproducibility of perfusion parameters with respect to the acquisition time length of the examination and the application of motion correction methods. Seven patients with liver tumour [204] and 10 patients with lung cancer [205] underwent CTP examination. In both the studies, results obtained in lung cancer, in tumour liver, and in normal tissue resulted to be more reproducible by using longer acquisition scan and by applying the motion correction algorithm. These findings were particularly true for *PS*. Indeed, as discussed in Sect. 2.4.3, to achieve a correct value, *PS* has to be computed on long acquisition sequences. Of course, using long acquisition time results in unavoidable patients respiratory motion, this requiring motion correction algorithms to reduce data variability.

Despite the encouraging results obtained in the studies discussed above, a lot of work still needs to be carried out. The activities can be resumed in two main tasks. First of all, it is important to analyse repeatability and reproducibility in a wider number of patients to achieve a higher statistical significance of results. Thereafter, it is necessary to carry out multi-centre studies that use examinations acquired in different Centres and therefore with different CT scanners, which can propagate differences on protocols and so on [8, 83]. These two tasks have been partly addressed in Chapter 7, where almost 400 liver CTP examinations acquired in 19 different Centres have been considered for perfusion analysis, although 87 examinations have been analysed at the end.

In addition, in order to achieve a correct and effective assessment of repeatability and reproducibility of perfusion results, it is also necessary to consider voxel-based perfusion values, instead of global ones (used in the works discussed above). Employing mean or median operators allows obtaining more repeatable and reproducible results that, however, cannot take into account local spatial heterogeneity of tissues analysed (see also Sect. 2.4.7). To also consider tissue's spatial features, it is therefore necessary to perform a voxel-based analysis, that however is much more sensible to the presence of random and systematic errors caused by both image acquisition and data analysis [206]. Indeed, the presence of noise, artefacts, and anatomical structures (*i.e.*, bronchi and vessels) can jeopardize the reliability of the computed perfusion parameters and, in turn, their repeatability. The fact that in the literature, all the perfusion values achieved have always been considered reliable, disregarding the presence of model or numerical errors, has represented a huge obstacle

to the achievement of repeatable perfusion results. Consequently, the lack of indexes to assess perfusion results accuracy and to detect and quantify at least the non-systematic errors is a crucial point for the achievement of repeatable results. Developing tools to assess results reliability is thus necessary in order to go towards large-scale trials [195]. This issue is faced in Chapter 4.

2.4.4 The problem of motion

Motion has always represented a great issue to be faced in CTP studies. Both voluntary (*e.g.* respiratory motion) and non-voluntary (*e.g.* peristaltic motion) motion can bring to voxel-based TCCs composed by signals coming from different tissue portion and consequently lead to incorrect perfusion results. Respiratory motions are those causing the most significant consequences on TCCs' quality and mainly affect tissues of the upper abdomen and thorax [81]. This issue has ever been very challenging, especially in those studies using CT scanners permitting a narrow z -coverage only. In these cases, indeed, the motion of tissue out of the FOV causes data loss [63]. Several approaches have been proposed in the literature to cope with this issue, the principals of which are: the use of immobilization devices and hypotonic agents, the acquisition of images in breath-hold conditions (that anyway can be limited in time), and the adoption of motion correction methods [52]. The use of motion correction algorithm has shown to yield more reproducible perfusion results [204, 205] and to be necessary to achieve reliable results, otherwise the examinations should have to be discarded [207]. Also the guidelines in [83] suggest the use of motion correction algorithms and recommend to exclude from the analysis those images particularly affected by patient motion. This issue has been partly faced in Sect. 7.2, dealing with the early prototypic algorithm for automatic motion correction of liver CTP images I have developed.

2.4.5 Signal post-processing

The application of spatio-temporal filters to the CT images and to the TCCs allows correcting for the presence of acquisition noise, discretization errors, and motion artefacts. However, the lack of guidelines about their application can cause variability in the results obtained through the use of different post-processing procedures [83]. As regards the spatial domain, the median filters with kernels of size 3 [208] or 5 [209, 210] are the most used, since they are effective on removing noise while preserving geometric structures present in the

images. However, the literature also reports the use of smoothing filters, such as the weighted means [211, 212], that cannot preserve edges as median filters do. Instead, as for the time domain, smoothing filters and fitting methods are often applied to the TCCs. To this purpose, Moreira *et al.* [213] proposed the use of a 7-point moving average filter to analyse cerebral CTP images. This temporal filter was selected between the moving average, the moving median, and the smoothing filter as the one showing the best trade-off between application simplicity and goodness of results achieved. Instead, 3-point moving average filters were adopted in CTP studies of the myocardium [211] and on simulated liver TCCs [214]. In particular, in the work of Romano *et al.* [214] the aBF values were computed by using three different methods of temporal smoothing. The moving average method applied to the simulated TCCs resulted to be superior to the other two methods based on parametric fitting strategy. To achieve denoised signal indeed, it is also possible to apply parametric and non-parametric fitting techniques. The former relies on assumptions regarding the diffusion model of CA inside the tissue voxel analysed and returns a signal reflecting these assumptions. The latter yields resulting TCCs that are more faithful to the original signal, meanwhile being more affected by the presence of outliers and noise. In [215], both non-parametric spline fitting method and the parametric Gamma-variate model are successfully used to compute aBF in 8 patients with HCC. The Gamma model described in [216, 217] has been widely adopted in perfusion studies [119]. However, by changing the assumption on the kinetic diffusion of CA inside the analysed tissue, it is also possible to apply other models such as the Weibull [218] or the Hill [219] ones. In particular, the Hill's model fits the assumption of no venous outflow, since its increasing sigmoidal shape well describes the arrival of the bolus of CA inside tissue, but not its flowing out. A family of curves for the Gamma-variate, Weibull, and Hill models are represented in Figure 2.14.

2.4.6 Methods and models to compute perfusion parameters

The choice of the best model or method to compute perfusion parameters is still widely debated. Each technique relies on different assumptions regarding CA distribution inside tissue, this leading to the computation of different perfusion parameters (as reported in Table 2.2). Moreover, the adequacy of methods or models to compute perfusion parameters may depend on the acquisition protocol used. A short acquisition protocol, ending before CA flowing out from IV

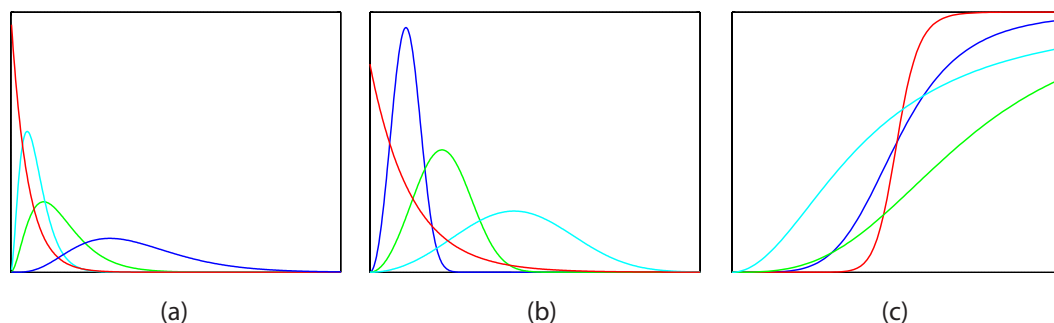


Fig. 2.14: Gamma-variate (a), Weibull (b), and Hill (c) model are represented.

space, can indeed be suitable to methods based on a single compartment. On the contrary, longer acquisition protocols allow assessing also the vascular permeability of the analysed tissue by computing perfusion parameters such as PS or k^{trans} through the application of two, or more, compartment models [54]. In case of retrospective studies, the selection of the method or model that has to be applied must take into account the limitations imposed by the acquisition protocol applied (such as duration and sample frequency). On the contrary, in case of a perspective study it is possible to decide *a-priori* which perfusion parameters to study, which method or model to apply to achieve those parameters, and which acquisition protocol, accordingly [64]. However, at present there is not any established agreement yet, regarding which parameters should be considered and, consequently, which model and acquisition protocol should be applied in the various perfusion studies [83].

Currently, only few studies exist that have compared perfusion parameters obtained with different kinetic models applied on human tumour tissues. Kanda *et al.* proposed two studies that compared perfusion parameters computed using different methods, based on the assumption of a single compartment. In [113], the mean values of aBF , pBF , and HPI were computed in 109 patients with a high risk of malignant liver tumour by using the dual-input maximum slope (DIMS) method and the 2I1CM. Results of statistical tests pointed out the differences between parameters obtained with the two methods and highlighted the fact that they are not directly comparable. The same results were obtained in [114], where aBF , pBF , and HPI were computed in 88 patients with liver metastases by using the MSM, the single compartment model, and the deconvolution method. Perfusion results computed by using the various methods and models were again hardly comparable. In-

stead, three more works compared perfusion parameters obtained by using two-compartment models. In particular, in [220] the values of BF , BV , MTT , and PS were computed in 19 patients with advanced HCC by using 2CM, TM, eTM, AATHM, and DPM. The study was repeated after 10-12 days from the administration of the anti-angiogenic treatment since its aim was to study whether any parameter could be a predictor of 6-month PFS. The results highlighted that both the absolute values of each perfusion parameter and the differences measured in the two examinations were significantly different among the models applied. Similar results were obtained in [188] in the evaluation of the capability of perfusion parameters to predict the 5-year OS in 46 patients with primary CRC. The value of BF , BV , MTT , PS , EF , v_{ev} , and k^{trans} computed by using four different models (2CM, eTM, AATHM, DPM) resulted to be significantly different. Instead, another study [221] carried out on 44 patients with CRC, compared k^{trans} and BV values achieved by applying AATHM and Patlak model. Also in this case, the perfusion results achieved with the two models were significantly different and could not be directly compared. Anyway, it is important to remark that in this last study, the use of different commercial software might have affected the obtained results. Indeed, in [222] the use of the same commercial software before and after the upgrade on the same datasets of 30 patients with suspected CRC, leads to significantly different values of BF , BV , MTT , and PS . This study demonstrates that also the use of different commercial software (even if produced by the same vendor) can deeply affect perfusion results and prevent comparison of parameters computed in different studies.

2.4.7 The analysis of results

Another source of inhomogeneity that could lead to different clinical consideration is the modality used to analyse perfusion results. To this purpose, it is possible to subdivide the problematic into three main issues, which regard the ROIs selection, the method of analysis used (global or voxel-based), and the number of tumour sections considered.

The first issue regards the lack of consensus on how the tissue ROIs should be drawn [83]. Due to tumour heterogeneity, the analysis of data coming from different tissue portion could yield different clinical consideration. In a recent study involving 27 patients with lung cancer indeed, the mean BF and BV values were computed in several ROIs of different size and placed in different position of the same tumour section. The results of statistical tests

highlighted that the computed perfusion parameters showed a high variability between ROIs of different size and position and that the highest reproducibility of results was achieved using the ROI encompassing the whole tumour surface [110].

The second issue regards the selection of one of the two methods that can be used to analyse perfusion parameters [223]. The first one is based on the use of statistical indexes (*e.g.* mean or median value of the perfusion parameters) that allows obtaining a unique perfusion value aiming at being representative of the whole ROI, or the whole tumour. This method permits a simple and fast analysis of perfusion results [223] and generates perfusion parameters with a great intra-observer and inter-observer reproducibility, whether global values are computed on a single slice [201] or on a number of tumour sections [200]. In any case, this method does not bring any information about the spatial distribution of perfusion patterns and masks the local tissue variability that are the characteristic feature of tumours (*i.e.*, tumour heterogeneity) [60]. The second method to be used consists in a voxel-based perfusion analysis. This method enables the study of local perfusion heterogeneity and the detection of hypo- and hyper-vascularized areas [223]. As reported by Petralia *et al.* in [52, 60], the voxel-by-voxel analysis can be done both qualitatively, by visually assessing perfusion maps, and quantitatively by analysing histograms of perfusion values [224] or by adopting fractal analysis [225, 226]. However, voxel-based analysis requires longer and more complex computational techniques [223] and the use of global perfusion parameters is still often preferred.

The third issue regards the selection of the number of tumour sections on which perfusion parameters have to be computed. Due to tissue heterogeneity, perfusion of a single slice may not reflect perfusion of the whole tumour [8]. More reproducible perfusion results were achieved in two studies of lung cancer [202] and CRC [203] by using a greater z -coverage. However, both these studies have been conducted by using global values that cannot take into account tumour heterogeneity. Also in this case, the lack of guidelines facilitates the spread of different, and sometimes not appropriate, solutions. Despite the knowledge that tumour heterogeneity can highly affect perfusion parameters computed on a single slice, there are still several studies that currently compute perfusion parameters on a single tumour section only [192, 227, 228]. In order to evaluate the representativeness of global and voxel-based perfusion results computed on the whole tumour and on a single slice with respect to tissue heterogeneity, a deep analysis has been carried out in Chapter 5.

Chapter 3

Computation of CTP parameters

In this Chapter, the methods and the indicators that have been defined, implemented, and tested during my PhD activities are presented and discussed. First of all, the pre-processing techniques applied to the CTP data of each examination and the methods used to compute perfusion parameters are presented (Sect. 3.1). Then, a series of error indexes is taken into account in order to evaluate the quality of the signal on which the perfusion parameters are computed. Four temporal indexes of goodness of fit are indeed investigated and compared to find out the most suitable one to evaluate TCCs' quality and to assess the reliability of the perfusion values computed. A couple of spatio-temporal indexes able to evaluate the evolution over time of tumour spatial heterogeneity is also presented (Sect. 3.2). In order to establish which perfusion values were characterized by the highest errors and hence had to be considered as being unreliable and excluded from the analysis, two automatic thresholding methods of the error index distribution are proposed (Sect. 3.3). Finally, two indicators used to evaluate local spatial coherence of perfusion maps (Sect. 3.4) and tumour functional heterogeneity are introduced (Sect. 3.5).

3.1 From image sequence to TCC

In this section, the pre-processing techniques applied to CTP images and to TCCs are presented. The liver and lung CTP image sequences studied in this manuscript have all been acquired in axial scan mode. Indeed, despite using an helical acquisition would allow obtaining a more accurate registration [183] and covering a wider volume coverage [229, 203], the improvement brought by

the “spiral” scan mode is light in case of hidden tumours or lesions extending for few slices only [230]. Moreover, the fact that the axial scan mode allows acquiring images at a higher temporal resolution meanwhile delivering a lower radiation dose to patients, makes this technique the most preferable one [60].

In the next paragraphs, the denoising methods applied to the CTP images and to the TCCs (Sect. 3.1.1) are presented as well as the method selected to compute perfusion parameters (Sect. 3.1.2), and the model chosen to fit the resulting TCCs (Sect. 3.1.3).

3.1.1 Denoising methods

In order to remove noise from the acquired images and from the TCCs, a couple of filters have been applied. The techniques presented have been selected in preliminary studies among several methods. The criterion applied to select these techniques was related to the achievement of the best trade-off between signal denoising and preservation of data information content. The first denoising step is applied to the sequence images and is implemented through the use of a median filter with a 5-pixel kernel size, that allows removing noise while preserving edges. The very small dimension of this filter allows to achieve an effective denoising that removes the bigger outliers mainly due to acquisition noise without losing the image information content. Subsequently, an autoregressive (AR) filter is applied to the TCCs in order to further reduce the effects of noise, motion artefacts and discretization. The application of this method is based on the assumption that the signal can be modelled as a sequence of correlated samples affected by random noise. This assumption holds in case of TCCs since they are characterised by a common trend that consists in a first increase due to CA uptake inside tissue, followed by a very slowly decay caused by the CA outflow. Each TCC can thus be described through the use of the AR process shown in Eq. 3.1:

$$y_{AR}(m) = \sum_{k=1}^p a(k)y_{AR}(m-k) + \eta(m) \quad (3.1)$$

where y_{AR} is the signal described through autoregression, $a(k)$ represents the generic AR coefficient, p is the order of the AR model and $\eta(m)$ is the white noise process. Both the coefficients and the order of the AR model are estimated by using the Yule-Walker method [231, 232]. This procedure permits to capture temporally local correlation between consecutive samples and to

denoise the signal, accordingly.

3.1.2 Perfusion values computation

Since the main goal of this Thesis is to provide methods allowing clinicians to make more correct and more aware clinical decisions, independently from the parameters that are computed and from the methods used to compute their values, I decided to work on BF values computed by using the MSM. As discussed in Sect. 2.3, BF has shown to be a multi-purpose parameter since it is one of the most versatile and useful. It can indeed be applied also to organs characterised by a dual vascular input, such as liver and lung, where it has shown to be correlated with tumour angiogenesis [143, 149] and to be very useful for the formulation of a correct diagnosis [167, 169] and prognosis [73, 74]. Despite the BF value can be computed by using several methods and models, I decided to use the MSM since it is robust (Sect. 2.2.2) and it does not need any prior assumption about the investigated tissue [84], thus allowing to preserve the generic purpose of this research work. Moreover, the mathematical simplicity of the MSM [52] permits to keep under control all the possible error sources related to the model. Indeed, the use of more complex methods or models can introduce a bias in the perfusion results computed. For instance, the deconvolution method leads to results whose robustness and precision strongly depend on the regularization methods applied [98]. Instead, the compartmental models, are based on the assumption that are made on the tissue vascular system and that consequently affect the value of the computed perfusion parameters [62]. On the contrary, the use of a simple and robust method free from any assumption about the analysed tissue permits to directly evaluate the efficacy of the algorithm applied without introducing further sources of uncertainty and instability. For these reasons, the MSM resulted to be the most suitable for our purpose.

3.1.3 The fitting model

Despite the application of spatio-temporal data denoising methods, TCCs can still remain very noisy and show an oscillating behaviour. Since to compute perfusion parameters we decided to use the MSM, we can focus our attention on the first portion of the TCCs (*i.e.*, the one before CA recirculation). Figure 3.1 (a) reports an example of liver TCC together with the curve interpolating its data points. For obvious reason, here the application of the MSM and

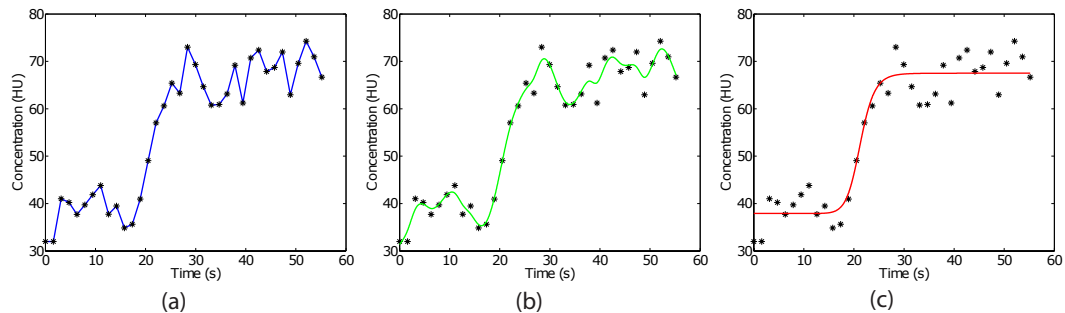


Fig. 3.1: Liver TCCs' data points (the black markers) are reported together with their linearly interpolating curve (in the blue colour) (a), non-parametric fitting curve (obtained with spline, in the green colour) (b), and parametric fitting curve (achieved with Hill's equation, in the red colour) (c).

the computation of the maximum slope value cannot be done directly on the interpolant curve. In fact, due to the presence of non filtered noise or artefacts affecting data, it is possible to incur in incorrect solutions that would bring to a wrong estimation of the BF value. Consequently, in the presence of noisy data, the use of fitting methods becomes indispensable. As discussed in Sect 2.4.5, it is possible to adopt both non-parametric (*e.g.* that of Figure 3.1 (b)) and parametric fitting strategies (*e.g.* that of Figure 3.1 (c)). However, in the presence of highly oscillatory tissue TCCs also the use of non-parametric fitting can be misleading, since TCCs may adapt to signal oscillations. Instead, the use of a parametric fitting method allows achieving as the best signal as possible describing the expected global behaviour of the tissue TCCs, thus being less sensible to the presence of noise and outliers. Since the MSM is based on the assumption of no venous outflow and the only portion of the tissue curve needed to compute the BF value is the increasing one, it is possible to choose the Hill's model as the parametric fitting [219]. This sigmoidal-shape parametric model permits to correctly describe the enhancement phase of the TCC caused by the arrival of CA. The Hill's equation indeed, has been often used to describe the non-linear drug response in pharmacodynamics models, but is also suited to model CA pharmacokinetics [233]. The Hill's equation can be described by Eq. 3.2:

$$y(t) = E_0 + (E_{max} - E_0) \frac{t^\alpha}{(EC_{50} + t)^\alpha} \quad (3.2)$$

where E_0 is the baseline concentration value of the tissue before CA arrival, E_{max} is the saturation value of tissue concentration, EC_{50} is the time instant of half-maximum response concentration of the curve, and α is the non-linear parameter that mostly affect the slope of the curve. A representation of these parameters can be find in Figure 3.2.

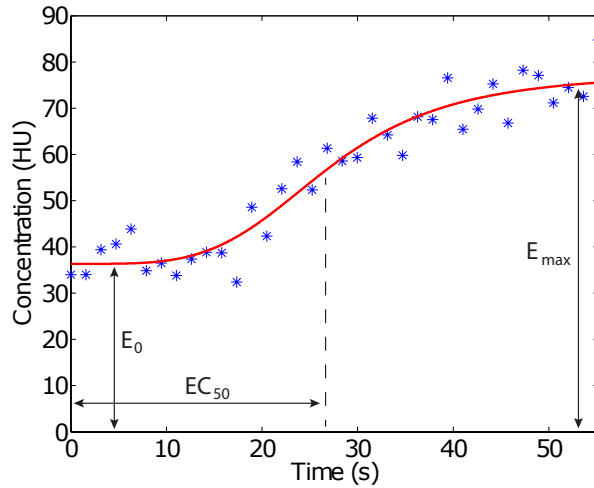


Fig. 3.2: Liver TCC's data points (the blue markers), their fitted version through the Hill's equation (the red line), and its parameters E_0 , E_{max} , and EC_{50} .

Figure 3.3 reports three liver TCCs pertaining to different voxels of the

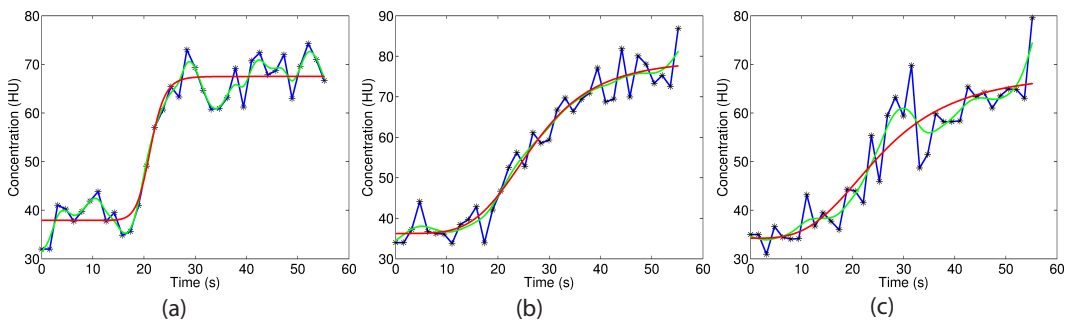


Fig. 3.3: Examples of liver TCCs (the black markers) with increasing noise level from left to right and their interpolating piecewise curve (in the blue colour), non-parametric fitting spline curve (in the green colour), and parametric fitting sigmoidal curve (in the red colour).

same CTP examinations with different noise levels. Each TCC is represented

together with its interpolating piecewise linear curve, its non-parametric fitting curve based on the spline model, and its parametric fitting curve achieved by using the Hill's equation. In Table 3.1, the values of the maximum derivative

Maximum first derivative and BF values in interpolating and fitting TCCs			
TCC	Type of curve	Maximum first derivative (HU/s)	BF value ($ml/min/100g$)
Fig. 3.3 (a)	Interpolating	5.13	61.5
	Spline	5.11	61.3
	Hill's equation	5.24	62.8
Fig. 3.3 (b)	Interpolating	5.30	63.6
	Spline	2.27	27.2
	Hill's equation	1.84	22.1
Fig. 3.3 (c)	Interpolating	8.73	104.8
	Spline	2.56	30.7
	Hill's equation	1.21	14.5

Tab. 3.1: Maximum value of the first derivative and consequent BF value achieved using interpolation (a), non-parametric fitting spline (b), and parametric fitting with Hill's equation (c).

and of BF computed on the enhanced phase of the curves are reported for each TCC and for each type of fitting or interpolating curve. In the first TCC (Figure 3.3 (a)) the noise characterizing the enhancement portion of the curve is negligible and the three curves (the interpolating, the non-parametric fitting, and the parametric fitting ones) similarly describe the evolution of the TCC's increasing portion. Indeed, the maximum value of the first derivative computed on the enhancement part of the three curves and BF values, accordingly are almost equivalent. Instead, the second TCC (Figure 3.3 (b)) is characterized by a little more noise in its enhancement part. In this case, the interpolating curve remarks each oscillation of the TCC, leading to an overestimated BF value. On the contrary, the global trend of the TCC that is clearly identifiable by visual evaluation is well represented by the two fitting methods yielding very similar BF values. Finally, the third TCC (Figure 3.3 (c)) is characterized by the widest oscillations. Also in this case, computing the maximum slope on an interpolating curve would lead to unrealistic BF values, very far from those

achievable through a fitting approach. Yet more, in this case the oscillations are so heavy that the use of non-parametric fitting would be unsuitable. In fact, the presence of strong noise in the enhancement part of the curve affects the non-parametric fitted curve that tends to adapt to the local trend of the TCC data points. In this case, the maximum first derivative value (and, consequently BF) is twice as big as that achieved through the parametric fitting. The model based fitting is the only one capable to follow the global trend of the TCC even with a high presence of noise, thus yielding more robust results.

In conclusion, the results achieved with a model based fitting in case of low noise are similar to those obtained with the other two methods. On the contrary, in case of a high noise level, the parametric model based fitting is the only one preventing BF computation from falling in local minima solutions. This approach, based on the Hill's equation has shown to be well suited to the MSM and it has been chosen in my Thesis to fit the TCCs. It is worth noting that all the results published in [230, 234, 235, 236, 237] rely on this method.

3.2 Goodness of fit: some error indexes

The quality of the data acquired can be affected by several factors (Sect. 2.4), such as CTP acquisition parameters, noise, and artefacts (in particular those coming from respiratory motion), that can have a strong influence on the shape and the smoothness of the TCCs and, consequently, on the perfusion parameters estimated. In the literature several attempts to reduce the impact of these error sources have been carried out, starting from the application of motion correction methods [238, 239] to the improvement of TCCs quality by removing outliers. In particular, these last types of method can be based on several principles such as the qualitative assessment [212], or the quantitative estimation of the degree of motion that can affect an image sequence [126], or the quantitative evaluation of the noise affecting each TCC [215, 234, 229].

In order to evaluate image quality some methods have been proposed in the literature. In [240] and [241] for instance, image quality is qualitatively evaluated by expert readers. Instead, in other works quantitative assessments of image quality are made through the measurement of tissue standard deviation std [242] and of the contrast-to-noise ratio [243]. Despite these efforts, the work of Miles *et al.* [83] highlights the need of quantitative indicators of signal and fitting quality (*e.g.* signal to noise ratio (SNR) and goodness of fit respectively) which the reliability of the computed perfusion parameters

depends on. By providing clinicians with goodness-of-fit indexes would make it possible for them to have an indicator of perfusion values' reliability, this helping them to make more aware clinical decisions.

To this purpose, I analysed and evaluated the capability of several temporal (Chapter3Section2Sub1) and spatio-temporal (Chapter3Section2Sub2) indexes to assess the consistency of the fitted curves with the original data and the evolution over time of the local spatial tissue features.

3.2.1 Temporal error indexes

This section is dedicated to the temporal quantitative indexes that have been tested to evaluate TCCs' quality. All these indexes are based on the analysis of residuals ϵ defined as the distance, measured at the time instant i between the observed TCC data points Y_i and the computed value \hat{Y}_i referring to the curve fitting the TCC (Eq. 3.3):

$$\epsilon_i = \left| Y_i - \hat{Y}_i \right| \quad (3.3)$$

Therefore, the higher the value of residuals, the worse the fitting model represents the original data. An example of the residuals of a TCC is reported in Figure 3.4, where each blue vertical bar represents a residual ϵ_i of the signal.

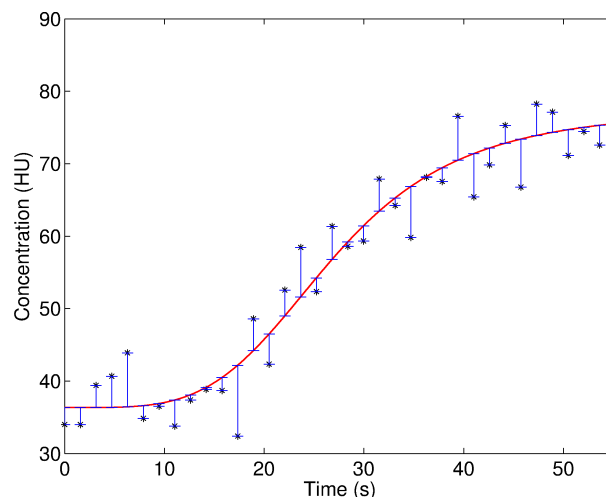


Fig. 3.4: The original TCC (represented with the black stars) is fitted by using the Hill's equation and the vertical blue bars are the residuals ϵ .

Four temporal indexes aiming at measuring the goodness of fit were evaluated:

- the residual's standard deviation (σ_ϵ)
- the residual's sum of squared errors (SSE)
- the coefficient of determination (R^2)
- the mean of the absolute value of residuals (μ_ϵ)

To allow a better understanding of the main strength and weakness points of the error indexes that are going to be discussed, let us refer to the synthetic TCCs represented in Figure 3.5. The TCCs of Figure 3.5 (a)-(c) (referred to

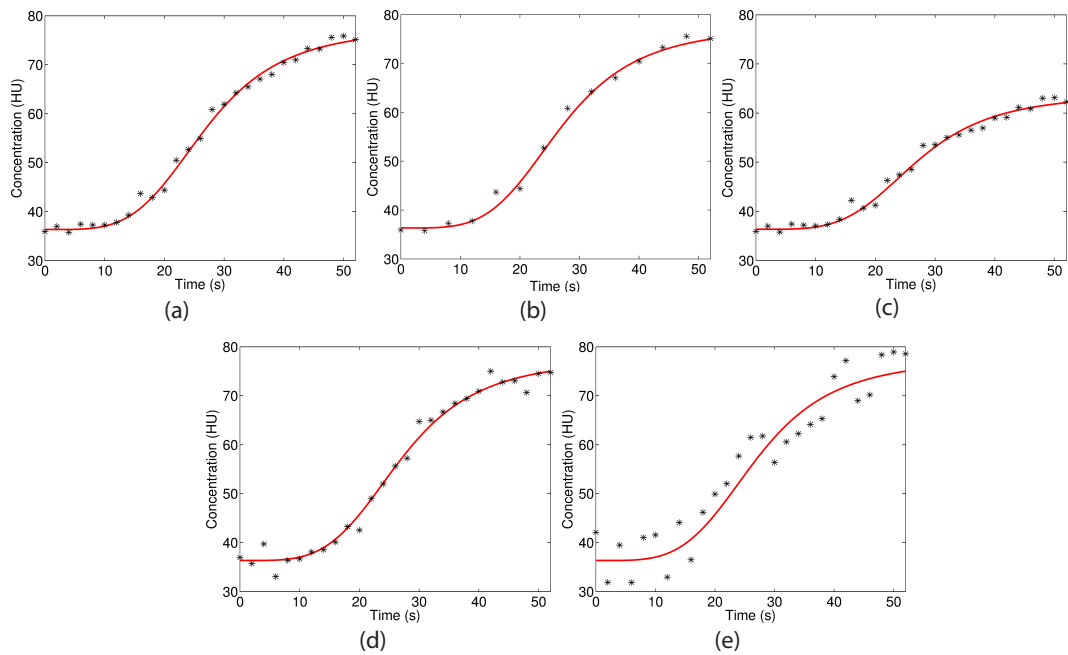


Fig. 3.5: Synthetic TCCs characterized by different noise levels and trends. TCCs A (a), B (b), and C (c) are characterized by a very low noise with TCC B having the fewest data-points and TCC C the lowest contrast enhancement. TCC D (d) is characterized by the presence of some outliers, thus having a noise higher than TCC A, B, and C. TCC E (e) instead, is the one with the highest noise level.

as TCC A, TCC B, TCC C respectively) are all characterized by a low noise level. In these three curves we have the same ϵ values in every time instant, but while TCC B has fewer data points than TCCs A and C, TCC C presents the

lowest concentration enhancement. In addition, with respect to TCC A, TCCs D (Figure 3.5 (d)) and TCC E (Figure 3.5 (e)) have the same number of data points, show a comparable concentration enhancement, but are characterized by a higher noise levels. Indeed, differently from TCC A, TCC D presents some outliers, while TCC E (Figure 3.5 (e)) show the highest noise level with high residuals almost equally distributed all over the time instants.

Table 3.2 reports the values of the four error indexes (σ_ϵ , SSE , R^2 , and μ_ϵ)

Temporal error indexes					
Error index	TCC A	TCC B	TCC C	TCC D	TCC E
σ_ϵ	0.69	0.85	0.69	1.24	0.83
SSE	30.66	20.55	30.66	70.78	519.50
R^2	0.995	0.994	0.989	0.989	0.923
μ_ϵ	0.80	0.86	0.80	1.02	4.23

Tab. 3.2: σ_ϵ , SSE , R^2 , μ_ϵ values computed on the TCCs of Figure 3.5.

computed on the five TCCs of Figure 3.5 that are going to be discussed.

In many perfusion studies the first and often the only one statistical parameter that is evaluated to assess the presence of irregularities, and thus considered as a marker of noise is the standard deviation. To this purpose, I have analysed σ_ϵ whose value is computed as the standard deviation of ϵ , according to Eq. 3.5:

$$\sigma_\epsilon = \sqrt{\frac{\sum_{i=0}^{N-1} (\epsilon_i - \bar{\epsilon})^2}{N}} \quad (3.4)$$

where N is the number of TCC's data points considered and $\bar{\epsilon}$ is the mean value of the residuals ϵ (Eq. 3.5):

$$\bar{\epsilon} = \frac{1}{N} \sum_{i=0}^{N-1} \epsilon_i \quad (3.5)$$

In particular, σ_ϵ is an index that is very sensible to the presence of outliers in the TCC. Indeed, comparing TCC A (or TCC C, that have the same residual distribution) with TCC D (that is the one with some outliers), in Table 3.2 we can see high differences in the values of σ_ϵ . A small difference of this error index between TCCs A and B can be observed due to the lower number of samples composing the TCC B. However, the main drawback of this index can

be noted by comparing TCCs A, D and E. Indeed, the value of σ_ϵ in TCC E is higher than that of TCC A, but is much lower than that of TCC D, that is much less noisy. This is because the presence of high, but almost uniform residuals is not detected by σ_ϵ aims at revealing the inhomogeneities between the residual values. Therefore, σ_ϵ results to be inappropriate to measure the TCC's quality.

The *SSE*, also known as the residual sum of squares or sum of squared residuals, is another error index that is often adopted to analyse the goodness of a regression. This indicator is computed according to Eq. 3.6:

$$SSE = \sum_{i=0}^{N-1} (\epsilon_i)^2 \quad (3.6)$$

As we can see from Table 3.2, the *SSE* is able to correctly detect the increasing presence of noise in TCCs. Indeed, this index has low values in the TCCs A, B, and C that are characterized by a low noise level, higher in TCC D, and yet more in TCC E. However, the value of *SSE* depends on the number of data points constituting the TCC. In fact, TCC B has the same noise level as TCC A, but has fewer data points and is consequently characterized by a much lower value of *SSE*. In this case, TCC B erroneously seems to have a much better fitting quality with respect to TCC A. This aspect can be particularly awkward if a method to remove outliers is applied to the TCCs before fitting [234]. Indeed, since in this case it is possible to have TCCs characterized by different number of data points (*e.g.* in case of random sampling [234]), the use of *SSE* would be misleading. TCCs with the same noise level (and the same fitting quality), but with different number of data points, would indeed differ by *SSE* and the perfusion parameters computed on TCCs having less data points would be considered as being more reliable.

Another goodness-of-fit index that has been widely used in regression analysis is R^2 . Its value ranges from 0 (bad fit) to 1 (good fit) and is computed as the rate between the total sum of data squares SS_{tot} and the *SSE* (Eq. 3.7):

$$R^2 = \frac{SS_{tot}}{SSE} \quad (3.7)$$

where SS_{tot} is calculated in Eq. 3.8 as:

$$SS_{tot} = \sum_{i=0}^{N-1} (Y_i - \bar{Y})^2 \quad (3.8)$$

and \bar{Y} is the mean value of the TCC data points (Eq. 3.9):

$$\bar{Y} = \frac{1}{N} \sum_{i=0}^{N-1} Y_i \quad (3.9)$$

R^2 has shown to be able to well detect the differences of noise level in TCCs A, D, and E. In addition, by comparing its value in TCCs A and B (Table 3.2), it is possible to see that the presence of a lower number of data points does not affect its value. However, R^2 has a drawback that needs to be considered. In fact, its value directly depends on SS_{tot} that in its turn varies according to the range of the TCC's concentration values. In case of high perfused tissues, there is a greater enhancement than that occurring in low perfused tissues. On the other hand, a higher enhancement results in a higher SS_{tot} , and R^2 values, accordingly. Consequently, by comparing TCCs A and C (Table 3.2) that are characterized by the same residual values, but a different contrast enhancement, one can see a lower value of R^2 in the TCC with the narrower range of concentration values (*i.e.*, TCC C). TCC C would then be erroneously considered as the one with the worst fit quality and the one yielding the less reliable perfusion values, accordingly. Because tumours are usually affected by high morphological and functional tumour heterogeneity, the use of R^2 is not appropriate for the evaluation of TCCs' quality.

μ_ϵ is an index that evaluates TCC residual values directly. This indicator is computed as the mean value of the absolute residuals, as follows:

$$\mu_\epsilon = \frac{1}{N} \sum_{i=0}^{N-1} |\epsilon_i| \quad (3.10)$$

μ_ϵ has shown to be able to correctly estimate the TCC's quality. Indeed, by comparing TCC A, D, and E, it is possible to note that the value of μ_ϵ is directly proportional to the noise level. Indeed, in TCC D where there are only few outliers, μ_ϵ value is only a little greater than that assumed in TCC A. On the contrary, in TCC E that is characterized by high residual values in every time instant, the value of μ_ϵ is much higher than that in TCCs A and D. Moreover, this error index, being averaged is independent from the number of TCC's samples and from the range covered by the concentration values of the curve, thus resulting in comparable values between TCCs A, B, and C.

Thanks to its capability, μ_ϵ is the temporal index that have been selected to assess TCC's quality. Its use in perfusion studies has been validated in [230]

(Sect. 4.2) while its usefulness in clinical studies has been demonstrated in [236] (Sect. 4.3).

3.2.2 Spatio-temporal error indexes

Two spatio-temporal indexes have been studied in order to investigate the temporal evolution of the local (image-based) spatial features of a group of TCCs:

- the mean of the local standard deviation (MS)
- the variability of the local standard deviation (SS)

Given a window $W(x, y)$ of dimension $w \times w$ and centred in the voxel with coordinate (x, y) , it is possible to achieve for the image acquired in the time instant i a group of concentration values $\Omega_W(i)$ with standard deviation $\sigma_i(\Omega_W)$. Low values of $\sigma_i(\Omega_W)$ point out a local homogeneity, while high $\sigma_i(\Omega_W)$ values hint at a region of the image analysed containing tissue with heterogeneous density values. Figure 3.6 reports two 9×9 windows $W(x, y)$ taken on the same tumour sections. While the upper window (with the red border, (b)) contains a more homogeneous tissue portion ($\sigma_i(\Omega_W) = 10.9$), the lower one (with the green border, (c)) contains density values more spatially heterogeneous ($\sigma_i(\Omega_W) = 20.2$). This difference is even more evident in the related histograms of density values reported in Figure 3.7. Indeed, while the histogram of the tissue region characterized by the lowest $\sigma_i(\Omega_W)$ value is narrower (Figure 3.7 (a)), the other one (Figure 3.7 (b)) spans over a wider (nearly twice) range of bins.

The index MS is computed for each voxel (x, y) according to Eq. 3.11:

$$MS = \frac{1}{N} \sum_{i=0}^{N-1} \sigma_i(\Omega_W) \quad (3.11)$$

as the mean of the values assumed by $\sigma_i(\Omega_W)$ in each time instant i by the voxel (x, y) in the centre of the window $W(x, y)$. This spatio-temporal index has been conceived to estimate the mean degree of spatial homogeneity over time in the local neighbourhoods of (x, y) . Accordingly, a low MS value corresponds to tissue regions that remains locally homogeneous over the acquisition period, independently from the variations of Ω_W intensity values.

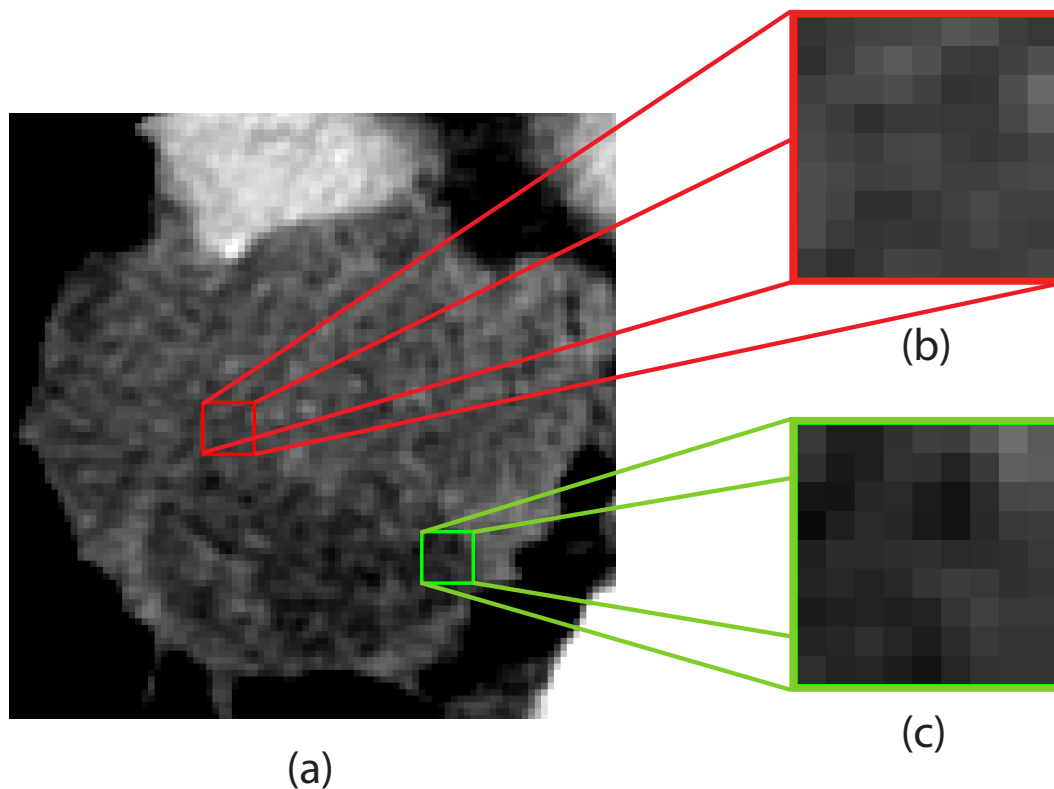


Fig. 3.6: An unenhanced lesion (a) and two 9×9 windows $W(x,y)$ related to tissue portions with different local density heterogeneity degrees (b,c).

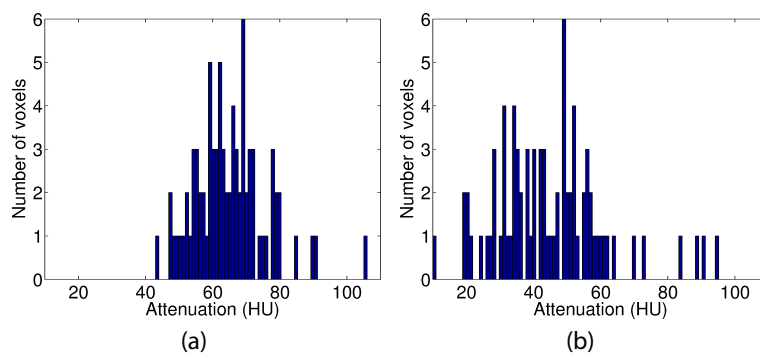


Fig. 3.7: Histograms of density values (a,b) of the two tissue regions shown in Figure 3.6 (b) and (c), respectively.

The index SS computed for each voxel (x, y) according to Eq. 3.12:

$$SS = \sqrt{\frac{\sum_{i=0}^{N-1} (\sigma_i(\Omega_W) - MS)^2}{N}} \quad (3.12)$$

as the standard deviation of the values assumed by $\sigma_i(\Omega_W)$ in each time instant i . This second index aims at monitoring the temporal variations of the texture range for neighbour voxels. Accordingly, SS presents a low value if the variability of spatial characteristics of the TCCs pertaining to $\Omega_W(i)$ are kept constant over time. For instance, this happens in case of uniform spatial enhancement. On the contrary, SS assumes high values when the local range of density values is not preserved over time. For instance, this can happen in case of not negligible motion, when voxels belonging to structures with a different tracer response fall in different time instants into the same window $W(x, y)$, or in the unusual case of neighbour tissue voxels with a markedly different tracer dynamics.

Both MS and SS can be represented through the use of colorimetric maps that can be very useful for radiologists and clinicians. Indeed, the combination of this two spatio-temporal indexes can allow drawing several considerations about the analysed tissue. For instance, low values of both MS and SS may indicate homogeneous regions undergoing a uniform enhancement. Instead, high values of MS associated with low values of SS point out heterogeneous tissue regions that keep their heterogeneity constant during the whole examination. On the contrary, high values of both MS and SS could represent heterogeneous regions with a heterogeneity varying over time.

The use of these two indexes that in the context of preliminary studies have shown to be good indicator of spatial homogeneity and temporal uniformity, has been deepened in a CTP study of the CVG [235].

3.3 Automatic error thresholding

In Sect. 3.2.1, a temporal index able to effectively evaluate the fit quality of the TCCs has been presented. The use of μ_ϵ colorimetric maps can allow clinicians to make more correct and aware clinical evaluation by weighing BF values visible inside the colorimetric maps. For instance, a tissue region characterized by very high perfusion values can be correctly considered as a hyper-perfused area if the values of the error index regarding that region are low. On the contrary, if the μ_ϵ values of that area are high, the corresponding perfusion

values should not be included in the analysis, since computed on TCCs that has been wrongly fitted. High μ_ϵ values are due to the presence of high residuals, that is, the TCC is far from the fitted curve and accordingly from the ideal model that has been adopted to describe the kinetic of CA inside the tissue. This may occur in the presence of noise and artefacts affecting TCCs' data points, or in cases of anatomical structures (*e.g.* as vessels or bronchi) that are functionally different from the tissue analysed. However, the use of μ_ϵ maps to evaluate the reliability of the corresponding BF values may be influenced by inter-observer variability. Indeed, without a cutoff value pointing out which BF values should be considered in the analysis and which one should be not, different clinicians could subjectively decide to consider or not the presence of tissue regions that could make the difference in the ultimate clinical decision making (*e.g.* hyper- or hypo-perfused areas). Moreover, the greatest part of CTP studies are based on global values computed as the mean or the median perfusion values achieved in one or more tumour sections. By considering all the perfusion values, without excluding those highly affected by errors, the resulting global perfusion value might be significantly different from the correct one, thus leading to different clinical conclusion. Therefore, the lack of a threshold value for the error indexes prevents clinicians from correctly deciding which perfusion values should be considered in the decision making process.

To this purpose, I studied some solutions permitting to automatically find out a cutoff value for μ_ϵ that could be specific for each CTP examination. First of all, I analysed the distribution of the μ_ϵ values of several examinations in order to take advantage from the statistical indexes, such as the mean ($E[\mu_\epsilon]$) and the standard deviation (σ_{μ_ϵ}) of μ_ϵ . An example of histograms and colorimetric maps of μ_ϵ values achieved in healthy liver and lung cancer tissues are reported in Figure 3.8. Here, the healthy liver tissue is not particularly affected by artefacts or noise and does not contain any big vessels. Its μ_ϵ histogram (Figure 3.8 (a)) has a Gaussian-like shape and it is spread over a very narrow range of values ($2 - 5HU$). On the contrary, the lung tumour tissue is much more heterogeneous and affected by partial volume effect (Sect. 4.3). In this case, the error index histogram is characterized by an unimodal bell-shaped curve with a long right tale (Figure 3.8 (c)). The right portion of the histogram, and especially its right tail, retains the highest error values corresponding to the voxels of the colorimetric map represented with the hotter colours (*i.e.*, those affected by partial volume effect). In order to automatically find out a threshold value able to identify the TCCs mostly affected by noise

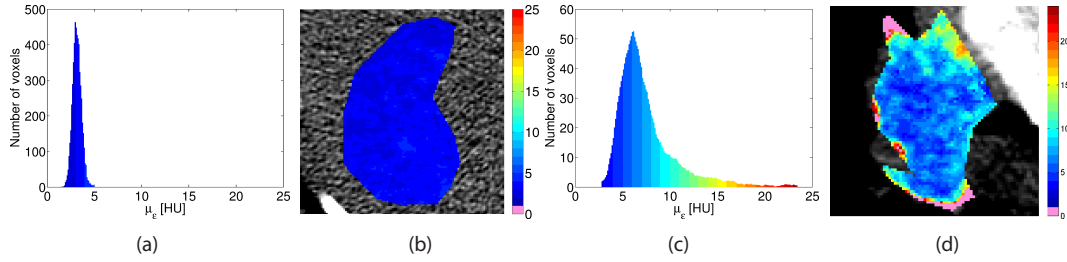


Fig. 3.8: Histograms and colorimetric maps of μ_ϵ values computed in healthy liver (a,b) and NSCLC (c,d).

(*i.e.*, those in the right tale of μ_ϵ histogram) that expectedly would have given rise to the most unreliable BF values, I tested two thresholding approaches that could be applied to μ_ϵ histogram:

- the 2σ method
- the triangle method

The first method is based on the $2 - \sigma$ rule stating that “for many reasonably symmetric unimodal distributions, approximately 95% of the population lies within two standard deviation of the mean” [244]. In particular, if x is an observation and μ and σ are respectively the mean and the standard deviation of the distribution, the $2 - \sigma$ rule can be described by the following mathematical notation:

$$Pr(\mu - 2\sigma \leq x \leq \mu + 2\sigma) \approx 0.9545 \quad (3.13)$$

However, since the hypothesis of Gaussianity does not perfectly hold, this approach just detects the voxels with a very high error only. This implicitly means accepting that high error could anyway returns reliable perfusion values. In our case, samples with a low μ_ϵ value point out a good fit and hence have not to be removed. A threshold value $T_{2\sigma}$ to be applied to the μ_ϵ histogram can thus be defined as:

$$T_{2\sigma} = E[\mu_\epsilon] + 2\sigma_{\mu_\epsilon} \quad (3.14)$$

By applying the $2 - \sigma$ rule to the μ_ϵ histogram of Figure 3.8 (c) it is possible to achieve the result represented in Figure 3.9. The bins of Figure 3.8 (a) represented in the blue colour are those with over-threshold error values and correspond to perfusion values that can be considered unreliable. In particular,

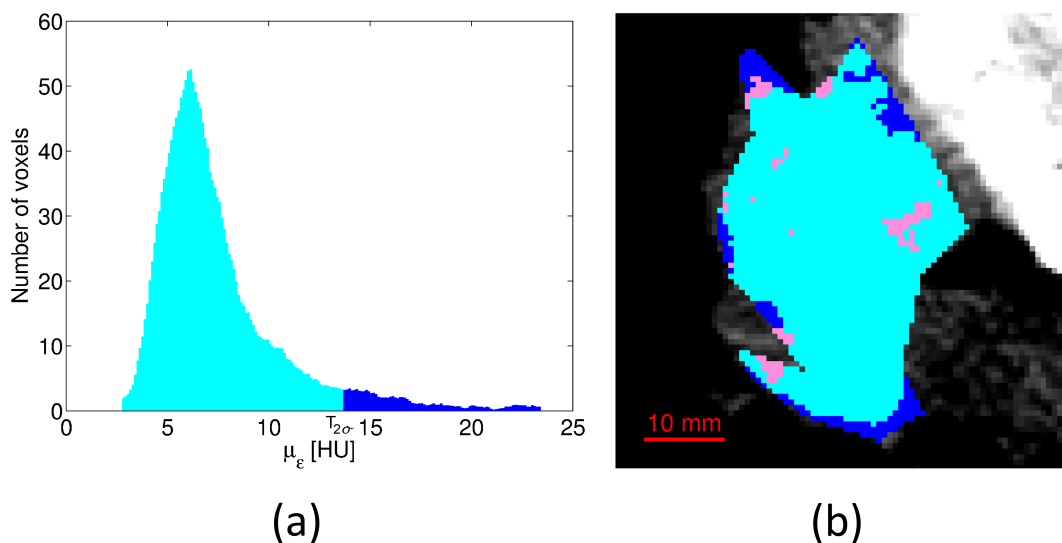


Fig. 3.9: Histogram (a) and TEM (b) pertaining to the same patient of Figure 3.8 (c), (d). The voxels and the bin in the cyan colour are those characterised by a μ_ϵ value lower than $T_{2\sigma}$ while those in the blue colour have an over threshold error value.

these bins correspond to those voxels that have been represented in the blue colour inside the thresholded error map (TEM) of Figure 3.9 (b). On the contrary, the bins of the histogram and the voxel of the TEM represented in the cyan colour are those with a μ_ϵ value lower than the threshold $T_{2\sigma}$ and that should be considered for the perfusion analysis.

Since the histogram has only positive values and is usually characterized by a long right tail, the exclusion from the analysis of μ_ϵ values greater than $T_{2\sigma}$ results to be a method quite conservative, tending to exclude very high values only. Therefore, in order to exclude the errors so to achieve a more simmetrical distribution, another well-established and more aggressive method was considered. Indeed, the triangle method has been conceived for removing tails in unimodal distributions [245]. The threshold T_T that can be found by applying the triangle method corresponds to the bin of the histogram whose top has the maximum perpendicular distance to the straight line joining the mode and the last bin of the distribution. This geometric method is less conservative than the $2 - \sigma$ rule and consequently the relation $T_T < T_{2\sigma}$ ever holds. However, due to the high risk to incur in local minima solutions, the application of the triangle method cannot be done directly on the raw histogram. Therefore, it is necessary to follow a two-step pre-processing procedure. First of all, it is

appropriate to remove the farthest outliers by cutting the 2.5% of voxels with the highest error values. This step needs to be done in order to avoid that the presence of few bins placed very far from the mode can cause an incorrect selection of the T_T value, greater than the correct one. For instance, Figure 3.10 shows an histogram of μ_ϵ values thresholded with the triangle method

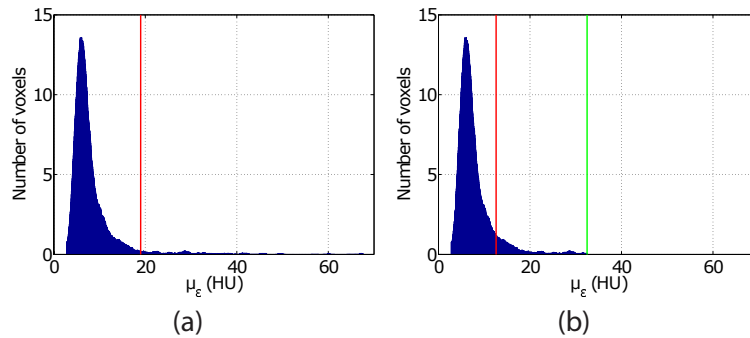


Fig. 3.10: Histogram of μ_ϵ with T_T value (the red vertical line) found by applying the triangle method on all data (a) and after having excluded voxels with the highest error (*i.e.*, those after the green vertical line) (b).

by considering all the values (Figure 3.10 (a)) or by excluding those voxels characterized by the highest errors (Figure 3.10 (b)). The second step to be performed is the application of a moving average filter to the bin values of the μ_ϵ histogram. The local inhomogeneity among bins and the accidental presence of a bin particularly high could indeed lead to the selection of an incorrect T_T value too. The size of the moving average filter is selected through the use of an adaptive algorithm that automatically chose the best window for each CTP examination in order to gain the best trade-off between histogram smoothness and preservation of data content. Figure 3.11 shows how the application of a moving average filter can affect the selected T_T value.

Finally, in Figure 3.12 a comparison between the two automatic threshold methods analysed is reported. In the histogram and in the corresponding TEM, the two different threshold values that can be chosen accordingly with the $2-\sigma$ rule and the triangle method are visible. In the cyan colour are represented those voxels characterized by low error values ($\mu_\epsilon < T_T$). In the red colour are represented those voxels whose BF values would be considered as being unreliable only by the triangle method ($T_T \leq \mu_\epsilon < T_{2\sigma}$). The blue colour, instead, points out those voxels that would be excluded from the analysis by

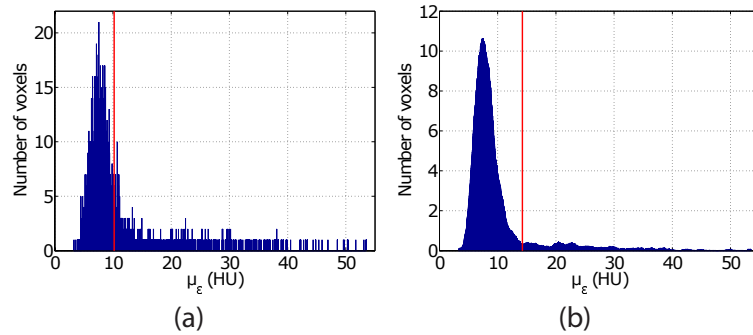


Fig. 3.11: Histogram of μ_ϵ with T_T value (the red vertical line) found by applying the triangle method to the original data (a) or to data filtered with a moving average filter (b).

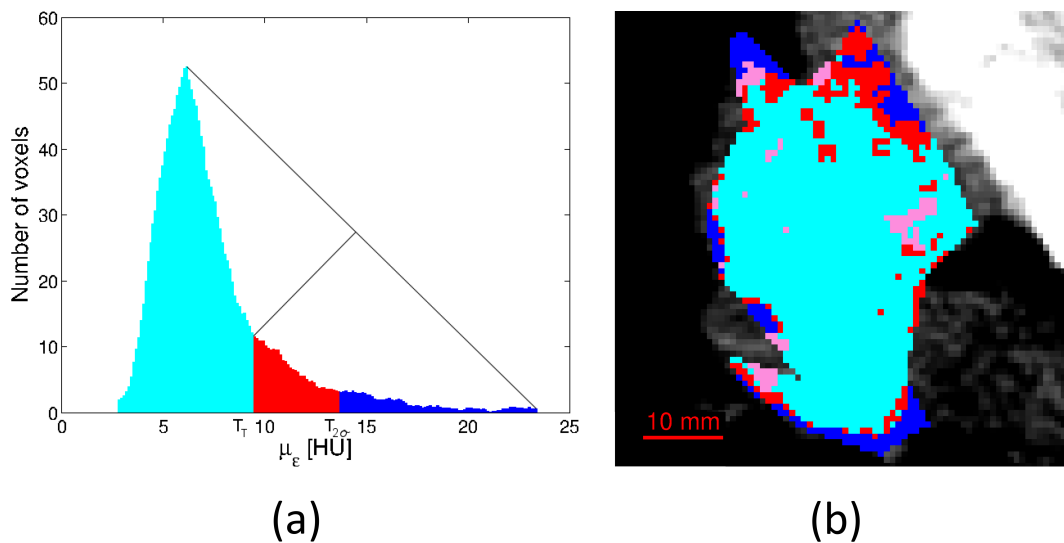


Fig. 3.12: Histogram (a) and TEM (b) pertaining to the same patient of Figure 3.8 (c), (d) and 3.9. The voxels and the bin in the cyan colour are those characterised by a μ_ϵ value lower than T_T . The red bins and voxels are associated to those TCCs having error index between T_T and $T_{2\sigma}$. The blue colour instead, is used for those bins and voxels with very high error value (greater than both T_T and $T_{2\sigma}$).

both thresholding methods ($\mu_\epsilon \geq T_{2\sigma}$).

The $2 - \sigma$ rule has been used for the first time to remove outliers from lung and liver CTP examinations in the study [230] carried out by the CVG. Moreover, its clinical usefulness has been proved and compared with that of the triangle method in [236], using several CTP examinations pertaining to patients with primary lung cancer. Finally, triangle method, that has shown to be the most effective ones, has been selected and applied in other recent CVG studies [235, 237].

3.4 Quantitative assessment of perfusion local spatial coherence

An important feature that has to be taken into account to evaluate the goodness of the algorithm applied to compute perfusion parameters is the spatial coherence of the results obtained. All the methods and models discussed in Sect. 2.2 permits the computation of perfusion parameters by evaluating the signal coming from a single voxel without taking into account the trend of the neighbour TCCs. Since tissue TCCs pertaining to a small window should usually tend to follow quite gradual and coherent transitions instead of undergoing abrupt changes from voxel to voxel, the measure of spatial coherence can provide information regarding the reliability of the estimated perfusion maps. An index that can be used to assess the dispersion of a distribution of values around their mean is the coefficient of variation (CV). For instance, considering all the BF values of a ROI, the CV (expressed in arbitrary units) can be computed as the rate between the BF standard deviation σ_{BF} and the BF mean μ_{BF} , according to Eq. 3.15:

$$CV = \frac{\sigma_{BF}}{\mu_{BF}} \quad (3.15)$$

This index has been adopted in CTP studies in order to assess the perfusion uncertainty and variability of BF values [209, 246]. However, by using the CV on the whole ROI, it is not possible to take into account the spatial relations of perfusion values. Accordingly, in order to achieve a measure of the local spatial perfusion coherence, the local CV (lCV) has been proposed. This index is computed for each voxel (x, y) as the CV of the window of dimension $w \times w$ centred on (x, y) . The colorimetric map of lCV that can be achieved allows to visually evaluate the spatial coherence of BF values.

Furthermore, by computing the mean and the standard deviation of all the ICV values (μ_{ICV} and σ_{ICV} , respectively) it is possible to achieve a measure of the global spatial coherence of the analysed tissue. For instance, Figure 3.13 reports four colorimetric maps of the same section of a lung lesion computed

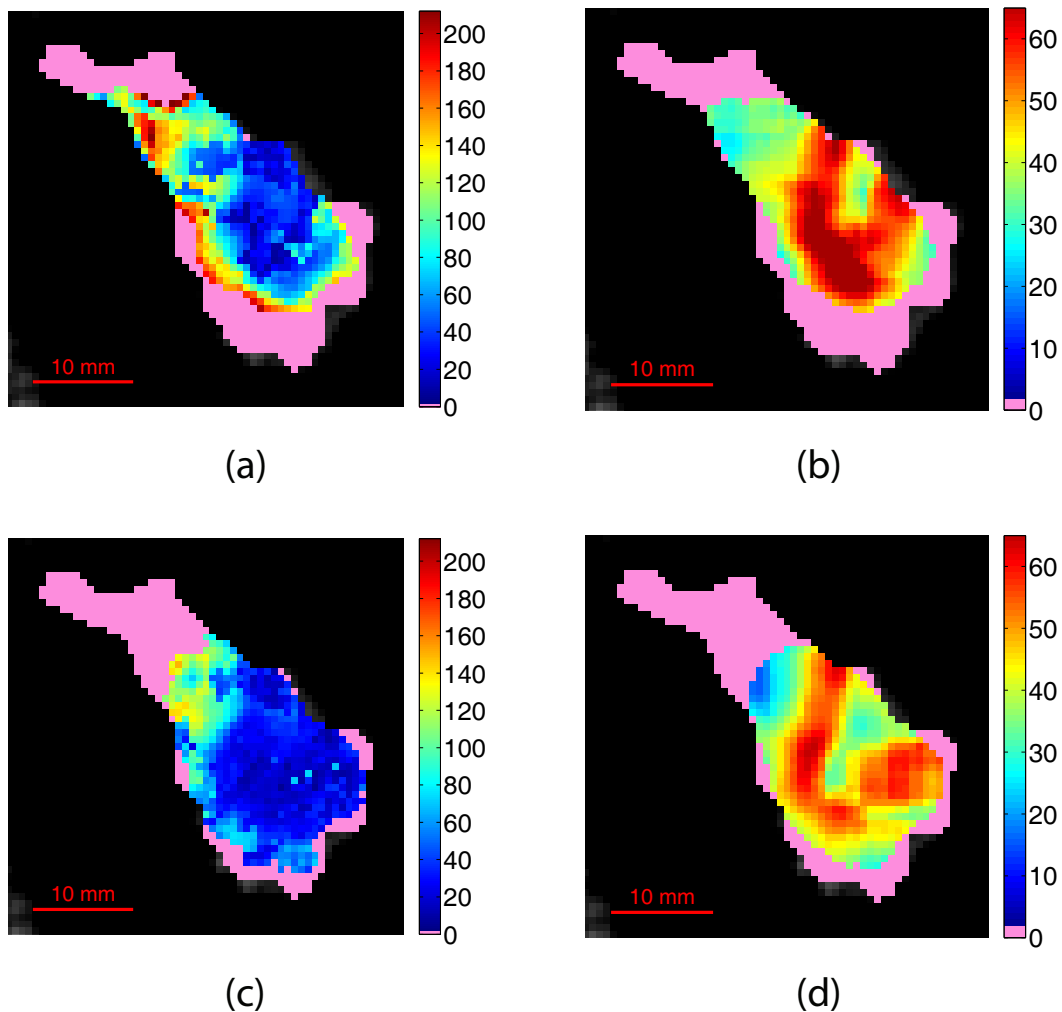


Fig. 3.13: BF (a,c) and ICV (b,d) maps of a lung lesion computed on TCCs before (a,b) and after (c,d) considering motion correction. The pink colour is used to represent unreliable BF values and those voxels where the ICV values cannot be computed because there are not enough reliable BF values in the adjacent voxels.

on TCCs of different qualities¹. In the first row the BF (Figure 3.13 (a)) and the ICV (Figure 3.13 (b)) colorimetric maps computed on TCCs affected

¹Credits to Eng. Serena Baiocco for providing these data.

by motion are represented. Instead, in the second row (Figure 3.13 (c), (d)) the same colorimetric maps are computed on TCCs that have been corrected through the use of a motion correction method. As one can see, the *BF* map (Figure 3.13 (c)) computed on the motion corrected data is locally more homogeneous than the other *BF* map (Figure 3.13 (a)). However, while μ_{ICV} values well describe this feature by decreasing from 47.91 to 42.12, as the TCCs quality improves, the *CV* computed on the whole ROI increases from 68.06 to 75.33, showing not to be able to capture the local map coherence.

The *ICV* has been adopted in two studies carried out by the CVG. In particular, in the first one [234] an algorithm based on random sample selection (RANSAC) to remove outliers from the TCCs was proposed. Thanks to the capability of this algorithm to provide better TCCs on which computing perfusion parameters it was possible to achieve *BF* colorimetric maps with a higher spatial coherence. The improvement brought by the use of this algorithm of outlier removal was tested on 14 examinations pertaining to as many patients with NSCLC and verified both qualitatively and quantitatively through the use of *ICV*. In the second work [237], the use of *ICV* was deepened and validated in 15 patients with primary lung cancer. In this study, *ICV* proved its capability to provide information about tissue local heterogeneity independently from the amount of noise affecting images.

3.5 Quantitative measurement of functional heterogeneity

Despite heterogeneity is one of the main features of tumour tissue and can be present both at morphological and at functional level (Sect. 2.1), it has often been neglected (Sect. 2.4.7). Since CTP aims at giving the possibility to assess the functional characteristics of the analysed tissue, I looked for an index that could allow the quantification of tissue hemodynamic heterogeneity.

The Shannon entropy (or briefly, Entropy) constitutes a well-known measure of data information content [247]. This parameter was introduced in the information theory in the late 1948 [248] and since then it has been applied in several fields, image analysis included. The Entropy (*E*) is computed as

$$E = - \sum_{i=0}^{k-1} p(v_i) \log_2 p(v_i) \quad (3.16)$$

where k is the number of the possible outcomes and $p(v_i)$ is the frequency of the i^{th} outcome. Entropy measures are reported in arbitrary units (a.u.).

In Figure 3.14 there is an example of three photo sorted by increasing



Fig. 3.14: Three photographs depicting different landscapes are sorted from left to right by increasing Entropy values.

Entropy values. The landscape with the lowest Entropy value ($E=5.97$, Figure 3.14 (a)) is indeed the one containing fewer details, while the one with the highest Entropy value ($E=7.83$, Figure 3.14 (c)) is the one showing more elements, most of which introduced by human beings. Instead, the photograph in the middle (Figure 3.14 (b)) is the one with an intermediate complexity and consequently is also characterized by a mid Entropy value ($E=6.50$).

The Entropy has been often used in texture analysis and it has also been applied in oncology. For instance, it has been used to evaluate texture irregularities [249], and have proved to provide important information for the formulation of tumour diagnosis [250, 251] and prognosis [192, 252]. However, to the best of our knowledge, Entropy has never been applied to the colorimetric maps of perfusion parameters. In order to achieve a measure of tissue hemodynamic heterogeneity I computed Entropy on the BF colorimetric maps. In this case, the $p(v_i)$ of Eq. 3.16 represents the frequency of BF values inside the BF map. Figure 3.15 reports the BF colorimetric maps pertaining to five adjacent sections of the same tumour, sorted from left to right by increasing Entropy values. As in the example of the landscape photos, Entropy has shown to be once again able to detect the information content of the BF maps that here is the functional heterogeneity. The colorimetric maps related to the second level of the tumour is the most homogeneous one (Figure 3.15) (a) and presents the lowest Entropy ($E = 7.43$). Its adjacent slice at level 3 instead, is the colorimetric map of the tumour with the highest heterogeneity (Figure 3.15) (e) and consequently is characterized by the high-

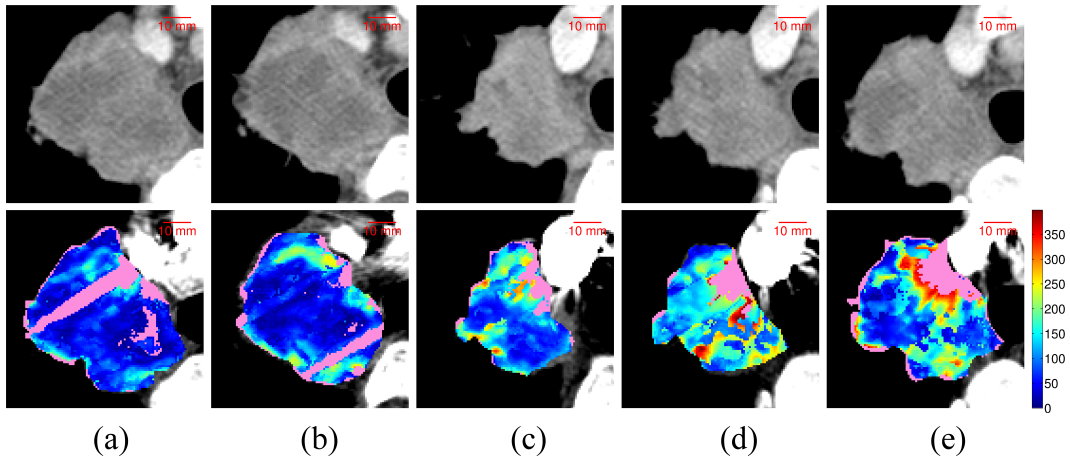


Fig. 3.15: Five CT images (first row) and BF colorimetric maps (second row) pertaining to consecutive sections of the same tumour and sorted from left to right by increasing Entropy values: the slice at level 2 ($E = 7.07$) (a), level 1 ($E = 7.43$) (b), level 5 ($E = 7.62$) (c), level 4 ($E = 7.92$) (d), level 3 ($E = 8.10$) (e). The BF values represented in the pink colour are those considered as non-reliable and are not included in the computation of the Entropy value.

est Entropy value ($E = 8.10$). An intermediate functional heterogeneity can instead be observed in the more external sections of the lesion that accordingly present mid Entropy values with respect to sections 2 and 3. Indeed, levels 1 (Figure 3.15) (b), 4 (Figure 3.15) (d), and 5 (Figure 3.15) (c) are characterized by Entropy values of $E = 7.43$, $E = 7.92$, and $E = 7.62$ respectively.

The use of Entropy on BF values has been applied for the first time in [253] to quantify the functional heterogeneity of different sections of the same tumour or of different lesions (Chapter 5).

Chapter 4

A method to assess perfusion values reliability

In this Chapter, the issue of the lack of indexes capable to assess the reliability of perfusion results described in Sect. 2.4.3 is faced. In particular, in Sect. 4.1, a specific background regarding issues related to respiratory motion and the presence of noise and artefact in CT images is reported. In Sect 4.2, the validation of the temporal index μ_ϵ presented in Sect. 3.2.1 as an indicator of signal quality and of perfusion values reliability is carried out. After that, an automatic method employing μ_ϵ values to automatically detect unreliable perfusion values is presented and compared with the manual method used in literature to exclude perfusion values apparently out of the physiological range (Sect 4.3).

4.1 Background

As discussed in Sect. 2.4.3, reliability and reproducibility of the functional results still represent open issues. Among the factors affecting the outcomes of CTP examinations, three of the most relevant ones are the presence of motion, noise, and acquisition artefacts in the CT images. In addition, the presence of anatomical structures, such as vessels and bronchi, can further affect reliability of the obtained results and jeopardize perfusion maps. In this section, all these aspects are discussed.

As regards motion, it has been proved that respiratory movements induce artefacts that can break the spatial fidelity of the imaged structures, causing inconsistent intensity trends for the generic spatial location of interest. Figure 4.1 depicts a clear example of motion artefacts found in a liver CTP



Fig. 4.1: Liver CTp image deeply affected by motion artefacts.

image of a patient with CRC. In addition, respiratory movements and tumour spatial heterogeneity can lead to mis-registrations in both transverse (x - y plane) and craniocaudal (z axis) directions and yield misleading rapid or slow inflow/outflow patterns, affecting reliability of the resulting perfusion parameters.

Many methods to reduce and to compensate for patient motion have been proposed in the literature (Sect. 2.4.5). However, here I want to draw reader's attention on the alignment methods applied to the acquired CT images and on their effects on TCCs and on perfusion values, accordingly. In the literature, erroneous estimations of perfusion parameters for a single tumour level analysis (*i.e.*, fixed slice at z -location) have been reported in [212, 254] for liver CTp, so that multi-level methods, based upon retrospective visual selection of image sets contiguous to a reference z -axis position, are suggested [202, 254]. Manual translation of ROIs [208] as well as manual and anatomic-based image registration with respect to a reference slice are applied in lung [255] and liver [239] CTp, where motion effects can be even more evident. However, only few methods take into account x - y misalignments jointly with z -axis misalignments, meaning that a specific assessment of 3D manual registration is absent [255]. As a matter of fact, recent clinical studies are still conducted employing x - y or craniocaudal compensation only [210], or not even that [159].

Some registration methods aim at assessing the effectiveness of image alignment only [255, 239], or the reproducibility of perfusion parameters [204, 205],

while none of them, to our best knowledge, measure the effect of motion on TCC signal, also correlating these measures with the reliability of perfusion analyses. In fact, the impact of motion artefacts on CTp reproducibility for such methods is discussed for liver and lung tumours in [204, 205], emphasizing how variability in the estimation of perfusion parameters can reach 70% – 90% in the absence of any kind of compensation, while decreasing to relatively lower values (10% – 20%) when data registration is applied. However, these works do not mention the reliability of perfusion patterns, which were not even submitted for evaluation to radiologists.

The study and the measurement of the effects of motion artefacts on TCCs and on perfusion values reliability is carried out in Sect. 4.2.

Another issue hampering the achievement of reliable and reproducible results is the presence of noise and acquisition artefacts in CT images. Despite software embedded in CT scanner are capable to reduce their presence, streaks and dark bands are often well visible on CT images, sometimes so heavily as to impede the use of CT examinations [256].

Image noise (also known as Poisson noise) is an effect caused by the statistical error of low photon counts that can be seen on CT images in the form of bright and dark streaks mainly in direction of the greatest attenuation. Noise presence can be reduced only with the use of CT system's reconstruction algorithm [257]. Figure 4.2 reports an example of liver CTp image affected by



Fig. 4.2: Liver CTp image affected by Poisson noise.

Poisson noise.

CT artefacts can be grouped into three categories:

- physics-based artefacts, resulting from the physical processes involved in the data acquisition
- patient-based artefacts, strictly related to the patient such as those due to motion or to presence of metallic materials
- scanner-based artefacts, due to hold ups of some scanner components

Examples of physics-based artefacts are the well-known beam hardening effect, the partial volume effect, the photon starvation, and the undersampling. Beam hardening is caused by the passage of x-ray beam through a tissue. Low-energy photons are absorbed by the tissue more than high-energy photons and accordingly, the mean energy value of the beam leaving the tissue increases (*i.e.*, the beam becomes “harder”). This would result in artefacts, such as streaks and dark bands appearing between two dense objects, and in cupping artefacts, consisting in different attenuation of the photon beam when crossing tissue middle portion and edges [258]. Beam hardening artefacts, such as those represented in Figure 4.3, could also arise in the presence of a high

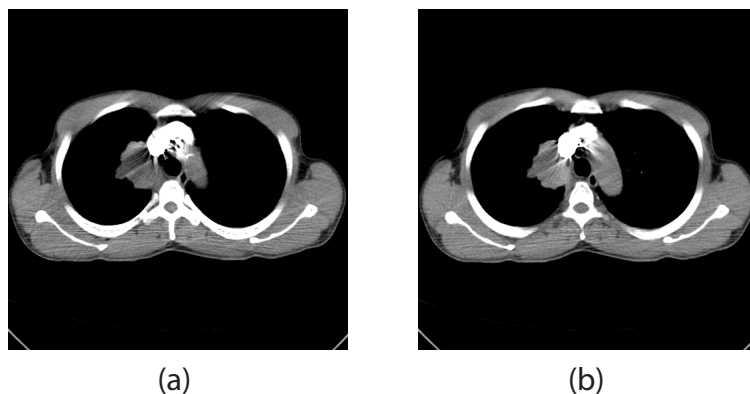


Fig. 4.3: Lung CTp images affected by beam hardening causing dark bands (a) and streaks (b).

CA concentration. The effects of this type of artefacts can be reduced by using iterative reconstruction and by combining data from multiple scans [257]. Partial volume instead, is an effect related to spatial resolution and is caused by the loss occurring when an object partially occupies the sensitive volume (*i.e.*, the volume from which emitted photons would be detected at a given detector location) of the imaging instrument [259]. For instance, when the

tissue analysed is affected by rapid motion or when there are inconsistencies between two views (*i.e.*, the detectors see an object from one angle of view, but not from the others), partial volume artefacts will occur. An example of inconsistencies between two views is represented in Figure 4.4. This effect can

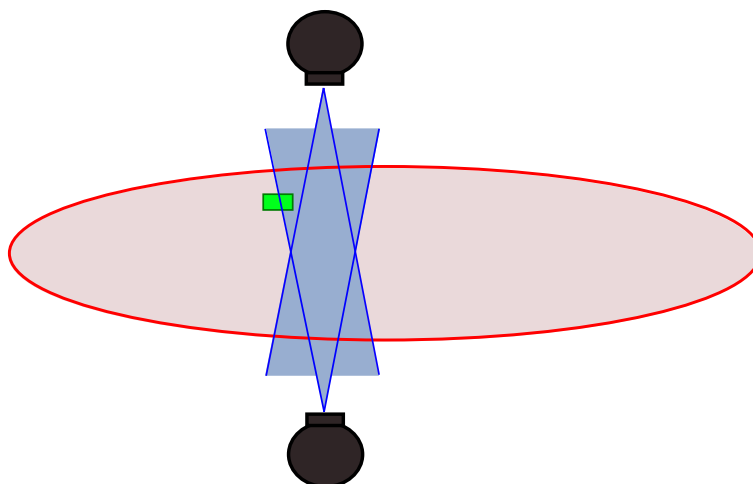


Fig. 4.4: Inconsistency between two views: only one of the two detectors see the object in the green colour.

be reduced by using thinner acquisition sections [256]. Photon starvation is an effects occurring when a too low number of photons reach the detector, leading to heavy streaking artefacts. This effect is often visible at pelvis or shoulder level (Figure 4.5) where several attenuating anatomical structures are present [260]. Photon starvation can be reduced by using methods of tube current modulation and algorithm of active filtration. The increase of tube current indeed, allows reducing the effects of the problem, but at the expense of a higher radiation dose delivered to the patient [256]. Finally, undersampling occurs when few projections are used to reconstruct a CT image (view aliasing) or when few detectors are used within a projection (ray aliasing). This effect is very important in pixel-based analysis where fine details are important and can be solved by using high resolution acquisition techniques [256].

As regards patient-based artefacts, the most important are those related to motion and to the presence of metallic objects, such as prosthetic devices and surgical clips. In Figure 4.6¹ a patient-based artefact caused by the presence of a hip's prosthetic devices is shown. This last category yields streaking artefacts that can be partially attenuated through the use of proper correction

¹courtesy of <http://abcradiology.blogspot.it>



Fig. 4.5: Lung CTp image acquired at shoulder level and presenting clear photon starvation artefacts.

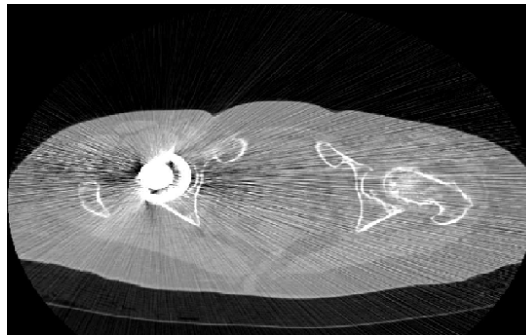


Fig. 4.6: Patient-based artefacts caused by the presence of prosthetic devices.

software [261].

Scanner-based artefacts mainly derives from the miscalibration of one or more detectors. The constant error given by the detector in each angular position results in a ring artefact centred on the isocentre of rotation [262], such as those shown in Figure 4.7. This type of effects can be reduced with the application of correction software and solved by recalibrating CT detectors [257].

Besides artefacts [263], also vessels [204] and bronchi [264] are usually manually excluded from the perfusion analysis not to jeopardize the visual analysis of perfusion colour maps nor the automatic computation of local or global statistical indexes regarding perfusion values.

In general, the unreliable perfusion values in colour maps are simply con-



Fig. 4.7: Liver CTp image affected by scanner-based artefacts caused by the miscalibration of several detectors.

sidered as those being out of range of physiological parameters, for instance, due to vessels [152] and are detected and excluded by manually drawn an excluding ROI or adjusting an appropriate window level [83]. So far, the TCC fitting errors and goodness of fit indexes have been mainly used to evaluate the reliability of given simulated model fitting, from a theoretical point of view, in lung CTp [209] or liver MRI [265] perfusion studies, rather than to assess the voxel-based reliability of perfusion values.

In order to face the problems given by the presence of anatomical structures (*e.g.* vessels and bronchi) and CTp reconstruction and acquisition artefacts that could compromise the correct interpretation of a CTp colour map, an automatic method to detect and exclude from perfusion analysis the regions affected by this problem has been proposed in Sect. 4.3.

4.2 Validation of the temporal error index μ_ϵ

The aim of this section is to study and measure the effects of motion artefacts on TCCs and on the consequent reliability degree of perfusion colorimetric maps through visual assessment by expert Readers. To this purpose, three different motion compensation approaches that must show increasing effectiveness were considered: no compensation, x - y only and 3D (which includes rigid shifting along both the x - y plane and the z -axis). The temporal error

index μ_ϵ presented in Sect. 3.2.1 is computed on each sets of TCCs resulting from the alignment procedure. In this way, it is easier to assess whether our quantitative index is really able to detect this expected increasing effectiveness, which would confirm its capability to correlate with quality of image alignments. For the sake of completeness, a fourth registration method (hereafter, 1D), aligning on the z direction only, was considered. This method is sometimes used in lung and liver perfusion [210], but its rank of effectiveness with respect to the other three methods just mentioned, is unknown a priori. In addition, the sets of perfusion maps achieved were submitted for assessment by radiologists, so as to check if better alignments in any way yield more reliable colorimetric maps. In fact, if a better image registration expectingly brings more reliable TCCs on the available data, it cannot be taken for granted that these yield more reliable perfusion patterns in the colorimetric maps, also because alignments themselves might always introduce “regional artefacts”.

The set of CTp examinations used in this study are described in Sect. 4.2.1. Each of them were acquired following the protocol described in Sect. 4.2.2. After that, a ROI was drawn on lesion contour and aligned according to four different strategies as reported in Sect. 4.2.3. On the whole, each patient provided a different set of results for each of the four motion compensation approaches, for a total amount of 44 different configurations. Voxel-based BF values were computed on all the 44 sets of data by applying the image and signal denoising procedures reported in Sect. 3.1.1, TCC fitting through Hill’s equation, and computation of perfusion values according to the single-input maximum slope (SIMS) method (Sect. 2.2.2). The temporal error index μ_ϵ presented in Sect. 3.2.1 was then computed on each TCC of the 44 sets of data and validated through the procedure described in Sect. 4.2.4. Statistical tests were carried out on the achieved data as described in Sect. 4.2.5. Experimental results are finally presented and discussed in Sect. 4.2.6, while concluding remarks are reported in Sect. 4.2.7.

4.2.1 CTp examinations

In order to validate our temporal error index (*i.e.*, μ_ϵ) as indicator of both TCC quality and perfusion values reliability, a set of lung and liver CTp examinations pertaining to a study approved by the Institutional Review Board of IRST was used². The patients considered showed one primary NSCLC le-

²This study was approved by the IRB (Comitato Etico Area Vasta) of the IRCCS-IRST, Istituto Scientifico Romagnolo per lo Studio e la Cura dei Tumori, Meldola (FC), ITALY,

sion or liver metastases. In particular, the examinations selected for this first retrospective study pertained to patients who had not been able to hold their breath for the whole duration of the acquisition. All these examinations show residual breathing and undergo artefacts from motion. However, only examinations with at least 25% of slices to be replaced with different z levels were included in the study. Finally, 11 CTp examinations pertaining to as many patients (age range 36 - 81 y.o.) were enrolled. Tumour type and extent of the analysed sections are reported in Table 4.1.

Tumours' features				
Patient	Tissue	Type	Stage	Section (cm^2)
ID1	Liver	metastasis	-	2.74
ID2	Liver	metastasis	-	1.95
ID3	Liver	metastasis	-	4.04
ID4	Liver	metastasis	-	2.39
ID5	Lung	adenocarcinoma	IV	22.11
ID6	Lung	adenocarcinoma	IV	15.82
ID7	Lung	adenocarcinoma	n.a.	20.58
ID8	Lung	squamocellular carcinoma	IIIB	7.29
ID9	Lung	adenocarcinoma	n.a.	17.33
ID10	Lung	adenocarcinoma	IV	8.57
ID11	Lung	squamocellular carcinoma	n.a.	4.33

Tab. 4.1: Table summarizing the eleven cases requiring multi-slice alignment (n.a. stands for “not available”).

4.2.2 Acquisition protocol

The patients' datasets were collected according to two different scanning protocols, depending on the investigated tissue (*i.e.*, lung or liver). CT scans were performed on a 256-slice CT system (Brilliance iCT, Philips Medical Systems, Best, The Netherlands), with patients in the supine (feet first) position. An initial, low dose, unenhanced full-body CT scan was performed to identify the target lesions at baseline conditions. A 50 – ml intravenous bolus of CA

with ID: IRST 162.04, on Oct 27, 2010, as a part of a wider study: Perfusion multidetector computed tomography (256 slices) in patients with advanced NSCLC: evaluation of tumour response after chemotherapy and radiation therapy.

(Iomeron, Bracco, Milan, Italy) was then injected at $5ml/s$ for axial cine DCE-CT, according to two different protocols for liver and lung examinations.

In liver perfusion protocol, a single acquisition of duration $55s$, consisting of 36 scans with $50mm$ of z -coverage (10 slices \times $5mm$ thickness, $0.33s$ rotation time, at $120kV$, $140mA$, $70mAs$). Image data are reconstructed to 360 cine images (512×512 pixel, $350mm \times 350mm$, $5 - mm$ slice spacing, $1.57s$ temporal resolution).

In lung perfusion protocol, a single acquisition of duration $25s$, with patient instructed for breath-hold, giving 20 scans with $55mm$ of z -coverage (11 slices \times $5mm$ slice thickness, $0.4s$ rotation time, at $80kV$, $250mA$, $100mAs$). Image data are reconstructed to 220 cine images (512×512 pixel, 11 slices, $350mm \times 350mm$, $5 - mm$ slice spacing, $1.25s$ temporal resolution).

Accordingly, the generic protocol provides for M scans, each corresponding to different sampling instants, of K levels each (*e.g.* for the lung perfusion protocol $M = 20$, $K = 11$).

4.2.3 Image alignment

The target lesions and the arterial input (aorta) were selected in agreement by two radiologists on a *reference slice* and the temporal sequence of slices related to the corresponding (couch) z -location (level) was annotated as *reference sequence*. For each lesion, an ROI was then manually outlined by the radiologists on the *reference slice*.

Three alignment methods were assessed in this study and compared with the unregistered approach. Altogether, these are the four procedures used:

Standard fixed mode (SF): the reference ROI is unregistered, that is, kept fixed along the reference sequence, as it usually occurs for standard CTp protocols supported by most perfusion software provided by CT manufacturers. TCCs are built by sampling the HU (image) values at the same pixel location for all the slices of the reference sequence. In case of motion, TCCs obtained with this alignment method are expected to be the most subject to artefacts.

Transverse manual registration (2D): the reference ROI is manually translated on the x - y plane of each slice of the reference sequence so that it visually matches the borders of the lesion. In each image of the reference sequence, each TCC is built by sampling the HU values found in the same ROI's pixel. According to this method, motion compensation is performed only for x - y translations.

Multislice manual registration (3D): given the reference slice, adjacent

slice levels (up to two levels before and after the reference level) are visually explored by the radiologists who choose, for each of the M scans, the level which visually presents the best matching with the reference lesion. The resulting slice sequence is then referred to as the *best sequence* (in Figure 4.8, the lesion ID5 from lung perfusion dataset is shown as an example), and 2D is then performed on this sequence. According to this procedure, a 3D manual alignment is achieved by also taking into account motions in the craniocaudal direction.

Transverse manual registration (1D): the reference ROI is kept fixed along the best sequence selected in 3D. According to this method, motion compensation is performed only for z translation, along the craniocaudal direction.

However, although four correction approaches were considered, I would like to draw reader's attention mainly on SF, 2D and 3D since, by construction, they perform with increasing quality and I expect our quantitative index to be capable of detecting this order relationship, accordingly. To this purpose, 2D and 1D are alternative, both expected to perform better than SF and worse than 3D.

4.2.4 Validation procedure

So for the registration accuracy has been evaluated by assessing visual or automatic alignment (*e.g.* overlap) with respect to ground-truth anatomical structures achieved by manual segmentation [255, 239], or by evaluating the repeatability of perfusion estimations in multiple acquisitions [204]. However, no indication has been provided about the effects of image alignment on the resulting TCCs which represent, on the other hand, the source data used to calculate the perfusion parameters. More specifically, a recent approach considers the quality of TCCs over the whole liver merely as a predictor for patient motion [210]. Besides that, there is no mention of further quality check steps by radiologists. As a matter of fact, in real studies (where no synthetic ground-truth is available) clinical evaluation of the perfusion maps should be performed by radiologists through visual inspection of the perfusion scan, in order to validate the outcome of the perfusion software, confirming the presence of plausible spatial perfusion patterns. For these reasons, to validate μ_ϵ as a reliability index of perfusion values, two procedures have been proposed: a quantitative one, based upon the *temporal regularity* of TCCs (*i.e.*, the tendency of the real signal to approach the trend of the ideal one, represented by the fitting curve), and a *qualitative* one, performed by radiologists and based

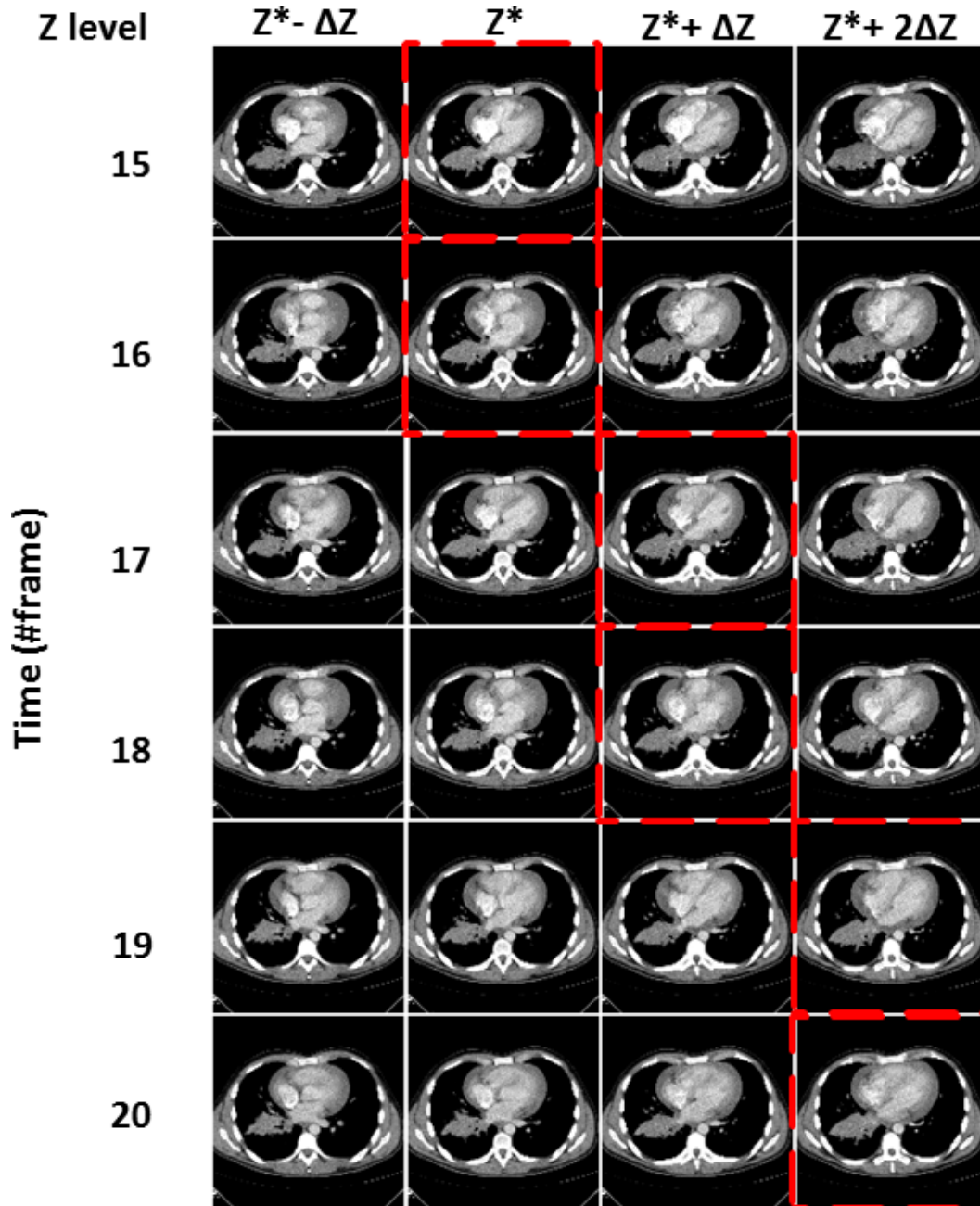


Fig. 4.8: An example of selection of the best sequence from a lung perfusion dataset (ID5) on several (four, in this case) contiguous z levels (*i.e.*, adjacent slices), where Z^* is the reference slice and ΔZ represents one z level. Accordingly, sampling of HU levels at consecutive time instants is performed by selecting multiple levels.

upon visual evaluation of the resulting perfusion patterns.

As a measure of the spatial fidelity of the sampled time concentration signal and, accordingly, of its *reliability* in the presence of acquisition motion artefacts, μ_ϵ value was computed in each voxel. Accordingly, a colorimetric map can be generated from the processed image sequence. Four colorimetric maps of μ_ϵ were consequently achieved for each examination, one for each alignment method. The expected value $E[\mu_\epsilon]$ and the standard deviation $\sigma(\mu_\epsilon)$ of the quantitative index values were finally calculated for each alignment approach and for each patient.

In addition, the automatic threshold method based on the $2 - \sigma$ rule (Sect. 3.3) has been applied to the histograms of μ_ϵ to find out unreliable perfusion values.

The use of this threshold as the reliability index offers a fair comparative analysis for assessing the effects attributable to the alignment methods only. In particular, I would expect that SF, 2D/1D and 3D, respectively, have increasingly lower values for $E[\mu_\epsilon]$.

As regards qualitative index, two Readers with more than 25 years of experience in interpreting CT studies in oncology ranked the four alignment procedures through visual exploration of the perfusion maps, using a 4-point scale, according to the likelihood of the resulting perfusion maps with respect to the expected enhancement patterns. The rank is an integer number ranging from 1 to 4, where “1” corresponds to the expected perfusion pattern. The evaluation was performed for each examination in three stages, two of which were performed in a blinded fashion. In the first stage, each radiologist examined the full CTp sequence in order to form his own opinion regarding the perfusion pattern. After selecting the reference sequence for the SF, through consensus, the Readers outlined the ROIs and built the 1D, 2D and 3D sequences. Then, in the second stage, each Reader was provided with the four colorimetric maps, built on the sequences just defined and corresponding to the different alignment procedures. The colorimetric maps were proposed with no label and in random order and each Reader assigned each map its proper rank. In the last stage, the Readers established the final rank through agreement. Accordingly, the *rank* constitutes the qualitative index.

4.2.5 Statistical analysis

The paired two-sided Wilcoxon signed rank test implemented in R software (version 3.0.1, The R Foundation for Statistical Computing) was used to assess

the differences in $E[\mu_\epsilon]$ between the three correction schemes (2D, 3D, 1D) and the fixed approach (SF) and between the 3D alignment configuration and the remaining 2D, 1D motion correction methods. $p\text{-value} \leq .01$ were considered for statistical significance.

4.2.6 Experimental results

The results of the visual ranking of perfusion patterns for the four alignment procedures are summarized in Table 4.2, together with $E[\mu_\epsilon]$ and $\sigma(\mu_\epsilon)$ com-

Quantitative and qualitative indexes related to perfusion maps												
IDs	SF			2D			1D			3D		
	$E[\mu_\epsilon]$	$\sigma(\mu_\epsilon)$	R									
ID1	4.69	1.19	3	4.63	1.12	2	4.33	0.74	2	4.33	0.77	1
ID2	7.05	3.29	2	7.14	2.97	2	5.52	1.70	1	4.63	0.74	1
ID3	5.58	1.68	3	5.39	1.27	4	5.13	1.37	2	4.50	0.75	1
ID4	6.43	2.28	4	6.34	2.08	3	5.27	1.36	2	4.78	0.82	1
ID5	12.12	7.66	2	10.49	5.15	2	8.51	2.26	1	8.57	2.30	1
ID6	8.62	4.10	2	8.24	3.25	3	7.57	1.45	1	7.53	1.46	1
ID7	9.46	16.17	4	8.26	2.62	3	8.09	1.50	2	7.82	2.53	1
ID8	19.65	25.15	3	9.56	5.56	2	12.07	9.81	2	9.05	2.30	1
ID9	12.32	3.21	2	12.20	2.99	2	11.69	2.67	1	11.63	2.53	1
ID10	8.67	4.46	2	7.79	2.84	1	8.34	3.43	2	7.50	2.12	1
ID11	14.01	16.95	2	9.87	10.58	2	6.21	1.89	1	5.69	1.17	1

Tab. 4.2: Table summarizing both quantitative and qualitative indexes related to perfusion maps, for the four different alignment configurations (R stands for Rank).

puted on the ROI. The results pertaining to the quantitative index are also reported in Figure 4.9, with bar plot of $E[\mu_\epsilon]$ and error bars representing $\sigma(\mu_\epsilon)$. Firstly, it can be seen that the improvements brought by motion correction are more evident for lung tumours (ID5-ID11), both in terms of $E[\mu_\epsilon]$ and $\sigma(\mu_\epsilon)$, where the lack of breath-hold causes more marked movements and structures with very different densities with respect to the lesion (*e.g.* air) can be included, if the ROI is fixed. In fact, while the SF and 2D bars have almost same height for liver tumours, in general, for lung tumours, $E[\mu_\epsilon]$ is far higher for SF, and 2D, or 1D, alone may lead to a good improvement (*e.g.* ID11), even in terms of $\sigma(\mu_\epsilon)$. In addition, while movements in the liver are often

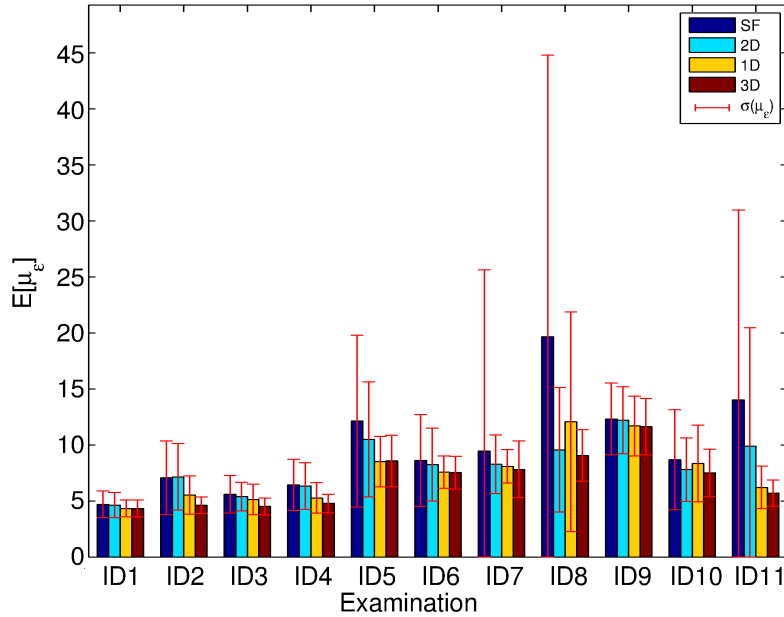


Fig. 4.9: Bar plot of $E[\mu_\epsilon]$, with error bars equal to $\sigma(\mu_\epsilon)$, for the eleven cases with the four alignment modes.

oscillatory, in the lung the ROI may have a longer craniocaudal translation (as shown in Figure 4.8). In fact, while liver metastases required just two z levels, often lung tumours required three or four of them, mainly in cases where the lesion lays in the inferior lobes, near to the diaphragm. This is why between 2D and 1D motion compensation, the latter usually yields better results.

As it can be seen, also by looking at Table 4.2, the 3D alignment procedure determines, in all cases, the lowest value of $E[\mu_\epsilon]$, highlighting a general better fit of the model to data, also with a more homogeneous behaviour (the lowest, or comparable, values of $\sigma(\mu_\epsilon)$). This confirms that smoother signal transitions occur if both translational and craniocaudal compensation are applied. In addition, as far as $E[\mu_\epsilon]$ and $\sigma(\mu_\epsilon)$ are concerned, Figure 4.9 shows that 3D is always better than 2D, which, in turn, is strictly superior to SF (except for ID2, when $E[\mu_\epsilon]$ are statistically comparable), as expected. Moreover, this analysis still applies when considering SF, 1D, 3D (except for ID1, ID5, ID6, ID9, where 3D and 1D have statistically comparable values for $E[\mu_\epsilon]$). Therefore, the quantitative index conceived confirms its capability to measure the quality of alignments with respect to the available data. In this way, it also becomes possible, and interesting, even to include in the comparison two unrelated alignments, such as 2D and 1D. As a matter of fact, our quantitative

index shows that on two occasions (ID8, ID10) only 2D performs better than 1D.

After ascertaining that $E[\mu_\epsilon]$ can measure and rank the quality of alignments, I now aim at assessing whether, and to what extent, better alignments yield more reliable perfusion patterns. Shifting to the qualitative index, it is possible to see that, although the perfusion maps achieved with 3D are consistent with what the radiologists expected, the visual analysis highlights some more uncertainties regarding the likelihood of colorimetric maps resulting from SF and 2D with respect to the expected perfusion patterns. In fact, although in the majority of cases perfusion maps from 2D are considered more reliable than those from SF, four times they are considered as being equivalent and, above all, two more times (in one liver and in one lung tumour case) they are even perceived as being worse. Nonetheless, 1D maps are always considered to be better than SF's.

Usually, also due to global correlation between fitting pre-correction errors and changes in BF values, it is taken for granted that better alignments yield more reliable perfusion patterns [229, 266]. Therefore, I would like to draw reader's attention on those cases where coherence between quantitative and qualitative ranks does not hold, that is where the quantitative and the qualitative indices do not agree, with respect to the expected behaviour, mainly limiting this comparison to SF with 2D/1D, and to 2D/1D with 3D. In fact, as already stated, nothing can be expected a priori by comparing 2D and 1D motion compensations. Accordingly, I start analysing cases where comparable errors yield different ranks (ID1, ID4), moving on to those cases where statistically significant differences in $E[\mu_\epsilon]$ are not reflected in the perfusion maps (ID2, ID5, ID11), concluding with the most relevant situations, where significant differences in the quantitative index yield opposite ranks (ID3, ID6).

Starting by ID1, although the couples SF, 2D and 1D, 3D have comparable values for $E[\mu_\epsilon]$, the perfusion maps from SF, 2D are ranked differently as well as those from 1D, 3D. In fact, this lesion mostly oscillates along the x - y plane, with a rather uniform "wide" hypo-perfused core, surrounded by a more perfused thin region, in the shape of an outer circle. Failing in aligning this region correctly, yields a perfusion map where the core actually extends up to the border, breaking off the perfused outer circle. On the whole the errors are similar, but the information generated changes. This is also what happens, to a different extent, with 2D and 1D alignments, when performed alone. In addition, although 1D and 3D have the same errors, only the pattern of the 3D map is fully reliable. Similar considerations can be made for ID4, although a

more relevant motion along the z direction makes 1D more effective, but with a significantly higher error than 3D.

On the contrary, there are cases where significant differences in the quantitative error have not effect on the information content of the perfusion maps. ID2 is the smallest liver lesion (Table 4.1) also showing a “blinking” behaviour (*i.e.*, disappearing from the reference slices now and then) and translational compensation is almost useless, as confirmed by the $E[\mu_\epsilon]$ values (both, quite low) achieved when compensating along the craniocaudal direction only or according to the 3D approach. ID5 (lung lesion of Figure 4.8) has very a heterogeneous BF , and perfusion maps from SF and 2D yield a comparable information content (with relevant unreliable parts), although 2D compensation yields a statistically significant improvement ($P \leq 0.001$), while 1D and 3D show comparable errors and reliable perfusion patterns. This is due to the real shifting being mainly along the craniocaudal direction, but the asymmetry of the lesion makes its changing section captured on the reference slice, shifting along the x - y plane, simulating a translational motion that, actually, is almost negligible. Finally, ID11 is the most stable lesion, apart from just very few slices, where it shows a motion mainly along the craniocaudal direction. This is why ID11 has the lowest values for the quantitative index among the lung tumours, as regards 1D and 3D. Accordingly, although 2D compensates, this does not improve the overall perfusion pattern, as can be seen in Figure 4.10 (b), also due to a high number of unreliable values. On the other

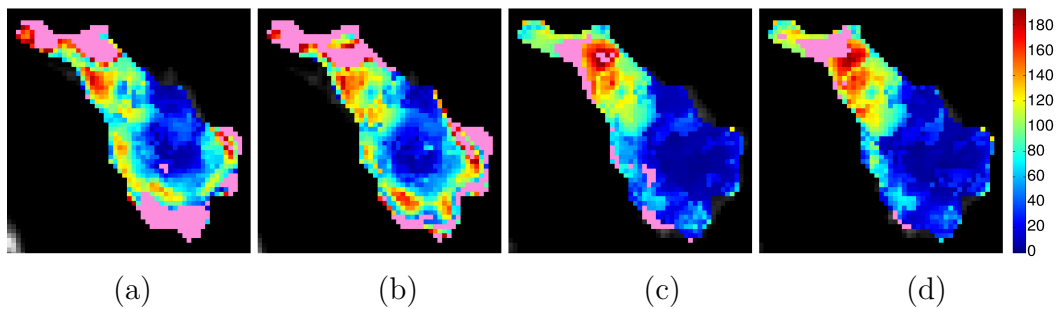


Fig. 4.10: BF colorimetric maps of ID11 resulting from SF (a), 2D (b), 1D (c) and 3D (d) alignment approaches. The pink colour highlights pixels whose perfusion values have been considered unreliable.

hand, 1D compensation lowers the error and yields a perfusion map (c) which is considered as being as much reliable as that from 3D motion compensation (d), although the latter has an even a lower value. In addition, the range of BF values for perfusion maps from SF (a) and 2D (b) is comparable, as well

as their mean value (about $73\text{ml}/\text{min}/100\text{g}$). On the other hand, the range is narrower for 1D (c) and 3D (d) perfusion maps, although being comparable with each other, as well as their mean value (about $56\text{ml}/\text{min}/100\text{g}$).

Still remaining are the two most meaningful cases where qualitative and quantitative assessments are reversed for SF and 2D alignments. I firstly consider ID3 (Figure 4.11) for the liver, a so-called target lesion that represents

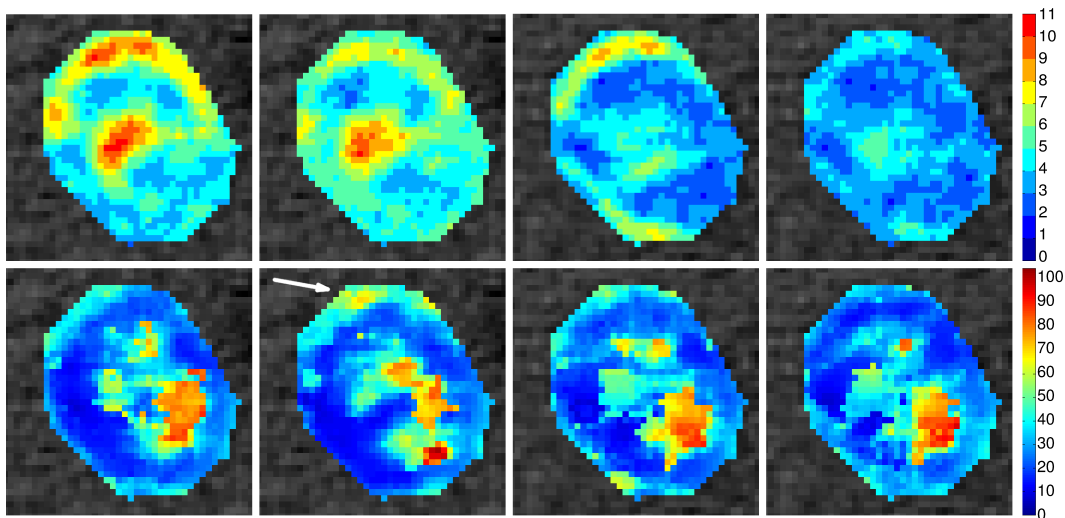


Fig. 4.11: Details of colorimetric maps of ID3 for μ_ϵ (first row) and BF (second row), resulting from the different alignment approaches (from left to right: SF, 2D, 1D, 3D). The white arrow points to an increase of perfusion that appeared even more unexpected as it relates to a region where the error decreased, as shown in the corresponding error map.

a meaningful perfusion study due to marked respiratory motions, both along the x - y plane and craniocaudal direction. However, this lesion has quite a high-perfusion core surrounded by a low perfused region, and it is the widest liver lesion (Table 4.1), meaning that despite its motion the core of a fixed ROI may sample different parts of a low-perfusion tissue. This is why $E[\mu_\epsilon]$ and $\sigma(\mu_\epsilon)$ are quite limited (Figure 4.9 and Table 4.2). In addition, this is why a much greater improvement is brought by 1D. Figure 4.11 shows the resulting colorimetric maps related to μ_ϵ (first row) and BF (second row). The first two columns (from left) refer to the SF and 2D results, respectively. As it can be seen, the manual compensation of translational motion yields improvements on the μ_ϵ map - the errors are attenuated in 2D, especially for boundary pixels (red pixels in the maps roughly corresponds to unreliable pixels according to

the two- σ rule previously described). As for corresponding BF maps, they show both a central region with a high perfusion, surrounded by less perfused pixels, with a more extended perfused area on the outer boundaries for 2D. It is worth noting that according to a visual evaluation (Table 4.2), the perfusion map from 2D (rank 4) was considered worse than SF's (rank 3), mainly right because of more evident signs of perfusion in the upper side (white arrow) of 2D error map. In addition, SF map is more similar to 3D even to a non-expert eye. In fact, if just translational compensation could improve the quantitative index (*i.e.*, the reliability of TCCs), contemporary and non-independent motion on craniocaudal direction could even worsen the map. On the other hand, 1D compensation only (Figure 4.11, third column) yields a greater improvement and, when considering the 3D alignment (fourth column), the effect of the reduction of motion components in the craniocaudal direction can clearly be appreciated, leading to the best results both at numerical and visual level. The μ_ϵ map shows the best values with a range that is halved with respect to the previous two maps from SF and 2D and the associated perfusion map is more realistic, presenting a very thin perfused region in the upper periphery, with a high-perfusion area for bottom-right pixels of the ROI, with a pattern that best resembles what the radiologists expected to see after their visual inspection.

I have just discussed colorimetric maps of a hepatic lesion whose perfusion patterns are somehow related to each other, at qualitative level. On the other side, the lung lesion I am about to analyse, ID6, is paradigmatic of what the real effect of 3D alignment on TCC and, accordingly, on perfusion patterns could be. This is even more interesting because, among the lung lesions, ID6 is the most static one according to the x - y plane and 2D yields the minimum improvement, as it can be seen at a glance from the plot of Figure 4.9. Figure 4.12 shows the colorimetric maps of BF values for ID6, referring to the different alignment methods, where unreliable pixels are set to "pink". As it can be seen, the amount of discarded values ranges from very few pixels for 3D (Figure 4.12 (c)), while it increases when moving towards SF (Figure 4.12 (a)). The most important point, however, is the position of pink pixels and of the most perfused patterns. By comparing Figure 4.12 (a) and (b), the slight improvement yielded by the manual translation in the upper borders of the lesion is visible, where movements include air samples that jeopardise the reliability of TCCs and, accordingly, of the maximum slope computation. However, the overall map visually seems to worsen in 2D with small sparse aggregates of unreliable pixels. This is the reason why the radiologists chose SF, although

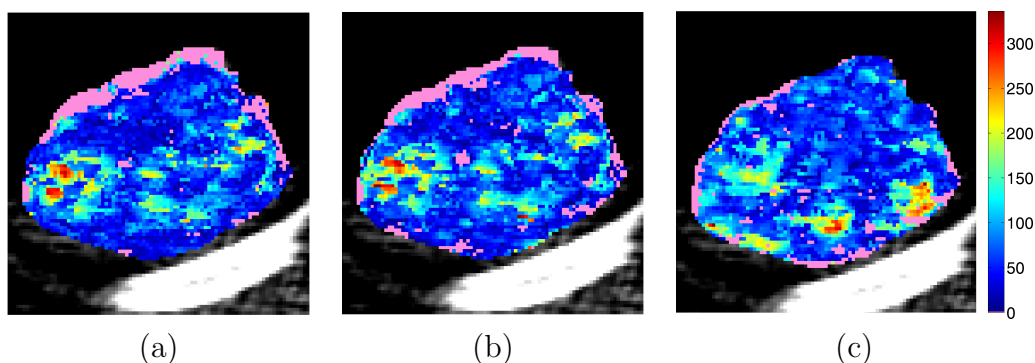


Fig. 4.12: *BF* colorimetric maps of ID6 resulting from SF (a), 2D (b) and 3D (c) alignment procedures. The pink colour highlights pixels whose perfusion values have been considered not reliable.

the quantitative indices in Table 4.2 are slightly better for 2D. It is worth remarking that there is no way to further improve the perfusion map without resorting to compensation along the craniocaudal direction (also, the map from 1D, not shown here, is considered comparable to 3D's for both the indices). Figure 4.12 (c) has been built by choosing four different z levels and it is clearly the best image and, yet more, this is the lung examination showing the most uniform behaviour ($E[\mu_\epsilon]$, $\sigma(\mu_\epsilon)$ ranging from 7.53 to 8.62, and from 1.45 to 4.10, respectively), also being among the most stable one (see $E[\mu_\epsilon]$, $\sigma(\mu_\epsilon)$ for SM in Table 4.2). However, the perfusion pattern in Figure 4.12 (c) is quite different from Figure 4.12 (a), (b). More specifically, in Figure 4.12 (c) it is still possible to appreciate some trace of the most perfused regions in Figure 4.12 (a), (b), although the most perfused pattern is at the bottom right, rather than at the bottom left.

I should highlight that this could be an unavoidable side-effect of motion compensation along the craniocaudal direction, where the definite colorimetric map actually results from different slices, in spite of the accurate tracking. In fact, while a section of a lesion shifting along the x - y plane only could be tracked (only theoretically) with no errors, the tracking along the z direction is (practically) always prone to “errors” which, for small lesions, could be of a half a slice thickness, or even more. This means that what sampled in 3D could represent a sort of “mixture” of different slices. Practically speaking, since translation motion is rarely alone, 2D compensation could represent different lesion' sections. Nevertheless, the radiologists considered the colorimetric map from 3D as the most reliable one, after considering both SF and 2D which, by

coincidence, they saw previously, as being reliable. In practice, although this behaviour is apparently unknowable, we should not forget that radiologists form their own opinion by examining all the slices of the whole CTP scan. Therefore, it is possible to state that both inner parts (*i.e.*, non-pink pixels) of Figure 4.12 (b), (c) could contain reliable patterns, just referring to different lesion sections.

4.2.7 Concluding remarks

First of all, results achieved in Sect. 4.2.6 shows that a better alignment could not yield more reliable perfusion patterns, also because regionally high errors could give a low contribution to the overall fitting error $E[\mu_\epsilon]$. For instance, high errors mainly due to initial motion (*i.e.*, related to the first few slices) may slightly affect the slope of the TCC. On the contrary, a motion in the interval around the maximum slope time instant would significantly alter the BF value, meanwhile being compliant with a low fitting error. Nevertheless, the automatic thresholding method based upon statistical analysis of distribution of our fitting error can highlight and exclude unreliable perfusion values in both lung and liver lesions. The recommendation for all the foregoing is that every perfusion maps should be critically re-evaluate by radiologists, independently from the alignment procedure followed.

A further point is that when radiologists “play” a cine sequence to form in their mind a perfusion map, what they expect can be found on perfusion maps built with different registration methods, and slice sequences, accordingly. This is because what radiologists see while observing the whole sequence of CT images often happens at different z -depths, and not just on the reference slices.

Finally, I have proven that considering a 3D alignment, albeit being based on rigid translations, is not an option, it is a necessity, since there are cases where perfusion maps arising from x - y alignments are considered to have a worse quality than those maps originating from no alignments.

In conclusion, the method presented to assess the reliability of perfusion patterns after motion compensation contributes towards achieving a more accurate and reproducible computation of perfusion values, this representing a ground stage towards the clinical use of CTP studies.

The results presented in this Section have been published in [230].

4.3 An automatic method to detect unreliable perfusion values

After studying the signal pertaining to a single voxel through the use of the index μ_ϵ , I move my attention to the analysis of the signal coming from a whole tumour slice. The aim of this section is to present a novel quantitative and automatic method to detect those anatomical structures (mainly vessels and bronchi) and those regions undergoing CTP reconstruction and acquisition artefacts, that could compromise the correct interpretation of a CTP colour map and, ultimately, the clinical outcome. The approach is again based on the computation of the TCCs' error index μ_ϵ associated with the thresholding methods presented in Sect. 3.3. The ability of our method to automatically remove the “misleading” regions is assessed and compared with the performance of two 25-year experienced radiologists who detected, and manually bounded for further exclusions the anatomical structures and the regions undergoing artefacts. Moreover, changes of mean perfusion values and, above all, of their standard deviation and CV, were analysed before and after removing the automatically segmented regions. Finally, some meaningful comparisons between colour maps achieved by using our approach and the manual thresholding on BF values commonly used by Readers are discussed.

The set of examinations that have been selected for this study is described in Sect. 4.3.1. Acquisition protocol and data processing are resumed in Sect. 4.3.2. Sect. 4.3.3 presents the manual procedure carried out by the radiologists to identify vessels, bronchi, and artefacts visible on the CTP sequence of each examination. In order to “quantify” the proficiency of the two very expert Readers on detecting and outlining the possible signs of errors in perfusion values stemming from the CT sequence, the ROIs manually drawn were compared with corresponding TEM, using statistical indexes. The comparison procedure is described in Sect. 4.3.4, while the statistical tests applied are mentioned in Sect. 4.3.5. In addition, some perfusion maps are compared where errors are removed through our approach versus manual thresholding on perfusion values. Finally, BF mean, standard deviation, and CV values of the examination before and after thresholding are computed and compared. Experimental results are presented and discussed in Sect. 4.3.6. Finally, Sect. 4.3.7 draws some concluding remarks.

4.3.1 CTp examinations

In this study, some CTp examinations of patients with primary NSCLC have been selected among those of the study used in Sect. 4.2. In particular, lesions having maximum transverse diameter greater than 2.5cm , and area wider than 3.14cm^2 were used. Lesions whose boundaries could not be accurately identified, such as in case of highly inflamed tissues surrounding the tumour, were excluded from the study. Finally, 22 patients (age range 36 - 81 y.o.) were enrolled for the study, for a total amount of thirty-four examinations, with as many lesions.

4.3.2 Acquisition protocol and data processing

The acquisition protocol followed to acquire the CTp examinations is that for lung tumours described in Sect. 4.2.2. Two ROIs were drawn, on the aorta and on the lesion contour, respectively. As a consequence of the results presented in Sect. 4.2, the tissue ROIs were aligned following the 3D procedure. The TCCs extracted from each voxel of the ROI were again fitted through the use of Hill's equation. Both μ_ϵ and BF values were computed for each voxel of the ROI and represented through the use of colorimetric maps, following the same procedures described in Sect. 4.2.

Since μ_ϵ histograms were all characterized by a bell-shape with a long right tale (as described in Sect. 3.3) and higher μ_ϵ are associated to unreliable perfusion values (Sect. 4.2), the two thresholding methods described in Sect. 3.3 have been applied to the μ_ϵ distribution of each examination so as to achieve two threshold values: $T_{2\sigma}$ and T_T . TEMs as those presented in Sect. 3.3 were created for each examination.

4.3.3 Manual annotation

For each examination, the initial sequence of 20 scans is looked through to detect and manually annotate the main causes affecting the analysis of perfusion maps, represented by artefacts, and anatomical structures such as vessels and bronchi. The purpose of this annotation stage was twofold. On the one hand, I wanted to achieve the best possible performance, and to this purpose the first radiologist (hereafter, Reader A) was given no time limit for his analysis. On the other hand, I aimed to obtain realistic results, and for this reason the second radiologist (hereafter, Reader B) had to complete his analysis in a time

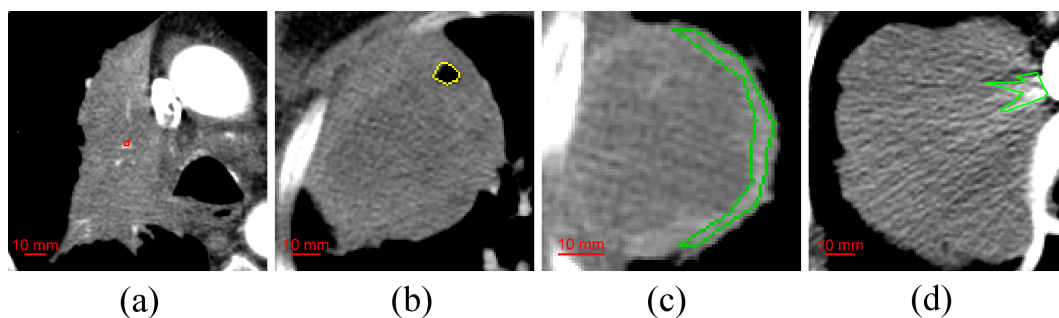


Fig. 4.13: From left to right, lesions ID15, ID34, ID14, ID17. A small vessel (a) and a bronchus (b) manually contoured by Readers A and B, respectively; artefact regions induced by motion (c) and beam hardening (d), graphically annotated by Readers A and B, respectively.

compliant with a “routine” CTP study, under the same conditions as those in a clinical environment. The analyses were accomplished in a blind fashion.

First of all, the two Readers analysed the whole set of images in cine-mode and detected the presence of vessels and bronchi inside the lesion. After that, they manually outlined in the reference slice the anatomical structures also visible in the reference sequence (Figure 4.13 (a) and (b)) using a graphic device (Intuos[®]Pro, Wacom, Krefeld, Germany). Then, the radiologists identified, and manually annotated in the reference slice, the lesion’s regions undergoing the different type of artefacts, although mainly arising from partial volume effects induced by residual motion and from beam hardening (Figure 4.13 (c), (d)). As one can see in Figure 4.13, while vessels and bronchi are usually well identifiable, detecting artefacts is much harder and, even when succeeding, both boundaries and extent cannot be detected with accuracy.

4.3.4 Comparison between annotated slices and thresholded error masks

The way the anatomical structures and artefacts were detected and outlined, mainly the uncertainty in delineating artefacts, drove our choice regarding the approach to compare the regions manually outlined with the outcome of our automatic error detection approach. For this reason, the number of numerical structures found (or missed) and the presence of artefacts in a given region were considered, since their extent was not visually assessable. Nevertheless, different types of artefacts, in the same lesion are considered separately. Ac-

cordingly, there are four different outcomes from the matching procedure: “hit” or true positive (TP), false positive (FP), true negative (TN), “miss” or false negative (FN), all arranged into three 2×2 contingency tables, for vessels, bronchi, and artefacts, respectively [267]. Also, it is worth recalling that we are interested in detecting only those acquisition and reconstruction artefacts, vessels, and bronchi that can hamper the perfusion values, rather than artefacts or anatomical structures in themselves. Therefore, the thresholded error masks was chosen as the reference (*i.e.*, the “ground truth”) and the regions manually outlined by radiologists were considered as the test condition. For instance, when a Reader detects an item that has no correspondence on the thresholded error mask (this representing a FP), this does not necessarily hints a mistake, rather most probably what detected does not hamper the computation of perfusion values. On the other side, in case that a Reader does not outline any item in correspondence of an error structure present in the thresholded error map, this is considered a FN only after that a radiologist confirmed the nature of that error structure, that is vessel, bronchus or artefact. The simplest case is when no error structures are detected, nor visually neither automatically, when the TN number in each contingency table is increased by one. As far as the TP are concerned, at the beginning I hypothesized to segment the thresholded error maps into connected ROIs and perform an automatic matching between manual and computed ROIs. Then, several known strategies could have been considered to decree a match, ranging from inclusion criteria to overlapping thresholds, even weighted to allow for possible different sizes [268]. As a matter of fact, this could work for anatomical structures, but would fail for artefacts and using different approaches would not have been fair. Besides that, in any case determining the FNs would require the intervention of radiologists. In addition, if our purpose is to quantify the Readers errors (with the meaning defined at the beginning of this paragraph), then it is enough to find out how many error causes, in terms of structures and artefacts, are missed visually. For all these reasons, I decided that a visual matching performed by the Readers would be the most appropriate for our purposes.

4.3.5 Statistical analysis

To assess the Readers’ performance I measured how their errors, in terms of FP and FN, impact on the the total number of negative ($N=FP+TN$) and positive ($P=TP+FN$) cases, respectively. This is given by the frequency of their errors

over the total number of cases, namely, the FP rate ($FPR=FP/N$) and the FN rate ($FNR=FN/P$), computed on each of the three contingency tables. FPR and FNR are also known as Type I and Type II statistical errors, respectively. Also, in order to better understand the implications of these errors, it could be useful to think of them as functions of specificity (SPEC) and sensitivity (SENS), these being entities more used in clinics, where $FPR=1-SPEC$ and $FNR=1-SENS$.

The paired two-sided Wilcoxon signed rank test was used to compare the mean BF values before and after thresholding, while the one-tail F test and Z test were computed to assess the reduction of standard deviation and CV, respectively, after thresholding. All tests are implemented in R software (version 3.2.1, The R Foundation for Statistical Computing). $p-value \leq .01$ were considered as being statistically significant.

4.3.6 Experimental results

Table 4.3 shows the outcome of the comparison between manual annotations

Contingency tables and statistical indexes														
Type	P	N	Reader A						Reader B					
			TP	TN	FP	FN	FPR(%)	FNR(%)	TP	TN	FP	FN	FPR(%)	FNR(%)
Vessels	18	26	16	26	0	2	0	11	12	24	2	6	8	33
Bronchi	8	27	7	27	0	1	0	13	7	26	1	1	4	13
Artefacts	41	9	26	7	2	15	22	37	20	3	6	21	67	51

Tab. 4.3: Table summarizing contingency tables and statistical indexes relative to the analysis conducted by the two radiologists regarding the presence of vessels, bronchi, and artefacts.

and computed thresholded error maps, related to the 34 examinations. The first consideration concerns the possible causes of alteration of perfusion data (column ‘P’), that in this study were artefacts (41), vessels (18, with mean area of about $16mm^2$), and bronchi (8, mean area around $23mm^2$). Also, FPR and FNR columns highlight that Reader A always performed better than, or at most as the same as, Reader B. In particular, Reader A had a specificity of 100% regarding the detection of bronchi and vessels, although Reader B also showed quite a good performance in terms of FPR for these physiological structures. As an example, Figure 4.14 (a) shows an example of manual detection by Reader A of bronchi and vessels, all of them detected automatically also

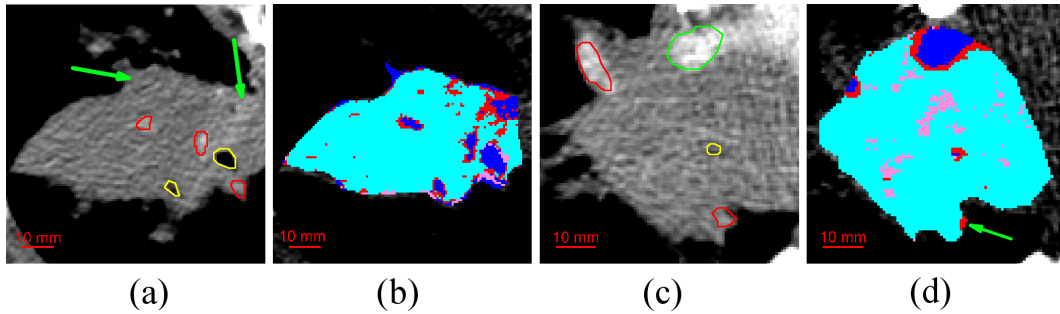


Fig. 4.14: Lesions ID29 (a,b), and ID19 (c,d). Three vessels (in red) and two bronchi (in yellow), manually highlighted by Reader A, together with two missed artefact regions (green arrows) (a), with corresponding thresholded error masks (b); two vessels (in red) detected by Reader A only, one bronchus (in yellow), and one artefact from beam hardening (in green), manually contoured by Reader A (c), with correspondent thresholded error mask (d).

by the $T_{2\sigma}$ threshold (Figure 4.14 (b), blue regions). However, both Readers' performance decrease when it does not come down to missing structures. For instance, Figure 4.14 (c) shows two vessels detected by Reader A only, and highlighted by our approach (one of which, pointed out by the green arrow in Figure 4.14 (d), detected through T_T only).

Things change as Readers face artefacts. Although manifest artefacts can be detected by both Readers (*e.g.* the beam-hardening artefact of Figure 4.14 (c), in green), apparently more subtle artefacts, like the two shown in Figure 4.14 (a), originating from partial volume effects (left green arrow) and beam hardening (right arrow), are missed by both Readers (this representing two FNs), whereas they are correctly detected by our automatic method Figure 4.15 (b). Or else, even when artefacts are correctly detected, with a surprisingly high precision (the three green sharpened ROIs in Figure 4.15 (a)), their ramifications (mostly highlighted by pink pixels in Figure 4.15 (b)) are left out of consideration – for the sake of honesty, they are almost impossible to be assessed to the naked eye. Nonetheless, in the lesion shown in Figure 4.15 (c), Reader B strives to argue the extent of this beam-hardening artefact induced by the high concentration of CA into vena cava, during the initial phase of CT acquisition. However, although the shape was not far wrong, again the extent is heavily underestimated, as shown by the outcome of the automatic method in Figure 4.15 (d). Moreover, this is an example where any clinical consideration regarding this case could be severely misleading, due to more than one third of the lesion (2537 out of 7299 voxels) being unreliable in a scatter

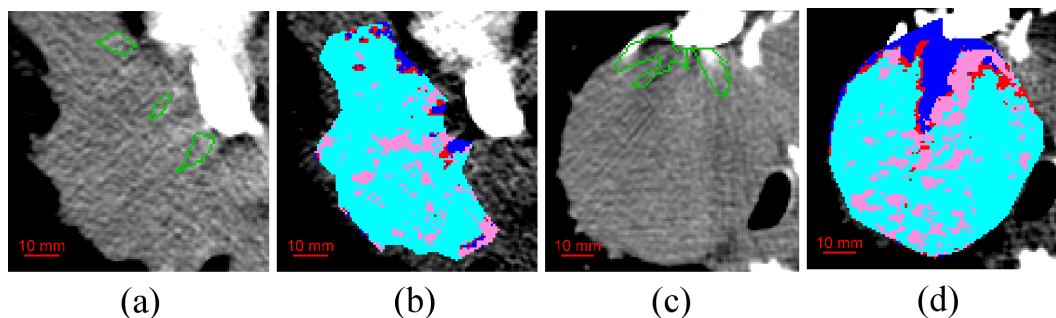


Fig. 4.15: Lesions ID12 (a,b), and ID33 (c,d). A beam-hardening artefact manually detected with a high accuracy by Reader B (a) and the corresponding thresholded error mask (b); a well-defined shape of an artefact drawn by Reader B (c), that however fails in detecting the wide extent of its effects, highlighted in the error mask (d).

manner, and the examination is strongly suggested to be definitely excluded.

The great benefits of using an automatic method to exclude unreliable pixels can be also appreciated when considering the most spread alternative, that is manual thresholding on perfusion colour maps. Figure 4.16 (a) shows an

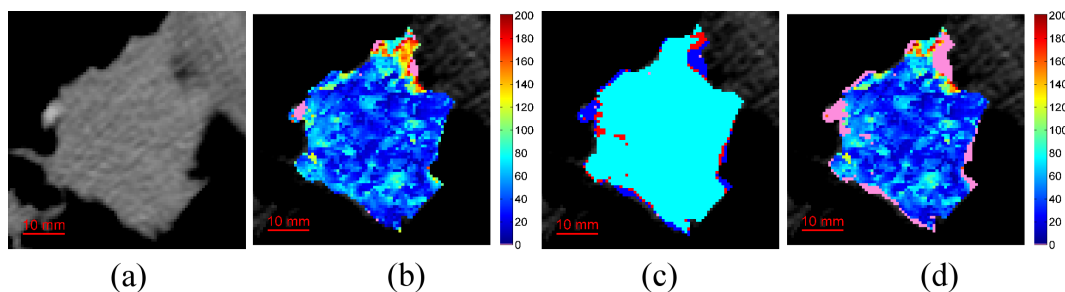


Fig. 4.16: Lesions ID32, where no misleading regions are detected (a), with its colour BF map manually thresholded (b); the thresholded error mask (c) and the final BF map achieved after excluding the error regions and a subsequent visual thresholding by using the same value as before (d).

interesting example of lesion, coming from quite a stable CT sequence, where neither physiological structures nor artefacts were detected. Accordingly, the few pink pixels in the corresponding perfusion colour map (Figure 4.16 (b)) only arise from the voxels with too high perfusion values, removed by Readers through agreed manual thresholding. The resulting BF map is plausible and shows a perfusion peak, on the top right border, whose BF values are around

200ml/min/100g. However, the thresholded error mask in Figure 4.16 (c) clearly highlights a high-error region, just in correspondence of the perfused area, correctly removed as shown by the presence of the pink pixels in the BF map in Figure 4.16 (d). This is a meaningful example where a simple manual thresholding fails, since the error affects voxels with apparently acceptable perfusion values. The scatter plots in Figure 4.17 resume this concept, with

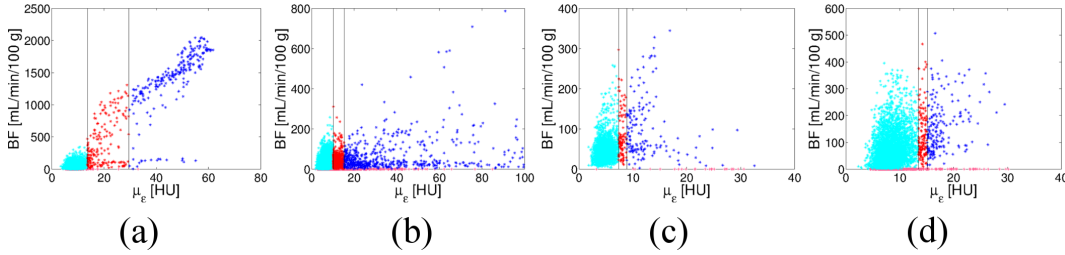


Fig. 4.17: Scatter plots to explore the relationship between BF values and μ_ϵ errors, referring to cases ID19 (Figure 4.14 (c)) (a), ID12 (Figure 4.15 (a)) (b), ID32 (Figure 4.16 (a)) (c), ID33 (Figure 4.15 (c)) (d). As one can see, errors also affect physiological BF values. Blue dots are detected by the $2\text{-}\sigma$ rule, while the red ones are detected by the triangle method only.

colour convention as the same as Figure 3.12 (a). Although, as expected, there are cases where the errors are almost exclusively associated to non-plausible BF values (Figure 4.17 (a), referring to lesion of Figure 4.14 (c)), most of times errors are shared between high and low perfusion values, as shown in Figure 4.17 (b) (referring to lesion of Figure 4.15 (a)) and Figure 4.17 (c) (pertaining to Figure 4.16 (a)). Nonetheless, in case of wide extending artefacts is not rare to find lesions where errors affect almost exclusively the voxels whose BF values fall in the physiological range, as shown in Figure 4.17 (d), referring to the lesion shown in Figure 4.15 (c).

The resulted presented above can be better acknowledged when looking at the meaningful BF histograms of Figure 4.18, referring to lesions ID14 (a) and ID33 (b), showing which BF values are removed by thresholding (for a better readability, only the triangle method is shown, in the red colour). As one can see, there are cases (Figure 4.18 (a)) where non-physiological BF values mostly lie on tail as well as there are lesions (Figure 4.18 (b)) where removed BF values are spread throughout the whole range, almost proportionally, and the average of removed BF values is nearly the same as that of the original distribution. As a consequence, as shown in Figure 4.19 mean values basically remain unchanged for $2\text{-}\sigma$ thresholding (6 cases out of 34), almost half of them

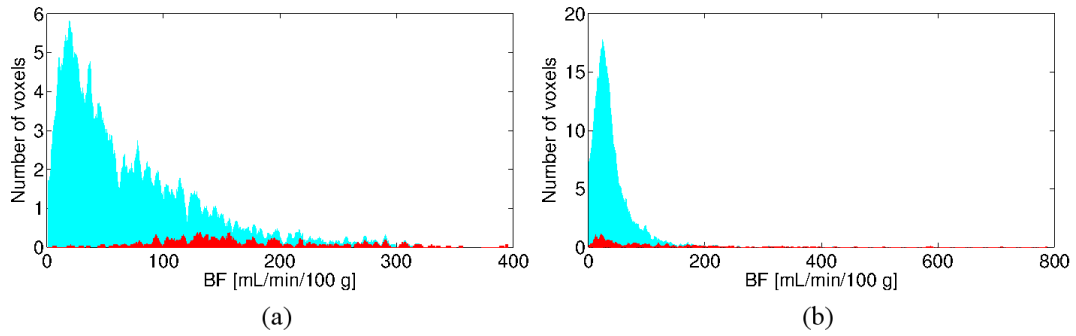


Fig. 4.18: BF values of the whole lesion (cyan colour) and those removed by the triangle method (red colour), referring to lesion ID14 (a) and ID33 (b).

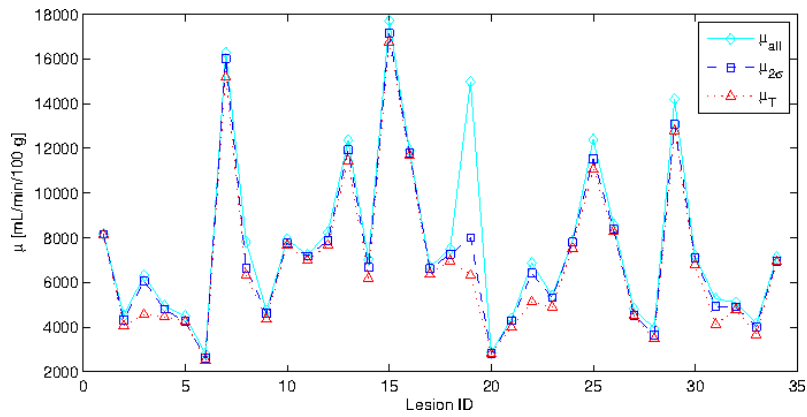


Fig. 4.19: Mean of BF values (μ) in the original examination (solid cyan line, diamonds), after $2\text{-}\sigma$ (dashed blue line, squares) and triangle (dotted red line, triangles) thresholding.

(18 out of 34) with triangle thresholding reduce. As regards standard deviation, they all reduce (Figure 4.20), most of them with statistical significance (20

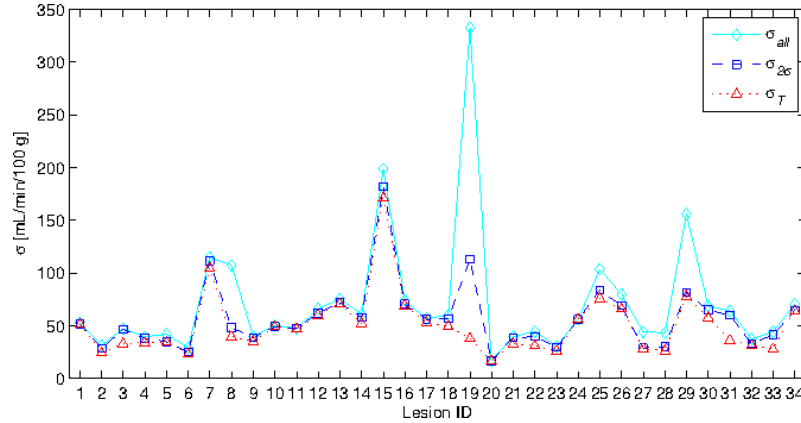


Fig. 4.20: Standard deviation (σ) of BF values in the original examination (solid cyan line, diamonds), after $2\text{-}\sigma$ (dashed blue line, squares) and triangle (dotted red line, triangles) thresholding.

cases with $2\text{-}\sigma$ thresholding, and even 29 using triangle). These reductions partly reflect in CVs, reported in Figure 4.21, which diminish in 12 cases with

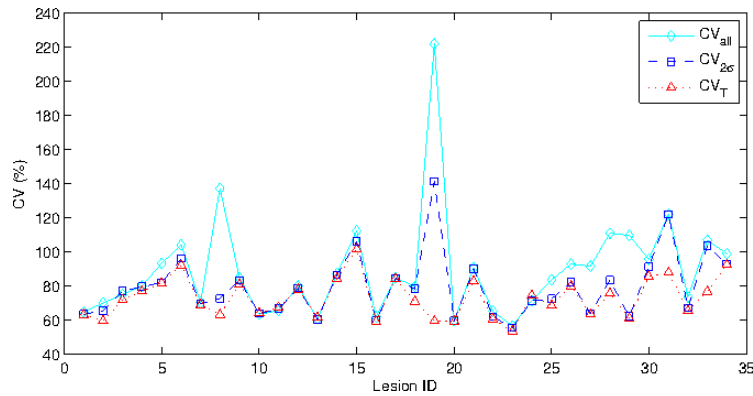


Fig. 4.21: CVs related to BF values in the original examination (solid cyan line, diamonds), after $2\text{-}\sigma$ (dashed blue line, squares) and triangle (dotted red line, triangles) thresholding.

$2\text{-}\sigma$ and 16 cases with triangle thresholding.

4.3.7 Concluding remarks

In the first place, this research work shows that the highest values of μ_ϵ are related just to those regions corresponding to anatomical structures (*i.e.*, vessels

and bronchi) or affected by artefacts, altering the computation of the perfusion colour map. In particular, the results presented confirm that removing unreliable BF values could yield significant changes (commonly, reductions) in the mean BF value of a lesion, often used as a significant statistical parameter in several clinical studies [170, 147], this contributing to carry out more precise clinical assessments. Also, what this study proves is that visual-based annotation is undoubtedly inadequate to discover the source of uncertainty in a CTP sequence. At most, devoting more time to this task reduces the number of FP and FN, always improving FPR and FNR (except for bronchi), but the improvement is quite relevant limitedly to the anatomical structures. On the other hand, this study highlights that the different types of artefacts represent the most spread causes possibly hampering perfusion parameter values, much more than physiological structures, perhaps this not being surprisingly and in line with what most probably every radiologists expect. However, what seems to be heavily underestimated is the extent of the negative effects of artefacts, this representing the highest risk if relying only on visual assessment of CTP perfusion sequences and maps.

In the second place, it has not to be forgotten that perfusion maps are usually provided “as is”, without any pixel-wise indication on their reliability and what radiologists usually do through visual analysis is, at most, just detecting perfusion peaks not compliant with physiological values and exclude them. This behaviour is prone to either neglect local perfusion peaks or including all local errors if compatible with physiological outcome. This work shows that in most cases errors are present also in the whole range of physiological perfusion values, mostly due to the presence of artefacts, highlighting at least one examination where an apparent perfusion peak would have been kept when clipping the colour scale manually.

The automatic error detection strategy presented, represents a methodological approach towards a more and more quantitative CTP imaging, this constituting an ineluctable way towards achieving a routine clinical use of CTP.

The results that have been presented in this Section have been published in [236].

Chapter 5

Multi-slice analysis of BF values

In this Chapter, I extend the analysis conducted so far on the signal coming from single voxel (Sect. 4.2) and single slice (Sect. 4.3) to the whole tumour. While in the literature it is widely agreed that considering tumour volumes provides more information than using a single section, usually single slices are merged together to provide global parameters. However, the clinical representativeness of global perfusion values and their capability to deal with tumour heterogeneity has never been investigated. This issue is faced in this Chapter. In particular, a specific background is reported in Sect. 5.1 and the set of CTP examinations selected for this study is described in Sect. 5.2. The methodologies previously discussed to automatically detect and exclude unreliable perfusion values from the analysis (Sect. 4.3) are applied to all the lesion sections, as well as the indicator of functional heterogeneity presented in Sect. 3.5 (Sect. 5.3). A deep statistical analysis is carried out to assess the clinical representativeness of global perfusion values and their capability to deal with tumour heterogeneity (Sect. 5.4). Experimental results and some concluding remarks are finally reported in Sects. 5.5 and 5.6.

5.1 Background

Tumour heterogeneity, representativeness of tumour regions, reliability of results, and reproducibility of CTP examinations represent different as well as interconnected issues that should be addressed as a whole. In fact, as discussed in Sect. 2.1, heterogeneity is an intrinsic characteristics of all tumours that is also reflected in the hemodynamic behaviour, for instance, in areas of angiogenesis or necrosis [249]. As a consequence, which part of the tumour could be the most *representative* one for clinical assessments has been widely debated.

Traditionally, the first CTP examinations were performed on one slice, due to technology limitation of data acquisition and processing apparatuses [87]. Afterwards, the improvement of technology has permitted to work on the whole tumour [269], or groups of slices, as the central ones [171]. However, authors have still continued working on a single section only [236], chosen as the one representing the largest tumour “diameter” [175], or better incorporating the solid-appearing part of the target lesion [270], or else being in the middle scan position [186, 271, 272]. Nonetheless, several researchers choose the single tumour section based on visual considerations only [210], such as that having the best quality [227], or the widest area [192], jointly to the least variability [228].

Undoubtedly, the most important issue to make CTP entering the clinical practice is the possibility to achieve between-patient and among-patients standardization. To this purpose, the *reproducibility* of *reliable* results is an essential requirement, but it must be coupled to the clinical representativeness of numerical results. In the literature, it has been widely stated that by considering the whole tumour [202], or even group of slices [205], perfusion parameters may improve reproducibility and repeatability [238], against a single slice. That is, considering a wider “population” (*i.e.*, more slices), averaging values helps achieving a “global” tumour behaviour. Using global mean or median values can also work for diagnosis purposes, where CTP has been used to discriminate between benign and malignant in different types of lung lesions, including pulmonary solitary nodules. For instance, the overall mean of pulmonary index, pulmonary and bronchial BF is computed on multiple slices in [76] and on three tumour sections chosen according to the axial, coronal and sagittal planes, in [273]. The overall median of all the CTP parameters for the whole tumour is computed in [269], where the median was preferred over the mean operator to avoid outliers.

All the studies considered refer to global perfusion parameters, whether they are mean or median values, encompassing all the tumour characteristics. However, in this way, besides the uncertainty intrinsic to the CTP acquisition and processing procedure, global parameters also reduce the variability due to tumour heterogeneity. This is acknowledged by several authors, which recognize that global values only provide an overall measure of variability [203] and that “may not be optimal for tumour evaluation prior to treatment or therapy response evaluation” [224]. Nevertheless, very few attempts have been made to try assessing the capability of CTP parameters to evaluate the treatment response of patients with NSCLC, but the lack of reproducibility could not confirm the results. For instance, the study in [183], dealing with CTP monitoring

of anti-angiogenic therapies in lung cancer, concludes that CTP can detect therapy-induced changes in perfusion, but the lack of reproducibility depletes these findings. Similar outcomes regarding the CTP capability of monitoring anti-angiogenic therapies were reported in [187], even though in this case, no reproducibility studies have been performed. On the other side, more recently the authors in [192] could not find any correlation between CTP parameters and survival of patients treated with anti-angiogenics and chemotherapy. Also, they concluded that entropy only, computed on the HU, could be considered as an independent prognostic factor for OS, this suggesting the importance of tumour heterogeneity in assessing tumour aggressiveness.

5.2 CTP examinations

The same set of 22 patients with one primary NSCLC, previously enrolled in the retrospective study described in Sect. 4.3 were considered. Here, as an added inclusion criteria, I selected lesions having the longest axial diameter larger than $15mm$ in at least three sections. Altogether, 12 patients (9 men, 3 women, mean age 64.7 y.o., range 42-81 y.o.) with a target lesion having mean longest axial diameter of $43.5mm$ (range $25.3-75.2mm$) and a mean area of $1625mm^2$ (range $433-1995mm^2$) remained. Five of them underwent at least one follow-up (FU), for a total amount of 26 CTP examinations.

5.3 Acquisition protocol and data processing

All the examinations were acquired following the acquisition protocol designed for lung tumours, described in Sect. 4.2.2, and underwent the same treatments used for the lesions of Sect. 4.3. In fact, tissue ROIs were drawn on each tumour section and aligned following our 3D approach. Spatial filtering was applied on CT images according to what described in Sect. 3.1 and the Hill's equation was used to fit the extracted TCCs. Voxel-based BF values were computed according to the SIMS method. Unreliable BF values were excluded from the analysis by using the triangle thresholding method. Mean BF values representative of each slice (μ_s) and of the whole lesion (μ_w) were computed for each examination. Median values were also computed for each slice (M_s) and the whole lesion (M_w). The ranges (r) between minimum and maximum of μ_s and M_s , r_μ and r_M respectively, were computed as a variability measure referred to the whole volume.

The entropy, E , presented in Sect. 3.5 was computed on the BF maps of the whole tumour (E_w) and of each slice (E_s), with the purpose to get a measure of the hemodynamic heterogeneity. The range r_E between minimum and maximum E_w values is also considered as a measure of the heterogeneity variability in the whole tumour. E measures are reported in arbitrary units (a.u.).

5.4 Statistical analysis

Three groups of statistical tests were performed to assess the capability of global values, computed on the whole tumour, to represent the clinically relevant perfusion features of a tumour, assuming that the heterogeneity is among the most important ones [36]. First, the one-way analysis of variance (ANOVA) was performed to check whether all slices (the “groups”) of the same tumour have the same mean value, that is, whether they can represent the same population, in terms of BF values. An analogous assessment was carried out for medians, through the Chi-squared test of independence. The second group consists in the two-tail t -test and the Wilcoxon rank sum test, which were utilized for three different purposes. In fact, they were applied to test, for each lesion, the difference of means and medians, respectively, between each slice and the whole tumour, with the purpose to check whether a slice exists which can represent the whole tumour (*i.e.*, having the same global value). The same tests were also carried out to check for μ_s or M_s differences between couples of slices, whether they belonged to same tumour or different ones. Finally, they were employed to select which tumours have the same statistical μ_w or M_w values, to further compare their perfusion patterns (*i.e.*, their E_w). In fact, computing and using a global mean, or median, perfusion value for CTP studies implicitly means that sets of BF values (*e.g.* slices or whole tumours) with same μ_s (or M_s) as μ_w (or M_w) are clinically equivalent. The third group of tests is composed by the one-tail t -test only, which was performed to assess the differences between the means of E_s for baseline and FU examinations.

p -value $\leq .05$ were considered for statistical significance. Statistical analysis was performed by using statistical software (R, version 3.2.1, The R Foundation for Statistical Computing).

5.5 Experimental results

In this section, a subset of the most interesting results achieved is presented. Results obtained for baseline and FU examinations are kept separate and resumed inside different sections in order to allow detecting possible differences between untreated lesions, preserving their natural vascular structure, and lesions whose vascular network has been modified by the action of anti-angiogenic treatments.

As the first outcome, it is worth reporting that the hypotheses that means or medians BF values of slices were all equivalent were rejected for each examination. Actually, this finding was expected and suggests that the variability between slices is significantly greater than the variability within slices [267].

Tables 5.1 and 5.2 report the most significant measures (entropy, mean, median, and range) for all examinations, calculated on BF values of each slice and the whole tumour.

5.5.1 Baseline CTp

Table 5.1 resumes the most significant measures for the baseline CTp examinations. Statistical analysis shows that ten slices exist which have the same global BF as the respective whole tumour, seven times regarding mean values, and eight ones median values. Five times the whole tumour could be represented by the same slice detected by both μ_w and M_w values. μ_w and M_w values never selected the slice with maximum E_s and one time selected the slice with minimum E_s (ID12 and ID4, for mean and median, respectively). Figure 5.1 reports the five slices of ID12, one of the most interesting lesion, where the average BF value of the whole tumour ($\mu_w = 125.0$) corresponds to that of the first slice ($\mu_s = 124.5$, Figure 5.1 (a), last row). It is worth noting that this slice also retains the minimum $E_s = 7.48$, that is the lowest heterogeneity. In fact, it shows quite a uniform, low, perfusion. On the contrary, the last slice (Figure 5.1 (e)) shows a marked heterogeneity, the highest one ($E_s = 8.37$), having in its upper part a hyper-perfused region (with BF values higher than 300), and a lower hypo-perfused region with BF values nearly 40.

5.5.2 Follow-ups CTp

Table 5.2 resumes the most significant measures for the FU CTp examinations. Fifteen slices were representative of the whole tumour, thirteen of which regarding mean BF values, and eight pertaining to median values. Five times,

Baseline examinations									
patient	measure	slice					whole tumour		
		1	2	3	4	5	measure	value	r
ID1	E_s	7.27	7.27	7.26	6.75	6.61	E_w	7.14	0.66
	μ_s	67.9	62.9	62.3	45.8	40.5	μ_w	56.0	27.4
	M_s	56.9	50.9	45.7	33.8	28.4	M_w	41.4	28.5
ID2	E_s	8.17	8.15	8.22	8.05	7.91	E_w	8.20	0.31
	μ_s	124.1	115.8	128.5	118.2	108.3	μ_w	120.1	20.2
	M_s	107.3	96.6	110.8	99.8	93.2	M_w	102.0	17.6
ID3	E_s	7.81	7.75	7.89	7.85	7.67	E_w	7.87	0.23
	μ_s	117.6	111.3	116.4	115.1	102.3	μ_w	111.8	15.2
	M_s	101.3	103.1	102.4	103.7	93.5	M_w	100.1	10.2
ID4	E_s	7.26	7.38	7.31	7.36	7.44	E_w	7.39	0.18
	μ_s	65.7	69.7	65.1	68.1	71.2	μ_w	68.0	6.1
	M_s	54.9	56.9	47.9	50.0	53.6	M_w	52.8	9.0
ID5	E_s	7.81	7.84	7.36	6.60	7.79	E_w	7.70	1.23
	μ_s	115.1	106.8	80.7	43.2	107.3	μ_w	87.2	71.8
	M_s	93.2	87.1	67.4	38.2	90.6	M_w	67.6	55.0
ID6	E_s	6.10	5.96	6.38	6.62	6.59	E_w	6.54	0.66
	μ_s	33.3	31.7	41.3	52.7	63.9	μ_w	42.9	32.2
	M_s	27.5	28.5	34.5	47.0	58.8	M_w	36.8	31.3
ID7	E_s	6.37	6.27	6.53	–	–	E_w	6.67	0.26
	μ_s	46.2	38.2	60.9	–	–	μ_w	47.9	22.7
	M_s	38.6	30.5	55.3	–	–	M_w	40.7	24.8
ID8	E_s	7.43	7.07	8.10	7.92	7.62	E_w	7.95	1.03
	μ_s	74.9	61.5	138.4	156.0	118.6	μ_w	105.2	94.5
	M_s	57.1	53.9	119.0	141.7	104.1	M_w	85.3	87.8
ID9	E_s	8.54	7.59	7.65	8.03	8.53	E_w	8.24	0.95
	μ_s	175.7	79.6	81.4	104.6	160.1	μ_w	118.4	96.1
	M_s	158.3	60.0	62.3	73.0	133.2	M_w	88.9	98.3
ID10	E_s	6.75	6.66	6.42	6.52	6.76	E_w	6.66	0.34
	μ_s	45.9	44.2	38.2	40.8	48.5	μ_w	43.4	10.3
	M_s	37.8	37.3	32.5	34.6	42.6	M_w	36.4	10.1
ID11	E_s	7.46	7.34	6.89	7.63	–	E_w	7.50	0.74
	μ_s	92.2	80.7	58.9	92.6	–	μ_w	80.0	33.8
	M_s	76.5	61.4	51.3	74.1	–	M_w	63.3	25.2
ID12	E_s	7.48	7.64	7.86	8.01	8.37	E_w	8.07	0.89
	μ_s	124.5	110.0	113.6	116.8	157.4	μ_w	125.0	47.4
	M_s	118.7	106.1	104.0	112.7	145.9	M_w	116.0	41.9

Tab. 5.1: Summary of measures for slices and whole tumour referred to baseline CTp examinations: Entropy (E), Mean (μ) and Median (M) BF values, where the subscripts s and w stand for *slice* or *whole*, respectively. For the whole tumour, r of each slice-based measure is computed as well. Italicized and bold-italicized values point out minimum and maximum value of a given measure, respectively. Bold non-italicized values highlight an equivalence between μ_s and μ_w , or M_s and M_w .

		Follow-up examinations									
patient	FU	measure	slice					whole tumour			
			1	2	3	4	5	measure	value	r	
ID2	1	E_s	7.85	8.06	7.99	7.88	7.72	E_w	8.08	0.34	
		μ_s	99.6	130.6	118.3	111.4	97.6	μ_w	112.8	33.0	
		M_s	85.2	110.4	99.9	85.6	75.2	M_w	92.4	35.2	
	1	E_s	6.50	6.26	7.33	7.70	–	E_w	7.50	1.44	
		μ_s	47.7	38.0	76.8	145.6	–	μ_w	77.5	107.6	
		M_s	41.1	33.6	70.4	120.7	–	M_w	60.1	87.1	
	2	E_s	6.63	6.21	6.40	6.90	–	E_w	6.82	0.69	
		μ_s	58.1	42.2	45.8	80.0	–	μ_w	53.5	37.8	
		M_s	49.2	38.6	32.5	71.4	–	M_w	43.2	38.9	
ID6	3	E_s	6.37	6.26	6.73	6.43	–	E_w	6.67	0.47	
		μ_s	40.8	40.9	45.7	54.6	–	μ_w	44.4	13.8	
		M_s	33.3	36.9	36.3	50.4	–	M_w	37.8	17.1	
	4	E_s	6.42	6.31	6.49	6.42	6.18	E_w	6.45	0.31	
		μ_s	42.7	38.1	40.3	39.3	35.3	μ_w	39.2	7.3	
		M_s	38.6	31.8	32.8	33.2	30.6	M_w	33.2	8.0	
	5	E_s	7.47	6.14	5.94	5.64	5.75	E_w	6.50	1.84	
		μ_s	96.1	33.3	24.7	19.9	24.7	μ_w	35.8	76.3	
		M_s	91.8	29.1	19.4	16.4	21.7	M_w	24.7	75.4	
ID7	1	E_s	7.57	6.57	7.20	–	–	E_w	7.64	1.00	
		μ_s	145.5	52.2	97.7	–	–	μ_w	95.5	93.3	
		M_s	133.8	42.6	78.4	–	–	M_w	78.4	91.2	
	2	E_s	5.82	6.33	5.90	–	–	E_w	6.33	0.51	
		μ_s	34.1	48.8	58.0	–	–	μ_w	45.0	23.8	
		M_s	32.2	42.8	56.7	–	–	M_w	39.8	24.4	
	ID9	1	E_s	7.45	6.47	6.60	6.50	6.58	E_w	6.80	0.98
			μ_s	80.8	36.9	45.1	38.7	41.6	μ_w	46.2	43.8
			M_s	67.6	31.4	39.6	34.1	36.2	M_w	38.4	36.2
1		E_s	7.04	6.83	6.63	7.46	–	E_w	7.20	0.83	
		μ_s	71.4	54.7	50.4	108.4	–	μ_w	66.9	58.0	
		M_s	60.7	47.3	44.6	96.5	–	M_w	55.5	51.9	
2		E_s	6.77	6.66	7.26	7.49	7.53	E_w	7.40	0.87	
		μ_s	52.4	43.3	67.7	90.9	107.9	μ_w	70.2	64.6	
		M_s	41.7	33.6	55.6	84.0	95.9	M_w	56.5	62.3	
ID11	3	E_s	7.20	7.17	7.30	7.49	–	E_w	7.40	0.32	
		μ_s	74.8	73.2	75.9	90.5	–	μ_w	78.1	17.3	
		M_s	70.4	66.2	69.7	81.0	–	M_w	71.0	14.8	
	4	E_s	7.05	7.20	7.22	7.28	7.32	E_w	7.29	0.27	
		μ_s	69.0	72.9	70.9	71.5	79.0	μ_w	72.3	10.1	
		M_s	64.3	64.1	60.1	61.1	70.1	M_w	63.3	10.0	
	5	E_s	7.57	7.39	7.52	7.87	8.24	E_w	7.81	0.85	
		μ_s	80.9	71.7	76.7	99.9	144.7	μ_w	90.1	73.0	
		M_s	60.7	55.2	61.3	74.2	123.2	M_w	66.8	68.0	

Tab. 5.2: Summary of measures for slices and whole tumour referred to FU CTp examinations. Notations are the same as those in Table 5.1. Here, the FU number is also reported.

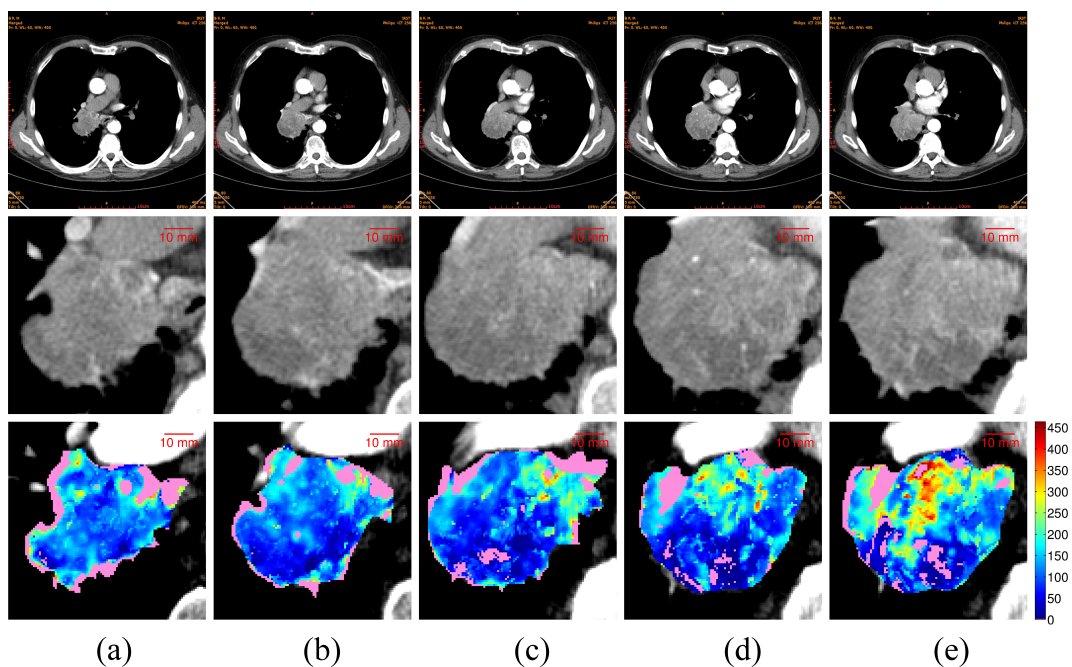


Fig. 5.1: ID12: the whole scan (first row), HU (second row) and BF maps (third row) ordered from left to right according to the scan position (the third section is the central one). The BF maps are visualized using the same colour scale. By chance, they are also sorted according to their E value: $E_s = 7.48$ (a), $E_s = 7.64$ (b), $E_s = 7.86$ (c), $E_s = 8.01$ (d), $E_s = 8.37$ (e).

mean and median global BF values identified the same slice. For lesion ID6-FU3 (Figure 5.2, $\mu_w = 44.4$ and $M_w = 37.8$) and ID6-FU4 (Figure 5.3, μ_w

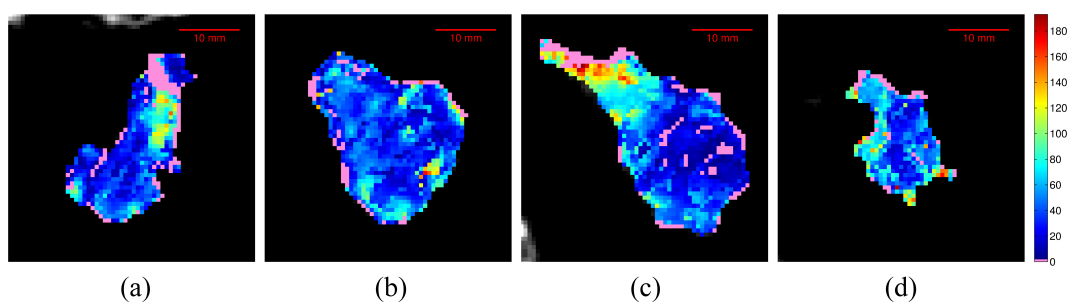


Fig. 5.2: BF maps of the four consecutive slices of ID6-FU3 (1-4, from left to right). $\mu_w = 44.4$, $M_w = 37.8$.

$= 39.2$ and $M_w = 33.2$), the same slices (*i.e.*, slice 3 for both) were those with maximum E ($E_s = 6.73$ and $E_s = 6.49$, respectively), probably due to these

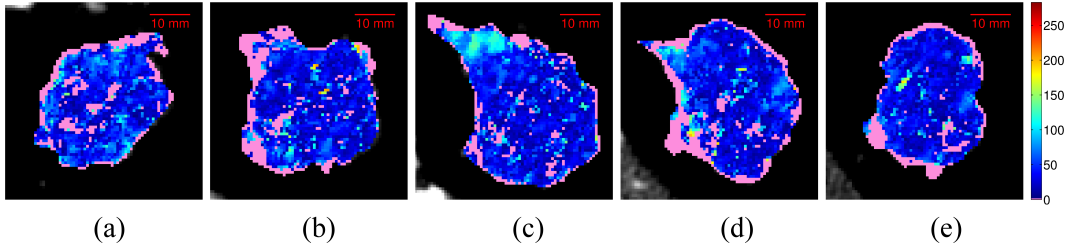


Fig. 5.3: BF maps of the five consecutive slices of ID6-FU4 (1-5, from left to right). $\mu_w = 39.2$, $M_w = 33.2$.

examinations being subsequent FUs of the same lesion. In addition, this is the only ID where mean and median select the highest E . As regards ID6-FU4, it shows limited BF ranges ($r_\mu = 7.3$ and $r_M = 8.0$, among the lowest values of all examinations) and μ_s and M_s are substantially equivalent for the three central slices. This consideration regarding mean range also holds for ID6-FU3, where $r_\mu = 13.8$ is a little higher, but still among the lowest ones. As for median, in ID6-FU3 it also selects slice 2 ($M_s = 36.9$) that has the lowest $E_s = 6.26$. On the other side, in ID11-FU4 (Figure 5.4), $M_w = 63.3$ selects slice 1 ($M_s = 64.3$)

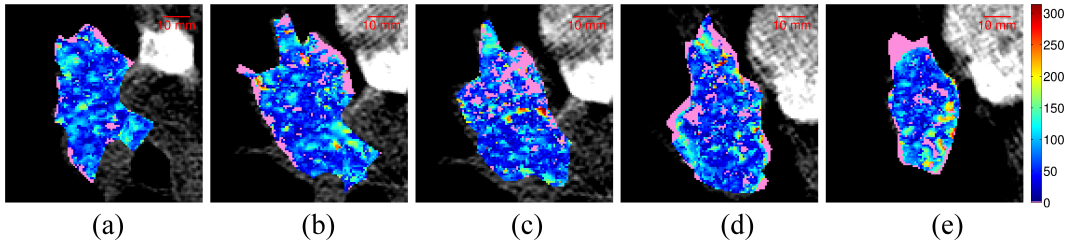


Fig. 5.4: BF maps of the five consecutive slices of ID11-FU4 (1-5, from left to right). $\mu_w = 72.3$, $M_w = 63.3$.

which is the one with the lowest $E_s = 7.05$.

5.5.3 Baseline and FU CTP

In this section, the analysis is extended over the whole dataset, by considering all the CTP examinations together. As regards the whole sets of slices, the most meaningful result is that, on the whole, 93 slices were not represented by the global BF values computed on the whole tumour. As for the sets of

whole tumours, here the sets of slices referring to two couples of meaningful lesions are analysed. Figure 5.5 shows the BF maps of the four consecutive

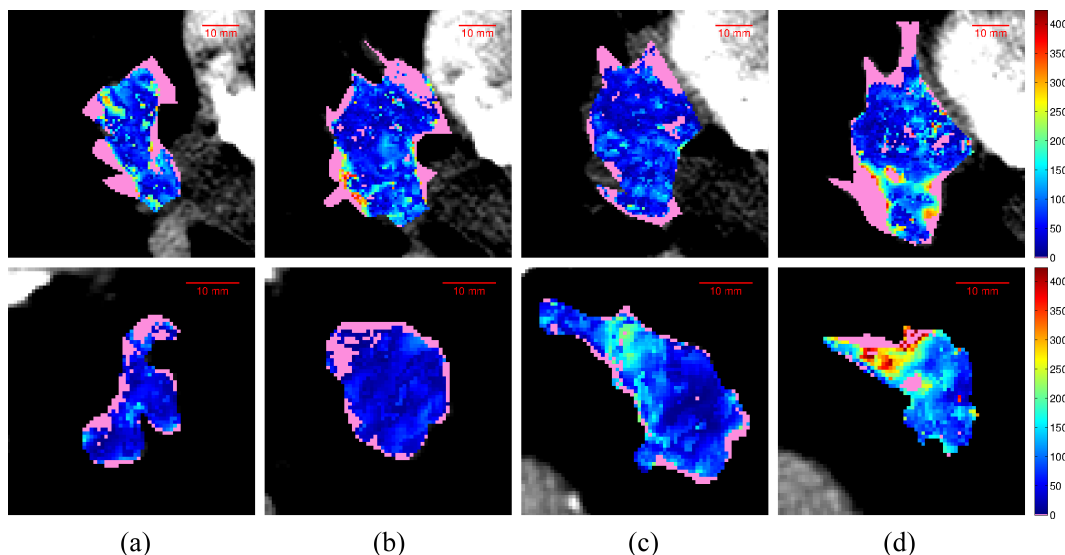


Fig. 5.5: BF maps of the four consecutive slices (1-4, from left to right) composing lesions ID11, baseline ($\mu_w = 80.0$, first row), and lesion ID6-FU1 ($\mu_w = 77.5$, second row). μ_w 's are statistically equivalent.

slices (1-4, from left to right) of ID11 ($\mu_w = 80.0$, first row) and ID6-FU1 ($\mu_w = 77.5$, second row). Although these lesions have statistically equivalent μ_w , the respective composing slices have a different heterogeneity distribution. In fact, the heterogeneity in all slices (except for slice 3) of ID11 is quite comparable, as it can be seen from E_s values of Tables 5.1. On the contrary, slices 1 and 2 of ID6-FU1 (Figure 5.5 (a) and (b), second row) are quite homogeneous and low-perfused, while slice 4 (Figure 5.5 (d), second row) has the highest $\mu_s = 150.8$ and $E_s = 7.75$. In addition, here the heterogeneity is made of local homogeneities, with a hyper-perfused upper region and a hypo-perfusion in the lower one.

Similar comments can be done for ID3 and ID2-FU1, made of five slices each, whose BF maps are shown in Figure 5.6, first and second row, respectively. ID3 ($\mu_w = 111.8$), shows a heterogeneity that keeps quite “homogeneous” within all slices ($r_E = 0.23$, the second lowest value), also in terms of mean ($r_\mu = 15.2$) and median ($r_M = 10.2$) BF (among the lowest values), with all μ_s around $\mu_w = 111.8$. On the other hand, the heterogeneity in ID2-FU1 ($\mu_w = 112.8$), is made of well-defined hyper- and hypo-perfused regions, mostly

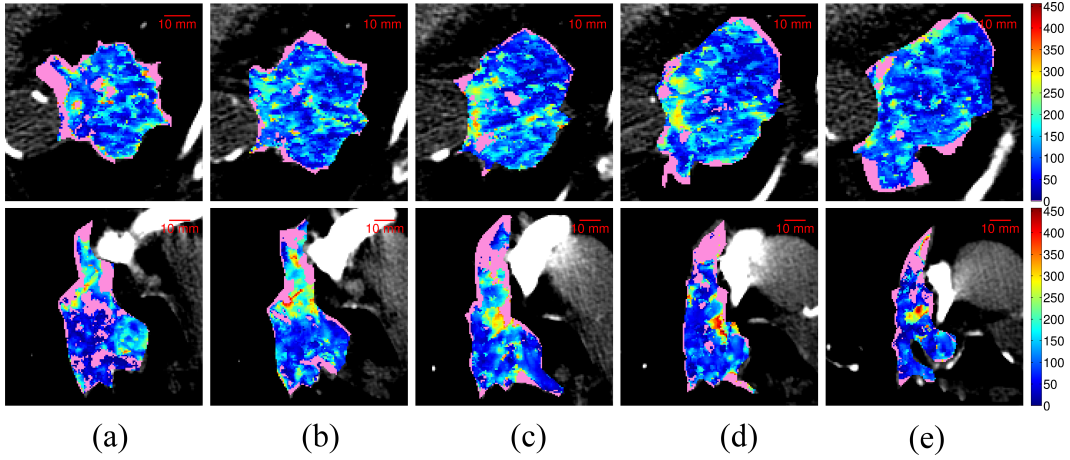


Fig. 5.6: BF maps of the five consecutive slices (1-5, from left to right) composing lesions ID3, baseline ($\mu_w = 111.8$, first row), and lesion ID2-FU1 ($\mu_w = 112.8$, second row). μ_w 's are statistically equivalent.

evident in the upper and lower part, respectively, of slices 2 and 3.

Finally, I also analysed the distribution of all slice entropies E_s for baseline and FU examinations, separately. Related histograms are reported in Figure 5.7 (a) and Figure 5.7 (b), respectively. Even at a glance, the histograms

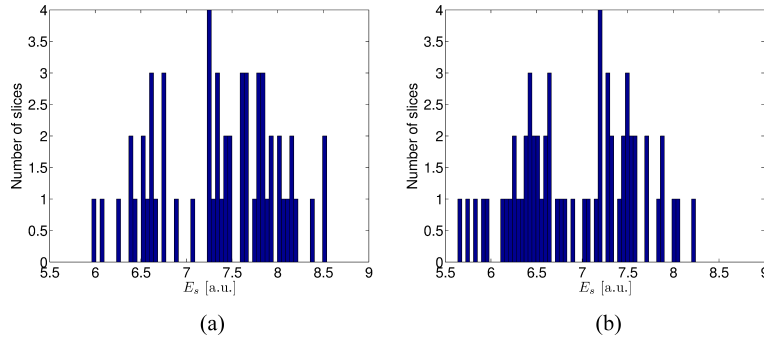


Fig. 5.7: Histograms of entropies E_s of all slices for baseline (a) and FU (b) examinations. Mean values, highlighted by the vertical red lines, are 7.4 and 6.9, respectively.

of baseline examinations appear shifted right with respect to the FU ones. In fact, for baselines mean and standard deviation are 7.4 and 0.75, respectively, while for FUs they are 6.9 and 0.64. Statistical tests confirm that the mean entropy of all slices is greater for baseline examinations ($p\text{-value} \leq 10^{-4}$).

5.6 Concluding remarks

In this Chapter, the representativeness of global mean and median values, as far as the heterogeneity is concerned, has been analysed starting from the assumption that computing and using a global mean, or median, perfusion value for clinical purposes means accepting that the characteristics of the tumour is represented by that value alone. Accordingly, this implies that sets of BF values (*e.g.* slices or whole tumours), with statistically equivalent mean or median values, are equivalently representative. However, the outcome presented in Sect. 5.5 proves that these are numerical equivalences only, not clinical ones. In fact, some cases of lesions, with same global mean or median BF values, which showed a very different heterogeneity were discussed. In addition, after analysing tumour slices having the same global values as the whole tumour, I realized that, when those slices existed, for baseline examinations they were never those with the highest information content. Rather, it happened that in two examinations the whole tumour had mean and median BF values corresponding to the slice with the lowest heterogeneity (ID12 and ID4, respectively), while the remaining slices showed relevant clinical signs of different heterogeneities. Consequently, global perfusion values computed on the whole tumour cannot be appropriate for therapy assessment and cannot improve the reproducibility of heterogeneity. As far as single slices are concerned, although preserving more details, they may be not representative of the clinical status of the whole lesion and this could severely mislead clinical considerations.

On the other hand, measuring heterogeneity is a key issue to achieve useful information to assess the effectiveness of anti-angiogenic therapies, that cannot be left out of consideration. This is confirmed by the comparison between the average BF entropy of all slices before (baseline) and after (FU) treatment, proving the effectiveness of treatments themselves, expectedly reducing the overall BF heterogeneity of tumours. Using all the single slices of a tumour, endowed with global BF values *and* a BF heterogeneity measures, would represent a step forwards, useful to help radiologists to draw more reliable clinical considerations.

Chapter 6

PIXEL: a multi-centre study

A necessary step before introducing perfusion imaging techniques in clinical practice is their validation in multi-centre studies. However, setting up this type of studies can be very complex and, at present, only very few multi-centre perfusion studies have been published. Probably, the project “Perfusion IndeX: Evaluation for Liver metastases (PIXEL)” is the first CTP *BF* multi-centre study on liver that has been carried out and I had the opportunity to work on its data. In this Chapter, after a brief introduction regarding *BF* multi-centre studies, the main issues related to this type of studies are discussed. An analysis of the most important intra- and inter-centres sources of variability that can affect the image quality and perfusion results achievable from CTP examinations is then carried out on PIXEL data. After that, an early analysis of image quality is performed on the examinations of each Centre in both frequency and temporal domain. Finally, several hints and suggestions to correctly set up a CTP *BF* multi-centre study are provided on the base of PIXEL experience.

6.1 The need for multi-centre studies

The white paper [45] disseminated by the European Society of Radiology and addressed to radiologists’ community is only one of the several attempts that have been done to prompt a greater awareness about the enormous wealth carried out by imaging biomarkers. Indeed, the role of image-based biomarkers has become increasingly important in several medical areas, such as oncological, cardiovascular, neurological, psychiatric, musculoskeletal, metabolic, inflammatory, and autoimmunity-based diseases [274]. Nonetheless, as highlighted by the authors in [275], the introduction of a biomarker in the clinical practice

results in a very complex procedure. Indeed, to substitute a clinical endpoint with an imaging biomarker, such as OS or PFS, the correlation between the biomarker and the clinical endpoint must be shown in a series of prospective multi-centre studies culminating in a formal meta-analysis.

The need for perfusion multi-centre studies has been widely claimed in the recent literature [64, 276, 277]. Nonetheless, the set-up of this type of clinical studies is quite complex, this thwarting their implementation. Actually, any guidelines specific for *BF* multi-centre studies have never been drawn. However, from the work presented in [275] some general hints can be inferred, aiming at investigating the main key-points of image-based markers validation. In this work, the authors state that to compare results across studies, the adoption of established standards is vital. Of course, this is also true in multi-centre studies in which standardization should be achieved at any level, starting from the recommendations regarding patient preparation acquisition protocols to image reconstruction process, post-processing procedures and data analysis. Indeed, the standardization of techniques is fundamental to limit the intra- and inter-centre sources of variability hidden in both the acquisition and processing steps, this enabling a correct comparison of results.

As regards all the clinical multi-centre studies, their protocol should be defined in detail before beginning the data acquisition and by taking into consideration all the limitations that may occur [275]. Indeed, as stated in [64], to include more than one Centre meanwhile preserving the study standardization as much as possible, it is necessary to adapt the study design to the “largest common denominator among participants”. This aspect undoubtedly represents a weak point of multi-centre studies since the achievement of the best standardization might not agree with the best technology available and constitute a limitation of the study, hampering the achievement of good results. Besides standardization, another aspect that should be assessed before beginning a multi-centre study is data quality. Indeed, in the guidelines by Miles *et al.* specific to CTP [83], it is suggested to measure DCE-CT image’s iodine sensitivity and noise (that are the two factors mostly affecting examinations quality) at the beginning of each clinical trials. The iodine sensitivity and noise measures should be carried out on phantoms that mimic the body size of patients and by using the same image acquisition protocol that is going to be adopted in the study [83]. As proved in the phantom study carried out on 9 different CT systems on [278], the adoption of this procedure might allow to find allow finding out a iodine calibration factor allowing to reduce variability introduced on quantitative measurements of contrast enhancement

by the different CT scanners, thus allowing a direct comparison of the results achieved.

Due to the complexity of the multi-centre studies set-up, actually there are still very few studies that have been conducted in the oncological field involving more than a single Centre. Among these studies there are two works carried out with PET [279] and PET/CT [280] that introduced and applied a series of calibration factors enabling data comparison between Centres. In the first study [279], the effects of differences between PET calibration, image resolution, and ROI size and positioning were investigated on phantoms and on 23 patients with oesophageal carcinoma or lymphom. At the end of this study, the authors proposed correction factors permitting to compare data pertaining to the three Centres involved in the study. These correction factors have been adopted also in the PET/CT multi-centre study on NSCLC [280]. In this work, the examinations of 52 patients collected in 7 different Centres were successfully analysed to assess the prognostic capability of PET/CT during radiotherapy. Nevertheless, none of these two studies carry out a perfusion analysis.

To the best of our knowledge, only three multi-centre perfusion studies have been carried out so far. The first one is a French DCE-US study, involving 19 oncologic Centers for the evaluation of anti-angiogenic treatments in 539 patients with different types of solid tumours (primary HCC or metastatic breast cancer, melanoma, colon cancer, gastrointestinal stromal tumours, or RCC). In this case, all the DCE-US examinations were acquired with the same type of machine and processed by using the same software [281]. The second perfusion *BF* multi-centre study regards DCE-MRI. In this case, the examinations of 9 patients with advanced squamous cell carcinoma of head and neck acquired in two different Centres were used to determine DCE-MRI efficacy to assess perfusion effects caused by response to lapatinib (a tyrosine kinase inhibitor) [282]. In this work, two patients were discarded due to the low quality of their examinations, but no analysis regarding multi-centre variability were carried out and not any issue introduced by the use of different MRI scanners was discussed. Finally, as regards DCE-CT two studies were carried out using examinations acquired in different Centres. The former enrolled 356 patients with lung nodules across 7 Centres [283] to investigate the capability of tissue contrast enhancement to predict benignity of nodules, but without computing any perfusion parameter. Instead, the latter carried out a perfusion analysis on examinations acquired in two Centres referring to patients with CRC, aiming at identifying the practical and technical challenges inherent to

the CTp technique. However, none of these works carried out any analysis regarding multi-centre variability or discussed any peculiarity introduced by the use of different CT scanners.

The first CTp study involving more than one Centre is a French study named “Perfusion IndeX: Evaluation for Liver metastases (PIXEL)”. During my period abroad, I had the opportunity to start working at this project initially involving 19 Centres and almost 400 patients. The aim of PIXEL is to assess the capability of *HPI* to predict the development of hepatic metastases in patients with initially non-metastatic CRC before the administration of anti-cancer therapies. As a derived goal of the study there is the identification of a threshold value for the *HPI* allowing discriminating between patients who developed liver metastases within 3 years from the CTp examination and patients who did not. The evaluation of other indexes besides *HPI* and the assessment of inter-observer variability represent further goals of the project. The inclusion criteria of the project were:

- adult patients (age > 18 y.o.)
- absence of previous cancer pathologies
- patients with CRC (with the tumour positioned more than 15cm far from the anal margin)
- patients without liver metastases (presence of metastasis in sites other than liver does not prevent patient inclusion)
- patients that gave their written consent
- patients followed at the hospital

Exclusion criteria are instead resumed by the following items:

- patients with liver metastases at the time of cancer diagnosis
- patients with chronic liver diseases
- patients who received chemotherapy before undergoing liver CTp
- patients who underwent cancer colorectal surgery before undergoing liver CTp
- patients allergic to CA
- patients with renal impairment

- pregnant patients

Finally 15 Centres and 338 patients took part in the study. Table 6.1 resumes

PIXEL Centres and patients					
Centre ID	Centre	CT scanner	CT model	Number of patients	Age range and mean
1	Beaujon	GE	Lightspeed VCT	71	33 - 89 (69)
2	Hegp Broussais	GE	Lightspeed VCT	32	35 - 86 (66)
3	Ambroise Paré	Philips	MX8000 IDT 16	18	41 - 89 (67)
6	Henri Mondor A. Chenevier	GE	Lightspeed VCT	1	(68)
7	Pitié Salpêtrière	Philips	Brilliance 64	7	49 - 78 (70)
8	Chu Nantes	GE	Lightspeed VCT	20	37 - 84 (68)
9	Chru Angers	Philips	MX8000 IDT 16	44	42 - 89 (71)
10	Haut-Lévêque Bordeaux	Siemens	Definition 64	13	50 - 79 (69)
12	Claude Huriez	Philips	Brilliance 40	11	52 - 81 (65)
14	Centre Hospitalier Lyon Sud	Philips	Brilliance 40	23	51 - 93 (70)
15	Institut Gustave Roussy Villejuif	GE	Lightspeed VCT	23	50 - 87 (64)
16	Chu Amiens	GE	Lightspeed Pro 32	49	43 - 92 (72)
17	Institut mutualiste Montsouris	GE	Discovery CT 750 HD	20	43 - 84 (65)
18	Chu Caen - Hôpital Cte De Nacre	Philips	Brilliance 40	2	60 - 81 (71)
19	Cabinet d'hépatologie et de gastro entérologie	Philips	MX8000 IDT 16	4	58 - 81 (67)

Tab. 6.1: Summary of the main information regarding the Centres included in PIXEL: ID, CT scanner, number of patients included in the study together with their age range and mean (between brackets).

some data regarding the Centres and the patients included. Hereinafter, each CTp examination is pointed out with an ID number where the number of the Centre and of the patient are written after letters C and N, respectively (*e.g.* ID C8N3 corresponds to the examination of the third patient of Centre 8).

The acquisition protocol was defined during a first meeting between the responsible people of each hospital. A first unenhanced spiral CT scan was carried out on the liver to identify the correct region that had to be analysed. Right after, an axial CTp acquisition was performed so as to include the portal vein trunk and the right hepatic parenchyma. The image acquisition started

contemporaneously with the administration at $5ml/s$ of $40ml$ of iodinated CA, with a concentration of $350mgI/ml$. The CA bolus was followed by the injection of $20ml$ of physiologic solution. Patients were asked to shallowly breath over the two minutes of the CTP acquisition phase. CT tube current and voltage were kept fixed at $100mA$ and $80kV$, respectively, with a $1s$ rotation time and exposure of $100mAs$. The tissue was acquired every $1sec$ during the first $30s$ and every $3s$ for the remaining $90s$, yielding a total amount of 60 scans, each composed of 8 sections of $5mm$ thickness.

Examinations were performed since 2008 to 2011, and the patients were monitored for 3 years after the CTP examination to assess weather they developed liver metastases. When the study started, not any indication about the proper way to set up a multi-centre study was available and no previous CTP multi-centre studies had ever been carried out. Therefore, no phantom measurements or check of the correctness of the acquisition protocol parameters were carried out. The only check carried out on the first three to five CTP examinations of each Centre was to verify whether the nominal sections of the liver had been included in the CTP images. In case it had not been, the responsible person for the Centre was reminded regarding the paramount importance of the correct selection of the liver level to be analysed.

6.2 Technical issues in multi-centre studies

As discussed in Sect. 6.1, to carry out a successful *BF* multi-centre study it is necessary to adopt common methodologies between Centres and achieve a standardization throughout all the stages of data acquisition, processing, and analysis. However, defining standard guidelines among Centres can be very challenging. Indeed, despite all efforts that can be made, the use of different scanners can hamper and sometimes prevent the achievement of comparable data [284]. In multi-centre studies, two types of issues may cause results variability. The former is related to the use of different devices in different Centres, while the latter is related to the application of different acquisition protocol. In this section, technical issues met during analysis of *PIXEL* data and strictly related to the use of different vendors and models of CT scanners in different Centres are reported and discussed.

Digital Imaging and Communications in Medicine (DICOM) is the standard adopted in medical imaging to handle, store, print, and transmit information [285]. DICOM files are provided of a header that can contain all the

details regarding the examination carried out, including information about patient, acquisition protocol, device used, or even the operator that accomplished the study. Each information is described in a DICOM tag which can be public or private, and collected in a DICOM field. Public information are those that can be included in the standard data elements, such as the patient name or the tube current value. On the contrary, private fields are often not visible with common DICOM viewers and are mainly used from vendors to include device-specific information. Despite DICOM files should contain all the information needed for a quantitative analysis and be an effective standard, this does not always happen. Indeed, in the review on [284] there is an important call for manufacturers to ensure that DICOM files include embedded data in well-defined public fields.

During the preliminary data analysis that I carried out together with the computer engineers of the CVG¹ on the CTP sequences acquired for PIXEL, we immediately had to face two technical issues preventing perfusion data analysis:

- the lack of some crucial information on the DICOM header
- the differences between the content of DICOM fields of different CT vendors

The former is related to the configuration of the Picture Archiving and Communication System (PACS) of the Centre. PACS is the system permitting to store, transfer, and access all types of medical images [286]. Despite PACS is usually configured to process and store all fields inside DICOM files, the storage of private tags often has to be specifically enabled. Consequently, if PACS is not configured to process also private tags, the DICOM transfer to PACS could cause an information loss [287]. This is what happened in some CTP examinations of PIXEL. Normally, the lost of information contained in private fields should not compromise image data processing since, as reported above, these fields should contain only information useful to the vendor. However, GE CT scanner store the image acquisition time instant, that should be stored inside a standard DICOM tag, in the private tag ‘MidScanTime’ (0019,1024). While the availability of the exact image acquisition time could not be of interest for the majority of clinical applications, the knowledge of this parameter is of fundamental importance in perfusion analysis. Unfortunately

¹a special thanks goes to Eng. Alessandro Gherardi for its help and the tools provided in the analysis of DICOM sequences.

there are no way to recover data missed by PACS and the only method to recover the lost information is to retrieve the examinations directly on the CT scanner. As regards PIXEL data, acquisition time instants were missed in 40 examinations pertaining to Centres 1 (25 examinations), 15 (2 examinations), 16 (13 examinations).

The second problem we met by analysing PIXEL data regards differences between DICOM tags of different CT vendors. Indeed, as introduced above, DICOM should be a standard, but vendors can modify the properties and the content of public and private tags. The authors on [288] report how difficult might be the analysis of the information encoded in CT DICOM metadata due to the embedding of some required information in private tags and to differences that can exist between fields with same tags of the same vendor and model make by using different acquisition modalities. In our case, the main problems we encountered regarded consistency of DICOM fields content. In particular, three types of problems could be found:

1. data format in the same standard DICOM field were non consistent
2. private tags were used to contain data useful for data analysis and that should be embedded in standard DICOM tags
3. the same standard DICOM tag was used by different vendors to hold information with a different meaning

As regards the first problem, differences in encoding of standard DICOM tags were found between different vendors. The value of the variables embedded in a specific DICOM field could indeed be encoded as a string or as sequence of bytes. To enable correct loading and usage of these parameters, an algorithm able to automatically interpret all data of DICOM fields and translate their values in a common format was implemented. A unique data format was chosen for each parameter on the base of the suitability to data analysis. For instance, fields containing a numeric value, such as time or tube current and voltage, were all converted to double format so as to allow automatic comparison between data acquired with different CT scanners. Another very important issue is represented by the precision of the temporal data stored. For instance, in some Centres, such as Centre 1 and 2, all the fields having a time content are expressed in seconds and have a resolution of 1s while in other Centres such as Centre 3 or 10, the resolution increases to less than 1ms, thus becoming more suitable for perfusion analysis.

The second issue regards the storage of information useful for data processing in private field instead of standard DICOM tags. For instance, while in Philips CT scanners the acquisition time is saved in the public field ‘ContentTime’ (0008,0033), in GE scanners this information is stored in the private tag ‘MidScanTime’ (0019,1024) that, besides being not standard, it may raise problems, and with PACS, it is much more difficult to be retrieved. In fact, as discussed above, private tags are not readable from all the DICOM viewers.

The third and last issue is related to the different usage that vendors do of the same standard DICOM tag. As an example, let us consider the DICOM sorting. To correctly carry out a perfusion study, the images acquired have to be correctly sorted. In Centres such as Centre 9, this can simply be done by referring to the value of the tag ‘InstanceNumber’ (0020,0013) that increases as the order of the slices acquired (by z level and acquisition time). However, this tag does not always assume the same meaning. For instance, in Centre 3 the tag ‘InstanceNumber’ contains the slice ID related to a specific volume. If 60 tissue volumes are acquired, ‘InstanceNumber’ contains only integer number between 1 and 60. To correctly sort DICOM images it is thus necessary to consider also the tag ‘AcquisitionNumber’ (0020,0012) containing the number of the volume acquired. However, in some other Centres, such as Centre 2, ‘AcquisitionNumber’ contains a number pointing out whether the image has been acquired during the first or the second phase of the acquisition (*i.e.*, the first or the second $30 - s$ acquisition interval). In order to fix the problem of data sorting, an algorithm considering information from the standard DICOM tags ‘AcquisitionNumber’, ‘InstanceNumber’, ‘ContentTime’, ‘SliceLocation’ (0020,1041) and from the private tag ‘MidScanTime’, when it exists, has been set up.

6.3 **PIXEL data: early analysis**

As we have seen, several issues in multi-centre studies that can cause results variability exist. Indeed, in addition to the difficulties related to the use of different CT scanners, variability introduced by the use of different acquisition parameters need to be considered. Since this is the first multi-centre study and no information or hints about which parameters could have mainly affected results, a complete and deep analysis of all the possible sources of intra-Centre and inter-Centre variability was carried out. Together with the member of CVG, all the aspects that could affect data and consequently perfusion results

reliability and comparability were examined. The main steps of the preliminary analysis carried out on *PIXEL* data together with the most significant results achieved are resumed and discussed in the following paragraphs.

6.3.1 The DICOM files

A first check was carried out on the whole dataset to verify that the CTP examinations were complete with all images and meta-files. When available, the DICOMDIR file encoding the DICOM directory structures (*i.e.*, how files are organized) and some metadata regarding patient and acquisition protocol were used. This file helps identifying and selecting the DICOM files proper of the perfusion protocol, which are often mixed together with files regarding other routine examinations, such as full-body non-enhanced or enhance CT. On the contrary, the lack of the DICOMDIR file makes this first check stage much more challenging, time-consuming and prone to errors. Indeed, a modality that can be used is to visually check all the DICOM files of each examination and then extrapolate only those hundreds files pertaining to perfusion protocol. However, this manual procedure can lead some DICOM file to be erroneously excluded from the analysis. A semi-automatic method that could help in such selection is that of exploiting the content of the DICOM tags ‘SeriesDescription’ (0008,103E), which contains a description of the series acquired. However, this tag is optional (*i.e.*, its corresponding field could also be empty, as happens for the examinations of Centre 16) and it may also have different contents, depending on the operator selecting its value. For instance, in Centre 1 this DICOM tag is described as “Perfusion Foie” (*i.e.*, “liver perfusion” in French), in Centre 9 it assumes the value “PERFUSION”, while in Centre 10 it can be equal to “Dyn2min 4.8 B30s” or “DynMulti 2min 5.0 B30s”. In particular, in this last Centre, the several acronyms composing the tag refer to features of the acquisition parameters adopted. Indeed, “Dyn” and “Multi” refer to the type of acquisition, which is dynamic and multi-slice (although the term “multi” is not always specified), and are followed by the total duration of the acquisition (2 min), the slice thickness (4.8 mm or 5 mm) and the CT software’s convolution kernel used for data reconstruction (“B30s”). Due to the variability of the content of this tag, in some cases the use of the manual method for DICOM selection is inevitable.

6.3.2 The dataset

Once the DICOM files pertaining to perfusion analysis have been correctly identified, it is necessary to verify that the dataset is complete. For each examination, the number of DICOM files must equal the result of the product between the number of sections composing each tissue volume acquired (that, however, has not been defined in the nominal acquisition protocol (NAP)) and the number of acquisition time instants (according to the NAP, they should be 60). For instance, with 8 sections for each tissue volume, 480 DICOM files are expectedly collected for each examination, while with 16 sections per volume the number of DICOM files reach 960. The a priori knowledge of these numbers permits to easily find out whether some data have been missed. For instance, the examination of the third patient of Centre 8 has 479 DICOM, this suggesting that one DICOM file has been missed. Examinations where the missed DICOM files could not be found neither recovered from the source were excluded from the study.

6.3.3 Volume slices: number and thickness

The number of the acquired slices per volume depends on the sections' thickness: since the CT z -coverage is limited by a physical constraint, it is possible to achieve more sections by reducing their thickness. For instance, in some CT scanners with a maximum z -coverage of $4cm$, it is possible to acquire 8 sections of $5mm$ each or 16 sections of $2.5mm$. The nominal slice thickness in the acquisition protocol of *PIXEL* was equal to $5mm$. However, 8 Centres only adopted this slice thickness value in all the examinations (Centres 1, 6, 8, 12, 14, 15, 16, and 18). On the contrary, in Centres 3 and 17 some examinations were acquired with a slice thickness of $5mm$ and some others of $6mm$. In Centre 7, the slice thickness used was of $5mm$ or of $0.625mm$. The remaining 4 Centres, used a slice thickness other than $5mm$ in all the examinations: $2.5mm$ were adopted in Centre 2, $4.8mm$ in Centre 10, $6mm$ in Centres 9 and 19. A different slice thickness affects quality of the data acquired and consequently, of the perfusion results. Indeed, by reducing slice thickness it is possible to achieve more details about the tissue, to reduce partial volume effects, and to increase quality of motion correction, but at the expense of an higher noise level inside images. The comparison of results achieved with a different slice thickness should therefore be considered carefully.

6.3.4 Pixel size

Another aspect related to partial volume effect is pixel size. Voxel dimension was not established in the NAP, but it can have relevant effects on the precision of the perfusion values computed. Indeed, using bigger voxel sizes mean averaging more information that has to be represented in one voxel. Very different voxel sizes have been found in the same Centre and between different Centres, ranging from $0.29mm$ to $0.98mm$. The voxel size is also related to the FOV selected for the acquisition. Figure 6.1, reports an example of three



Fig. 6.1: In (a), a wide FOV has been used (examination C9N4), in (b), the FOV is correctly placed (examination C1N1) while, in (c), the FOV is very narrow (examination C1N62).

examinations acquired with a different FOV. In Figure 6.1 (a), the FOV is too wide, this resulting in the acquisition of CT images with big pixel size ($0.98mm$) and lot of background that is useless. In Figure 6.1 (b), the FOV is correctly centred on the patient and the acquisition covers all the abdomen section (voxel size of $0.54mm$). Finally, in Figure 6.1 (c) the FOV is narrow and focused on the liver only. In this case, the voxel size is smaller ($0.49mm$) than in the other two examinations, thus permitting to achieve more precise perfusion values. However, often the use of too a narrow FOV does not permit to visualize the spleen (that is fundamental for the application of the DIMS), besides causing sometimes a data loss, since respiratory movements can move liver outside the FOV. Accordingly, the examinations with a very narrow FOV have to be included with a great care.

6.3.5 Acquisition protocol and time information

The sampling time in the acquisition protocol is really a tricky issue to cope with. The knowledge of the correct time instants in which each image was acquired is fundamental to achieve reliable perfusion values. For instance, overestimating the time interval between two acquisition, yields to underestimate the BF , meanwhile overestimating BV and MTT . The example in Figure 6.2 reports a tissue curve of the examination C8N2. The data points

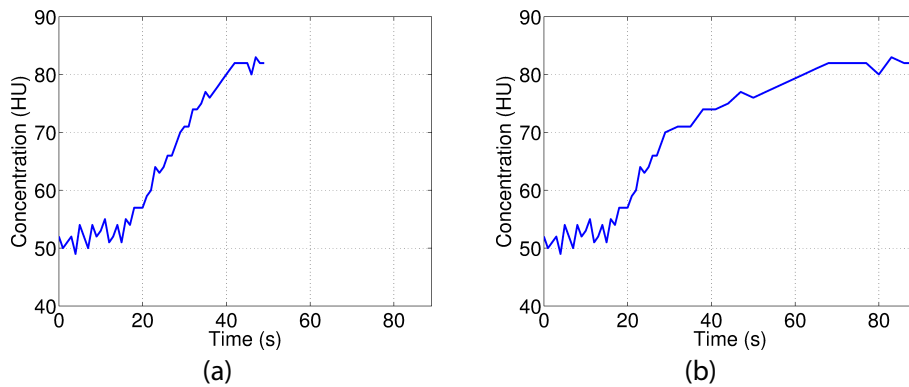


Fig. 6.2: The same TCC is represented by using two different timelines. In (a) the real acquisition time of each sample is used (BF of $37.9\text{ml}/\text{min}/100\text{g}$), while in (b) data samples are distributed according to the NAP (BF of $23.3\text{ml}/\text{min}/100\text{g}$).

of the same TCC have been placed using different time samples: in (a) the real reported acquisition time was used (*i.e.*, one image, and hence one data point, each second), while in (b) data points have been distributed according to the NAP (the first 30 samples are placed at 1s distance and the last 30 at 3s). BF values computed on the two curves differ of $14.6\text{ml}/\text{min}/100\text{g}$, this highlighting the importance of knowing and using the correct acquisition time instants.

As regards the acquisition time instants, the acquisition protocol was correctly followed in all the examinations of Centres 1, 6, and 16. However, even if the acquisition protocol has been correctly followed, some examinations present a time glitch (*i.e.*, one or more tissue volumes have been acquired with a lag, that might be of the order of milliseconds or even of seconds). A couple of examples of time glitch are presented in Figure 6.3, showing the time intervals between consecutive volumes acquired in three different examinations. In Figure 6.3 (a), the NAP has been followed and no time glitches are present. In

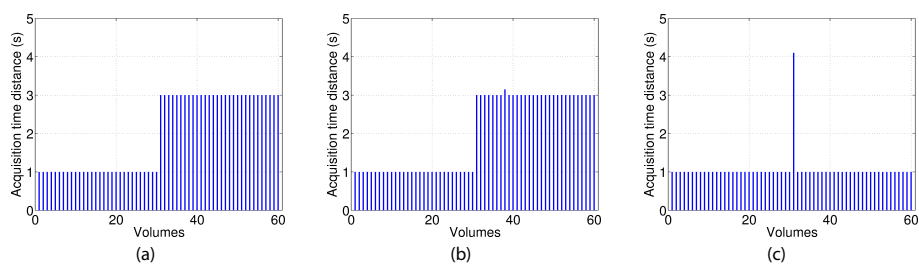


Fig. 6.3: Time intervals between consecutive volumes referred to three different examinations. Time intervals of C16N1 are presented in (a). In this case no glitches are present. In (b), the time intervals of C1N1 show a small glitch in the second part of the acquisition. Finally, (c) shows time intervals of C17N1 where a significant glitch is present in the middle of the sequence.

fact, between consecutive volumes there are exactly 1s in the first part and 3s in the second part of the acquisition. In Figure 6.3 (b), a short time glitch is visible in the second portion of the acquisition, where the interval between two consecutive sampling instants is longer than 3s. Finally, in Figure 6.3 (c) a big glitch (of more than 4s) is visible in the examination whose volumes have all been acquired with 1s of sampling time. These time glitches are completely operator independent and can be randomly present in different examinations of the same Centre, without any apparent reason. Consequently, the only way to achieve correct perfusion results is to use the acquisition time specified inside DICOM tags. The use of the acquisition time instant declared in the NAP is thus not recommended to compute perfusion and has to be accurately evaluated in those cases where time information are not available from DICOM files.

Particular difficulties to follow the NAP were met by those Centres with a Philips CT scanner, which does not allow switching the time sampling frequency as GE does. Therefore, some Centres such as 3, 9, 12, 18, and 19 adopted the solution of acquiring all the sequence of images with 1s sampling time. In some cases, images were acquired for 60 times (60s), this resulting in very short acquisitions. In other cases, the duration of the acquisition was kept fixed to 120s (*e.g.* Centre 12), this resulting in a huge number of data and an heavy radiation dose delivered to patients. In some other Centres the two phases have been separated by a pause of 2s (*e.g.* Centre 15) or 4s (*e.g.* Centre 10). In Centres 7, 8 and 17 instead, different temporal acquisition protocols have been adopted in different examinations. Indeed, while some examinations

of Centre 8 have been correctly acquired following the NAP, some others have been acquired by using two phases (the former having a time interval of 1s and the latter of 4s, separated by a pause of 2s), and another one using a one phase only. In Centre 17 instead, some examinations have been acquired by keeping the time interval fixed at 1s (with the exception of the glitch of 4s between the first and the last slot of 30 volumes) and some others by using a protocol similar to that followed in Centre 15. As regards Centre 7, each examination has been acquired using different time intervals. In particular, one examination only was acquired using a one phase protocol (with a time sampling fixed at 1s). The remaining examinations were carried out using a two phase protocol, adopting either a uniform time sampling for both phases, fixed at 1.5s or 1s time sampling for the first phase and 3s for the second one. In addition, the time interval between phases varies from 8s to 26s. The case of Centre 2 is different since the examinations have been all acquired using a multi-phase protocol composed by four different parts having different time intervals between volumes (3s, 2s, 3s, and 5s were sequentially used as time intervals). Finally, a yet different acquisition protocol was followed by Centre 14. Through the analysis of the acquisition time instant, it was possible to realise that all the examinations of that Centre had been acquired with a lag between the two phases of the protocol of nearly 14s. The lack of the acquisition portion during which CA diffuses inside tissue prevents the use of the data acquired by this Centre that had to be definitively excluded from all perfusion studies. The same conclusion can be drawn also for those examinations of Centre 7 acquired by using two phases and a very high time interval. Unfortunately, for 57 examinations of Centres 1, 3, 7, 10, 12, 15, and 16 it was not possible to retrieve the acquisition time instants neither to check out the acquisition protocol followed for these examinations. At the moment, not any test has been carried out yet to assess whether and to what extent, these glitches may affect the reliability of the obtained TCCs and of the computed perfusion values, accordingly.

Finally, it is worth noting that two examinations pertaining to Centre 12 (C12N10 and C12N11) could not be analysed, since their DICOM fields were all empty. The acquisition protocol applied and the sample timing used could thus not be verified and the two examinations were consequently not considered any longer.

6.3.6 Tube current and voltage

Other two parameters that deeply affect the quality of CT data acquired are the tube current and voltage. The nominal values are $100mA$ and $80kV$ respectively. However, several differences have been found between the values of these two basic parameters in several Centres. In three Centres only (Centres 1, 6, 10) indeed, the examinations were acquired by using the nominal tube current and voltage parameters. In Centres 8, 16 and 17, the same parameters were used for almost all the patients. In four patients indeed, one of the two parameters has been modified. In four Centres, the tube voltage was correctly kept at $80kV$, but different values of tube current were applied. For instance, Centre 2 applied a tube current of $80mA$, while Centres 12 and 18 used tube current values definitely higher (equals to $200mA$ and $260mA$, respectively). In Centre 15, the examinations are performed by using a variable and very high tube current, ranging from $204mA$ to $672mA$. The use of high tube current values does not jeopardize the quality of CT images, but mainly contribute to deliver patients a very high radiation dose. In Centres 9 and 19, tube current and voltage were kept at $90kV$ and $133mA$, respectively, for all patients. In Centre 7, the greatest part of examinations have been carried out at $80kV$ and $303mA$, respectively. However in this Centre, several exceptions have been made. Indeed, two examinations (C7N6 and C7N1) have been acquired at $30mA$ and $100mA$ (the former at $120kV$). In addition, a third examination (C7N3) has been acquired in two different phases having different acquisition parameters. In particular, part of the examination has been acquired with a tube current of $50mA$ and voltage of $120kV$, while in the latter part, $303mA$ and $80kV$, have been used, respectively. Therefore, the quality of these three examinations has to be assessed with a particular care, since too a low tube current could compromise image quality insomuch to prevent the achievement of reliable results. Accurate quality controls are finally needed also for the patients of Centres 3, where both tube and voltage current consistently vary between patients, assuming several different values without apparent motivations.

6.3.7 Radiation dose

Related to the tube current and voltage values, there is the radiation dose delivered to patients. This aspect does not directly influence quality results, but constitute a very important aspect of perfusion studies. The maximum nominal dose level in the acquisition protocol had to be lower than $100mAs$. To

verify whether the radiation dose has been kept low, I checked several DICOM tags. While the field ‘ExposureTimeInms’ (*i.e.*, the duration of exposure for the frame in milliseconds) is empty in all the examinations and ‘CTDIvol’ (*i.e.*, CT Dose Index describing the average dose for this frame, in mGy) is often incomplete, the only field available to evaluate the radiation dose delivered to patients is ‘Exposure’ (*i.e.*, the exposure expressed in milliamperere per second, calculated as the product of exposure time and tube current). By analysing this DICOM tag in the various examinations, I noticed that the exposure was kept low in almost all the examinations. An exception is represented by those few examinations of Centres 3, 7, 8, 16 and 18 where high values of tube current had been selected, making exposure vary between $130mAs$ and $200mAs$, and for all the patients of Centre 15 where the exposure reached a peak of $672mAs$.

6.3.8 Administration of the contrast agent

Another aspect of the acquisition protocol that could introduce variability in perfusion results regards CA. As reported in [289], the use of different quantities, concentration, and injection rate of CA can have deep effects on the shape of arterial and tissue TCCs. The nominal CA administration in PIXEL was of $40ml$ at $5ml/s$. However, the features of the injected CA should be specified in optional DICOM tags such as ‘ContrastBolusVolume’ and ‘ContrastBolusIngredientConcentration’ (pointing out the volume injected in ml of diluted CA and the mg of active ingredient per ml of diluted agent, respectively) that are often empty. Partial information about CA injection have been retrieved from DICOM tags in 6 Centres only. What emerged is that also in this case, many variations have been made in the different Centres, and even through the examinations of the same Centre. In Centres 2, 6, 8, different quantities of CA have been administered to patients. Indeed, while in Centre 6 the quantity of CA was proportional to patient weight ($1.5ml/kg$), in Centres 2 and 8 variable quantities of CA ($40ml$, $50ml$, $60ml$, and $80ml$) were administered in different examinations, apparently without any selecting criterion. In Centres 8 and 15 instead, different injection rate ($4ml/s$ and $5ml/s$) were applied for CA administration. On the contrary, in Centre 16, what varied is CA concentration (350 and $370mgI/ml$). Besides different CA quantities, injection rate, and concentration, even different CA were administered in different Centres and in the same Centre as well. For instance, in Centre 2 three different iodinated intra-vascular CA (Xenetin, Iomeron, Omnipaque) were administered to patients. To the best of our knowledge, there are still no studies comparing

the effects of using different CA on perfusion results. In this case, CA are all of the same type: iodinated and intra-vascular. However, it is important to pay attention on the possible variability introduced by these CA.

Finally, it is important to note that in examinations C9N43 and C10N16 no CA was administered to patients. Therefore, these two examinations were excluded from the analysis.

6.3.9 CT scanners

Further sources of variability that can affect quality of results achieved directly derive from the different CT scanners used. The use of different image reconstruction algorithms and filters in different CT scanner models or vendors may indeed affect the quality of CT images on which perfusion parameters are computed and induce variability, accordingly. As a matter of fact, different filter types and convolution kernels to reconstruct images in examinations were used in Centres 2, 3, 7, 15, 16, and 17, and even within the same Centre. In the absence of proper calibration studies using phantoms, it is not possible to evaluate how much these factors introduce variability in perfusion results. However, results achieved by analysing images of the same Centre, obtained by using different reconstruction algorithms, and used together, should be first analysed separately to assess the degree of variability introduced, before being compared.

6.3.10 Resuming of the acquisition parameters used in the different Centres

Table 6.2 resumes the main acquisition parameters used in the different Centres. We recall that Centre 14 was excluded from the analysis due to its temporal acquisition protocol being unsuitable for perfusion analysis (see Sect. 6.3.5). In addition, 5 examinations pertaining to different Centres have been excluded from this resuming Table. In fact, CA was not administered to two patients of Centres 9 and 10, this leading to a total amount of 43 and 12 patients in the two Centres, respectively. Two more examinations from Centre 12 have been excluded, because of the lack of any information inside DICOM tags. Finally, one patient from Centre 7 has been excluded since the examination was acquired using different acquisition parameters during the two phases of the examination (see Sect. 6.3.6).

Acquisition time protocol used in Centre 2 is not specified in Table 6.1 since

Acquisition parameters summary												
Centre ID	Tube current (mA)	Tube voltage (kV)	Exposure (mAs)	Slice thickness (mm)	D (ml)	CA S (ml/s)	CA C (mgI/ml)	n1	t1 (s)	Time sampling delay (s)	n2	t2 (s)
NAP	100	80	100	5	40	5	350	30	1	0	30	3
1	100	80	100	5	NA	NA	NA	30	1	0	30	3
2	80	80	80	2.5	40(2) 60(19) 80(7) NA(4)	NA	NA			Multi-phase		
3	149(7) 152(2) 200(4) 300(1) 303(4)	80(4) 90(11) 120(3)	50(2) 100(15) 150(1)	5(5) 6(13)	NA	NA	NA	60	1	-	-	-
6	100	80	100	5	*	5	NA	30	1	0	30	3
7	30(1) 100(1) 303(4)	80(5) 120(1)	100(5) 150(1)	5(5) NA(1)	NA	NA	NA	**	**	**	**	**
8	100(19) 200(1)	80(18) 100(1) 120(1)	100(19) 200(1)	5	40(13) 50(1) NA(7)	4(1) 5(13) NA(7)	NA	30 30 60	1 1 1	0 2 -	30 30 -	3 4 -
9	133	90	100	6	NA	NA	NA	60	1	-	-	-
10	100	80	100	4.8	NA	NA	NA	30	1	4	30	3
12	200	80	100	5	NA	NA	NA	120	1	-	-	-
15	204(1) 239(1) 261(1) 392(1) 405(1) 427(1) 438(15) 672(1)	80	204(1) 239(1) 261(1) 392(1) 405(1) 427(1) 438(15) 672(1)	5	40	4(3) 5(19)	NA	30	1	2	30	3
16	100(48) 150(1)	80	100(48) 150(1)	5	NA	NA	350(11) 370(12) NA(26)	30	1	0	30	3
17	100(19) 133(1)	80(19) 90(1)	100	5(19) 6(1)	NA	NA	350(15) NA(5)	30 30	1 1	4 4	30 30	3 1
18	260	80	130	5	NA	NA	NA	60	1	-	-	-
19	133	90	100	6	NA	NA	NA	60	1	-	-	-

Tab. 6.2: Summary of the acquisition parameters of the NAP and of those used in the different Centres. If different value of the same parameters have been used in a Centre, the number of examinations acquired with each parameter value is pointed out between brackets. D, S, and C have been used to indicate quantity, injection speed, and concentration of CA administered. * the quantity of CA was patient-based (see Sect. 6.3.8). ** a different time sampling was used for each examination of the Centre.

it is composed by several acquisition phases using different sampling frequency (see Sect. 6.3.5).

Finally, information regarding CA administration are often not available (NA) inside DICOM tags since included in optional public fields (see Sect. 6.3.8).

Undoubtedly, tube current and voltage and slice thickness are three of the acquisition parameters that mostly affect perfusion results. As one can see, only 6 Centres (1, 6, 7, 8, 16, and 17) acquired at least one examination using for these parameters the values agreed in the NAP. Therefore, a total amount of 158 examinations have been acquired using at least the agreed tube current and voltage and slice thickness (71 in Centre 1, 48 in Centre 16, 19 in Centre 17, 18 in Centre 8, 1 in Centres 6 and 7).

6.4 Assessment of image quality

In the CTP guidelines by Miles *et al.* [83], it is clearly stated that quality assurance is of fundamental importance. In its simplest definition, image noise is measured as the standard deviation of voxel values in a homogeneous area. Measures of image quality such as standard deviation or SNR are indeed suggested and necessary in multi-centre studies, where differences in CT scanners and related software may bias data analysis. In Sect. 6.3, the main sources of variability in the acquisition protocol of each Centre that can affect quality of results have been discussed. For instance, the use of a lower tube current can lead to a higher photon starvation effect, while a lower spatial resolution (*i.e.*, arising from using wider voxel area or thicker slice sections) results in heavier partial volume effects. Nowadays, all CT scanners are endowed with a reconstruction software that can somehow attenuate or correct artefacts and noise. However, each vendor has its own software and the computing pipeline applied to data are protected. The efficacy of the reconstruction and correction algorithms may vary between CT scanners of different vendors or even between different models of the same vendor.

In the following paragraphs, the main results achieved through image quality analysis in both frequency (Sect. 6.4.1) and temporal (Sect. 6.4.2) domains are reported and discussed. Three examinations were randomly chosen from each Centre. Centres 6 and 18 having less than three examinations were excluded, as well as Centre 14 whose examinations were not suitable for perfusion analysis (Sect. 6.3.5). The analysis carried out on these examinations is composed by four main steps, resumed in Table 6.3. First of all, I verified whether

Summary of image quality tests			
Domain	Test	Aims	Analysis
Frequency	1	Verify presence of noise peaks	Frequency analysis of CT images' spectrum
	1	Evaluate background noise	Background density values analysis
Time	2	Evaluate background noise temporal variability	Study of background density values variations over time
	3	Evaluate liver noise	Comparison of liver and background noise and analysis of SNR values

Tab. 6.3: Summary of image quality tests carried out.

noise affecting CT images could be identified in the frequency domain and removed through the use of frequency filtering techniques. To this purpose I visually analysed the frequency spectrum of CT images of each examination, searching for frequency peaks or patterns. After that, I carried out an analysis in the temporal domain made of three different tests. First, I evaluated the influence of beam hardening, scatter noise, and CT reconstruction algorithms on CT images through the analysis of the background noise. In particular, the histograms and the standard deviation of the background density values collected in the whole temporal sequence were analysed. In the second test, I verified whether noise caused by beam hardening, scatter noise, and CT scanner reconstruction algorithm keep constant over time. To this purpose, I analysed the variations of mean background density values between slices acquired in different time instants. Finally, I evaluated the presence of noise inside liver. Since in this portion of the image, noise depends both on factors affecting background and on features of the tissue analysed, I selected a uniform region of the liver (*i.e.*, without big vessels) and compared liver and background noise through the use of statistical indexes and the computation of SNR.

6.4.1 Frequency domain

First of all, an analysis of the frequency spectrum of the single slices was performed to find out possible peaks related to noise patterns. In Figure 6.4, three representative frequency spectrum related to as many different CT vendors, together with the images on which they were computed, are reported. All the examinations acquired with CT scanners of the same vendor are char-

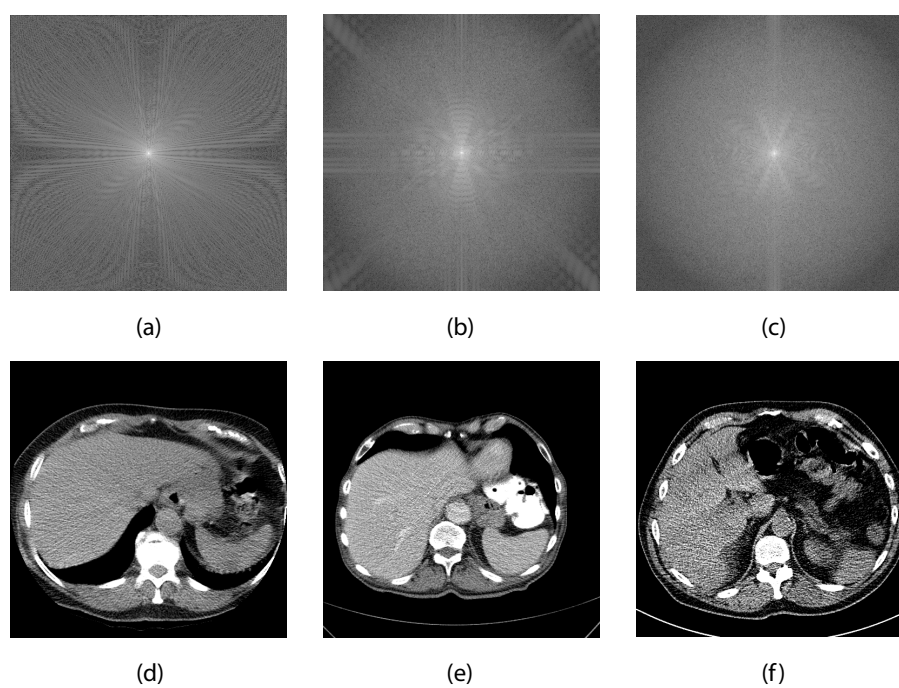


Fig. 6.4: Frequency spectrum and relative CT images acquired with GE (a,d), Philips (b,e), and Siemens (c,f) scanners, pertaining to examinations C1N1, C7N7, and C10N1, respectively, are represented.

acterized by similar frequency spectra, independently from the model of the scanner used. Probably, this is due to the different reconstruction algorithms used by vendors. In particular, by analysing several frequency spectrum, I realised that all those computed on CT images acquired with GE scanners (Figure 6.4 (a)) are characterized by features creating a sort of Moire pattern resembling the traits of a pepper-wort. On the contrary, the spectrum of CT images acquired with Philips (Figure 6.4 (b)) or Siemens (Figure 6.4 (c)) scanners are characterised by completely different features. In fact, their spectrum shows that data are mainly distributed on the four principal directions of the space (horizontal, vertical, and diagonal ones). Despite in some examinations the traits of the spectrum can be less or more pronounced, features of CT images acquired with Philips and Siemens scanners results to be very similar. All the frequency spectra analysed, do not show any frequency peak. This can be ascribed to the use of reconstruction algorithms (which are probably based on Fourier sampling) and to the presence of artefacts (*e.g.* beam hardening and scatter) and Poisson noise, that are unstructured. Therefore, typical frequency filtering methods cannot improve image quality in terms of noise and artefacts removal.

6.4.2 Temporal domain

The image analysis presented in this section considers CT images of the reference sequence (see Chapter 4) of each examination. Examinations of Centres 3 and 7 were excluded from the analysis since the lack of time information inside DICOM fields to correctly sorting the images prevented their usage. The analysis carried out in the temporal domain is subdivided into three main steps. The first one regards the analysis of the noise characteristic of the image generation process (*i.e.*, hardware and software reconstruction noise), mostly independent from the image content. Thereafter, the analysis moves towards liver tissue noise, also depending on the features of the tissue analysed. Finally, a comparison between outcomes of these two steps is carried out by means of apposite indexes.

First of all, I analysed the content of images in a void region of the scanner. A ROI was placed on the background visible in the reference slice of each examination. A great care was used to exclude blankets and patient clothes from the ROIs of all the slices of the reference sequence. Examinations with a FOV so narrow as not to allow drawing a ROI on the background (*e.g.* Figure 6.1 (c)) could not be used in this part of the analysis and were replaced by

examinations of the same Centre having a wider FOV. Therefore, histograms of the density values of the ROI collected in all the time instants of the sequence were created and standard deviation values were computed. Some examples of the ROIs drawn on the reference slice, together with the histogram of density values, is reported in Figure 6.5. All histograms represent a Gaussian

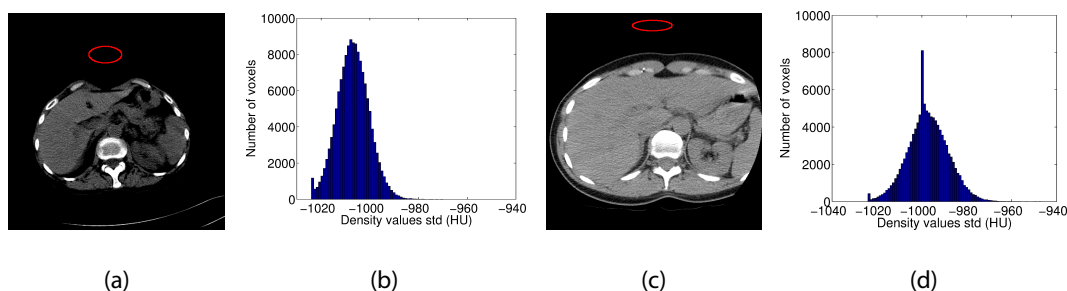


Fig. 6.5: CT images with the ROI placed on background region and histograms of background density values of examinations C19N12 (a,b) and C1N65 (c,d).

distribution centred on around $-1000HU$, which is the density value of the air in the ideal case (*i.e.*, without noise). Some of them (as the one shown in Figure 6.5 (b)) also present a peak in correspondence of $-1000HU$. Instead, the peak in all histograms on the lowest attenuation values (*i.e.*, $-1024HU$) is the density values set up a-priori for the voxels falling out of the FOV. The mean and standard deviation values computed on the whole sequence of each examination by excluding the peak on $-1024HU$ are resumed in Table 6.5. The noise found in these regions can be attributed to the reconstruction algorithms used in CT scanner, beam hardening effect and scatter noise. The standard deviation of background value distributions varies from negligible ($4.6HU$, Centre 8, second examination) to significant levels ($29.6HU$, Centre 16, first examination). The examinations more affected by acquisition noise are those of Centres 2, 10, 16, while those showing the lowest noise levels are those of Centres 8, 9, 15, 19.

After that, we investigated whether the noise in these background regions kept constant over time. To this purpose, we computed mean and standard deviation of background values in each slice of the sequence. Both the histograms of means and standard deviations are characterized by a Gaussian distribution (two examples are provided in Figure 6.6). However, while the histograms of means (Figure 6.6 (a), (b)) usually present similar range, those of standard deviation's can be more varying. For instance, while in C8N2 (Figure 6.6 (c))

Mean and standard deviation of background density values

Centre	Examination 1		Examination 2		Examination 3	
	Mean (HU)	Std (HU)	Mean (HU)	Std (HU)	Mean (HU)	Std (HU)
1	-998.2	10.8	-986.5	23.1	-997.4	8.9
2	-980.9	27.8	-987.7	22.1	-995.9	13.3
8	-1005.4	9.5	-996.5	4.6	-988.6	10.5
9	-991.7	13.1	-1003.2	8.3	-996.4	9.6
10	-993.5	17.6	-992.1	19.6	-989.3	21.0
12	-990.9	16.4	-994.4	16.0	-993.3	15.9
15	-991.5	6.8	-993.0	7.0	-997.7	14.7
16	-973.9	29.6	-995.3	11.7	-976.6	29.4
17	-994.0	16.6	-994.3	16.3	-995.8	15.3
19	-999.4	9.8	-1007.0	6.5	-994.2	13.5

Tab. 6.4: Mean and standard deviation of background density values computed on the whole sequence of the three examinations considered for each Centre.

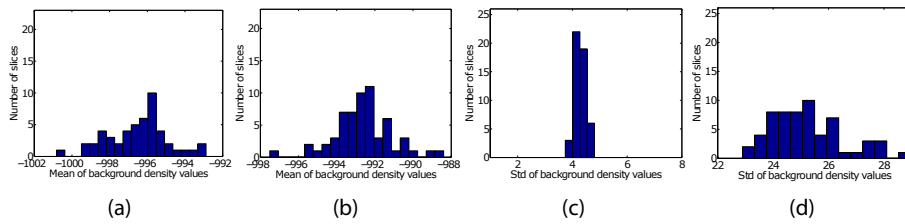


Fig. 6.6: Histograms of means (a,b) and standard deviations (c,d) of background density values collected in the slices of examinations C8N2 (a,c) and C1N27 (b,d).

the distribution of standard deviations is very narrow (range of about $1HU$), meaning that the noise keeps constant in all slices of the examination, in C1N27 (Figure 6.6 (d)) the range is wider (about $6HU$), this pointing out that noise changed over time. In addition, in order to have a measure of the variations of the density values in the background regions over time, the standard deviation of the mean density values computed on each slice were calculated for each examination. These results are represented in Figure 6.7, where standard

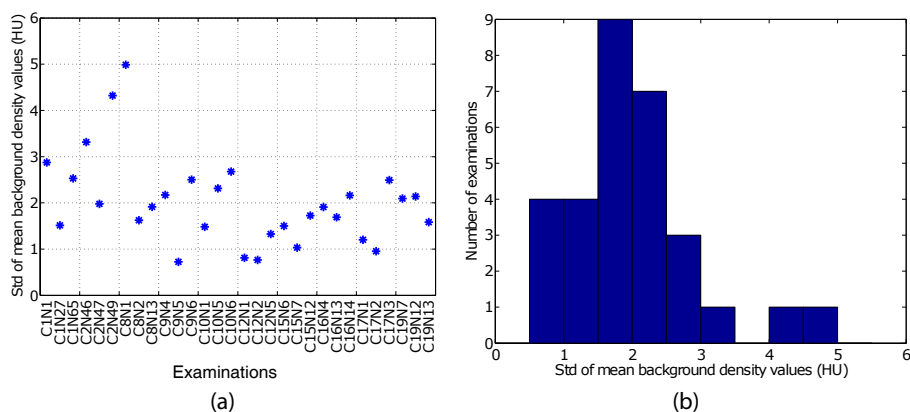


Fig. 6.7: Standard deviation of the mean of the background density values referred to all slices of the sequence (a) and related histogram (b).

deviation of mean background density values found in the 30 examinations analysed vary from $0.7HU$ to $5.0HU$. The examinations showing the highest variation are those characterized by the most variable noise. As one can see from both the graphics of Figure 6.7, there are only three examinations (*i.e.*, C2N46, C2N49 and C8N1) presenting values of mean background standard deviation greater than $3HU$. Instead, in the most part of the examinations (*i.e.*, those with standard deviation of mean values lower than $3HU$), the variations of system noise are limited. This is most probably due to periodical maintenance by manufacturers, which must ensure a stable performance of CT scanner over time.

As the second step of the analysis, we focused our attention on the noise present in the liver that is just partly related to the acquisition process, but also due to image content (for instance, patient motion can cause artefacts affecting tissue image, but not image background). To this purpose, a ROI has been drawn on a region of the liver excluding big vessels, that remained quite uniform over time. Since the presence of CA inside tissue affects liver

density values, only slices belonging to baseline portion of the sequence were considered in this part of the analysis. In order to select slices pertaining to the baseline portion only, the time instant of CA arrival in aorta was used as discriminant. Indeed, until CA does not arrive inside input vessels of the liver, it cannot reach the tissue. To this purpose, a ROI was placed on the aorta and the last local minima before the aortic peak was selected. Figure 6.8 reports an

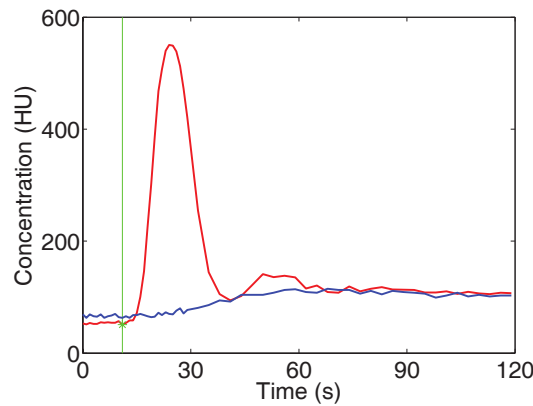


Fig. 6.8: The aortic curve (in the red colour) and one TCC of the examination C1N2 (in the blue colour) are shown. The green vertical line highlights the last local minimum of the aortic TCC before it starts enhancing.

example of the point selected on the aortic TCC of examination C1N2. This same point is also used also in the algorithm developed to compute correct baseline values and described in Sect. 7.3.2.

Liver density values found in the baseline portion of each examination are all characterized by a normal distribution, such as those shown in Figure 6.9. Table 6.5 resumes mean and standard deviation values of these distribution together with other fundamental data related to image quality, such as tube current and voltage, or background standard deviation. Despite distributions of baseline density values of liver show average values μ_D that are consistent with those found in the literature [290], some unexpected very low (less than $\mu_D - 2 \cdot std$) or even negative density values, mainly attributable to the presence of both noise and artefacts inside images, are present in all the examinations, as well as extremely high density values (above $\mu_D + 2 \cdot std$) also due to the presence of microvessels, artefacts and noise.

As the last step of this analysis, I evaluated noise related to tissue only. To this purpose, I compared the noise measured in the liver (*i.e.*, depending from

Main parameters regarding image quality

Centre	Examination	σ_B (HU)	σ_L (HU)	σ_L/σ_B	μ_l (HU)	SNR (dB)	Tube current (mA)	Tube voltage (kV)
C1	N1	10.4	31.1	3.0	68.2	16.4	100	80
	N27	24.4	37.3	1.5	66.3	8.7		
	N65	8.4	19.9	2.4	64.7	17.8		
C2	N46	27.4	67.4	2.5	51.7	5.5	80	80
	N47	27.2	54.0	2.0	57.7	6.5		
	N49	12.0	30.3	2.5	60.6	14.1		
C8	N1	8.8	25.5	2.9	41.0	13.4	100	100
	N2	4.6	11.1	2.4	52.0	21.1	200	120
	N13	9.8	24.6	2.5	68.5	16.9	100	80
C9	N4	12.8	26.2	2.0	54.9	12.6	133	90
	N5	8.4	16.7	2.0	66.9	18.1		
	N6	9.4	22.7	2.4	66.5	17.0		
C10	N1	18.55	47.79	2.6	59.3	10.1	100	80
	N5	21.1	58.6	2.8	63.4	9.6		
	N6	22.0	58.5	2.7	56.3	8.1		
C12	N1	16.9	56.4	3.3	54.5	10.2	200	80
	N2	15.8	34.1	2.2	59.5	11.5		
	N5	16.0	50.2	3.1	52.4	10.3		
C15	N6	14.9	22.3	1.5	42.4	9.1	438	80
	N7	6.5	14.8	2.3	64.7	20.0	405	
	N12	7.0	18.9	2.9	53.5	18.2	239	
C16	N4	31.6	45.8	1.4	63.1	6.0	100	80
	N13	11.1	34.3	3.1	52.0	13.4		
	N14	31.5	57.0	1.8	67.8	6.7		
C17	N1	17.5	33.5	1.9	57.6	10.3	100	80
	N2	17.1	27.1	1.6	64.6	11.5		
	N3	15.9	27.5	1.7	65.1	12.2		
C19	N7	9.5	16.7	1.8	62.1	16.3	133	90
	N12	5.9	11.1	1.9	73.4	21.9		
	N13	13.7	40.6	3.0	46.2	10.6		

Tab. 6.5: σ_B , σ_L , ratio between σ_L and σ_B , μ_L , SNR, tube current and voltage referred to the 30 examinations considered.

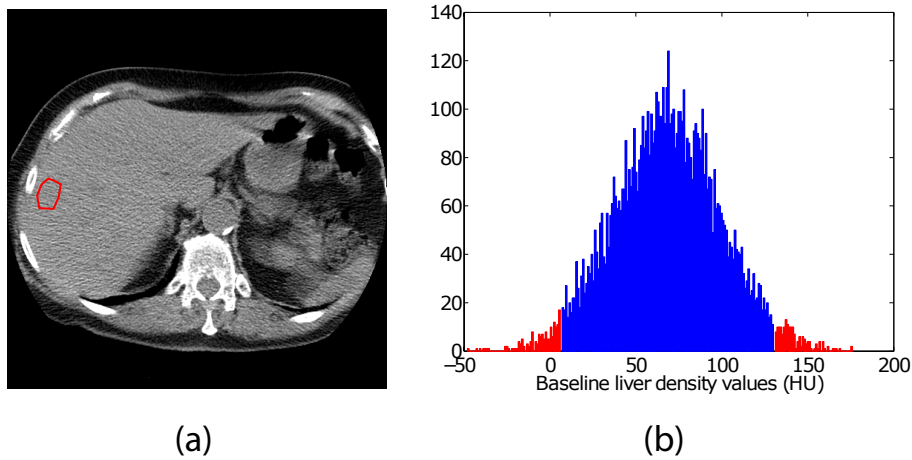


Fig. 6.9: CT slice of examination C1N1 with the ROI placed on a liver uniform region (a) and a histogram of liver density values (b). Density values exceeding mean $\pm 2 \cdot \text{std}$ are highlighted in the red colour and probably are those mainly affected by noise, artefacts or presence of microvessels.

tissue, beam hardening effect, scatter noise, and CT scanner reconstruction algorithm) with that of the background (*i.e.*, attributable to the same causes, except for tissue). The ratio between liver standard deviation σ_L and background standard deviation σ_B was computed. SNR (expressed in dB), was calculated according to Eq. 6.1:

$$SNR = 20 \log_{10}(\mu_L / \sigma_B) \quad (6.1)$$

where μ_l is the mean liver density value. σ_B and σ_L found in the examinations considered are represented in Figure 6.10. As expected, the noise on the liver, depending on both acquisition scanner and patient is higher than that on the background. In particular, the two histograms of Figure 6.10 highlight that the range of background standard deviation is about a half that of liver standard deviation. However, the CV of the two examinations are almost equal (50% in the liver and 47% in the background), this pointing out a high consistency between data acquired in the liver and in the background. Indeed, if by increasing the signal, also the noise increases proportionally, the SNR (*i.e.*, the inverse of CV) keeps constant, independently if measured in the tissue or in the background. The highest liver noise level has been found in two examinations of Centre 2 and in all those of Centres 10, 12, 16. Most of these

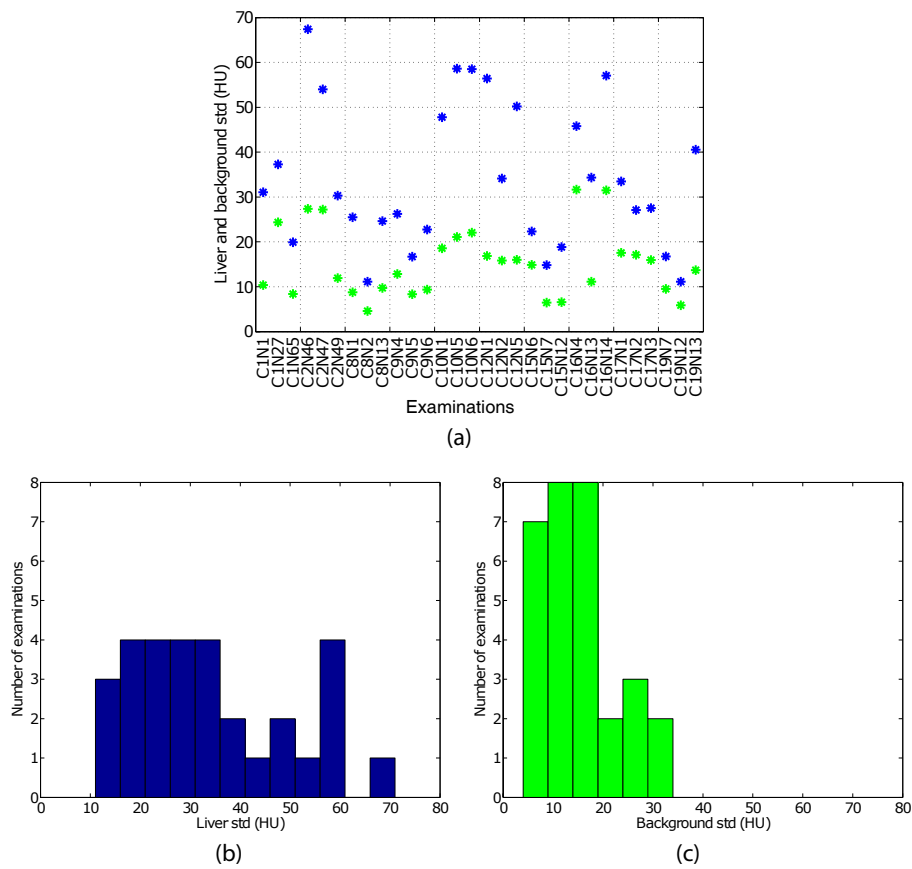


Fig. 6.10: Liver (in the blue colour) and background standard deviation (in the green colour) of each examination are represented (a), together with the related histograms (b,c).

examinations also show high background noise levels. It is important noting that Centres 2, 10, 12, and 16, showing the highest noise levels, are equipped with different CT scanner model (a GE Lightspeed VCT, a GE Lightspeed Pro 32, a Philips Brilliance 40, and a Siemens Definition 64). Consequently, the lower quality of examinations cannot be attributed to the CT scanner model used in the acquisition.

As regards the ratio between liver and background standard deviation value is greater than 1 in all the examinations (*i.e.*, the noise on the liver is always higher than that on the background). The highest values of the ratio can be found in some examinations of Centres 1, 8, 20, 12, 19. This probably means that the quality of CT scanner does not permitted to set proper acquisition parameters.

Finally, according to Eq. 6.1, I computed SNR whose values are resumed in Table 6.5 and represented in Figure 6.11. As one can see from the histogram

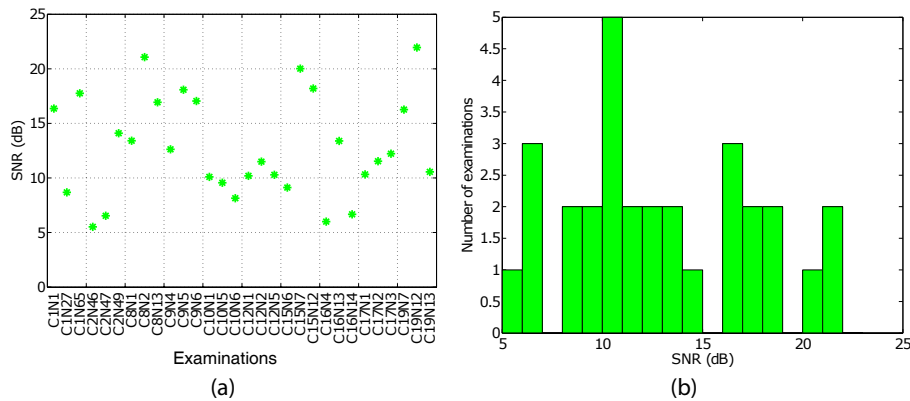


Fig. 6.11: SNR of each examination (a) and the related histogram (b)

(Figure 6.11 (b)), SNR varies from 5.5 to 21.9dB almost uniformly. Indeed, except for the peak around 10dB, there is almost an equal number of examinations showing each different value of SNR. Tube current used to acquire each examination represent one of the main causes making SNR varying in the same Centre. In fact, two of the examinations of Centre 2 (C2N46 and C2N47), that are those acquired with the lowest tube current, present very low SNR values (5.5 and 6.5dB), pointing out a low image quality. The agreement between acquisition parameters and image quality is even more evident in Centre 8, where examination C8N2 that has been acquired using a very

high tube current ($200mA$) has the highest SNR value ($21.1dB$), if compared with the other two examinations (SNR of 13.4 and $16.9dB$, tube current of $100mA$). However, an exception to this “rule” is represented by the examinations of Centre 15 where C15N6 the examination acquired with the highest tube current, is also the one showing the lowest SNR. The causes of this inconsistency can be found in the different pixel size and filters used during the phase of image reconstruction of these three examinations of the same Centre. Finally, it is interesting to note that examinations of Centres 10, 12, and 17 are those presenting the most similar SNR values, pointing out that in these Centres, the image quality is kept constant over patients.

6.5 Some hints to set up of a CTP multi-centre study

The set-up of a multi-centre study is something of very challenging. The selection of a standardized acquisition protocol and method of data processing to be used between Centres may not be enough to assure the success of the study. In fact, several issues and pitfalls can be hidden behind apparently simple choices, such as the adoption of a unique shared protocol, indeed very difficult to implement. Every information has to be collected with a high detail before beginning the acquisition campaign, so as to prevent as much as possible all the eventual sources of variability. Based on PIXEL experience, this section resumes some hints that besides the guidelines by Miles *et al.* [83] for the CTP studies should be taken into account to improve the set up of a CTP multi-centre study. The information described in the next paragraphs can be resumed in the following five groups:

- planning phase
- calibration phase
- medical staff training
- early check of the CTP examinations
- data analysis

The planning phase starts from the enrolment of candidate Centres that will take part to the study, till the selection of the acquisition protocol and the

details regarding data processing. The second phase is of fundamental importance to reduce between-Centres variability and performing a first skim of the Centres enrolled. Later on, a training period of the technicians and the medical staff of each Centre that will be involved in the execution of the CTP examinations is strongly advised so as to guarantee the foster homogeneity of the data acquired. A check of the first (3-5) CTP examinations acquired in each Centre is then necessary to detect and correct possible discrepancies between the expected and the achieved results. Finally, the last group of recommendations regards the way data are processed.

6.5.1 Planning phase

This phase is particularly delicate for all the clinical studies and in case of multi-centre studies is of vital importance. First of all, a board of experts including at least radiologists, physicists, computer engineers responsible of data processing should be set up. The information regarding technical characteristics of the medical devices that will be used in each Centre to carry out CTP examinations must be collected and analysed by this board. All the limitations and the problems related to the devices used in each Centre should be known, starting from those directly related to the CT scanner, such as the maximum spatial and temporal resolution achievable by the device, to those related to the connected devices, such as the injection pump used to administer CA or the storage system of the Centre.

Later on, a meeting between responsible people of each Centre and the board of experts features of devices used in the several Centres must be carried out to defined the protocol to be followed. During this meeting, all the aspects of the study should be faced. The appropriate patient population that can be included in the study should be defined as well as all the inclusion and exclusion criteria. The acquisition protocol to be used should be established considering radiation dose, quality issues, and devices limitations. Centres using devices with inappropriate requirements (*e.g.* CT scanners that are not able to allow a good temporal resolution [83]) should be excluded from the study. Moreover, as discussed in Sect 6.1 the acquisition protocol should be set so as it could be fulfilled by each Centre, in order to guarantee the lowest data variability, this improving further reproducibility studies. The inclusion of each Centre should also be evaluated based on how much the examination quality should decrease due to the inclusion. Of course, excluding some Centres may compromise study timelines and the global validity of the results achieved. A proper trade-off

has to be found before beginning the multi-centre study.

As regards longitudinal studies, it is important to note that they should be carried out by using the same equipment and acquisition methods adopted during the first examinations, in order not to add late sources of result variability.

6.5.2 Calibration phase

Before carrying out CTP examinations on patients, it is highly suggested to make static and dynamic analyses of quality on phantoms. Specific calibrations such as those carried out in [278], should be applied across Centres to ensure that consistent perfusion parameters can be obtained. Large differences between image quality of different Centres (that, for instance, can be assessed by using SNR) should be evaluated with particular care. To avoid any bias on data analysis, the adjustment of the acquisition protocol or the exclusion of those Centres giving a too low image quality should be also considered in the early stage of the study.

6.5.3 Training of medical and technical staff

Before beginning the acquisitions, the medical staff of each Centre that is going to perform the CTP examinations should undergo a specific training. This is fundamental to reduce as much as possible the sources of inter-Centre variability related to the acquisition phase. Information regarding patient preparation ([83]), acquisition protocol, information to be inserted in DICOM field, and data storage should be clearly communicate to the technical staff and acknowledged. Finally, a special recommendation should be given about the preparation of the data to be send to experts that will carry out the perfusion analysis. To avoid loss of data information, examinations should be downloaded and stored directly from CT scanner rather than from PACS. A check to assess the completeness of the stored data should be carried out for each examination. Moreover, events possibly affecting data quality such as detectors recalibration or change of the x-ray tube should be reported to the experts responsible of data analysis.

6.5.4 Check of CTP examinations

The first 3 to 5 CTP examinations acquired by each Centre should be examined from an expert before acquiring more data. The acquisition of the correct tissue

portion and the presence of all the parameters needed to carry out a perfusion analysis should be checked. The agreement between the acquisition parameters of the examinations and those declared in the standardize protocol should be verified. All the problems found out during this first analysis must be reported to the Centre involved, so that it can agree a possible solution. A second check should be carried out on these Centres to verify whether the problem encountered has been solved. In case of persisting problems, it is necessary to evaluate whether the effects caused on results by these inconsistencies can be negligible or if it is necessary to exclude the Centre from the study, thus avoiding administration of radiation dose to patients whose examinations will not be analysed in the study.

6.5.5 Data analysis

After receiving the first CTP examinations from the Centres, the experts should carry out a preliminary data analysis. An early check of the data received is important to prevent further exclusion of examinations from the study due to missing data. In this case, it is indeed important to request data to the Centre as soon as possible so it can be recovered before being missed. It is necessary to verify that all the acquisition parameters are stored in the DICOM header. Subsequently, it must be checked whether the acquisition parameters used for each examination have been kept constant throughout the whole duration of the study and if they correspond to those of the NAP. Finally, an image quality study has to be carried out for each examination in order to verify whether the quality has been changing over time. The results achieved during this preliminary data analysis should be evaluated in order to decide whether each examination can be included in the study.

After these checks, the same post-processing methods should be applied to each examination (exception made for calibration factors that could change between each Centre or examination). The same filtering techniques, alignment methods, fitting algorithm and model to compute perfusion parameters should be used as well as the same methodology to place the ROIs on tissue and vascular inputs. Finally, a standardised protocol to qualitatively and quantitatively interpret images must be used. Adoption of voxel-based techniques to evaluate perfusion values reliability and to discard misleading data (such those presented in Chapter 4) are suggested. Moreover, a statistical data analysis to test between-Centres variability should be carried out before using all data coming from different Centres. Clinical outcomes could indeed be affected by

between-Centres variability sources and separate data evaluations might be required.

Chapter 7

PIXEL: a multi-centre study

In order to extend our study on normal liver and on examinations acquired in several Centres, the algorithm previously developed to process CTP images and compute perfusion parameters in tumours has been deeply revised and improved (Sect. 7.1). In particular, in this Chapter, several algorithms have been implemented and tested, such as that to register liver ROIs on CTP image sequences (Sect. 7.2), or that to compute more correct baseline values¹. Finally, early analyses have been first carried out on patients of Centre 1, and subsequently extended to some more Centres to achieve landmark values of baseline (Sect. 7.3) and BF in normal liver (Sect. 7.4) and to verify whether the use of different CT scanners could affect the results achieved (Sect. 7.3 and 7.4).

7.1 Summary

During the first analysis of PIXEL examinations (Sect. 6.3 and 6.4), a lot of parameters were highlighted that introduce intra- and inter-centre variability and prevent the acquisition of data under the same standardized protocol. Since this is one of the first CTP multi-centre study that has ever been carried out, the effects of deviation of each parameters from the nominal ones are unknown. To reduce as much as possible the number of variability sources and carry out an analysis in which differences between results depend only on inter-patients and inter-scanner variability, I started by including in the analysis only the examinations acquired according to NAP. Both the studies on baseline and BF values (detailed in Sects. 7.3 and 7.4, respectively), have

¹The “baseline” is meant as the portion of the TCC before the arrival of CA inside tissue (Sect. 7.3)

been first carried out on a randomly selected set of patients belonging to a single Centre and subsequently extended to more Centres. The reason is that Centre 1 had the greatest number of examinations and, moreover, correctly applied NAP to all examinations. As regards multi-centre studies, Centres with at least 10 patients whose examinations have been acquired by using the same tube current and voltage, exposure, and slice thickness agreed in NAP were identified. In particular, Centres 8, 16, and 17 were selected and the highest number as possible of usable examinations were identified in each Centre. Multi-centre analysis was carried out by using the same number of examinations in each Institute.

Working on normal liver required that, besides the algorithms, the Graphical User Interface (GUI) ought to be upgraded as well. In particular, the GUI has been optimized in order to improve its performance on data processing, for both time processing and memory usage. Also, it had to be partly redesigned to allow for missing information due to inhomogeneities of acquisition protocol. For instance, the possibility for the user to insert a time vector corresponding to the acquisition protocol adopted by the Centre where DICOM acquisition time was lost, has been introduced. The DIMS method was finally implemented and inserted into the GUI.

Also the algorithm to compute perfusion values from data acquired with the liver protocol has been reviewed step by step. The algorithm pipeline is shown in Figure 7.1. In this section, all the steps of the algorithm pipeline are

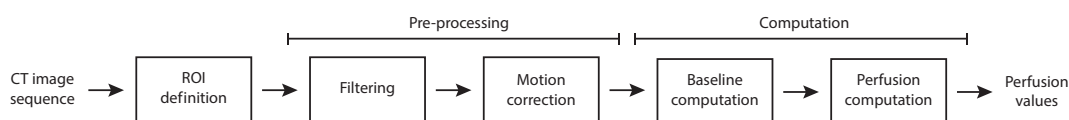


Fig. 7.1: The whole algorithm pipeline allowing to compute perfusion results from data acquired with liver protocol.

outlined, while some steps (*i.e.*, motion correction, baseline computation, and perfusion computation) are detailed in the next sections of the Chapter.

The first step of the pipeline regards ROI definition. In CTP (Chapters 3 and 4), a large ROI is drawn on the reference slice, outlining tumour borders. However, when dealing with normal tissues, no mass is present to be contoured. Tissue ROIs have then been manually drawn on a central section of the volume acquired and placed within the outer border of the liver. Whole ROI has to lay

within the liver borders in all the images of the CTP sequence and, possibly, should be placed quite far from liver margins so as to avoid partial volume effects. The ROI placement procedure must be carried out with a great care so as to exclude big vessels, such as portal vein or hepatic artery. An example of a typical ROI drawn on a liver section is represented in Figure 7.2.

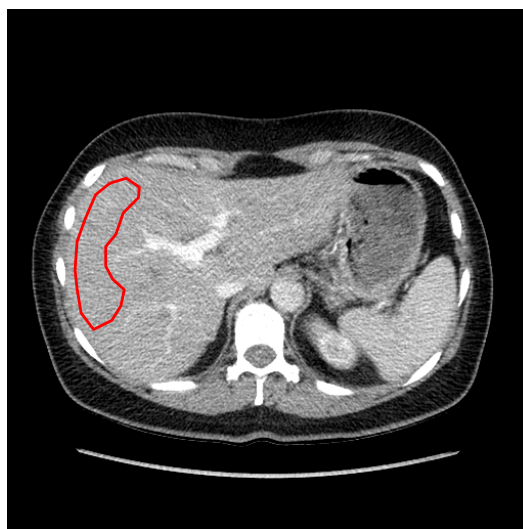


Fig. 7.2: ROI of examination C8N7 drawn on normal liver, far from liver margins and excluding big vessels.

After ROI definition, a two-stage pre-processing is performed: CT image filtering and motion correction. As regards the first step, several spatial filters applied to the raw data was considered. Mean and median filter of different size (3×3 , 5×5 , and 7×7) were tested on PIXEL data. Figure 7.3 reports the effects of these filters applied on the same liver image as Figure 7.2. As one can see, the application of filters characterized by increasing kernel size produces deeper effects on CT images. In fact, the 3×3 mean (Figure 7.3 (a)) and median (Figure 7.3 (d)) filters cause a very light effect on CT images that is almost imperceptible. Instead, a filter with kernel size 5 produce a little more evident effect. In fact, in Figure 7.3 (b) and (e), it is possible to detect the exact area on which the filter has been applied. Instead, 7×7 mean (Figure 7.3 (c)) and median (Figure 7.3 (f)) filters are even more aggressive and cause a strong blur on images. At the end of this preliminary analysis, I decided to keep the same 5×5 median filter previously used to process CT images of liver and lung tumours. The reason for this choice was that using

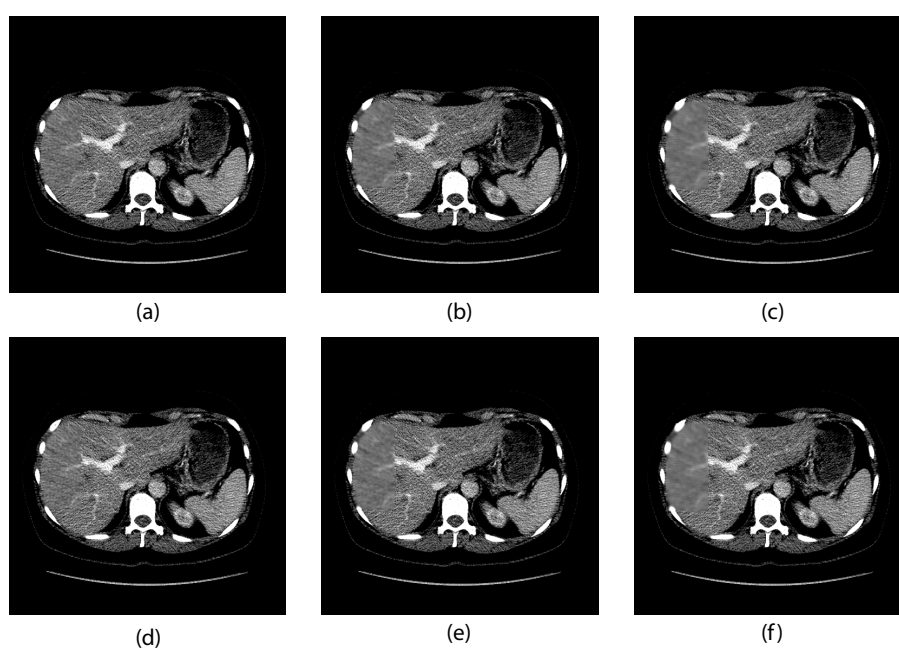


Fig. 7.3: Mean (first row) and median (second row) filter of different size are applied to DICOM image of examination C8N7. In particular, results of filtering obtained using kernel dimension 3×3 , 5×5 , and 7×7 , are represented in (a,d), (b,e), and (c,f), respectively.

median filters allows exploiting original HU density values, thus avoiding the introduction of new values resulting from mathematical operations, such as averaging. As regards filter kernel size, I selected the 5×5 since I considered it as a good trade-off between information preserving and noise removal.

Motion correction is another problem that had to be faced. Due to the long duration of the acquisition protocol (*i.e.*, 2 min), all the examinations have been acquired in condition of shallow breathing. Consequently, the effects of motion were evident in all directions and the application of motion correction methods was necessary. The ROIs pertaining to liver and lung tumour examinations analysed in Chapters 3 and 4 were manually aligned. However, this was possible thanks to the relatively low number of examinations and frames available for each acquisition (only 20 time instants for lung and 36 for liver, respectively). The high number of examinations of this project (almost 400) and acquisition time instants of each examination (60) roused the needs for an automatic motion correction algorithm. Unfortunately, to the best of our knowledge, there are no general purpose methods available for liver motion correction CTp applications. Consequently, I developed my own early prototypic algorithm that permitted to achieve good preliminary results and it is going to be improved with the collaboration of the computer science engineers of the CVG. The algorithm is presented in Sect. 7.2.

After defining the ROI and pre-processing the sequences, the first computation we decided to address was the baseline (*i.e.*, the density values assumed by tissue before CA arrival). In ideal conditions (*i.e.*, without noise), tissue density values before CA arrival (*i.e.*, the baseline attenuation value) should be constant in time. By subtracting from each TCC its baseline value, it is therefore possible to achieve the time attenuation curves (TACs) [86]. Practically, TACs are TCCs without offset that in ideal conditions assume value of zero before the arrive of CA in the tissue. In Figure 7.4 (a), a tissue TCC is reported together with the baseline value selected and the corresponding TAC achieved by subtracting the baseline value from the TCC.

Due to the influence of the baseline value, I decided to directly address baseline computation in my Thesis work. As discussed in Sect. 7.3, in the literature several methods to compute baseline values and TACs have been used. However, these methods often lead to different results that deeply affect the computed perfusion values finally achieved. For instance, an underestimation of baseline value (as the one represented in Figure 7.4 (b)) would lead to a TAC with a greater AUC, this resulting in overestimated *BV* values. Of course, since MSM is based on the computation of tissue TCC slope that re-

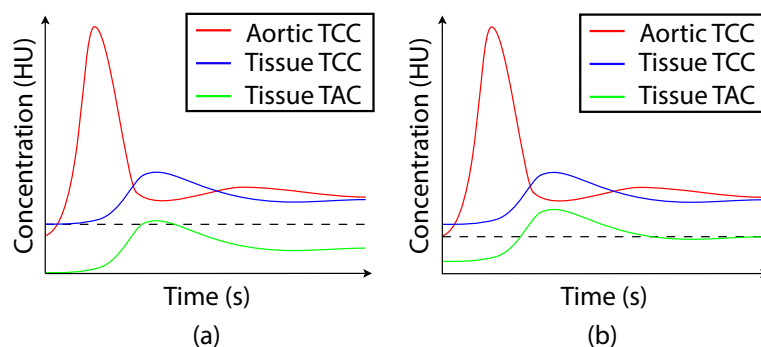


Fig. 7.4: An aortic (in the red colour) and a tissue TCC (in the blue colour) are shown together with the horizontal dot line representing baseline value selected and the TAC (in the green colour) that can be achieved by subtracting baseline value to TCC. In (a), the baseline is correctly selected while in (b) its value is underestimated, this resulting in a different TAC, having a greater AUC.

mains unchanged after the subtraction (or addition) of an offset, BF values computed with this method remains unchanged after the selection of one or another baseline values. However, as discussed in Chapter 3, the goal of this Thesis is not to develop algorithms specific for the application of the MSM, but to set-up methodologies that can be applied to all the methods and models. Since in PIXEL protocol, image acquisition started contemporaneously with the injection of CA, several images without presence of CA inside tissue were available. This allowed me to carry out a study on baseline values and to set-up an algorithm (see Sect. 7.3) to compute for each tissue voxel the best baseline value that should be used in perfusion studies. Results achieved with this algorithm were compared with those obtained by using the methods presented in the literature. Finally, two studies have been carried out. The former employed data of a single Centre to test the goodness of the algorithm developed by comparing baseline values obtained with those reported in the literature achieved with unenhanced CT scan. The latter study was based on multi-centre data analysis and have been carried out to analyse whether the use of different CT scanners could introduce variability on baseline values computed.

The last step of the algorithm pipeline of Figure 7.1 is the computation of perfusion parameters. This has been done by using the MSM by considering both single and dual vascular input, the latter being implemented from scratch. Finally, two studies have been carried out and described in Sect. 7.4. In the

former, examinations of a single Centre were considered while, in the latter, a multi-centre data analysis has been carried out to evaluate whether the use of different CT scanners could introduce variability on perfusion results.

7.2 Early prototype of rigid registration algorithm

As discussed in Sect. 7.1, *PIXEL* data were acquired by asking patients to breath shallowly. This kind of breathing causes motion throughout the sequence in all the three main directions. However, if the acquisition is long and without pauses so as to permit patients to breath, shallow breathing represents the best method to acquire images. Indeed, by asking patients to hold their breath as much as they can, it might happen that some deep breaths in the second part of the examination jeopardize the outcome and that the examination has to be discarded since affected by too a high motion moving the investigated tissues out of the FOV. For instance, the work in [155], using breath-hold protocol, finally excludes 14 out of 43 patients with CRC due to respiratory motion.

Since it was the first time I coped with examinations acquired in shallow breathing, first of all I tried understanding how deep the motion caused by breathing was. To this purpose, I randomly chose some examinations from Centre 1 and for each of them I drew a ROI on a central slice (the reference slice) of the sequence, following the liver contour. After that, I manually carried out a ROI alignment by using the 3D modality (see Sect. 4.2). Consequently, for each acquisition time instant, the slice showing the best matching with the reference slice was selected. Figure 7.5 reports an example of the slices that have been selected in five consecutive time instant. The ROI was then over imposed on the selected slice for each time instant and translated on the x - y plane to achieve the best matching with liver contour as possible. In Figure 7.6 (a)-(e), ROIs of examinations C1N7 aligned on the same five consecutive acquisition time instant are shown. In Figure 7.6 (f), the same ROIs are all superimposed to emphasize the displacement in x - y . Displacement of the ROI along the z direction and on the x - y plane could then be measured. For instance, the maximum ROI displacement between two consecutive time instants measured in examination C1N59 is equal to $4.4mm$ in x direction, to $14.2mm$ in y direction, and to 3 slices ($15mm$) in z direction. As for the maximum displacement of the ROI on the whole acquisition, it was equal to

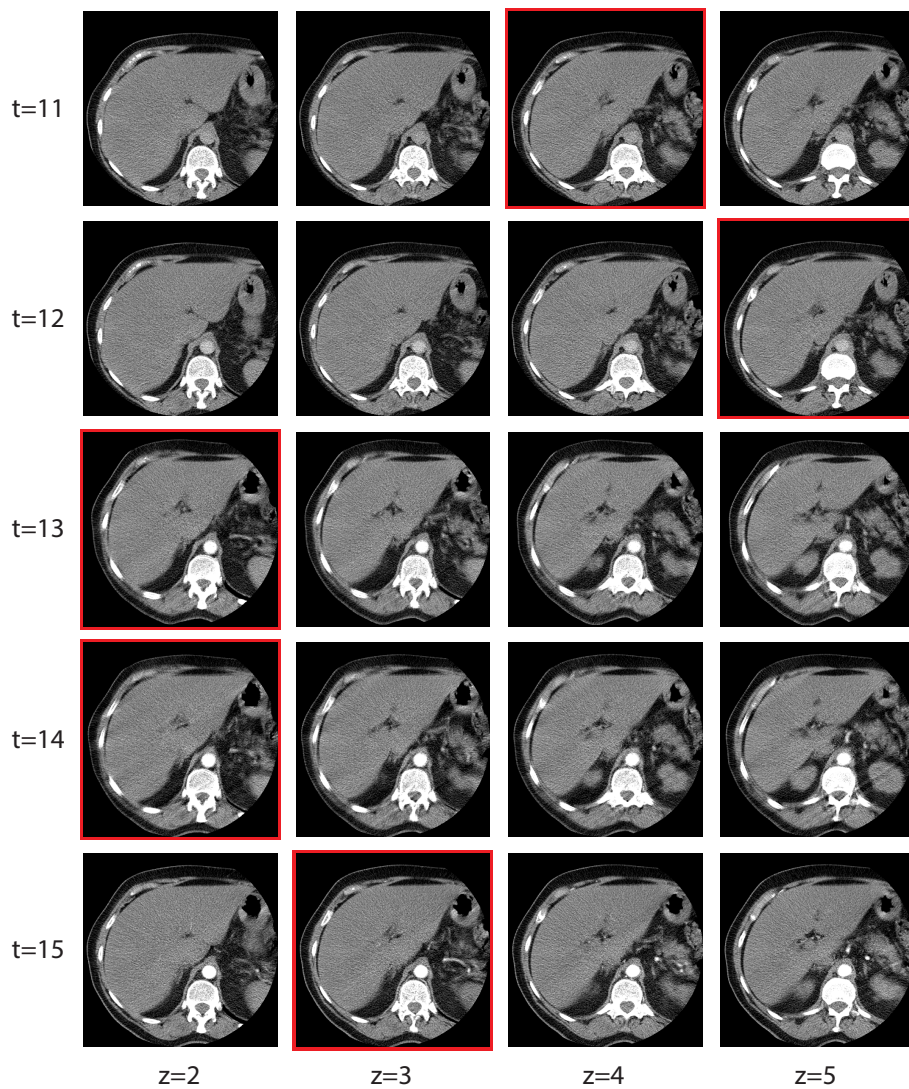


Fig. 7.5: Example of z level selection in consecutive time instant of examination C1N7. Each row represents a time instant while each column a different z level. The selected z level of each time instant is contoured by the red square.

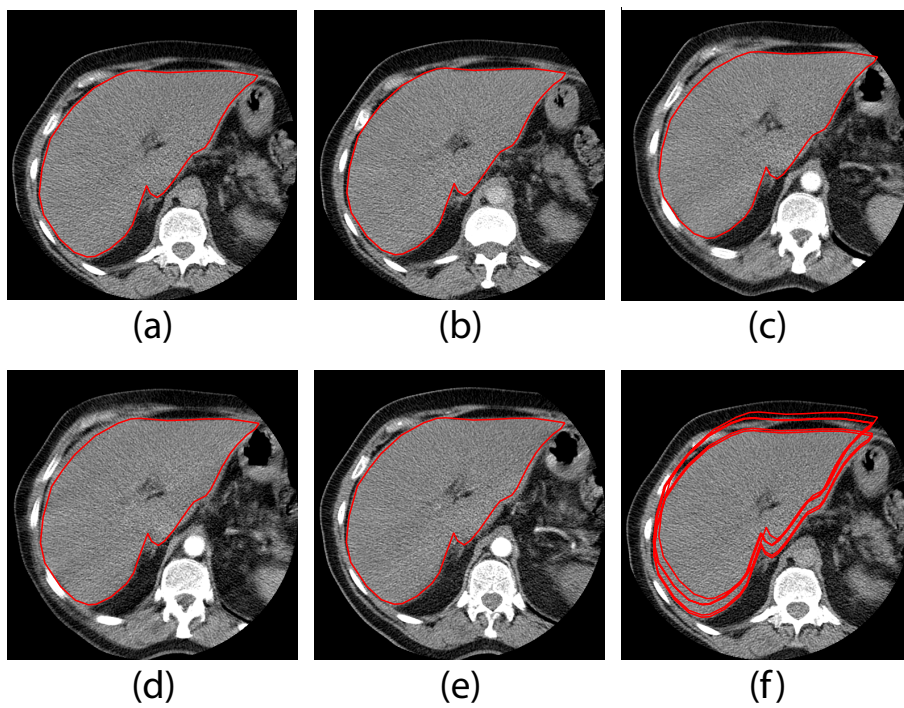


Fig. 7.6: Example of a ROI aligned on the x - y plane of different slices of examination C1N7, pertaining to different time instants. In (f), the ROIs in (a-e) are superimposed.

119.1mm, 148.6mm, and 4 slices (20mm) in x , y , and z direction, respectively. As one can see, even the motion between two consecutive time instants can be relevant, especially in the y and z directions.

One of the main difficulties, and probably the reason why no algorithms for liver motion correction specific for CTp examinations have been developed so far, is represented by the very narrow section of liver that can be analysed with CTp, this causing the loss of many anatomical reference points that could be used to make tissue alignment easiest. Moreover, the presence of a very narrow FOV (especially in case when only a portion of liver is acquired) makes motion correction even more challenging.

To face this issue, I developed a preliminary algorithm for automatic rigid motion correction. As the first step, I simplified the problem by decomposing motion in two parts: in the cranio-caudal direction and in the transversal plane. Accordingly, the alignment procedure of the tissue ROI drawn by the clinicians on a reference slice can be split in two main steps:

1. selecting the correct z level (*i.e.*, the slice on which placing the ROI)
2. aligning the ROI in the x - y plane

Thereafter, for both these steps, I looked for the most suitable anatomical reference points fulfilling the following criteria:

- being capable of providing clear information regarding liver motion
- being of general-purpose (*i.e.*, not specific for a single patient or acquisition protocol or CT scanner)
- being easily detectable by an automatic procedure

As regards the alignment in the craniocaudal direction, as a reference point I identified the space between liver and thorax. Indeed, as shown in Figure 7.7², liver is characterized by a wedge shape, with the base at the top and the vertex at the bottom. The space occupied by the liver on the transversal plane (that is the one on which images are acquired) allows evaluating with a great accuracy the liver z level. In particular, Figure 7.8 shows an example of 4 adjacent slices with a ROI encompassing this region. As one can see, the space between thorax and liver undergo relevant size changes by selecting different z levels.

Instead, as regards motion on the x - y plane, I realized how liver follows the motion of the rib cage caused by breathing. Indeed, during the inspiration phase, the rib cage expands and liver follow the ribs (Figure 7.9) that

²courtesy of <http://pie.med.utoronto.ca>

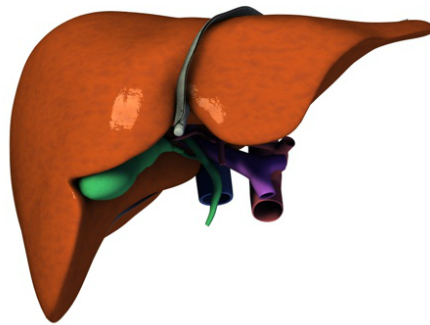


Fig. 7.7: Representation of liver, its vasculature (in the red and blue colours) and biliary ducts (in the green colour).

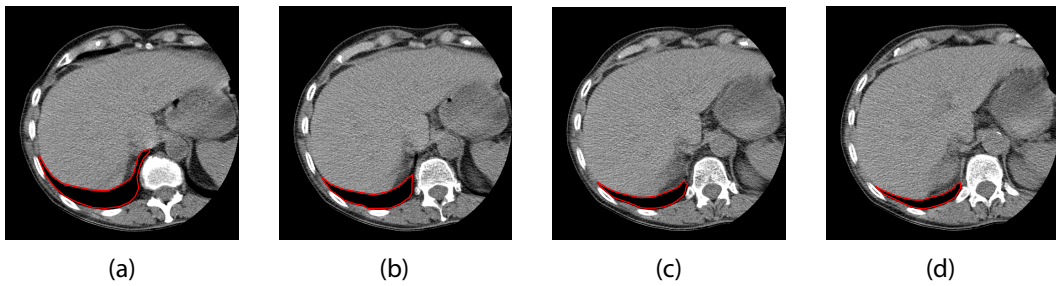


Fig. 7.8: Four adjacent slice of examination C1N7 with a ROI contouring the space between liver and thorax.

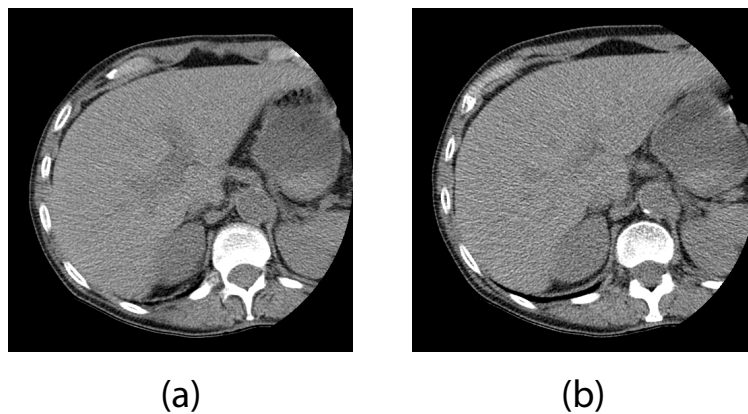


Fig. 7.9: An example of two CT images of examination C1N7 acquired at the end of the inspiration (a) and expiration (b) phases.

consequently, can be chosen as anatomical reference points. In the following paragraphs, the steps taken in order to achieve a correct 3D rigid alignment are reported and discussed. The procedure has to be applied to all the images acquired in each time instant.

The first part of the algorithm aims at selecting the correct z level on which translating the ROI by measuring the distance between liver border's and thorax. In order to automatically select the correct slice in each time instant, it is necessary to follow these three main steps:

1. bounding patient's body
2. selecting the image area on which algorithm has to work
3. bounding the region between liver and thorax

For the sake of clarity, the pipeline of this first part of the algorithm is represented in Figure 7.10.

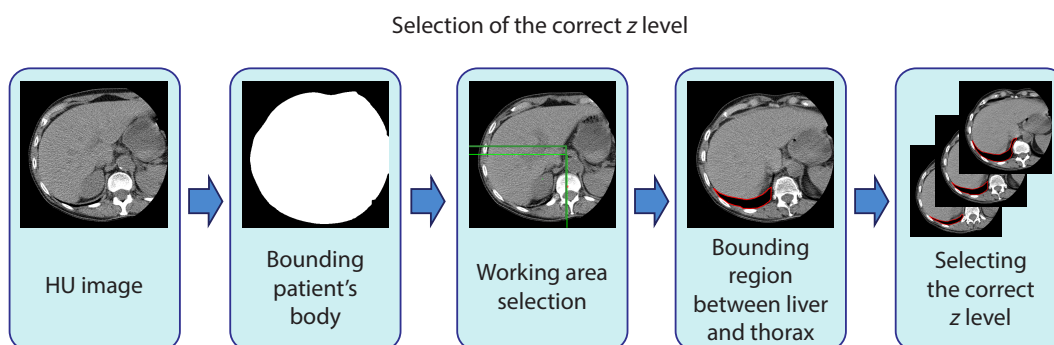


Fig. 7.10: Pipeline of the first part of the motion correction algorithm allowing selecting the correct z level at each time instant.

The first step needed to find the correct z level on which translate the ROI is the separation of patient's body from the background (*i.e.*, air, clothes, blankets, and patient's table). To this purpose, a mean spatial filter has been applied to the original CT image (Figure 7.11 (a)) in order to smooth details and differences between similar structures (Figure 7.11 (b)). After that, a threshold to exclude low density structures (mainly pertaining to the background) has been applied to the filtered CT images. The mask achieved has been first inverted (Figure 7.11 (c)), then modified through the application of

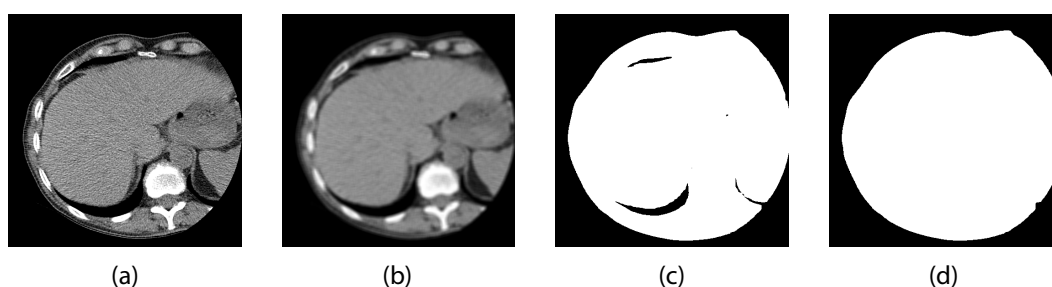


Fig. 7.11: Original CT image of examination C1N7 (a) and its filtered version (b). Mask achieved by thresholding low density values (c) and after closure operation (d), giving the mask of patient body.

a closing operation, allowing obtaining a second mask perfectly discriminating between patient's body and background (Figure 7.11 (d)).

To second step aims at speeding up the algorithm and excluding misleading anatomical structures from the analysis, to this purpose, the area of the image where the algorithm focuses its analysis has been restricted to the dorsal right side of the rib cage (that inside images corresponds to the bottom left of the patient). Since in some examinations patients were not centred in CT images (*e.g.* due to a restricted FOV centred on the liver) the centre of CT images (CCTI) could not be used to identify the posterior right portion of patient's rib cage. To this purpose, a method exploiting vertebrae position has been used. Since the vertebral column is one of the few anatomical structures that does not move during acquisition, its vertebrae position has been identified on a non-enhanced image, once and for all. In order to automatically detect vertebrae, a threshold on CT images has been performed (Figure 7.12 (a)), this permitting to select highest density values only (corresponding to bones, calcifications, or high concentration of density values inside vessels). Then, a morphological closing has been applied (Figure 7.12 (b)) to exclude the smallest objects and fill the "holes" due to the presence of bone marrow (that having a lower density with respect to bones has been excluded from the mask). Thereafter, the vertebra in the slice has been selected as the bigger object inside the obtained mask and the coordinates of its central point have been calculated (Figure 7.12 (c)). Finally, the area of interest where the algorithm have to focus on has been selected. In particular, the centre of the vertebra has been used as the point discriminating between the right and the left side of the patient. As regards the identification of the bottom and the top portion of

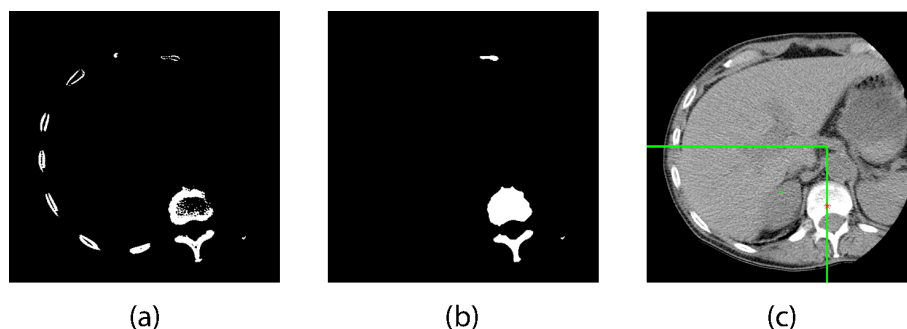


Fig. 7.12: Thresholded mask including only high density values of an unenhanced CT image of examination C1N7 (a) and its closure version (b). Original CT image with the centre of vertebra (red marker) and the border of the region selected (in the green colour) highlighted (c).

the rib cage, the CCTI has been used if the centre of the vertebra was placed under the CCTI (*i.e.*, the FOV is large and the posterior part of the patient is included in the bottom half of CT image). On the contrary, if the centre of the vertebra was found above the CCTI (*i.e.*, the FOV is narrow or the images are not centred on the patient), the whole left portion of the image was considered (Figure 7.12 (c)).

The third and last step of the algorithm used to select the correct slices is that detecting and outlining the region between liver and thorax. To this purpose, the original CT image (Figure 7.11 (a)) was thresholded to obtain a mask excluding background and anatomical regions having very low density values (*e.g.* those areas not pertaining to a specific anatomical structure such as an organ). In this case, the original CT image has been used, in place of the filtered image, to achieve the most precise profile of this region. Then, the obtained mask (Figure 7.13 (a)) underwent a closing operation to remove a great part of noisy voxels (Figure 7.13 (b)). In order to remove background elements, the mask of Figure 7.13 (b) was ANDed voxel-by-voxel with the patient's body mask obtained at the previous step of the algorithm (Figure 7.11 (c)), to obtain Figure 7.13 (c). After that, all the elements of the mask out of the region defined at the first step of the algorithm (Figure 7.12 (c)) were excluded from the analysis (Figure 7.13 (d)). At this point, the region between liver and thorax has been isolated. Therefore, the maximum thickness of this region (intended as the maximum orthogonal distance between liver and the thorax) can be measured as shown in Figure 7.13 (d).

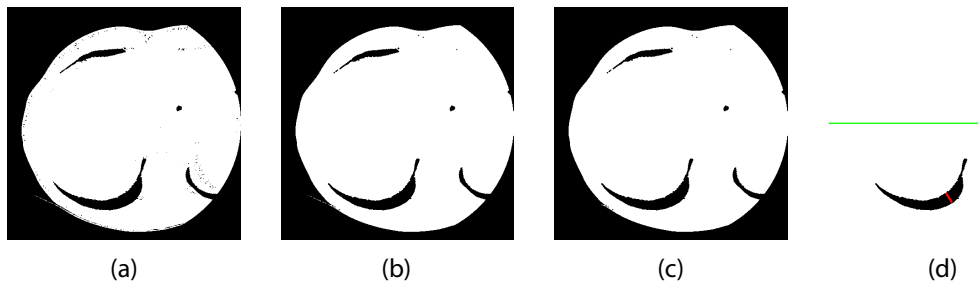


Fig. 7.13: Thresholded mask (a) obtained from the original CT image of examination C1N7 by excluding structures with very low density values, after the application of a closing operation (b), the AND operation with the body patient mask (c) and the selection of the region identified in the first step (d). The red line in (d) points out the maximum thickness of the region between liver and thorax.

Distance between liver and the thorax found on the reference slice is compared with that found in the other images of the sequence. In each time instant, the slice showing the most similar distance to that found on the reference slice was selected.

In order to evaluate the efficacy of this algorithm to select the correct slice, a 3D alignment have been manually performed on several examinations. The outcomes of these tests showed that the algorithm always selected the same slice manually chosen by clinicians.

After selecting the correct z level where copying the ROI in each time instant, it is necessary to translate the ROI on the $x-y$ plane. As discussed above, ribs are great reference points for this phase of the algorithm. Therefore, it is necessary to automatically identify ribs in each image of the sequence and use their relative distance to the ROI to correctly align it on the image sequence. To this purpose, it is necessary to follow these three steps:

1. identifying the ribs
2. detecting the set of proper points of the ribs (*i.e.*, their inner part with respect to patient's body)
3. fitting the ribs' points found at the previous step

These steps are also represented in the pipeline of Figure 7.14.

To identify ribs inside each CT image of the reference sequence, I applied a threshold to isolate high density structures. However, this would cause the inclusion of undesired structures (*e.g.* vessels filled with CA). To reduce the

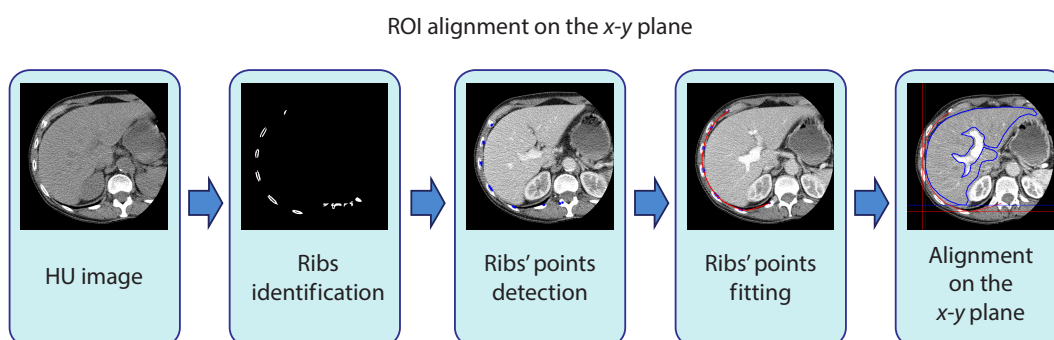


Fig. 7.14: Pipeline of the second part of the algorithm of motion correction allowing to obtain the ROI's alignment on the x - y plane.

possibilities of achieving misleading results, I excluded the majority of the areas found inside the rib cage. To this purpose, I first applied an erosion operation to the mask of patient's body (Figure 7.11 (d)) using a structuring element of a high dimension so as to preserve all ribs, including the dorsal ones that usually are far from body contour due to the presence of dorsal muscles in patient back. The eroded mask ANDed with the original CT image is represented in Figure 7.15 (a). The eroded portion of patient's body mask corresponding

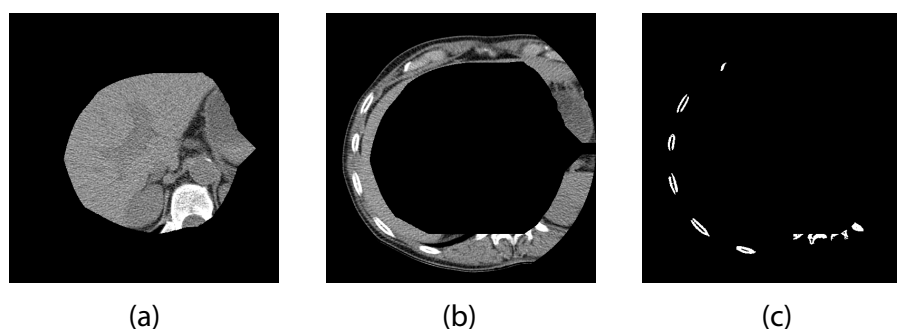


Fig. 7.15: Eroded CT image of examination C1N7 (a), portion of the image eroded (b), and results of thresholding in (c), performed to include in the analysis high density elements only.

to the region where ribs can be found has been used. The image obtained by applying the eroded mask to the original CT image (Figure 7.15 (b)) has therefore been thresholded in order to include in the analysis the high density elements only (Figure 7.15 (c)).

After having identified ribs, it has been necessary to identify the side of their border closest to the internal part of the patient. To this purpose, the point found in the middle of the mask of patient's body has been taken as reference point (RP). The closest points of each rib to RP are those we are looking for. In order to select them, a closing operation (Figure 7.16 (a)), has

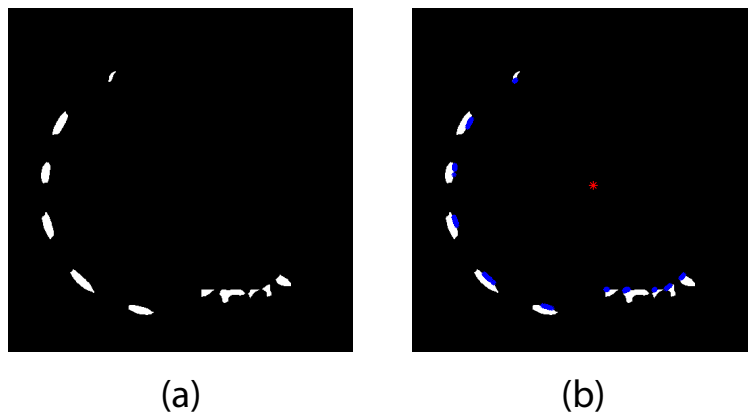


Fig. 7.16: Mask of high density structures obtained from Figure 7.15 (c) after closing operation (a). Selected points of the ribs (in the blue colour) and RP (in the red colour) (b).

been applied to the thresholded mask of Figure 7.15 (c), to close the holes caused by the presence of bone marrow. Thanks to this passage, it has been possible to obtain a unique continuous element for each rib. After that, the distance between RP and the points of each rib has been computed. The 5% of the closest points of each rib (Figure 7.16 (b)) have been considered as the internal side of the rib. A percentage number has been chosen to weight the number of points to be considered for each rib, depending on their dimension. However, in some cases, some points found do not belong to ribs. Indeed, if a vessel is close to liver borders (and hence to rib cage) and filled with CA, it could be erroneously included (Figure 7.17 (a)). In order to avoid the inclusion of misleading points not pertaining to the ribs, I exploited the characteristic convex shape of the rib cage. First of all, I created a mask having the points identified as the vertices (Figure 7.17 (b)). Thereafter, I created its convex hull (Figure 7.17 (c)). All those points placed inside rib cage and hence not belonging to ribs, responsible for concavities in the first mask, were excluded from the analysis (Figure 7.17 (d)). After isolating the points of each ribs, I fitted these points by means of smoothing splines (Figure 7.18). The fitting

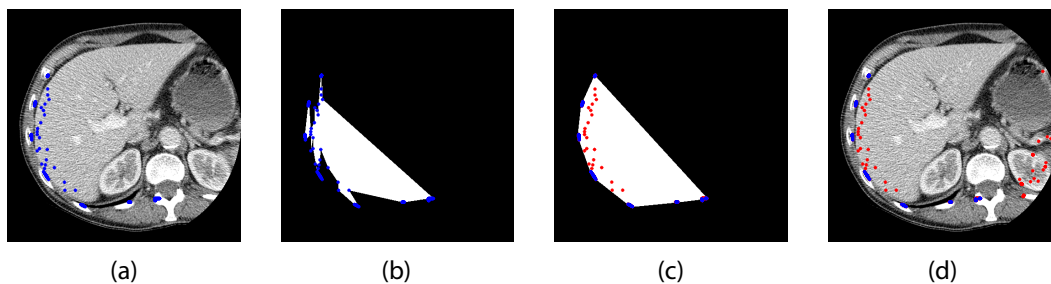


Fig. 7.17: Example of examination (C1N7) (a) in which small vessels filled of CA could mislead the analysis. Mask of the points identified (b), convex mask (c), and points excluded from the analysis (d) (in the red colour).

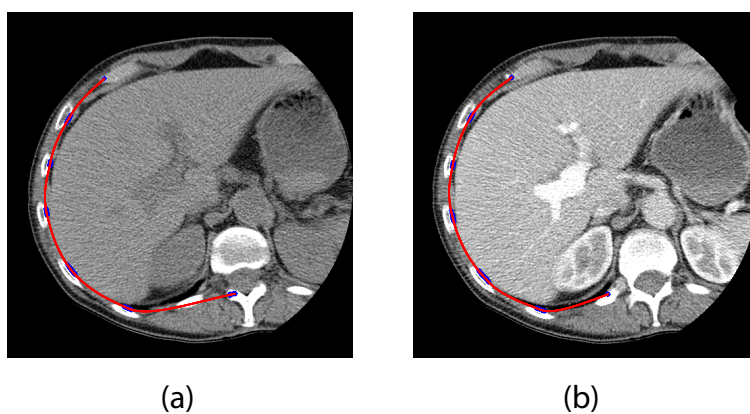


Fig. 7.18: Example of fitting applied to the points of the rib cage on an un-enhanced (a) and enhanced (b) CT images of examination C1N7.

curve draw the interior contour of rib cage that will be used as a guide for the translation of tissue ROI on the x - y plane.

In order to align tissue ROI on each slice, the horizontal and vertical distances between ROI and ribs' fitting curve have been measured. In particular, starting from the reference slice on which the clinician has drawn the tissue ROI, the horizontal distance is measured as the distance between the left-most points of the fitting curve and of the ROI. Instead, the vertical distance is measured as the distance between the bottom-most points of the fitting curve and the ROI. These distances can be better visualized in Figure 7.19 (a) where the

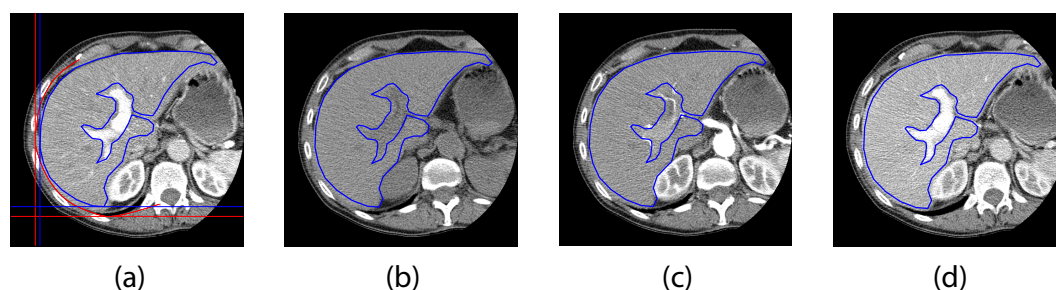


Fig. 7.19: ROI manually drawn on the reference slice of examination C1N7 and horizontal and vertical lines passing through the left-most and bottom-most points of the ROI (in the blue colour) and the ribs fitting curve (in the red colour) (a). Examples of a ROI automatically aligned on CT images acquired during baseline phase (b), in correspondence of CA arrival in aorta (c), and during the enhanced phase (d).

left and bottom-most points of the ROI and the fitting curve of the ribs are highlighted by vertical and horizontal lines. The distance between the red and the blue lines have been used in the other slices of the sequence to reposition the ROI. In particular, by finding in each CT image the left-most and the bottom-most points of the fitting curve, it is possible to replace the ROI by keeping the horizontal and vertical distances fixed. Figure 7.19 (b)-(d) depicts an example of ROIs aligned with the automatic algorithm and placed on slices acquired in different time instants. As one can see, the algorithm developed is capable to follow liver motion. Its flexibility allows obtaining good results on both un-enhanced and enhanced CT images, independently from size and position of tissue ROI. Comparison with manual alignment showed that positions of the ROIs manually aligned were comparable with those achieved automatically.

However, this automatic motion correction algorithm has some limitations.

First of all, it cannot be applied on examinations showing a too narrow FOV. Vertebrae and at least three ribs on the right flank and the dorsal side of the patient should be present inside images to permit the correct translation of the ROI on the x - y plane. Moreover, the algorithm could meet difficulties in the identification of the correct z level in those cases where the acquisition has collected data from the upper part of the liver. In these cases, the space between liver and thorax could not be so different between adjacent slices. Even though this is not the case of PIXEL examinations, because the acquisitions had to be focused on the central part of the liver. In order to apply this method to any type of liver CTp examinations, this algorithm should be refined.

Despite these limitations, this preliminary implementation of the algorithm has shown to work well on the most part of PIXEL examinations. The algorithm presented in this section constitutes the starting point for more advanced and complete methods of motion correction, allowing to include also those examinations previously excluded (*i.e.*, those with a very narrow FOV) and to carry out an elastic registration. Expert computer science engineers of the CVG are actually working on this topic.

7.3 Baseline

As discussed in Sect. 7.1, the selection of a correct baseline value is of fundamental importance to achieve reliable perfusion results [81, 86]. However, actually several methods to compute baseline and obtaining TACs have been adopted in the literature, but to the best of our knowledge, no studies have been carried out to determine which method could be the best one to achieve baseline values and which are the main advantages and disadvantages of the methods commonly used. In the following paragraphs, the methods that have been used in the literature to achieve baseline values and to obtain TACs are discussed (Sect. 7.3.1). An algorithm for the computation of the correct baseline values is then described (Sect. 7.3.2), compared with methods used in the literature (Sect. 7.3.3), and applied to some examinations of PIXEL. Results achieved considering examinations of Centre 1 only and of four different Centres are presented and discussed (Sects. 7.3.4 and 7.3.5, respectively). Finally, some concluding remarks are reported in Sect. 7.3.6.

7.3.1 TACs computing methods

The achievement of a correct TAC on which computing perfusion values depends on the baseline values selected that can differ according to the choices regarding the following three aspects:

- use of local or global baseline values
- number of slices considered to compute baseline
- method used to subtract baseline to TCCs

Both local and global baseline values have been used in the literature. Global baseline values are usually computed as the average of liver density values inside the tissue ROI on the first image acquired [63]. Global values have been used both in those studies where perfusion parameters are computed on a single TCC (obtained by averaging density values in the ROI at every time instant) [291, 292, 112], and in those studies where a voxel based analysis is carried out [135]. Despite liver is considered an organ characterized by a homogeneous texture [293], local density variations due to micro-vascular structures composing this tissue can be present. As discussed in Sects. 7.3.4 and 7.3.5, local baseline values in the same patients can cover a range of values even higher than $30HU$. The use of local baseline values, following local density variations of liver tissue are thus crucial to achieve reliable perfusion values and avoid incurring in under-or over-estimation.

Most of times, baseline is extracted from the first slice acquired in the sequence [294, 86] so as to be sure that CA has not arrived yet. If local baseline values are used, this means for each TCC considering its corresponding density value in the first CT image acquired as the baseline value. In this case, the presence of noise and artefacts affecting the first CT image can alter baseline values and lead to incorrect perfusion values. Of course, if the acquisition protocol used allows to have only one scan in which tissue is non-enhanced, the baseline value can be extracted from that image only. On the contrary, if further non-enhanced scan are available, it would be important to use all of them so to achieve as more reliable baseline values as possible. To this purpose, the authors in [193] used two volumes acquired before the arrival of CA in the heart to compute baseline, even if they do not explain how the baseline was computed on the two images. Probably, the work computing perfusion on rats [295] is the first one declaring to compute baseline as the average of the density values of more than one scan (the first 4-5 acquisitions

are indeed used). Therefore, the needs of baseline values less affected by the presence of noise and artefacts starts being a recognized necessity [81, 86].

A further source of variability can be found in the methods used to extract the TACs. To this purpose, several methods exist leading to as many different perfusion results. The first method consists in the subtraction of the first image from the images acquired after the arrival of CA inside tissue. TACs are therefore directly extracted from the resulting CT images [86, 254]. The main drawback of this method arises from motion issues being neglected. Indeed, if patient move (and this is our case since acquisitions are carried out in shallow breathing conditions), there will be a mismatch between the tissues to which baseline values pertain and the tissue from which these baseline values are subtracted. This problem does not hold when TACs are obtained by subtracting local baseline values directly from the data-point of the tissue TCCs considered [81, 193]. Indeed, since TCCs are usually extracted from already registered images, density values composing one TCC belong to the same tissue portion. Consequently, baseline values subtracted from the TCC correctly pertain to the same tissue portion to which all the TCC data points pertain.

To achieve the best baseline density values as possible, it is thus important to adopt local baseline values and to use as the highest number of data points as possible. Finally, to achieve TAC these baseline values are subtracted voxel-based directly from TCCs.

7.3.2 Baseline value computation

In this section, the method to compute baseline values is presented. This algorithm allows computing the best baseline values as possible for each tissue voxel through exploiting the maximum possible number of data-points.

The main problems related to baseline computation are:

1. deciding the baseline portion (BP), that is how many time instants to include, that is which are the time instants before CA arrival
2. setting up a proper processing method

As regards the second item, we simply perform an average operation on the data point selected in the first item. While the first point of BP is naturally chosen as the first time instant, the real problem is to find out what the ending point (EP) is.

The algorithm to find out voxel-based baseline EP values is an adaptive iterative algorithm subdivided into five steps:

1. tissue TCCs denoising
2. selecting the TCC portion on which looking for BP termination
3. iterative TCC fitting
4. computing TCCs fitting error index
5. selecting the time instant corresponding to EP

The first step needed to better distinguish between the two TCC portions (*i.e.*, BP and the portion after CA arrival) is the application of a 5-point moving average filter to each TCC. This procedure allows to better detect the global trend of the TCCs and to reduce quantity of noise inside the signal that could lead to the achievement of misleading results. Figure 7.20, reports an

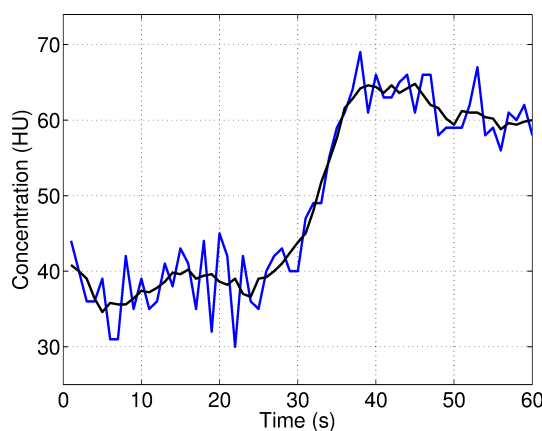


Fig. 7.20: Example of TCC (in the blue colour) randomly chosen among those of patient C1N1, and its corresponding filtered version (in the black colour) achievable by applying a 5-point moving average filter.

example of a liver TCC (in the blue colour) that has been randomly selected from the examination C1N1. As one can see, the signal resulting from the application of a temporal filter to the TCC (in the black colour) permits to achieve a denoised curve whose trend better follows the ideal one (see Sect. 2.2).

Thereafter, I started looking for the possible time instants of EP. While the first data points of each TCC certainly belong to BP, in order to speed up

the algorithm I selected the proper TCC portion on which looking for baseline EP. Both the extremities of this interval of possible EPs were selected in a conservative way so as to preserve all the possible solutions. In particular, the starting point of the interval (SI) is selected as the time instant of CA arrival in aorta, following the same principle used in Sect. 6.4.2. While SI is the same for all the TCCs (since it is extracted from the aortic signal that is one for all tissue voxels), the ending point of the interval (EI) is kept variable. In particular, EI is selected for each voxel as the minimum time instant between the peak time instant of the tissue TCC peak and of the averaged TCC (computed as the averaged tissue TCC on the whole ROI). The purpose of selecting the minimum between these two time instants is to reduce computation time in those cases where a high noise level causes a delay in the absolute peak of the tissue TCC. This step allows the algorithm to adapt the research of EP to the most appropriate signal portion, dependently on the time taken by CA to join that specific tissue voxel. In this way, EI always represents one of the points surely localised after the arrival of CA in the corresponding tissue voxel. This permits to include in the interval all the data points that could correspond to EP and to exclude those data that have been acquired after the arrival of CA inside tissue. Figure 7.21 reports an example of the EI selected:

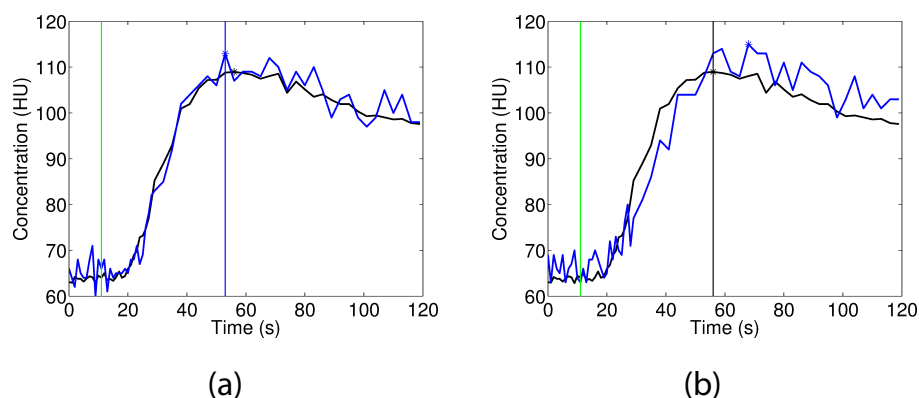


Fig. 7.21: The mean TCC (in the black colour) and one TCC of the examination C1N2 (in the blue colour) are shown together with SI (the green vertical line) and EI (the blue (a) or the black (b) vertical line). In (a) EI has been selected from the tissue TCC while in (b) from the mean curve.

in Figure 7.21 (a) the EI corresponds to the peak of the tissue TCC while in Figure 7.21 (b) it corresponds to the peak of the mean tissue TCC.

After defining the set of possible solutions, the part of the algorithm aiming

at computing the correct EP has been implemented. Based on the ideal case (*i.e.*, absence of noise) where the TCC data points belonging to BP have constant values, TCCs BP has been modelled with a horizontal line. In particular, an iterative algorithm considering at each iteration different possible EP has been implemented. Indeed, in the first iteration, the first TCC portion up to SI is fitted with a horizontal line. The ordinate of the fitting line is given by the average values of the TCC data points considered. Then, at each iteration, one more subsequent TCC point is included in the TCC portion that is fitted. This iterative fitting process goes on until EI is found. An example of the partial results of this process is reported in Figure 7.22 (a).

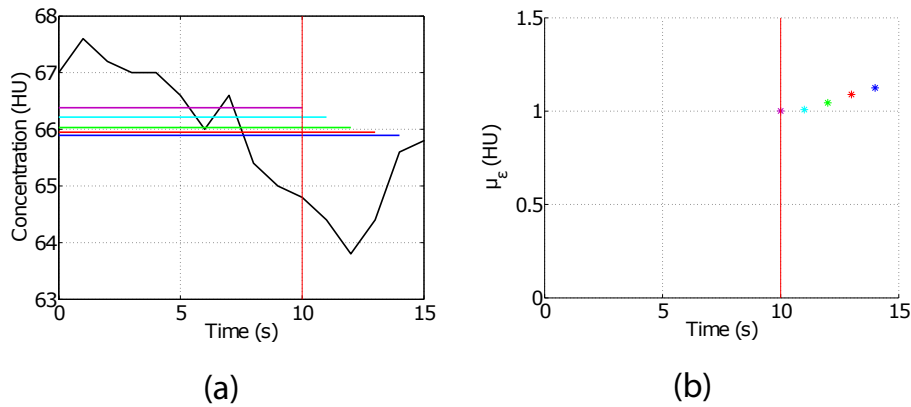


Fig. 7.22: A TCC of the examination C1N2 (in the black colour), its SI (the red vertical line) and the linear (horizontal) fit obtained during the first five iterations (a); the correspondent μ_ϵ values calculated at each iteration, reported by using the same colour (b).

Now that all the possible BPs of the TCC have been modelled, an index able to evaluate the coherence between the TCCs data points considered at each iteration and their ideal version represented by their fitting curve is needed. To this purpose, the goodness-of-fit error index μ_ϵ has been used. In this case, the residuals ϵ in each data point are calculated as usual as the distance between the original data and their fitted (expected) version. Every time that a data point is included in the analysis, the μ_ϵ value computed increases if it is far from the last mean TCC value computed, and decreases if it is closer. Figure 7.22 (b) shows μ_ϵ values computed at each iteration on the TCC data points considered. However, it is worth noting that an increase of the μ_ϵ value can be caused by both presence of noise and CA arrival inside tissue. In order

to reduce the influence of noise and the probability for the algorithm to fall in local minima solutions, a 5-point moving average filter has been applied on the time series of the μ_ϵ values (Figure 7.22 (b)).

Now that all the possible TCCs BP and an index evaluating BP data points coherence with their expected version are available, the correct baseline EP value has to be selected. To this purpose, I decided to take advantage from the features of the first and second derivative of the signal. To achieve precise derivative values of signal, I exploited the analytic derivatives properties. Therefore, μ_ϵ values achieved after the application of the moving average filter have been fitted through the use of smoothing spline, by using a very low smoothness degree. Figure 7.23 shows an example of TCC (a), with related

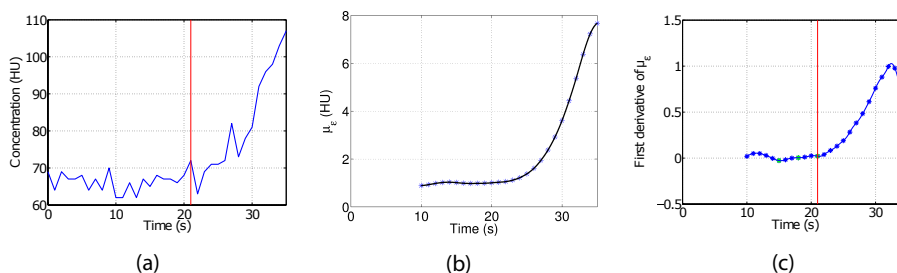


Fig. 7.23: A TCC of examination C1N2 and its EI (the red vertical line) (a); the μ_ϵ values achieved after the application of moving average filter (the blue stars) and of spline (the black solid line) (b); the first derivative of the fitted μ_ϵ values, its local minima (the green markers) and EI (the red vertical line) (c).

μ_ϵ values achieved after the application of the moving average filter and its continuous version (b). Thereafter, the first analytic derivative of the fitted μ_ϵ has been computed (c) and its local minima values identified. The local minima values of the first derivative correspond to points after which the original signal (in this case μ_ϵ) increases. As discussed above, the increase of μ_ϵ can correspond both to the inclusion of an outlier or to the arrival of CA inside the tissue voxel. In this last case, the increase of μ_ϵ will be constant for several time instant (*i.e.*, for all the enhancement portion of the TCC). Consequently, the last local minima value of the first derivative of fitted μ_ϵ could be assumed as the time instant when enhancement starts. An exception arises in those cases where the first derivative of μ_ϵ is constant and does not present a local minima, in correspondence of CA arrival (Figure 7.24). To also detect these points, I computed the local minima of the second derivative of μ_ϵ and selected those data points with an absolute value lower than a specific threshold

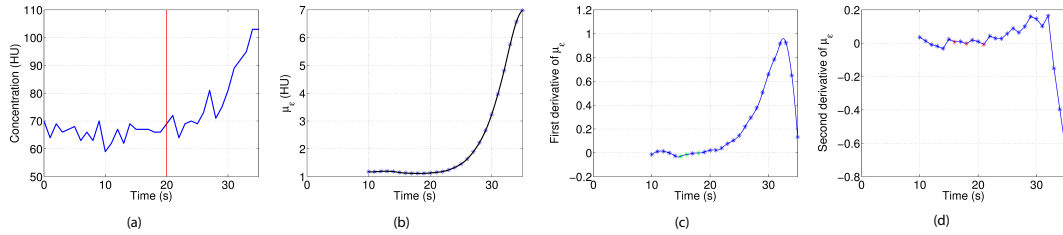


Fig. 7.24: A TCC of examination C1N2 and its EI (the red vertical line) (a); the μ_ϵ values achieved after the application of moving average filter (the blue stars) and of spline (the black solid line) (b); the first derivative of the fitted μ_ϵ values and its local minima (the green markers) (c); the second derivative of the fitted μ_ϵ values and the points where the first derivative is constant (red markers) (d).

(experimentally found and fixed equals to 0.01). The time instant of end BP has been then selected for each TCC as the last of the local minima on the first and the second derivative. Accordingly, the baseline value of the TCC is finally computed as the mean value of the TCC data points of the BP.

7.3.3 Baseline algorithm: preliminary test

In this paragraph, a comparison of results achieved with the algorithm developed and the state-of-the-art algorithms is carried out. To this purpose, the algorithm to compute baseline values was first tested on some CTp examinations randomly chosen between those of Centre 1. In this paragraph, data regarding three representative examinations (C1N23, C1N37, C1N38) are presented and discussed. Colorimetric maps and histograms of baseline values achieved for these examinations are reported in Figure 7.25 while Table 7.1 collects the main statical parameters, such as mean, median, standard deviation, and range values, respectively. As one can see, baseline histograms, can be of several shapes. For instance, histogram of Figure 7.25 (a) presents a sort of Gaussian-like distribution with a short tale on the right that is heavy till 65HU and very light for higher density values. The histogram in the middle (Figure 7.25 (b)) is bimodal, presents a heavy left tail, and is the one with the wider range of baseline values (26.7HU). The histogram of the last examination (Figure 7.25 (c)) instead, is multimodal, but the range of baseline values represented (16.4HU) is similar to that of the first histogram (15.2HU). None of these histograms present groups or sparse baseline values far from the principal distribution. This is reflected also in the three colorimetric maps

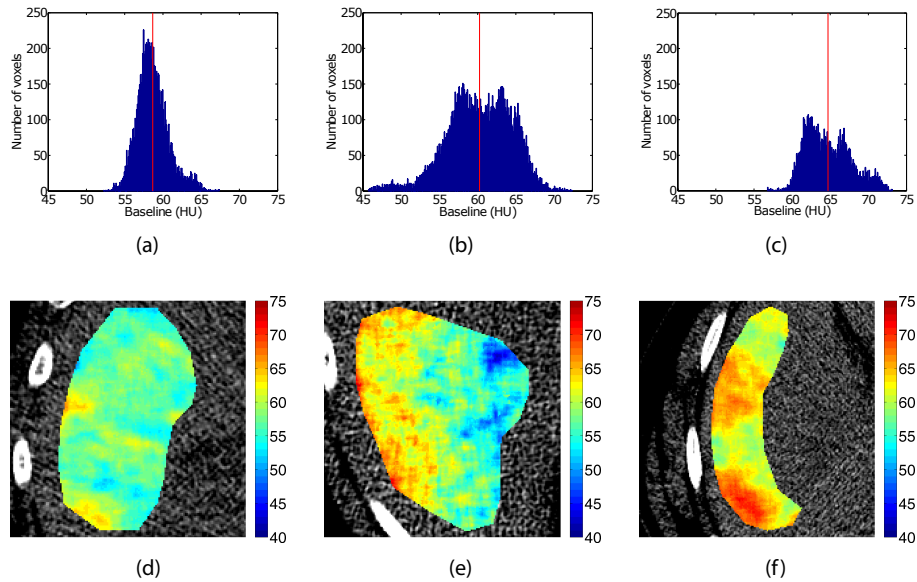


Fig. 7.25: Baseline histograms and colorimetric maps achieved with our adaptive algorithm and pertaining to examinations C1N23 (a,d), C1N37 (b,e), C1N38 (c,f). The red vertical line on histograms points out the mean baseline value of that examination.

Baseline values				
Examination	Mean (<i>HU</i>)	Median (<i>HU</i>)	std (<i>HU</i>)	Range (<i>HU</i>)
C1N23	58.7	58.4	2.1	15.2
C1N37	60.3	60.4	4.2	26.7
C1N38	64.7	64.3	3.0	16.4

Tab. 7.1: Mean, median, standard deviation, and range of baseline values achieved in three examinations (C1N23, C1N37, and C1N38) by using the algorithm proposed in Sect. 7.3.2.

(Figure 7.25 (d), (e), (f)) that does not show groups of voxels with homogeneous colours quite close to the hot ones. All neighbouring voxels assume colours in a continuous range, this hinting at similar tissue features inside the ROI. By observing the colorimetric maps it is also possible to achieve information about the spatial distribution of baseline values. As one can see, all the colorimetric maps are locally highly homogeneous. The presence of a local spatial correlation is demonstrated by the gradual passage of baseline values from lower to higher baseline values that in colorimetric maps results in progressive colour gradients. This spatial correlation of baseline values reflects local spatial coherence of tissue features. Moreover, since baseline values obtained through the use of our algorithm are computed in each voxel by using only data pertaining to one TCC, independently from the signal of the neighbour voxels, baseline local spatial homogeneity can be considered as a qualitative indicator of algorithm goodness.

Below, results obtained with the algorithm described in Sect. 7.3.2 are compared with those of the methods proposed in the literature and discussed in Sect. 7.3.1. For the sake of a better readability, the adaptive algorithm of Sect. 7.3.2 is referred to as “BFA” (*i.e.*, Baseline finding algorithm), while the methods proposed in the literature are referred in a different way, according to the approach utilized. Thereafter, with the label “G1”, we refer to the one global baseline value obtained as the average of the density values of the ROI of the first CT image [135]. “V1” points out the method where the voxel-based baseline values are assumed as being the corresponding density values of the ROI of the first CT image [294]. Finally, “V5” refers to the method where the voxel-based baseline values are computed as the mean density values assumed by each voxel in the first five CT images [295]. The main features of these four methods to compute baseline are resumed in Table 7.2.

Since before CA arrival the tissue density should be constant, this portion of TCC could be fitted by a horizontal line whose ordinate is equal to the baseline value. Therefore, to have a measure of the goodness of the baseline value chosen, μ_ϵ has been computed on the BP of each TCC automatically selected by our algorithm as the absolute mean value of residuals between the original TCC value and the computed baseline value. Table 7.3 resumes mean and standard deviation of baseline and μ_ϵ computed with the four different methods.

Figures 7.26 and 7.27 present baseline histograms and colorimetric maps achieved for the three examinations by computing baseline values according to V1 and V5, respectively, where histograms of Figure 7.26 are composed by

Baseline methods		
Method	Number of volumes considered	Type of value
G1	1	Global
V1	1	Voxel-based
V5	5	Voxel-based
BFA	As many as possible	Voxel-based

Tab. 7.2: Summary of the main features of the methods used to compute baseline.

Baseline values computed with four different methods							
Examination	Algorithm	Baseline			μ_ϵ		
		Mean (<i>HU</i>)	std (<i>HU</i>)	Range (<i>HU</i>)	Mean (<i>HU</i>)	std (<i>HU</i>)	Range (<i>HU</i>)
C1N23	BFA	58.7	2.1	15.2	3.86	0.66	5.5
	V1	59.3	5.3	37.0	5.23	1.98	15.3
	G1	59.3	–	–	4.23	0.81	5.7
	V5	58.6	2.8	19.2	4.08	0.75	5.8
C1N37	BFA	60.3	4.2	26.7	5.58	0.86	6.8
	V1	58.5	8.5	58.0	7.81	2.91	22.3
	G1	58.5	–	–	6.67	1.47	10.6
	V5	59.1	5.4	37.4	6.12	1.21	11.4
C1N38	BFA	64.7	3.0	16.4	3.74	0.94	6.7
	V1	66.4	5.1	34.0	4.92	2.03	14.1
	G1	66.4	–	–	4.73	1.20	8.2
	V5	64.4	3.4	20.8	3.94	0.97	6.7

Tab. 7.3: Baseline's and μ_ϵ 's mean, standard deviation, and range values obtained on the three examinations of Table 7.1 by using four different algorithms for the computation of baseline values.

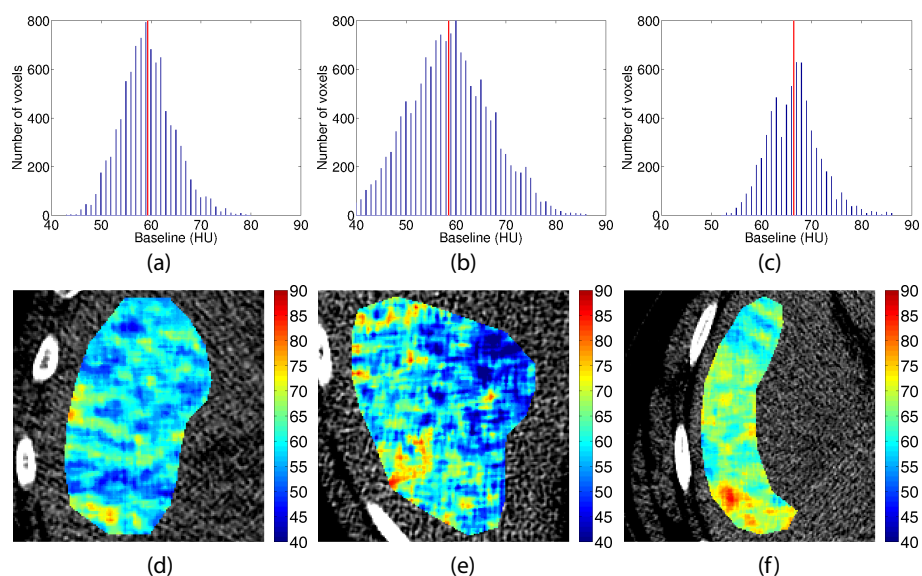


Fig. 7.26: Baseline histograms and colorimetric maps achieved with V1 and pertaining to examinations C1N23 (a,d), C1N37 (b,e), C1N38 (c,f). The red vertical line on histograms points out the mean baseline value of that examination.

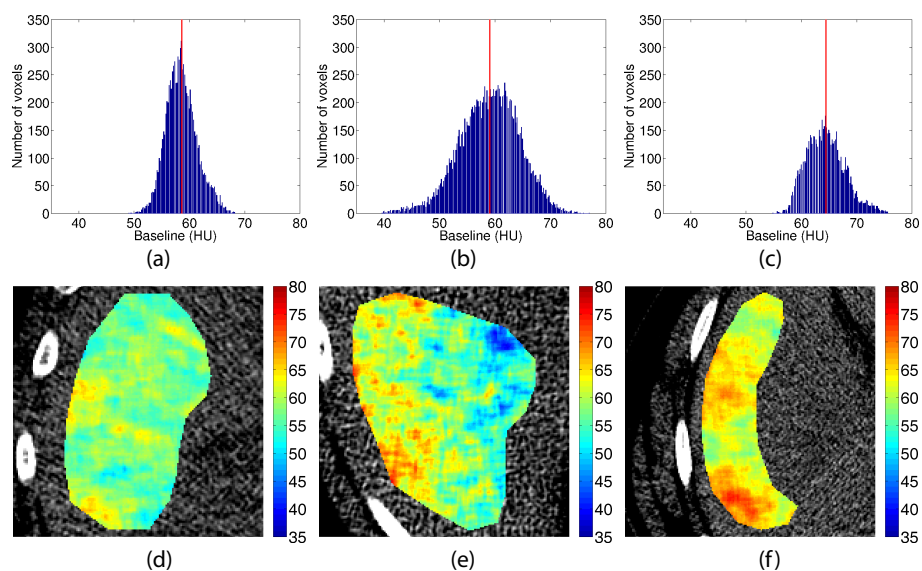


Fig. 7.27: Baseline histograms and colorimetric maps achieved with V5 for patients C1N23 (a,d), C1N37 (b,e), and C1N38 (c,f). The red vertical line on the histograms point out the mean baseline value.

integer-valued bins (as the density values inside CT images).

As one can see from Table 7.3, mean and standard deviation values of μ_ϵ are ever lower in BFA that is the algorithm computing baseline on the highest number of time instants of each TCC as possible. The second method in terms of goodness of baseline chosen is V5. Indeed, this algorithm that is voxel-based exactly as BFA, compute baseline values by averaging the first five density values assumed by the TCC, this resulting in a more robustness with respect to methods based on a single image only. Indeed, the highest values of μ_ϵ mean and standard deviation are assumed by V1 and G1 that compute baseline considering a single image only. In particular, V1 is the one showing the highest error index, since any averaging operations that could attenuate the influence of local noise and artefacts are not used.

Colorimetric maps of Figure 7.26 obtained with V1 are much less homogeneous than those obtained by using BFA in all the three examinations. Moreover, V1 baseline histograms of the three patients show a wider range with respect to the other methods (see Table 7.3). On the contrary, baseline values achieved with V5 are more similar to those obtained with BFA. Indeed, colorimetric maps are much more homogeneous than those achieved with V1, even though a lower local variability can be noted, with respect to those obtained with BFA, mainly due to the lower number of points considered. Greatest differences between neighbouring baseline values are most of all visible in examination C1N37. As expected, also the range of baseline values achieved with V5 is intermediate between those obtained with V1 and BFA. The histograms' range values is related to colour content found in perfusion maps. Indeed, the greatest difference of baseline range values computed with V5 and BFA is visible in the examination C1N37 (*i.e.*, the one showing the highest local colour differences for the baseline values computed with V5).

Since BFA has shown to be the best method to compute baseline values, differences between results achieved using the proposed algorithm and the other three methods have been computed in each voxel for the three examinations. Histograms of absolute differences between baseline values achieved with BFA and the methods used in the literature are reported in Figure 7.28. As one can see, average differences increase according to the value of μ_ϵ computed.

The use of different methods to compute baseline value leads to different results that affect reliability of perfusion values computed. The two methods mainly used in the literature (V1 and G1) are those yielding the least correct baseline values. As regards V5, despite it allows achieving good results, differences with BFA can differ of even more than $5HU$. The use of voxel-based

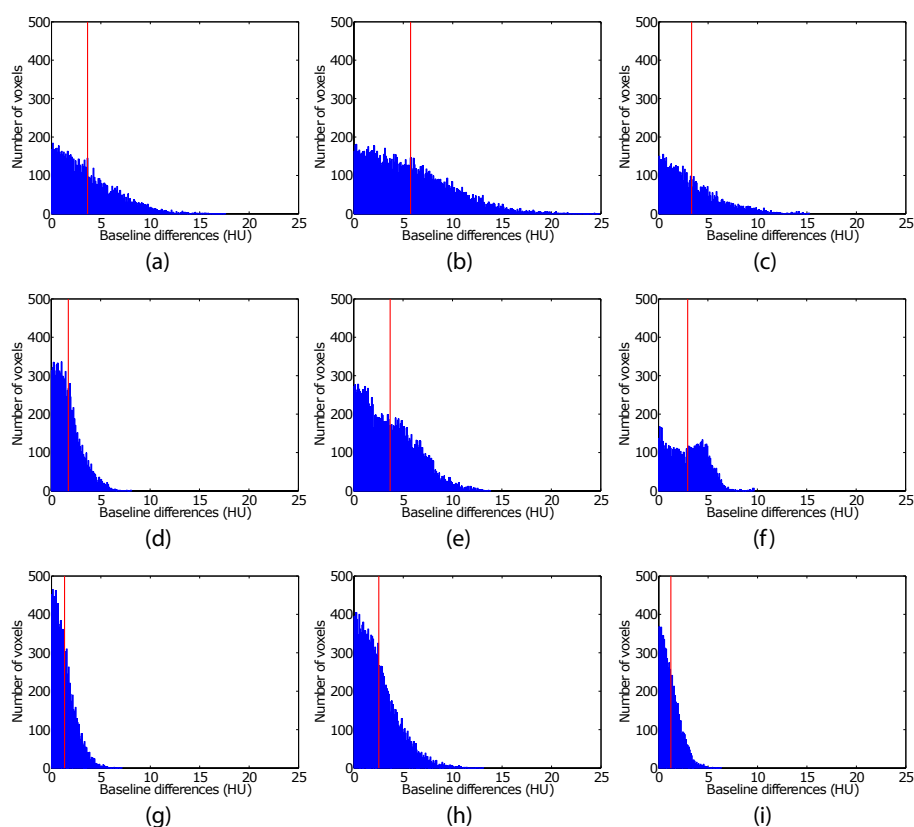


Fig. 7.28: Histograms of absolute differences between baseline values computed according to BFA and to V1 (first row), G1 (second row), and V5 (third row), referring to different examinations; from left to right: C1N23, C1N37, C1N38, respectively. Vertical red lines point out histograms mean value.

baseline values computed on the largest number of time instants is therefore highly suggested, in order to achieve the best perfusion results as possible.

7.3.4 Baseline values in a single Centre

In this section, the BFA algorithm has been applied referring to 40 examinations randomly chosen from Centre 1. One central section of each CTp sequence has been selected and a ROI has been drawn free-hand on the liver, following the modalities described in Sect. 7.1. ROIs area mean and standard deviation was of $23.18 \pm 10.3cm^2$. Voxel-based baseline values have been computed for each ROI and represented through the use of a colorimetric map. Mean, median, standard deviation, and range values have been computed for each patient.

Baseline values obtained in each examination together with their mean values are represented in Figure 7.29. Each data column represents one ex-

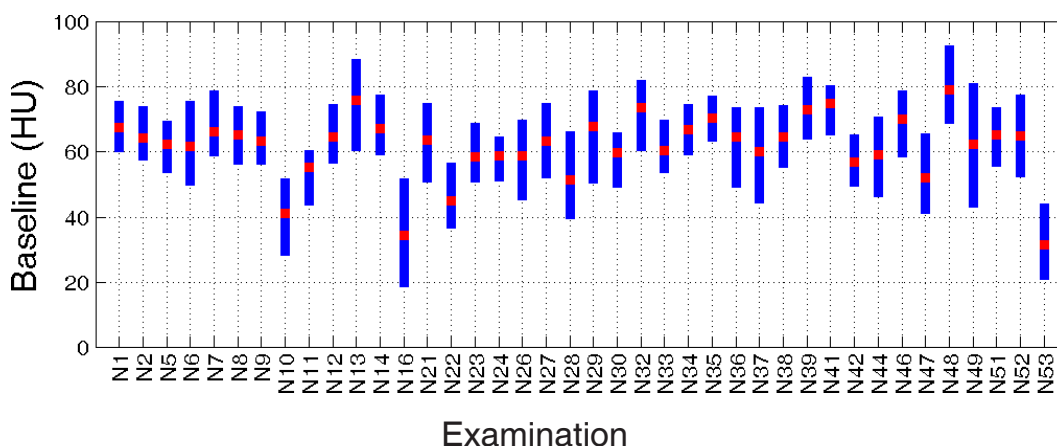


Fig. 7.29: Baseline bins of each examination, represented with blue dots, appearing like continuous blue lines. Red markers represent mean baseline values for each examination.

amination. The blue points composing each column represent the bin having non-zero values in the related histogram of baseline values. As one can see, range of baseline values of each examination are quite similar in almost all the examinations. Averaged baseline values under $40HU$ have been found in two examinations only and could point out presence of steatosis [296].

Averaged baseline values over all the examinations are resumed in Table 7.4

Baseline values in Centre 1			
Mean (<i>HU</i>)	Median (<i>HU</i>)	std (<i>HU</i>)	Range (<i>HU</i>)
61.7	63.6	10.1	32 – 79

Tab. 7.4: Mean, median, standard deviation, and range of baseline values achieved in 40 examinations of Centre 1 using BFA algorithm.

In the literature, normal mean density values for the liver have been measured through the use of unenhanced CT scans and are around $50 - 65HU$ [297]. Other works, extend their range value to $30HU - 70HU$ [290, 298, 299]. In a recent retrospective study involving 48 patients with normal liver who underwent two CT examinations carried out with two different CT scanners in less than one year [300], the mean liver density values measured ranged respectively from 9.6 to $63.2HU$ and from 20 to $77.2HU$. Therefore the mean values achieved for baseline in our study are compliant with values of normal liver reported in the literature. Consequently we can conclude that baseline values of normal liver of patients with CRC are compliant with values of normal liver in healthy subjects reported in the literature.

In Figure 7.30, the histogram of the absolute differences between mean and

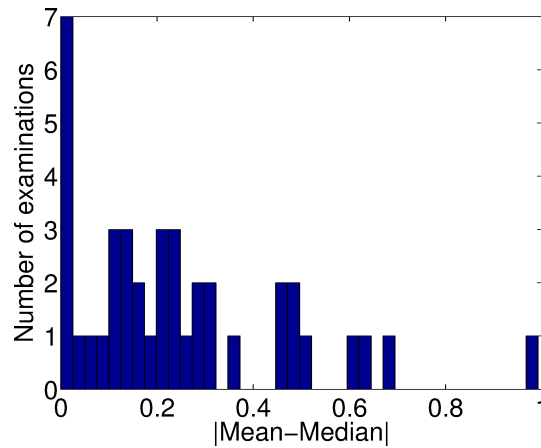


Fig. 7.30: Histogram of the absolute differences between mean and median baseline values of the various examinations.

median baseline values of the 40 examinations is shown. As one can see, mean and median baseline values are very similar in all the examinations (difference

values lay under $1HU$), this suggesting quite symmetric distributions (as those achieved in Sect. 7.3.3, Figure 7.25 (a), (b), (c)).

Finally, all the baseline colorimetric maps computed showed a high spatial correlation, this confirming preliminary results achieved in Sect. 7.3.3 (Figure 7.25 (d), (e), (f)). Indeed, presence of spatial coherence hints at local similarities of tissue features and at the goodness of the algorithms developed.

7.3.5 Multi-centre study of baseline values

In this section, a multi-centre study has been carried out on baseline values of examinations pertaining to 4 different Centres. Centre 8 was the one with the smallest number of patients that could be enrolled in the study since 10 of them had to be discarded. Indeed, in 6 examinations some DICOM files were missed, in 2 examinations a different acquisition protocol from the one agreed in PIXEL (Sect. 6.1) was followed, and two more patients developed liver metastases within three years from the CTp examination. Finally, 10 examinations remained available in Centre 8 and, in order to have a fair comparison between Centres, the same number of patients was selected in the other three Centres as well. 40 examinations (10 from each Centre) were chosen on the whole that met the criteria discussed in Sect. 7.1.

Tissue ROIs were drawn on each examination following the method discussed in Sect. 7.1. Baseline values of each examination were computed by using the BFA algorithm described in Sect. 7.3.2 and represented through the use of a colorimetric map. Baseline mean, median, standard deviation, and range values were computed for each examination. One-way ANOVA ($p\text{-value} \leq 0.05$) was applied to check for differences of mean baseline values among Centres.

ROIs area mean and standard deviation values in Centres 1, 8, 16, and 17, were of $20.1 \pm 6.0cm^2$, $25.9 \pm 7.6cm^2$, $22.3 \pm 7.0cm^2$, $21.7 \pm 8.7cm^2$, respectively. Baseline mean, median, standard deviation, and range values computed for each Centre are resumed in Table 7.5. Again, as occurred in the single-centre study discussed in Sect. 7.3.4, baseline values of patients with CRC found in these 4 Centres are compliant with values of normal liver reported in the literature [297, 290, 298, 299, 300].

Histograms of the baseline values collected in each Centre are represented in Figure 7.31. As the first consideration, all the histograms are multimodal meaning that the baseline values can be arranged into groups. As one can see, Centre 8 is the one presenting the largest range of baseline values. By com-

Baseline values of 40 examinations acquired in 4 different Centres				
Centre	Mean (<i>HU</i>)	Median (<i>HU</i>)	std (<i>HU</i>)	Range (<i>HU</i>)
1	56.0	58.3	13.1	67.6
8	60.6	64.4	15.0	87.0
16	59.0	58.8	11.1	66.2
17	62.3	62.0	4.7	29.6

Tab. 7.5: Baseline mean, median, standard deviation, and range values in 40 examinations acquired in 4 different Centres.

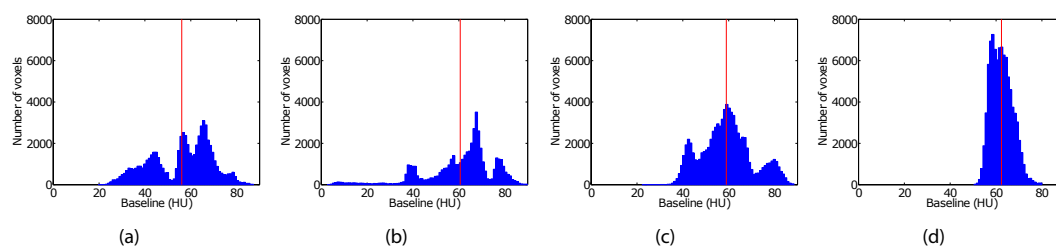


Fig. 7.31: Histogram baseline values referring to all the examinations of Centres 1 (a), 8 (b), 16 (c), 17 (d).

paring baseline ranges of the various Centres on the histograms, it is possible to note that in Centre 8 there are some baseline values that are very low with respect of those achieved in the other Centres. By deepening the analysis, I realized that these baseline values mostly pertained to one patient affected by liver steatosis (being his mean liver value $8.9HU$ lower than mean spleen value $21.6HU$ of more than $10HU$ [296]). Patients with this kind of disease were not excluded from PIXEL cohort and liver values of this examination were compliant with this type of pathology [301]. While histograms of Centres 1 and 16 show distributions with similar range, Centre 17 is characterized by a very narrow distribution (this is also confirmed by standard deviation value, that in Centre 17 is almost one third with respect to the other Centres).

As an example, in Figure 7.32 four baseline colorimetric maps pertaining

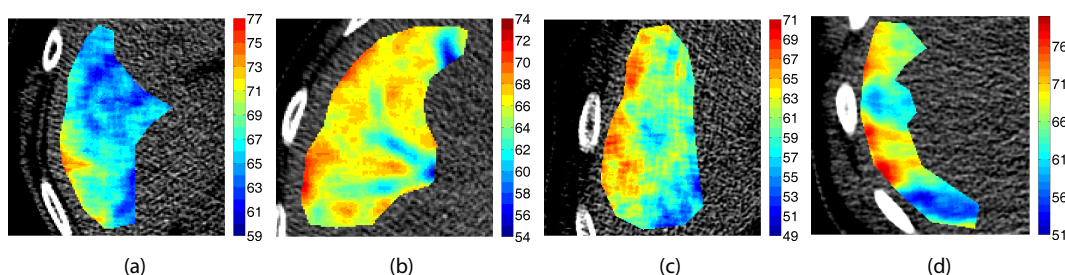


Fig. 7.32: Baseline colorimetric maps of Centres 1 (a), 8 (b), 16 (c), and 17 (d).

to examinations randomly chosen from Centres 1, 8, 16, 17, respectively, are shown. As one can see from Table 7.5, all the four Centres present statistically equivalent mean baseline values, as confirmed by one-way ANOVA. In addition, also in this multi-centre study, all the baseline colorimetric maps pertaining to the different Centres show a spatial local correlation, with quite gradual colour changes between different regions of the ROI. This spatial correlation reflects the local spatial coherence of tissue features. Moreover, since the baseline values obtained with our algorithm are computed in each voxel by using only data pertaining to one TCC, independently from the signal of the neighbouring voxels, the baseline local spatial homogeneity can be considered as a qualitative indicator of the algorithm goodness.

7.3.6 Concluding remarks

One of the first operation to perform a CTP study is the subtraction of baseline values from TCCs (Sect. 2.2). Therefore, the selection of a correct baseline value is of fundamental importance in order to achieve accurate perfusion results. In the literature, several methods to compute baseline values are presented, although no comparative studies decreeing the best method exist. However, no studies to evaluate which could be the best one have been carried out so far.

A novel algorithm to compute baseline values has been conceived to improve the methods used in the literature by considering as the highest number of data points as possible. The data analysis highlighted the effectiveness of this new method and its capability of providing better results if compared to the other methods. The use of our adaptive voxel-based approach method to compute baseline values is therefore highly suggested for all the liver CTP studies.

Moreover, the analysis carried out on patients of Centre 1 pointed out that the baseline values of normal liver in patients with CRC are compliant with values of normal liver reported in the literature for healthy subjects. This result was also confirmed in the examinations acquired in Centres 8, 16, 17. In addition, the outcome of statistical analysis carried out on baseline values obtained in the multi-centre study pointed out that the use of different CT scanners does not affect baseline values.

7.4 Computation of perfusion values

In several hepatic CTP studies, perfusion values obtained in cancer tissue have been compared with those computed on normal liver. However, in case of liver diseases, perfusion values are obtained on normal liver in often small tissue regions, just apparently free from pathology, without considering that the obtained results could somehow be influenced by the presence of occult metastases or by the pathology itself. In the next paragraphs, I refer to perfusion values computed on patients with CRC, but free from any hepatic disease. Patients who developed liver metastases within three years from CTP examination, or that might be affected by liver steatosis, were excluded from the study. Perfusion values obtained in patients of the same Centre (Sects. 7.4.1 and 7.4.2) and of four different Centres (Sects. 7.4.3 and 7.4.4), respectively, are compared with each other to assess whether the use of different CT scanners might affect perfusion parameters. Although in the literature the use of

dual vascular input is highly suggested, many works are still carried out by using a single vascular input. Here, all the measures presented are obtained by considering both single (Sects. 7.4.1 and 7.4.3) and dual (Sects. 7.4.2 and 7.4.4) vascular input. Some concluding remarks are finally reported in Sect. 7.4.5.

7.4.1 Single input BF values in normal liver

In this first study, perfusion values have been computed in all the examinations of Centre 1, on patients with healthy liver that did not developed metastases. In addition, in order to ensure nominally more homogeneous values, I excluded two patients with proved liver steatosis and one not-well defined circular formation. In three more cases, CTp acquisition was not centred on liver and perfusion analyses were not possible. Three more examinations were finally discarded since artefacts were too heavy. Altogether, 14 examinations were excluded from the study and 57 patients were finally considered.

ROIs were drawn in each examination following the same criteria used in Sect. 7.1. A single central section was selected and a ROI was drawn on the liver, avoiding big vessels. BF was computed in each voxel of the ROI through the use of the SIMS. BF values were shown through the use of colorimetric maps and their mean and standard deviation values were computed for each patient. Mean, median, standard deviation, and interquartile range (IQR) of all mean BF values were finally computed.

Mean of ROIs' area was of $22.3 \pm 12.1 \text{cm}^2$. BF values of each examination together with their mean values are shown in Figure 7.33. Each column of data is representative of one examination. The blue data of each column represent the bin having non-zero values in the related histogram of BF values. The other statistical parameters are resumed in Table 7.6.

Single input perfusion parameters in normal liver					
Perfusion parameter	Unit of measure	Mean	Median	std	IQR
BF	$ml/min/100g$	34.3	32.5	13.1	14.6

Tab. 7.6: Mean, median, standard deviation, and interquartile range values of mean BF values of the examinations of Centre 1.

Let us define the mean and the standard deviation of the BF mean values of each examination as m_{mBF} and s_{mBF} , respectively, and the mean and the

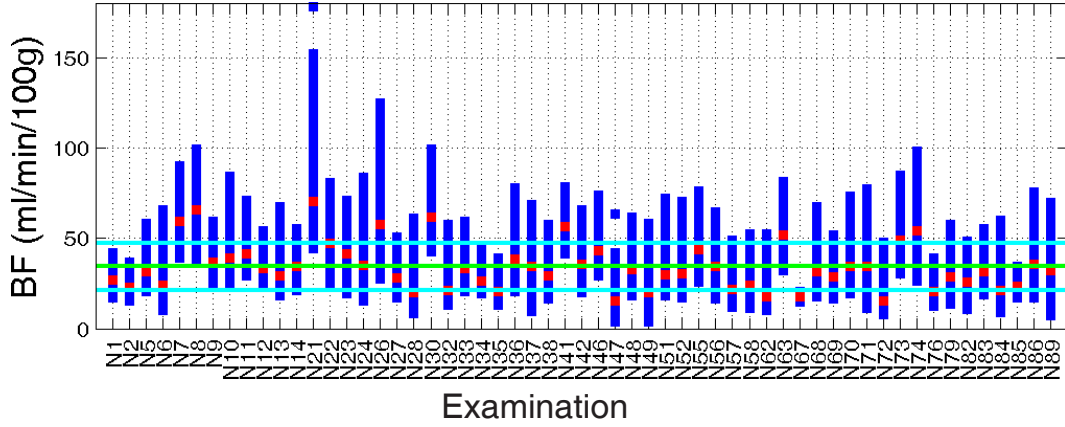


Fig. 7.33: Representation of BF values of each examination considered in Centre 1. Red markers represent mean BF values for each examination. Green horizontal line represents the mean BF values computed over all the examinations of Centre 1. Blue horizontal lines delimit the range between mean and one standard deviation of the BF values computed over all the examinations of Centre 1.

standard deviation of the BF standard deviation values of each examination as m_{sBF} and s_{sBF} , numbered from bottom to top, left to right, respectively. By calculating the two thresholds T_1 and T_2 as follows:

$$T_1 = m_{mBF} + s_{mBF} \quad (7.1)$$

$$T_2 = m_{sBF} + s_{sBF} \quad (7.2)$$

it is possible to classify the distributions of BF values in four different groups (Figure 7.34). The former represents most of the examinations (76%) while the other three only a minority of cases. The first group includes all the examinations having a BF mean value lower than T_1 and a BF standard deviation value lower than T_2 (these examinations are represented in the green colour in Figure 7.34). C1N1 and C1N32 are two examples of examinations pertaining to this group and having different distributions of BF values. Indeed, as one can see from Figure 7.35, both the examinations are characterized by a Gaussian-like distribution of BF values, but while the histogram of C1N1 (Figure 7.35 (a)) is symmetric, that of C1N32 (Figure 7.35 (c)) has a long-right tail. The high perfusion values of this tail pertain to the highly perfused region in the middle-upper portion of the ROI (Figure 7.35 (d)), possibly due to the presence of a vessel. However, by excluding this highly perfused region (Fig-

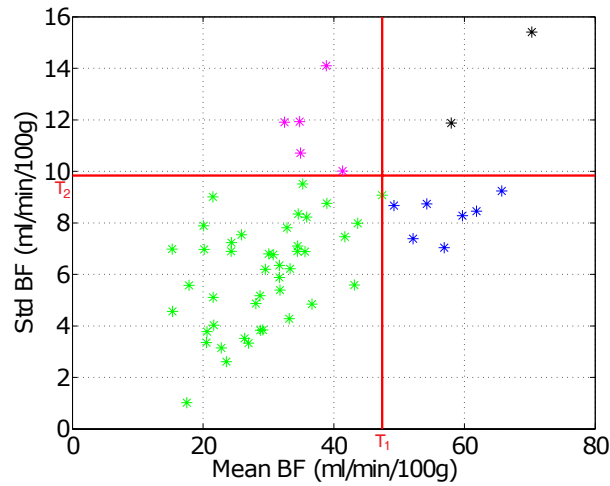


Fig. 7.34: Scatter of mean and standard deviation BF values. Red vertical and horizontal lines represent the threshold values T_1 and T_2 used to subdivide the four groups of examinations, respectively.

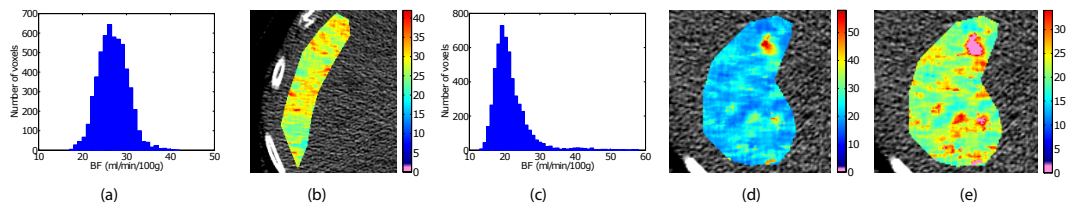


Fig. 7.35: Histograms and BF colorimetric maps of examinations C1N1 (a,b) and C1N32 (c,d). In (e) the colorimetric map of C1N32 after the exclusion of BF values higher than 35HU.

ure 7.35 (e)), one can see that tissue is heterogeneously perfused with BF values varying from 10 to $35\text{ml}/\text{min}/100\text{g}$. The colorimetric maps of Figure 7.35 (b) and (e) are representative of normal liver functional features, showing gradual spatial variations from low to high perfusion values, this hinting at the coexistence of alternating adjacent high and low vascularized regions. The same heterogeneous coarse texture is visible in all the examinations of Centre 1.

The second group (represented in Figure 7.34 by the markers in the magenta colour) collects the examinations having a low BF mean (less than T_1) value, but a high BF standard deviation (above T_2). In Figure 7.36, two rep-

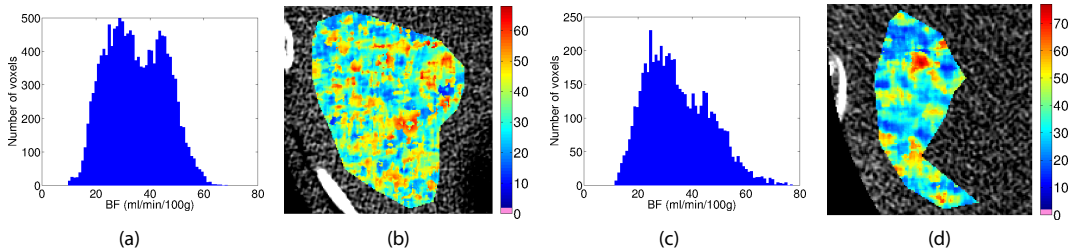


Fig. 7.36: Histograms and BF colorimetric maps of examinations C1N37 (a,b) and C1N71 (c,d).

representative examples of examinations pertaining to this category are reported. As one can see, both the histograms of Figure 7.36 (a), (c) are bi-modal. Also in this group of examinations, the tissue is still composed by both high and low vascularized regions. However, despite the presence of local perfusion correlation between neighbouring voxels (Figure 7.36 (b), (d)), the spatial transitions between low and high BF values are sharper with respect to those found in the first group of examinations, this causing a lack of voxels with medium perfusion values and the bi-modality of the relative histograms, accordingly. Of course, the symmetry of the BF histograms strictly depends on the percentage of the area of the two regions composing the tissue. Indeed, while in C1N37 the area of the tissue showing the highest perfusion equals that of the regions with the lowest perfusion, this causing a sort of histogram symmetry (Figure 7.36 (a)), in C1N71 the regions lowly perfused are predominant and this is reflected in the histogram shape that is heavily right skewed (Figure 7.36 (c)). For the sake of completeness, the right tale (perfusion values higher than $65\text{ml}/\text{min}/100\text{g}$) is constituted by the voxels of the vessel present in the middle-upper portion of the ROI.

The third group (represented in the blue colour in Figure 7.34) is that collecting examinations having a high mean BF (higher than T_1) and a low BF standard deviation (lower than T_2). In Figure 7.37, two representative

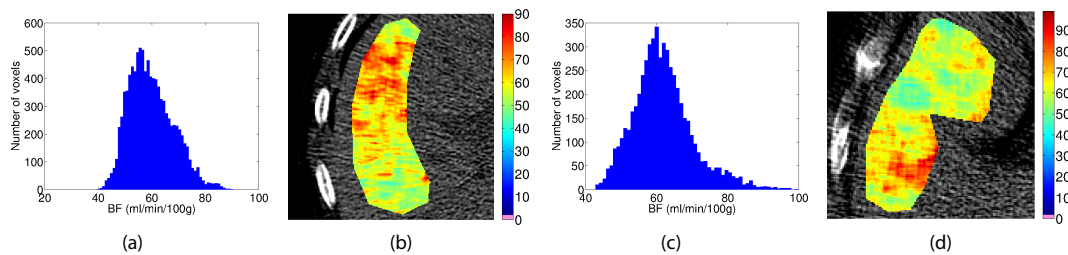


Fig. 7.37: Histograms and BF colorimetric maps of examinations C1N7 (a,b) and C1N30 (c,d).

examinations (C1N7 and C1N30) pertaining to this category are reported. As one can see, the tissue of these examinations results to be more perfused than those found in the previous groups. The histograms (Figure 7.37 (a), (c)) are both Gaussian-like and present just light right tails, this meaning that a great portion of the tissue analysed is characterized by high perfusion values. Indeed, differently from examinations C1N32 and C1N71, where the voxels presenting the highest perfusion values are grouped in one small connected region, in the colorimetric maps of C1N7 and C1N30 (Figure 7.37 (b), (d)), the high perfusion values are distributed on extended connected areas. Therefore, in this case, the very high perfusion values are not ascribable to the presence of a vessel, but rather to the intrinsic features of the tissue analysed which is highly vascularized.

Finally, the last category (represented in the black colour in Figure 7.34) include examinations having high BF mean and standard deviation values (higher than T_1 and T_2 , respectively). In this group, two examinations only have been included. Both C1N21 and C1N26 present a wide range of perfusion values, also including very high BF values (higher than $100\text{ml}/\text{min}/100\text{g}$). Their corresponding histograms (Figure 7.38 (a), (c)) have a Gaussian-like shape with a long right tale. The highest perfusion values (*i.e.*, those in the right tail of the histograms) are all collected in small connected regions of the colorimetric maps (Figure 7.38 (b), (d)), corresponding to quite big vessels.

In order to remove unreliable perfusion values caused by the presence of vessels, artefacts, and noise, the triangle method has been applied to threshold

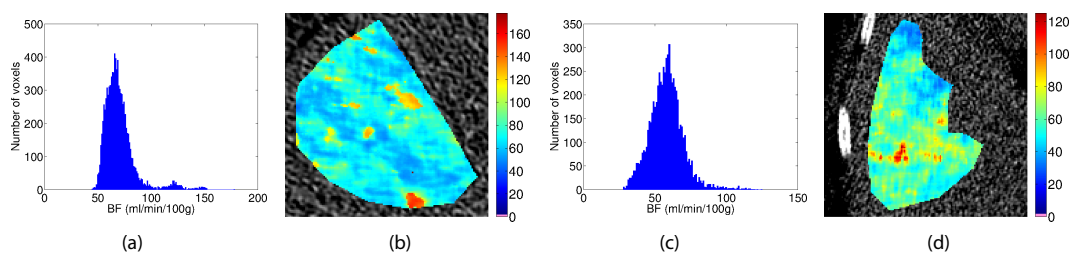


Fig. 7.38: Histograms and *BF* colorimetric maps of examinations C1N21 (a,b) and C1N26 (c,d).

the colorimetric perfusion maps of each examination. The distributions of perfusion values obtained for each examination after applying thresholding are represented in Figure 7.39. As one can see, comparing it with Figure 7.33,

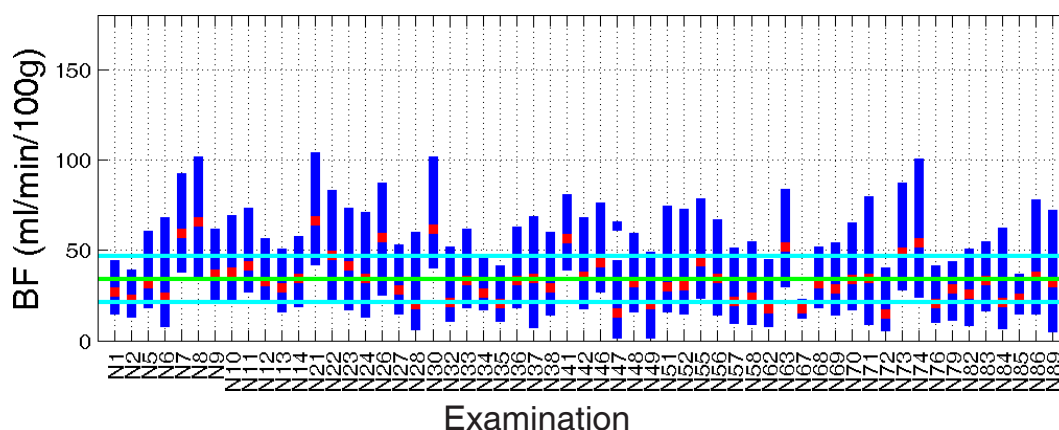


Fig. 7.39: Representation of *BF* values of each examination considered in Centre 1 after thresholding. Red markers represent mean *BF* values for each examination. Green horizontal line represents the mean *BF* values computed over all the examinations of Centre 1. Blue horizontal lines delimit the range between mean and one standard deviation of the *BF* values computed over all the examinations.

BF values distributions of most of the examinations are practically unchanged after thresholding, since characterized by very low fitting errors. Nonetheless, in other examinations, such as C1N21 and C1N26, the highest perfusion values are mainly attributable to the presence of vessels and the effects of thresholding become clearer and well visible in Figure 7.39. Figure 7.40 reports histograms and colorimetric maps of examinations C1N21 and C1N26 obtained after the

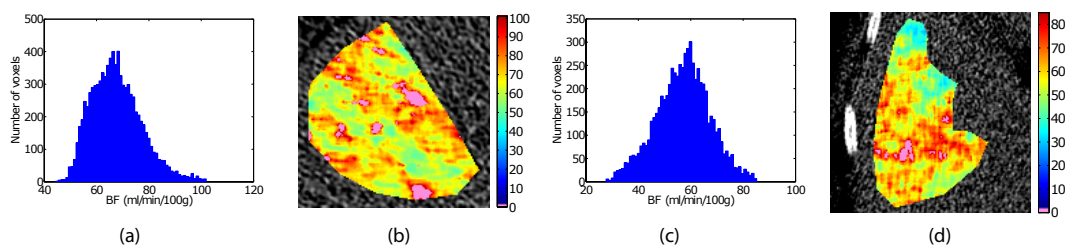


Fig. 7.40: Histograms and BF colorimetric maps of examinations C1N21 (a,b) and C1N26 (c,d) after thresholding.

application of thresholding method. As one can see, by comparing Figures 7.38 and 7.40 the right tale of the two histograms (Figure 7.38 (a) and (c)) heavily shrank and the typical liver heterogeneous texture found in the examinations of the other groups is now well visible (Figure 7.40 (b) and (d)).

Mean, median, standard deviation, and interquartile range values of all mean BF values of each examination are resumed in Table 7.7. As one can

Single input perfusion parameters in normal liver after thresholding

Perfusion parameter	Unit of measure	Mean	Median	std	IQR
BF	$ml/min/100g$	34.1	32.5	12.9	14.0

Tab. 7.7: Mean, median, standard deviation, and interquartile range values of mean BF values achieved after the application of the triangle method in the examinations of Centre 1.

see, the exclusion of unreliable perfusion values has yielded a moderate decrease of the statistical parameters resumed in Tables 7.6 and 7.7. Indeed, the exclusion from the analysis of the highest BF values (*e.g.* those related to the presence of vessels) causes the reduction of mean perfusion values, while the removal of the most unreliable BF values (both high or low) leads to a decrease of both standard deviation and interquartile range values. This can be noted also by looking at the histograms of mean and standard deviation of BF values of each examination before (Figure 7.41 (a), (c)) and after (Figure 7.41 (b), (d)) thresholding. In particular, after thresholding, both the histograms (Figure 7.41 (b), (d)) are narrower and with a higher concentration of data on the left side than those achieved without thresholding

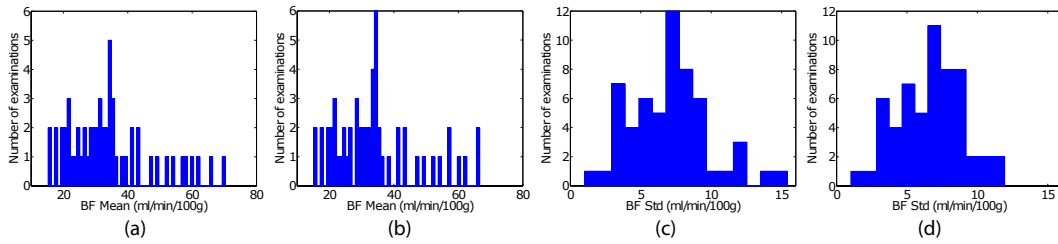


Fig. 7.41: Histograms of mean (a,b) and standard deviation (c,d) of BF values before (a,c) and after thresholding (b,d).

(Figure 7.41 (a), (c)), this causing a reduction of the distributions' mean, standard deviation, and interquartile range values. However, since examinations of Centre 1 were not particularly affected by high noise levels or the presence of artefacts and vessels, the application of thresholding causes only slight variations on the distributions of BF mean and standard deviation values and, consequently, the reduction of the overall statistical indexes (*i.e.*, those reported in Tables 7.6 and 7.7) can be considered negligible, although for single examinations they could be relevant.

7.4.2 Dual input BF values in normal liver

The same examinations and ROIs of Sect. 7.4.1 were also used to compute perfusion values considering a dual vascular input. In addition, a ROI was placed on the portal vein and on the spleen of each examination of Centre 1 (Figure 7.42). 22 examinations were excluded from the study since it was not possible to detect either the spleen or the portal vein. Indeed, spleen was not visible inside CT images of 17 examinations due to the too narrow FOV or to splenectomy (Figure 7.43 (a)), while in 5 more examinations the portal vein either the spleen were not visible because of the z level selected that was different from different from the one agreed (Figure 7.43 (b)). A total amount of 35 examinations were finally analysed. Voxel-based aBF , pBF , and HPI values were computed using the MSM and shown through the use of colorimetric maps.

aBF , pBF , and HPI were computed on each voxel of the tissue ROI. Mean and standard deviation values of these perfusion parameters were calculated for each patient. Distribution of aBF , pBF , and HPI values are represented in Figure 7.44. Mean, median, standard deviation, and interquartile range of

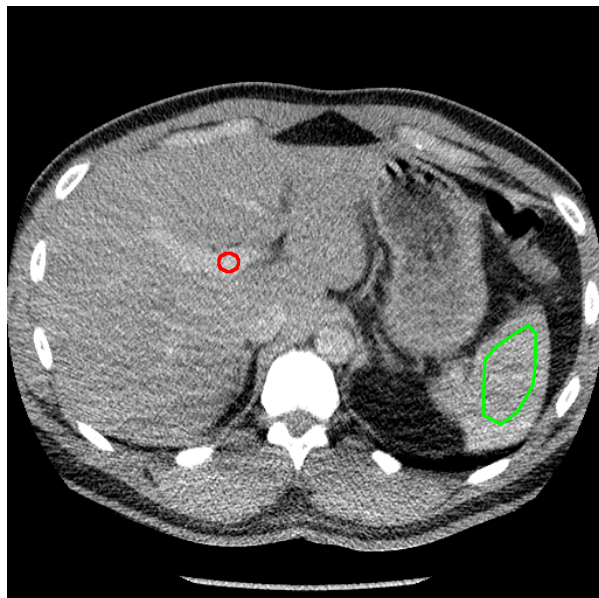


Fig. 7.42: ROIs placed on portal vein (in the red colour) and spleen (in the green colour), referring to examination C1N24.

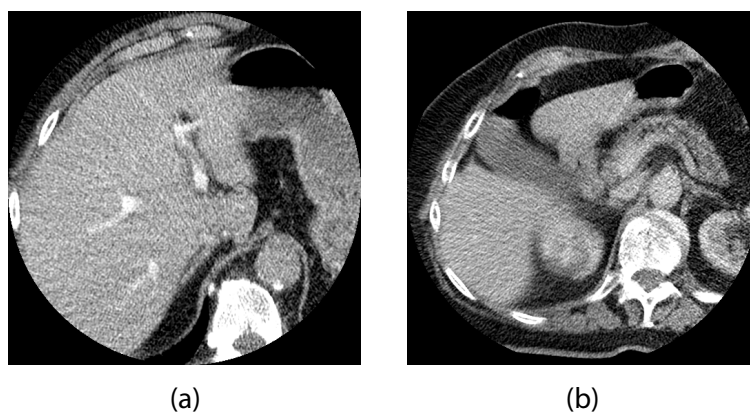


Fig. 7.43: CT images of examinations C1N21 (a) and C1N79 (b), excluded from dual input analysis due to the too narrow FOV and a wrong z level acquired, respectively.

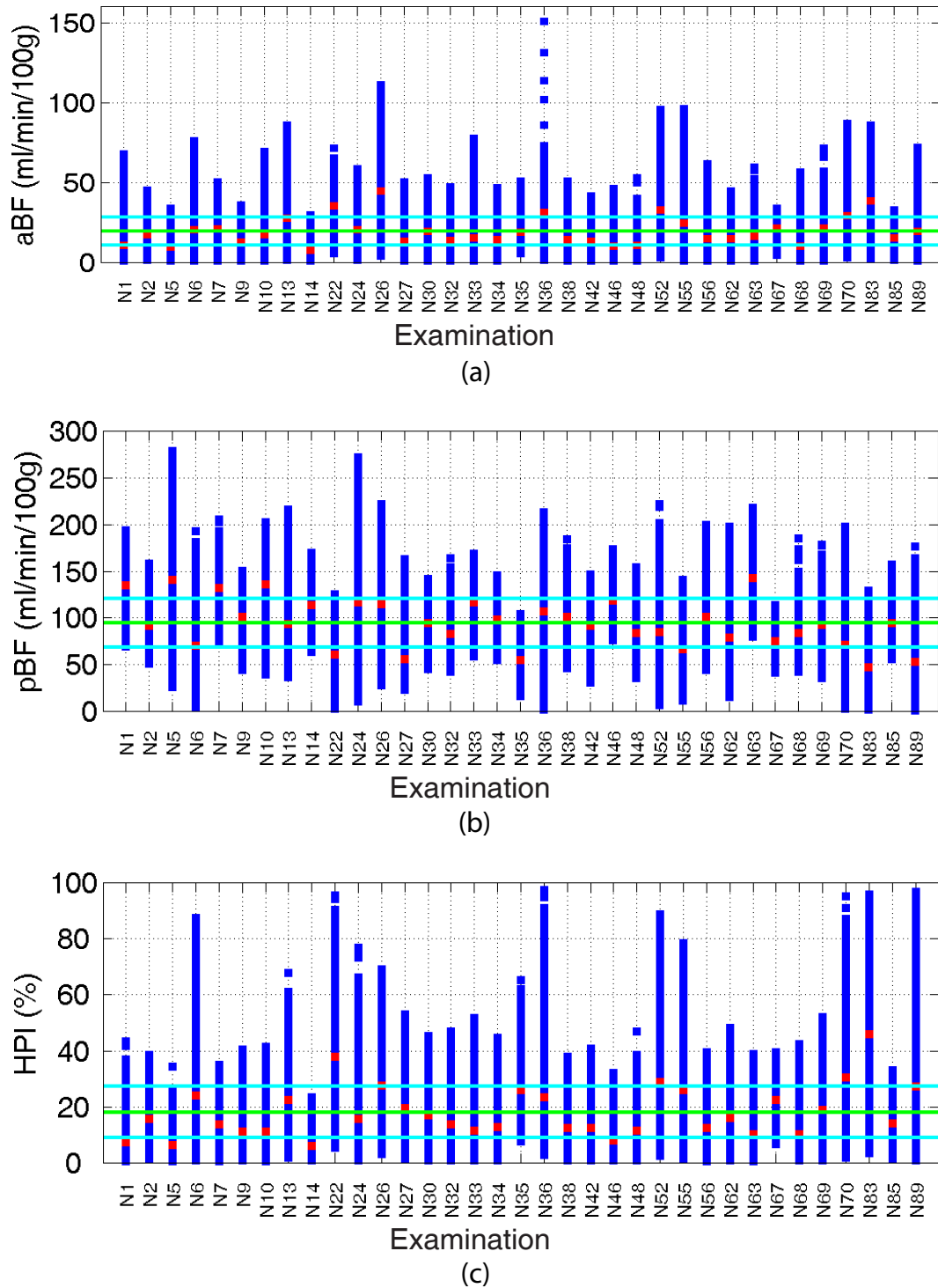


Fig. 7.44: aBF (a), pBF (b), and HPI (c) found in the examinations of Centre 1. Red markers represent mean BF values for each examination. Green horizontal line represents the mean BF values computed over all the examinations of Centre 1. Blue horizontal lines delimit the range between mean and one standard deviation of the BF values computed over all the examinations of Centre 1.

mean aBF , pBF , and HPI values were finally computed and are resumed in Table 7.8.

Dual input perfusion parameters in normal liver					
Perfusion parameters	Unit of measure	Mean	Median	std	IQR
aBF	$ml/min/100g$	19.4	17.3	8.8	8.0
pBF	$ml/min/100g$	94.4	93.6	26.6	37.3
HPI	%	18.0	15.7	9.1	12.1

Tab. 7.8: Mean, median, standard deviation, and interquartile range values of mean aBF , pBF , and HPI values found in the examinations of Centre 1.

In healthy subjects, the major part of blood is supplied to liver by the portal vein [302, 303]. The data shown in Table 7.8 and in Figure 7.44 highlight that this condition holds even in case of patients with CRC. Indeed, mean aBF is lower than mean pBF in all the examinations and consequently, the mean HPI assumes values always lower than 50%. However, as one can see by analysing the distributions of HPI (Figure 7.44 (c)), the local HPI values can also reach very high peaks, revealing the presence in some examinations of voxels characterized by a prevalence of arterial vascularization. Nonetheless, these examinations are all characterized by very wide range of HPI values. In fact, no examinations showing a narrow range (lower than the 70%) and containing very high HPI values (higher than 80%) exist. Therefore, generally, liver tissue is prevalently characterised by portal vascularization and in those cases where there are some tissue voxels mostly receiving blood from arterial circulation, they represent only a minority of cases. In Figure 7.45, is reported an examples of an examination having some voxels characterized by prevalent arterial vascularization. High local HPI values (Figure 7.45 (c)) are all grouped in continuous regions, mainly corresponding to those hypo-vascularized areas of pBF represented in the blue colour inside the corresponding colorimetric map (Figure 7.45 (b)). Therefore, despite the global prevalence of blood supply is portal, inside liver there can be adjacent regions receiving blood in different percentage from the aorta and the portal vein. This result is also supported by data found in the literature, which report HPI values in normal liver that are higher than 50% [229, 240, 304] and in some cases reach peaks of even more than 80% [240].

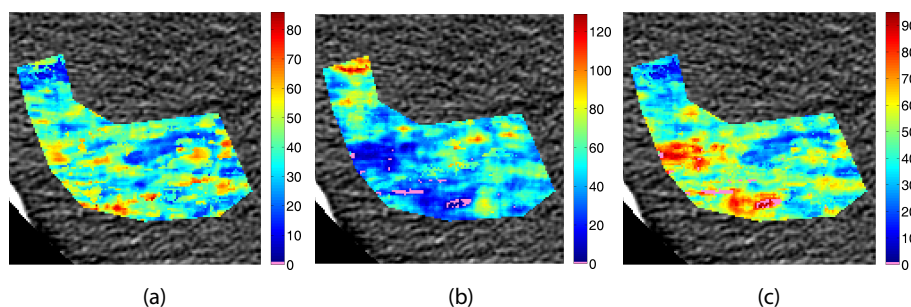


Fig. 7.45: Examples of aBF (a), pBF (b), and HPI (c) colorimetric maps, referring to patient C1N83 having very high HPI values.

The scatter plots of aBF and HPI mean and standard deviation values (Figure 7.46) point out that there is a relationship of direct proportionality be-

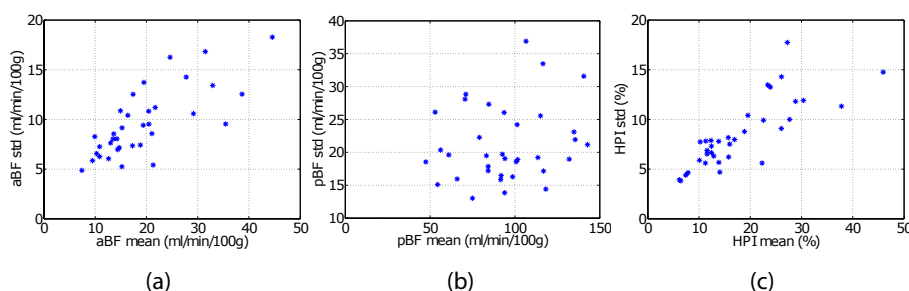


Fig. 7.46: Scatter of aBF (a), pBF (b), and HPI (c) mean and standard deviation values.

tween mean and standard deviation of these parameters, that is, aBF and HPI standard deviation are data dependent. In Figure 7.47, colorimetric maps of different examinations having low (Figure 7.47 (a)) and high (Figure 7.47 (b)) aBF mean and standard deviation values are reported. As one can see, the couple of colorimetric maps apparently show comparable distributions of perfusion values. However, by analysing the two maps from a quantitative point of view, it is possible to see that colours are split on completely different ranges and that consequently, resulting mean and standard deviation values are totally different. The same considerations can be drawn for the couple of HPI colorimetric maps of Figure 7.47 (c) and (d). Perfusion mean and standard deviation values for the colorimetric maps represented in Figure 7.47 are reported

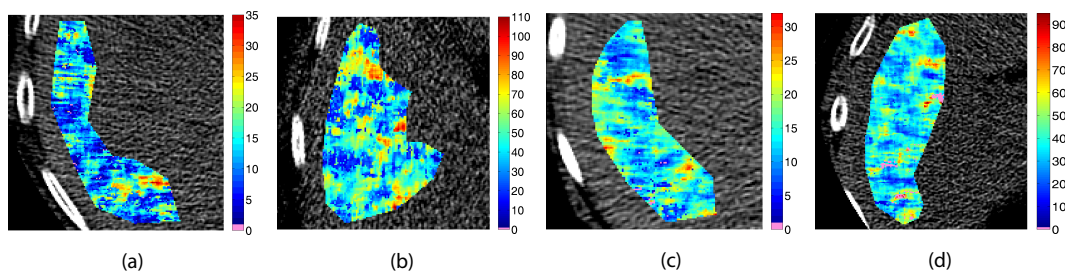


Fig. 7.47: aBF (a,b) and HPI (c,d) colorimetric maps pertaining to examinations having low (a,c) and high (b,d) mean and standard deviation values.

in Table 7.9.

Perfusion mean and standard deviation values					
Figure	Examination	Perfusion parameter	Unit of measure	Mean	std
7.47 (a)	C1N9	aBF	$ml/min/100g$	12.6	6.0
7.47 (b)	C1N26	aBF	$ml/min/100g$	44.6	18.3
7.47 (c)	C1N85	HPI	%	14.1	4.7
7.47 (d)	C1N22	HPI	%	37.8	6.2

Tab. 7.9: Perfusion mean and standard deviation values of maps represented in Figure 7.47.

As regards pBF , no relationships are present between its mean and its standard deviation values (Figure 7.46 (b)).

Now, let us apply the triangle method (Sect. 4.3) to aBF and pBF distributions of each examination to exclude unreliable perfusion values. The results obtained are reported in Figure 7.48 where the distributions of aBF , pBF , and HPI values of each examination are represented. Here, HPI values of each examination are taken into consideration only in those voxels where both aBF and pBF are considered as being reliable. As for BF values in the single input analysis, the most clear effects of triangle thresholding method are visible on the highest aBF and pBF values caused by the presence of noise, artefacts, and misleading anatomical structures (*i.e.*, vessels) that have been removed from the analysis. Meaningful examples are C1N1, C1N36 as regards aBF and C1N5, C1N24 for pBF . On the contrary, effects of thresholding are

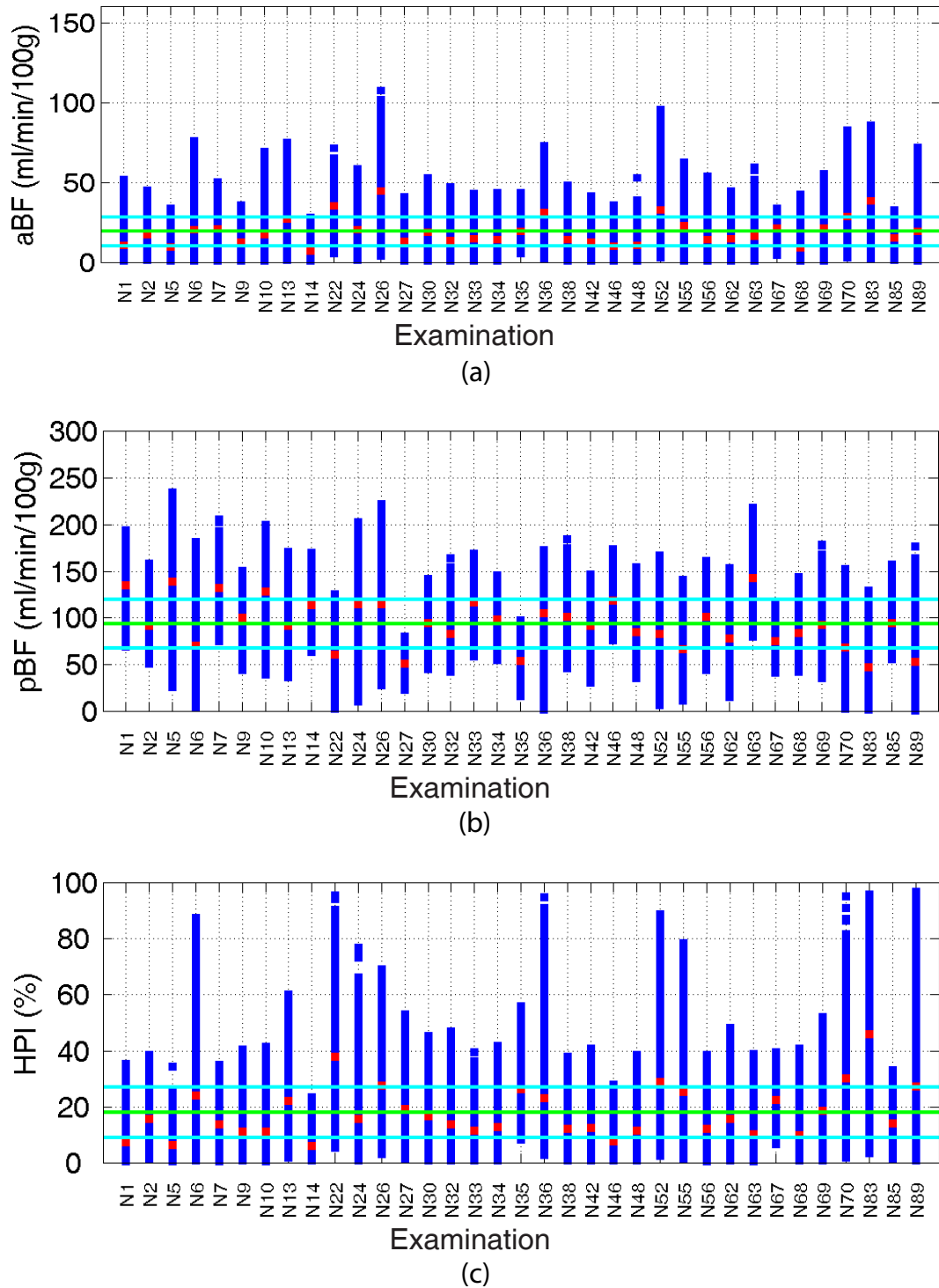


Fig. 7.48: *aBF* (a), *pBF* (b), and *HPI* (c) found in the examinations of Centre 1 after excluding the most unreliable perfusion values. Green horizontal line represents the mean *BF* values computed over all the examinations of Centre 1. Blue horizontal lines delimit the range between mean and one standard deviation of the *BF* values computed over all the examinations of Centre 1.

less evident on distribution of *HPI* values, although they can be better highlighted through the comparison of Figures 7.44 and 7.48 (*e.g.* see C1N13 and C1N70).

Mean, median, standard deviation, and interquartile range of mean *aBF*, *pBF*, and *HPI* obtained after the application of the triangle method are resumed in Table 7.10. Once again, global results collected after thresholding are

Dual input perfusion parameters in normal liver after triangle thresholding					
Perfusion parameters	Unit of measure	Mean	Median	std	IQR
<i>aBF</i>	<i>ml/min/100g</i>	19.2	17.3	8.9	8.1
<i>pBF</i>	<i>ml/min/100g</i>	93.6	92.7	26.3	37.6
<i>HPI</i>	%	17.9	15.7	9.1	12.0

Tab. 7.10: Mean, median, standard deviation, and interquartile range values of mean *aBF*, *pBF*, and *HPI* values found in the examinations of Centre 1 after the exclusion of the most unreliable perfusion values.

very similar to those of Table 7.8 obtained from the original data. Of course, this is not surprising, since these values come from global operators (*e.g.* mean or median) that flatten the differences.

7.4.3 Multi-centre study on single-input *BF* values

In this section, single-input *BF* values are computed on 40 examinations acquired in four different Centres. The aim of this multi-centre study is to evaluate whether and to what extent the use of different CT scanners may affect *BF* values in normal liver. To this purpose, patients free from liver diseases and who did not develop liver metastases within three years from CTp examination, were randomly selected from Centres 1, 8, 16, and 17. In order to carry out both a single-input (in this section) and a dual-input perfusion analysis (in Sect. 7.4.4), the 10 examinations selected from each Centre have both portal vein and spleen visible inside CT images.

A circular ROI has been drawn inside aorta and another one has been outlined on one section of the liver, following the same criteria adopted in Sect. 7.4.1. Voxel-based *BF* values have been computed for each examination by applying the SIMS method and shown through the use of colorimetric maps. Mean, median, standard deviation, and interquartile range have been

calculated for each Centre on the mean BF values of each examination. One-way ANOVA and Kruskal-Wallis tests ($p\text{-value} \leq 0.05$) have been applied to BF values of the four Centres to verify whether the use of different CT scanners could introduce variability on computation of the averaged perfusion values.

BF values distributions of each examination, together with their mean values, are represented in Figure 7.49. The black line highlighting BF mean

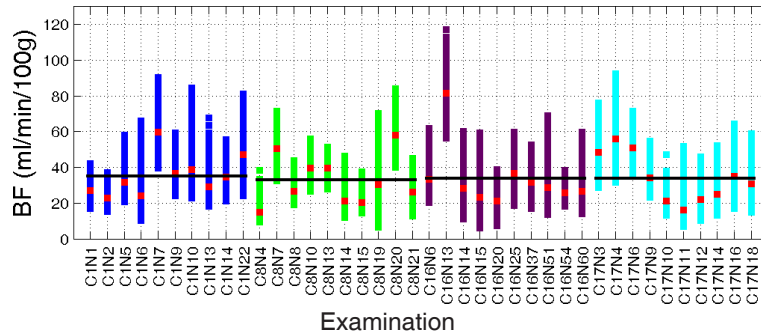


Fig. 7.49: BF values of each examination of Centres 1 (in blue), 8 (in green), 16 (in purple), and 17 (in cyan) are represented. BF mean value of each examination is highlighted with the red marker while the BF mean value obtained in each Centre is represented by the black line.

value over the 10 examinations of each Centre has nearly the same height in all the groups. Their values are reported in Table 7.11, together with median,

BF values of normal liver acquired in 4 different Centres

Centre	Mean ($mg/ml/100g$)	Median ($mg/ml/100g$)	std ($mg/ml/100g$)	IQR ($mg/ml/100g$)
1	35.2	33.1	11.3	10.9
8	32.8	28.5	13.9	17.4
16	33.8	28.5	17.3	6.9
17	34.0	32.4	13.7	22.2

Tab. 7.11: BF mean, median, standard deviation, and interquartile range of BF mean values achieved from the 40 examinations acquired in Centres 1, 8, 16, 17.

standard deviation, and interquartile range of each Centre. Median BF values of the four Centres are all lower than their means and less homogeneous. In fact, BF values histograms of each Centre are all right skewed, this pointing out

that in each group there is a greater number of examinations having BF value lower than the global mean value of the Centre. The highest standard deviation of BF values can be found in Centre 16, where examination C16N13 stands out from the others due to its particular high perfusion values. However, Centre 16 also shows the lowest BF interquartile range. Since standard deviation considers all data while the interquartile range ignores the outliers, such a low value of interquartile range points out that despite the presence of C16N13, perfusion results of Centre 16 are those with the lowest variability. For the sake of completeness, let us show the colorimetric map of examination C16N13. BF values of this examination are particularly high both with respect to the examination of Centre 16 and to those of the other Centres. However, as one can see from Figure 7.50 (a), functional tissue features of this examination

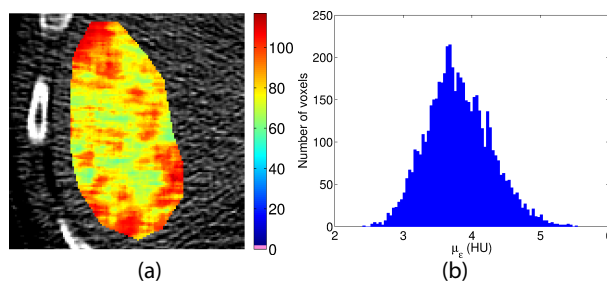


Fig. 7.50: BF colorimetric map (a) and μ_ϵ histogram of examination C16N13 (b).

does not differ from those described in Sect. 7.4.1 (*i.e.*, alternated adjacent regions characterized by low and high levels of vascularization). In addition, by analysing colour gradients inside BF colorimetric map (Figure 7.50 (a)) and the shape of the μ_ϵ values histogram (Figure 7.50 (b)), it emerges that the computed perfusion values are correct. Indeed, the local spatial coherence and the gradual variation from low to high adjacent perfusion values gives hint of a good quality of the map (Figure 7.50 (a)). As regards the histogram of μ_ϵ values (Figure 7.50 (b)), the very low range of the error values and their nearly normal distribution without right tails (that as described in Chapter 3 is typical of normal liver tissue not particularly affected by noise or by the presence of artefacts and vessels), prove that the achieved perfusion values have to be considered as being reliable since computed on reliable TCCs. The visual analysis of the CT image sequence also confirmed that no big vessels or artefacts were visible on tissue ROI. Therefore, the high perfusion values

found in C16N13 can be exclusively attributed to features of tissue, that in this patient results to be exceptionally vascularized.

In addition, I would like to bring reader's attention on the trend of BF values and distributions among sets of subsequent patient's IDs, that is possible to identify in Figure 7.49, especially for the examinations of Centre 17. As a matter of facts, patients ID have been assigned in this Centre according to increasing acquisition time, except for the first two examinations (since C17N3 has been acquired after C17N4, in the same day as C17N6). A possible motivation could be looked for a gradual change of acquisition parameters (also including CA administration), however there are not enough information to check it. Finally results of one-way ANOVA and Kruskal-Wallis tests confirm that differences between mean and median BF values in the four Centres are not statistically significant (p -value = 0.99 and p -value = 0.84, respectively).

This analysis has been repeated by applying thresholding triangle method to error data, but results remain the same and no appreciable changes can be detected.

7.4.4 Multi-centre study on dual-input BF values

Perfusion parameters of the same examinations used in Sect. 7.4.3 are computed by considering a dual vascular blood supply. ROIs have been drawn on the portal vein and on the spleen of each examination (see Sect. 7.4.2). aBF , pBF , and HPI have been computed for each patient as reported in Sect. 7.4.2. One-way ANOVA and Kruskal-Wallis tests (p -value ≤ 0.05) have been computed for data of the four Centres to verify whether the use of different CT scanners could introduce variability on dual input perfusion mean and median values respectively computed on healthy liver.

Figure 7.51 shows the distributions of aBF , pBF , and HPI values found in the various examinations. Examination C16N14 presents some aBF values higher than $130ml/min/100g$ (the highest one has value $493.9ml/min/100g$). These outlier values are caused by the presence of artefacts and noise that can be removed through the application of the triangle method (see Figure 7.52). In order to correctly visualize aBF distributions of all the examinations, the highest limit of the y axis has been fixed to $130ml/min/100g$.

In Table 7.12 mean, median, standard deviation, and interquartile range of aBF , pBF , and HPI found in each Centre are reported.

As one can see from both Figure 7.51 and Table 7.12, Centre 17 is the one showing the lowest inter-patient perfusion values dispersion (*i.e.*, in this

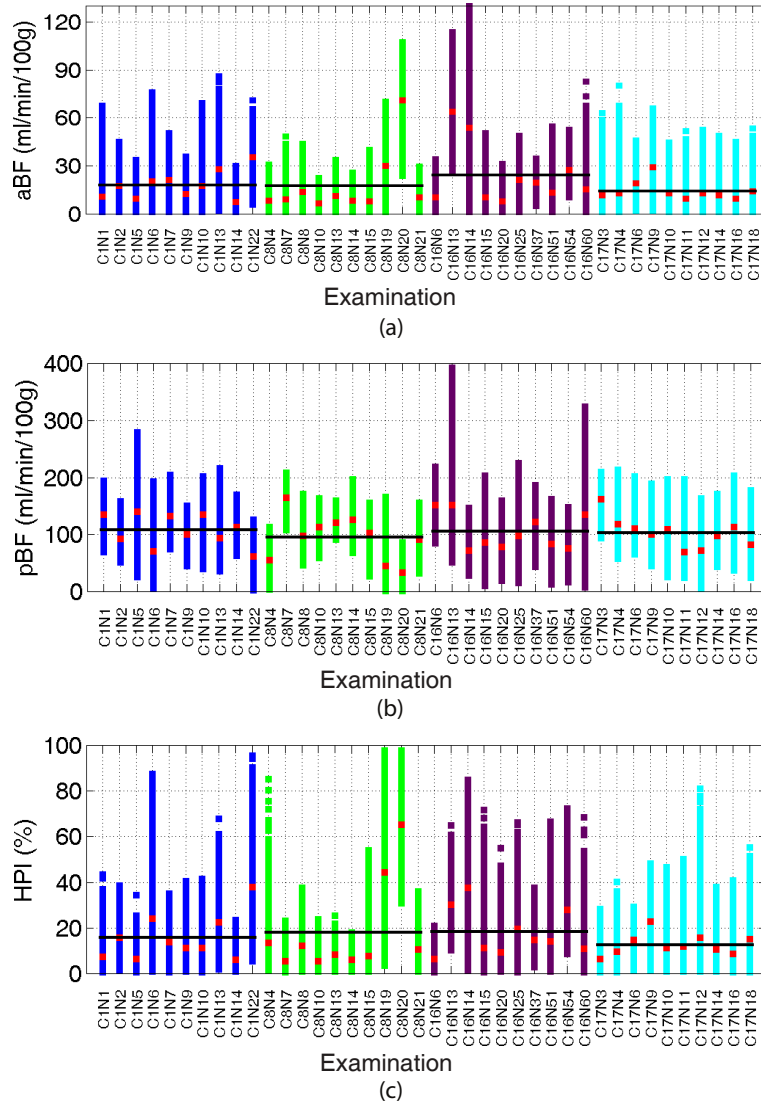


Fig. 7.51: *aBF* (a), *pBF* (b), and *HPI* (c) values of each examination of Centres 1 (in blue), 8 (in green), 16 (in magenta), and 17 (in cyan) are represented. *BF* mean value of each examination is highlighted with the red marker while the *BF* mean value obtained in each Centre is represented by the black line.

Dual input perfusion parameters in normal liver						
Centre	Perfusion parameters	Unit of measure	Mean	Median	std	IQR
1	<i>aBF</i>	<i>ml/min/100g</i>	18.0	17.3	8.7	9.6
	<i>pBF</i>	<i>ml/min/100g</i>	107.4	107.2	28.4	41.8
	<i>HPI</i>	%	15.6	12.6	9.9	12.5
8	<i>aBF</i>	<i>ml/min/100g</i>	17.6	9.8	20.0	4.7
	<i>pBF</i>	<i>ml/min/100g</i>	94.9	100.1	40.8	55.0
	<i>HPI</i>	%	17.9	9.4	20.3	6.7
16	<i>aBF</i>	<i>ml/min/100g</i>	24.3	17.5	19.3	15.1
	<i>pBF</i>	<i>ml/min/100g</i>	105.2	91.4	31.9	52.9
	<i>HPI</i>	%	18.2	14.5	10.4	14.9
17	<i>aBF</i>	<i>ml/min/100g</i>	14.3	12.7	5.9	2.3
	<i>pBF</i>	<i>ml/min/100g</i>	103.3	104.4	27.0	25.8
	<i>HPI</i>	%	12.6	11.5	4.6	5.3

Tab. 7.12: Mean, median, standard deviation, and interquartile range values of mean *aBF*, *pBF*, and *HPI* values found in the examinations of Centres 1, 8, 16, 17.

Centre distributions of aBF , pBF , and HPI in the various patients are more similar than in the other Centres), as shown by its lowest standard deviation and interquartile range values. On the contrary, when considering Centres 1, 8, and 16 only, Centre 8 is the one showing the highest standard deviation values. However, as regards aBF and HPI , Centre 8 is also the one showing the lowest interquartile range, this meaning that by removing the “most outlier” examinations (*e.g.* C8N19 and C8N20), the remaining ones show very similar perfusion mean values.

Also in this dual-input study, aBF results much lower than pBF in all the examinations, except for C8N20 showing HPI mean, median, and standard deviation of 65.3%, 66.6%, 13.9%, respectively. Despite these values could seem exceptionally high, such HPI values (of even about 77.9%) have been already found in the literature for patients with CRC, free from liver metastases and steatosis [304]. However, the presence of this exception does not affect global HPI values of the Centre whose median value is the lowest one and whose mean value is very low (17.9%), compliant with those values found in the literature [305].

Results of both one-way ANOVA and Kruskal-Wallis tests point out that differences between perfusion parameters obtained in different Centres are not statistically significant for all the perfusion parameters analysed. p -value obtained for aBF , pBF , and HPI using the two statistical tests are resumed in Table 7.13.

Summary of p -value		
Perfusion parameter	One-way ANOVA	Kruskal-Wallis
aBF	0.50	0.29
pBF	0.84	0.92
HPI	0.74	0.49

Tab. 7.13: Summary of p -value obtained for One-way ANOVA and Kruskal-Wallis tests applied on dual-input perfusion values.

In order to remove the most unreliable perfusion values possibly affecting the accuracy of perfusion results, the triangle thresholding method have been applied to data. Distributions of aBF , pBF , and HPI values are shown in Figure 7.52. Mean, median, standard deviation, and interquartile range values obtained after removing unreliable results are resumed in Table 7.14. As seen

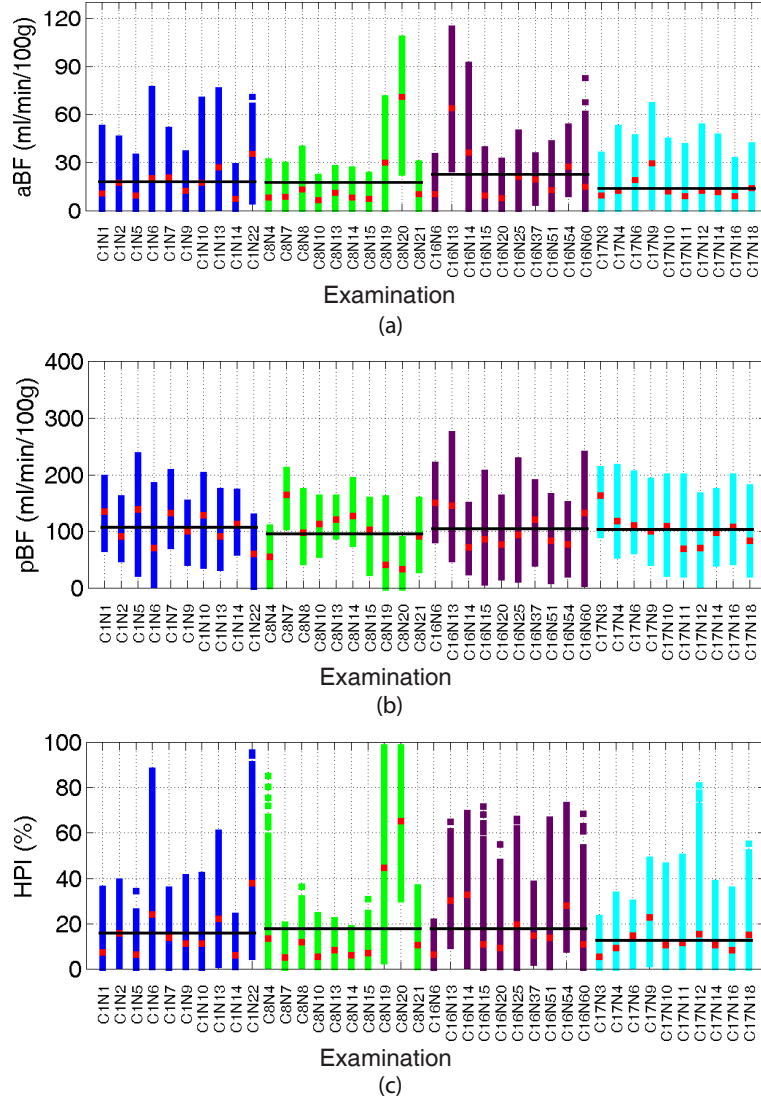


Fig. 7.52: *aBF* (a), *pBF* (b), and *HPI* (c) values obtained after the application of the triangle thresholding method for each examination of Centres 1 (in blue), 8 (in green), 16 (in magenta), and 17 (in cyan) are represented. Mean values of each examination are highlighted with the red marker while the mean value of each Centre is represented by the black line.

Dual input perfusion parameters in normal liver						
Centre	Perfusion parameters	Unit of measure	Mean	Median	std	IQR
1	<i>aBF</i>	<i>ml/min/100g</i>	17.8	17.3	8.6	9.7
	<i>pBF</i>	<i>ml/min/100g</i>	106.3	107.1	27.7	39.3
	<i>HPI</i>	%	15.6	12.6	10.0	12.4
8	<i>aBF</i>	<i>ml/min/100g</i>	17.5	9.6	20.1	4.7
	<i>pBF</i>	<i>ml/min/100g</i>	94.6	100.3	41.3	55.0
	<i>HPI</i>	%	17.7	9.4	20.4	6.8
16	<i>aBF</i>	<i>ml/min/100g</i>	24.0	17.3	19.0	15.1
	<i>pBF</i>	<i>ml/min/100g</i>	103.8	89.8	30.5	51.2
	<i>HPI</i>	%	18.1	14.3	10.3	15.0
17	<i>aBF</i>	<i>ml/min/100g</i>	13.9	12.2	6.2	3.5
	<i>pBF</i>	<i>ml/min/100g</i>	102.8	104.0	26.9	23.5
	<i>HPI</i>	%	12.3	11.0	4.8	5.4

Tab. 7.14: Mean, median, standard deviation, and interquartile range values of mean *aBF*, *pBF*, and *HPI* values found in the examinations of Centres 1, 8, 16, 17 after thresholding most unreliable perfusion values.

in the previous sections, removing unreliable values just bring a little variation of global perfusion values, in this case within absolute values lower than 1.5%. However, more evident improvements can be appreciated in the distribution of perfusion values achieved for each examination. For instance, the examination C16N14 first characterized by *aBF* values higher than $200\text{ml}/\text{min}/100\text{g}$, after thresholding shows *aBF* values lower than $100\text{ml}/\text{min}/100\text{g}$.

By analysing the global results collected in Table 7.14, it is possible to note that, once again, Centre 17 is that characterized by the lowest standard deviation and interquartile range values, while Centre 8 is that showing the highest standard deviation value and the lowest *aBF* and *HPI* interquartile ranges (if considering Centres 1, 8, and 16 only).

Despite the removal of unreliable perfusion values, examination C8N20 still presents a prevalently arterial vascularization (*HPI* value higher than 50%), this confirming that this feature is attributable to tissue features only, and not to computing errors introduced by the high presence of noise or artefacts.

p-value of *aBF*, *pBF*, and *HPI* obtained by applying one-way ANOVA and Kruskal-Wallis tests to respectively verify whether mean and median of

perfusion values could show any inter-Centre variations are resumed in Table 7.15. The statistical analysis carried out on thresholded data confirms the

Summary of <i>p-value</i>		
Perfusion parameter	One-way ANOVA	Kruskal-Wallis
<i>aBF</i>	0.61	0.25
<i>pBF</i>	0.86	0.91
<i>HPI</i>	0.75	0.48

Tab. 7.15: Summary of *p-value* obtained for One-way ANOVA and Kruskal-Wallis tests applied on dual-input perfusion values after thresholding the most unreliable perfusion values.

results obtained by the same tests applied to the original data. Indeed, as one can see, no statistically significant differences have been highlighted between Centres. *p-value* are very similar to those obtained on non-thresholded data. The highest variation between *p-value* can be noted for the tests applied on *aBF* that consequently, can be considered as the perfusion parameter mostly affected by presence of noise, artefacts and vessels inside the tissue analysed.

7.4.5 Concluding remarks

Several CTP studies compute perfusion values on healthy tissue in order to have a reference point. However, frequently these studies get these reference values on few patients, often from a small tissue region of liver considered as being normal. In addition, the liver of these patients are often affected by pathologies, even tumours, that are not excluded to possibly affect normal tissue. Accordingly, these *BF* values could not be appropriate as a reference. On the contrary, results reported in Sects. 7.4.1 and 7.4.2 have been computed on a wide set of patients free from any liver pathologies and by considering in each examination as the widest tissue regions as possible. Therefore, these results represent an important landmark for all the future hepatic single- and dual-input perfusion studies using healthy tissue as a reference point.

Finally, as regards the two CTP studies that have been carried out in Sects. 7.4.3 and 7.4.4, the outcomes are definitely encouraging. Indeed, results obtained in four Centres of PIXEL on examinations acquired by using different CT scanners, but same acquisition protocol and parameters are directly comparable. Therefore, these results create a fast track for the set up of further

multi-centre studies that represent the first step to permit CTP to be adopted in clinical routine. The development of further studies, comparing a higher number of examinations, acquired with other different CT scanner models, but with the same acquisition protocol, would indeed confirm the capability of CTP to provide reproducible results. After that, further multi-centre studies investigating CTP capability of providing diagnostic and prognostic information would allow moving forward a definitive decision regarding the usefulness of this technique.

Chapter 8

Conclusions

Lung and liver cancers are the most common causes of tumour death. Several steps forward have been done in cancer care through the introduction of anti-angiogenic therapies, but the lack of techniques to be used in the standard clinical practice to early assess their efficacy is an obstacle to make the most of their usage. This Thesis addresses CTP, one of the most promising techniques for the earlier assessment of the efficacy of the anti-angiogenic therapies. Despite CTP can provide fundamental functional information regarding both tumour diagnosis and prognosis, some open issues still exist that prevent its use in the standard clinical practice. This Thesis aims at filling in some gaps so as to advance CTP technique towards ordinary use in oncology. The most relevant achievements can be summarized as follows:

- methods and indexes to detect unreliable CTP perfusion values
- assessment of the clinical representativeness of the global averaged perfusion values
- tentative guidelines to set up a multi-centre CTP study
- signal processing algorithms to improve accuracy of perfusion values
- comparison of perfusion results of examinations carried out in different Centres

First, a method conceived and realized to automatically detect and exclude from perfusion analysis those unreliable perfusion values associated to the presence of noise, artefacts, vessels, and bronchi has been validated. The advantage brought by using this method over the classical manual approach is twice. The first is the huge amount of time saved by radiologists, due to

the automation of the post-processing stage. Besides that, this method allows detecting those structures affecting perfusion results which are missed by radiologists, or at least allows determining their correct extent. It is also worth noting that our results confirm that removing unreliable perfusion values yield a significant improvement on the accuracy of perfusion results, and of clinical assessment, accordingly.

As regards the representativeness of the global perfusion values, often used in CTP studies to achieve a higher reproducibility, a deep analysis has been carried out. The results of statistical tests combined with the evaluation of a specific statistical index used to assess the degree of perfusion heterogeneity, highlighted that global perfusion values cannot be appropriate for therapy assessment, since they disregard the heterogeneities and “flatten” the range of perfusion values. Moreover, the inconsistencies found between numerical and clinical equivalences highlight that the use of global values may even lead to misleading clinical considerations. Therefore, in order to make reliable clinical diagnosis, radiologists should use all the tumour slices, endowed with a perfusion heterogeneity measure.

During my PhD period, I have also had the opportunity to work at the widest European multi-centre CTP study (PIXEL) on liver and to analyse all the examinations collected in the 15 different Centres, providing my contribution at both methodological and technical level. First of all, the detection and the analysis of all the intra- and inter-centre sources of variability allowed me to draw some hints on how to correctly set-up a multi-centre study. Hopefully, these hints will give a deep contribute to build up more accurate guidelines, prompting the spread of multi-centre studies that represent a crucial step to translate CTP in the standard clinic. Moreover, the signal processing algorithms I developed, such as those to compute the baseline values of the unenhanced stage of CTP or to automatically register ROIs on liver CTP images, provide a real contribution to the achievement of more accurate perfusion parameters. In addition, the results of perfusion analysis carried out on normal liver show that they can be used as a benchmark for hepatic single- and dual-input perfusion studies, thus becoming very useful for the assessment of effects of liver pathologies on normal tissue. Finally, the two perfusion studies carried out on examinations acquired in different Centres, following the same NAP, highlighted that perfusion results could be directly compared, for both single- and dual-input models. These encouraging outcomes could favour proliferation of multi-centre studies needed to assess the reproducibility of CTP technique, by analysing a huge number of examinations, performed with CT scanners of

different models and vendors.

For the sake of completeness, it is worth remarking that all the methods and the algorithms presented in this Thesis (except for the algorithm to align liver CTP images) can be applied on both liver and lung tissues, also being independent from either the methods used to compute perfusion parameters or the perfusion parameters themselves. Actually, in this work I have discussed results achieved through the maximum slope method that permits BF computation only. However, all the considerations drawn regarding the methods to automatically detect unreliable perfusion values, the representativeness of global perfusion values, or the correct computation of baseline values, also hold if considering other perfusion models or computing methods and perfusion parameters, such as BV , MTT or PS .

In conclusion, the work presented in this Thesis provides a clear upgrade of the state of the art. Researchers and clinicians have now at their disposal methods and techniques helping them to achieve more accurate and reliable results and making more aware clinical considerations. However, more accurate models and methods have to be explored in multi-centre studies set up using updated guidelines stemming from previous experiments. As a matter of fact, assessing reproducibility of results through multi-centre studies or meta-analysis is a crucial step to make CTP-based image biomarkers entering the clinical practice. Despite the solution is not at hand, I strongly believe that the integration between medical, bioengineering and computer science techniques, will play a key role in the next future to help translation of CTP into clinics.

Appendix

In this section, the steps needed to obtain Eq. (2.9) presented in Chapter (2) are reported. It is worth noting that this part is almost never included in the papers discussing models and methods to compute perfusion parameters, probably because it is dense of mathematical concepts that could jeopardize reader's attention. For this reason, I chose to create a dedicated appendix so as to keep a better fluency of the reading inside Chapters.

First of all, I recall some properties of convolution and therefore I illustrate the procedure used to obtain Eq. (2.9).

Given two functions $f(t)$ and $g(t)$, their convolution is defined as:

$$f(t) \otimes g(t) = \int_0^{\infty} f(\tau) \cdot g(t - \tau) d\tau \quad (\text{A.1})$$

The convolution of a continuous function $f(t)$ with the discontinuous unit step function $\sigma(t)$ (whose values are equals to 0 for $t < 0$ and to 1 for $t \geq 0$) is represented in Eq. A.2:

$$f(t) \otimes \sigma(t) = \int_0^t f(\tau) d\tau \quad (\text{A.2})$$

Eq. (A.2) in combination with the associative and distributive property of the convolution product yields Eq. A.3:

$$\begin{aligned} \int_0^t f(\tau) \otimes g(\tau) d\tau &= [f(t) \otimes g(t)] \otimes \sigma(t) = \\ &= f(t) \otimes [g(t) \otimes \sigma(t)] = f(t) \otimes \int_0^t g(\tau) d\tau \end{aligned} \quad (\text{A.3})$$

and thus

$$\begin{aligned}
 \int_0^t [f(\tau) - f(\tau) \otimes g(\tau)] d\tau &= [f(t) - f(t) \otimes g(t)] \otimes \sigma(t) = \\
 = f(t) \otimes \sigma(t) - f(t) \otimes g(t) \otimes \sigma(t) &= f(t) \otimes [\sigma(t) - g(t) \otimes \sigma(t)] = \\
 &= f(t) \otimes [\sigma(t) - \int_0^t g(\tau) d\tau]
 \end{aligned} \tag{A.4}$$

After recalling these mathematical concepts, let us come back to Eq. (2.4). Since the organ of interest gives volume tissue concentration $C_t(t)$ rather than mass concentration $Q(t)$, it is possible to work with the quantity $C_t(t)$, instead of $Q(t)$, by multiply both sides of Eq. (2.4) by tissue density ρ . In this way we obtain Eq. (A.5):

$$\rho \cdot BF \cdot C_a(t) - \rho \cdot BF \cdot C_v(t) \tag{A.5}$$

where

$$\rho \cdot \frac{dQ(t)}{dt} = \frac{dC_t(t)}{dt} \tag{A.6}$$

Because tissue density is closed to unity in most cases (and this is true in both liver and lung), in the literature ρ is often neglected to simplify notations. Therefore, we can rewrite Eq. (A.5) according to Eq. (A.7):

$$\frac{dC_t(t)}{dt} = BF \cdot C_a(t) - BF \cdot C_v(t) = BF \cdot [C_a(t) - C_v(t)] \tag{A.7}$$

By integrating Eq. (A.7), it is possible to obtain Eq. (A.8):

$$C_t(t) = BF \cdot \int_0^t [C_a(\tau) - C_v(\tau)] d\tau \tag{A.8}$$

After that, by substituting $C_v(t)$ with its definition given in Eq. (2.1), it is possible to rewrite Eq. (A.8) according to Eq. (A.9):

$$C_t(t) = BF \cdot \int_0^t [C_a(\tau) - h(\tau) \otimes C_a(\tau)] d\tau \tag{A.9}$$

By exploitinig Eq. (A.4), it is possible to rewrite Eq. (A.9) in Eq. (A.10):

$$C_t(t) = BF \cdot C_a(t) \otimes [\sigma(t) - \int_0^t h(\tau) d\tau] \tag{A.10}$$

Since in real time domains t is always equals or greater than zero, the function

$\sigma(t)$ is always unitary. Therefore, we can write Eq. (A.11):

$$C_t(t) = BF \cdot C_a(t) \otimes [1 - \int_0^t h(\tau) d\tau] \quad (\text{A.11})$$

that according to the definition of $R(t)$ (given in Eq. (2.8)) becomes Eq. (A.12):

$$C_t(t) = BF \cdot C_a(t) \otimes R(t) \quad (\text{A.12})$$

Finally, by applying the commutative principle, it is possible to obtain Eq. (2.9) presented in the literature.

List of Abbreviations

Abbreviation	Definition
1D	Transverse manual registration
2CXM	Two-compartment exchange model
2D	Transverse manual registration
2I1CM	Dual-input one-compartment model
3D	Multi-slice manual registration
α	Non-linear parameter affecting curve slope (Hill's equation)
ϵ	Residuals
$\bar{\epsilon}$	Residuals' mean value
η	White noise
μ	Distribution mean
μ_ϵ	Mean of absolute residuals
μ_{BF}	<i>BF</i> mean
μ_{ICV}	ICV mean value
μ_s	Mean <i>BF</i> values representative of each slice
μ_w	Mean <i>BF</i> values representative of the whole tumour
Ω_W	Group of concentration values inside <i>W</i>
σ	Distribution standard deviation
σ_ϵ	Standard deviation of residuals
σ_{μ_ϵ}	Standard deviation of μ_ϵ values
σ_{BF}	<i>BF</i> standard deviation
σ_{ICV}	ICV standard deviation value
$\sigma_i(\Omega_W)$	Standard deviation of Ω_W
τ_a	transit time of CA from aorta to tissue in 2I1CM
τ_p	transit time of CA from portal vein to tissue in 2I1CM
a	AR coefficient
AATHM	Adiabatic approximation to the tissue homogeneity model
<i>aBF</i>	Arterial <i>BF</i>
AIRTUM	Italian Association of Cancer Registries

ANOVA	Analysis of variance
AR	Autoregressive
AUC	Area under the curve
BF	Blood flow
BFA	Baseline finding algorithm
BV	Blood volume
CA	Contrast agent
$C_a(t)$	Arterial inflow
C_{ev}	CA concentration inside EV
C_{iv}	CA concentration inside IV
CRC	Colorectal cancer
CT	Computed tomography
CTp	Computed tomography perfusion
CV	Coefficient of variation
$C_v(t)$	venous outflow
DCE	Dynamic contrast enhanced
DICOM	Digital Imaging and Communications in Medicine
DIMS	Dual-input maximum slope
DPM	Distributed parameter model
E	Entropy
$E[\mu_\epsilon]$	Mean of μ_ϵ values
E_0	Baseline tissue concentration value (Hill's equation)
EC_{50}	Instant of half maximum tissue concentration (Hill's equation)
EF	Extraction fraction
EI	Interval ending point
E_{max}	Saturation concentration value of tissue (Hill's equation)
EP	Baseline ending point
E_s	Entropy of each slice
eTM	Extended Tofts model
EV	Extravascular space
E_w	Entropy of the whole tumour
F_{iv}	Plasma flow
FN	False negative
FNR	False negative ratio
FOV	Field of view
FP	False positive
FPR	False positive ratio
FU	Follow-up

G1	Method to compute global baseline value considering a single slice
GUI	Graphical user interface
h	Probability density function of CA particles
HCC	Hepatocellular carcinoma
HU	Hounsfield units
IDT	Indicator dilution theory
IQR	Interquartile range
IV	Intravascular space
k_{1a}	Arterial inflow rate constant in 2I1CM
k_{1b}	Portal inflow rate constant in 2I1CM
k_2	Outflow rate constant in 2I1CM
k^{trans}	Flow rate constant
L	Length of the vascular bed
ICV	Local coefficient of variation
MIUR	Italian Minister of Education, Universities and Research
MRI	Magnetic resonance imaging
MS	Mean of the local standard deviation
MSM	Maximum slope method
MTT	Mean transit time
MVD	Microvessel density
N	Number of TCC data points
n.a.	Not available
NAP	Nominal acquisition protocol
NC	Number of compartment
NSCLC	Non-small cell lung cancer
OS	Overall survival
p	AR model's order
pBF	Portal BF
PCM	Pharmacokinetic compartment models
PET	Positron emission tomography
PFS	Progression-free survival
PI	Perfusion index
PS	Permeability surface
Q	Mass concentration of CA in tissue
R	Impulse residual function
R^2	Coefficient of determination
r_μ	μ_s range
r_M	M_s range

RECIST	Response Evaluation Criteria in Solid Tumor
ROI	Region of interest
SEN	Sensitivity
SF	Standard fixed mode
SI	Interval starting point
SIMS	Single-input maximum slope
SNR	Signal to noise ratio
SP	Baseline starting point
SPEC	Specificity
SS	Variability of the local standard deviation
SSE	Sum of squared error
SS_{tot}	Total sum of data squares
std	Standard deviation
$T_{2\sigma}$	$2 - \sigma$ method thresholding value
TCC	Time concentration curve
TEM	Thresholded error maps
THM	Tissue homogeneity model
TM	Tofts model
TN	True negative
TP	True positive
T_T	Triangle method thresholding value
US	Ultrasound
V1	Method compute voxel-based baseline value considering a single slice
V5	Method to compute voxel-based baseline value considering five slices
v_{ev}	Interstitial space volume
VEGF	Vascular endothelial growth factor
v_{iv}	Plasma volume
$W(x, y)$	Window of dimension $w \times w$ and centered in (x, y)
WHO	World Health Organization
y_{AR}	AR signal
Y_i	TCC's data point at the time instant i
\hat{Y}_i	Fitting curve's data point at the time instant i

List of Figures

2.1	Dual-input liver ROIs and corresponding TCCs	13
2.2	CT image and BF colorimetric map of a lung lesion.	16
2.3	Single input and single output mono-compartmental model . . .	18
2.4	Parameters used in the MSM	19
2.5	Dual-input and single-output mono-compartmental model . . .	20
2.6	MSM applied on a dual-input system	20
2.7	Input residual function	21
2.8	Fluids classification	23
2.9	Well-mixed and plug-flow compartments	24
2.10	Two-compartment exchange model	26
2.11	Tissue homogeneity model	27
2.12	Adiabatic approximation to tissue homogeneity model	27
2.13	Distributed parameters model	28
2.14	Temporal TCCs fitting models	42
3.1	Examples of interpolating and fitting curves	48
3.2	Hill's equation parameters	49
3.3	Liver TCCs with their interpolating and fitting curves	49
3.4	Examples of TCC residuals	52
3.5	Examples of TCCs for the computation of the error indexes . .	53
3.6	Tissue regions showing different heterogeneity degrees	58
3.7	Density values' histograms of different tissue regions	58
3.8	Histogram and colorimetric map of μ_ϵ	61
3.9	Application of $2 - \sigma$ rule thresholding method	62
3.10	Triangle method, first step	63
3.11	Triangle method, second step	64
3.12	Application of $2 - \sigma$ rule and triangle thresholding methods . .	64
3.13	ICV and BF maps before and after motion correction	66
3.14	Entropy on landscape photographs	68

3.15	Entropy on BF maps	69
4.1	Motion artefacts on a liver CTp image	72
4.2	Poisson noise in a liver CTp image	73
4.3	Beam hardening artefacts	74
4.4	Partial volume effect	75
4.5	Photon starvation artefacts	76
4.6	Patient-based artefacts	76
4.7	Scanner-based artefacts	77
4.8	Best sequence selected in a lung CTp examination	82
4.9	Examinations error bars found using different alignment methods	85
4.10	Lung BF colorimetric maps obtained using different alignment approaches	87
4.11	Liver BF and μ_ϵ colorimetric maps obtained using different alignment approaches	88
4.12	Lung BF colorimetric maps obtained using different registration methods	90
4.13	Anatomical structures and artefacts manually identified by ra- diologists	94
4.14	Misleading structures identified by radiologists and TEMs	97
4.15	Failure of the manual method with respect to TEMs	98
4.16	Comparison between manual thresholding and TEMs	98
4.17	Relationship between BF and μ_ϵ	99
4.18	Histogram of the removed BF values using triangle method	100
4.19	Comparison between BF mean values computed before and af- ter error thresholding	100
4.20	Comparison between BF standard deviation values computed before and after error thresholding	101
4.21	Comparison between BF CV values computed before and after error thresholding	101
5.1	Whole scan, HU, and BF maps of different lung tumour sections	110
5.2	BF colorimetric maps of a lesion whose global value select the slice having the highest E	110
5.3	BF colorimetric maps of a lesion whose global value select the slice having the highest E	111
5.4	BF colorimetric maps of a lesion whose global value select the slice having the lowest E	111

5.5	BF maps of two lesions having the same global BF values, but different heterogeneity levels	112
5.6	BF maps of two lesion having the same global BF values, but different heterogeneity levels	113
5.7	Baseline and FU histograms of E_s	113
6.1	Examinations with three different FOV	126
6.2	TCCs with different timelines	127
6.3	Time intervals between consecutive volumes acquired	128
6.4	Frequency spectrum	136
6.5	CT images and histograms of background density values	138
6.6	Histograms of background density values	139
6.7	Variation over time of background density values	140
6.8	SP selected for baseline algorithm	141
6.9	CT slice and histograms of liver density values	143
6.10	Liver and background noise	144
6.11	SNR of liver examinations	145
7.1	Algorithm pipeline	152
7.2	Example of ROI drawn on normal liver	153
7.3	Spatial filters applied to normal liver tissue	154
7.4	Examples of TCCs and TACs	156
7.5	z level selection	158
7.6	ROI alignment on the x - y plane	159
7.7	Liver anatomy	161
7.8	Space between liver and thorax	161
7.9	Liver during inspiration and expiration phases	161
7.10	Pipeline of the first part of the motion correction algorithm	162
7.11	Bounding patient body	163
7.12	Working area selection	164
7.13	Bounding region between liver and thorax	165
7.14	Pipeline of the second part of the motion correction algorithm	166
7.15	Identification of high density structures	166
7.16	Ribs identification	167
7.17	Exclusion of misleading data	168
7.18	Ribs' points fitting	168
7.19	ROI alignment on the x - y plane	169
7.20	Application of temporal filtering to tissue TCCs	173

7.21	SP selection	174
7.22	BP iterative fit	175
7.23	μ_ϵ fitting and its first derivative	176
7.24	μ_ϵ fitting and its first and second derivative	177
7.25	Baseline histograms and colorimetric maps achieved with BFA algorithm	178
7.26	Baseline histograms and colorimetric maps achieved using V1 .	181
7.27	Baseline histograms and colorimetric maps achieved using V5 .	181
7.28	Histograms of baseline values differences between different meth- ods to compute baseline	183
7.29	Baseline values in Centre 1	184
7.30	Distance between mean and median baseline values in Centre 1 .	185
7.31	Histogram baseline values in four different Centres	187
7.32	Baseline colorimetric maps in four different Centres	188
7.33	BF values in Centre 1	191
7.34	Scatter of mean and standard deviation BF values in Centre 1 .	192
7.35	Histograms and BF colorimetric maps of examinations pertain- ing to the first group	192
7.36	Histograms and BF colorimetric maps of examinations pertain- ing to the second group	193
7.37	Histograms and BF colorimetric maps of examinations pertain- ing to the third group	194
7.38	Histograms and BF colorimetric maps of examinations pertain- ing to the fourth group	195
7.39	BF values in Centre 1 after error thresholding	195
7.40	Examinations with high BF mean and standard deviation values after thresholding	196
7.41	Histograms of BF mean and standard deviation values before and after error thresholding	197
7.42	ROIs on portal vein and spleen	198
7.43	Examinations excluded from dual input analysis	198
7.44	Dual input perfusion colorimetric maps	199
7.45	Dual input perfusion colorimetric maps in Centre 1	201
7.46	Scatter of dual-input perfusion mean and standard deviation values	201
7.47	aBF and HPI colorimetric maps showing mean and standard deviation relationship	202

7.48 Dual-input perfusion colorimetric maps after error thresholding
in Centre 1 203

7.49 BF values in four different Centres 205

7.50 BF colorimetric map and μ_ϵ histogram of examination C16N13 206

7.51 Dual input perfusion values in four different Centres 208

7.52 Dual input perfusion values in four different Centres after thresh-
olding 211

List of Tables

2.1	Practical features of functional imaging techniques.	10
2.2	Methods and models applied to compute perfusion parameters .	30
3.1	First derivative maximum value and BF value achieved by using interpolant, non-parametric, and parametric fitting curves . . .	50
3.2	Temporal error indexes.	54
4.1	Features of the eleven cases analysed	79
4.2	Quantitative and qualitative indexes related to perfusion maps .	84
4.3	Contingency tables and statistical indexes	96
5.1	Baseline global BF and E values for slices and whole tumours .	108
5.2	FU global BF and E values for slices and whole tumours	109
6.1	PIXEL Centres and patients.	119
6.2	PIXEL acquisition parameters.	133
6.3	Image quality tests	135
6.4	Mean and standard deviation of background density values . . .	139
6.5	Main parameters regarding image quality	142
7.1	Statistics on baseline values achieved applying BFA on three examinations	178
7.2	Summary of the method used to compute baseline	180
7.3	Baseline and μ_ϵ values computed applying four different baseline algorithms	180
7.4	Statistical baseline values in Centre 1	185
7.5	Statistical baseline values in 4 different Centres	187
7.6	Statistical single-input BF values in Centre 1	190
7.7	Statistical single-input BF values in Centre 1 after error thresh- olding	196
7.8	Statistical dual-input BF values in Centre 1	200

7.9	Perfusion mean and standard deviation values of some representative examinations	202
7.10	Statistical dual-input BF values in Centre 1 after thresholding .	204
7.11	Statistical single-input BF values in four different Centres . . .	205
7.12	Statistical dual-input BF values in four different Centres	209
7.13	Summary of p -value obtained for dual-input perfusion values analysis	210
7.14	Statistical single-input BF values in four different Centres after error thresholding	212
7.15	Summary of p -value obtained for dual-input perfusion values analysis after error thresholding	213

Bibliography

- [1] C. Fitzmaurice et al. “The global burden of cancer 2013”. In: *JAMA oncology* 1.4 (2015), pp. 505–527 (cit. on p. 1).
- [2] *AIRTUM*. <http://www.epicentro.iss.it/temi/tumori/airtum16.asp>. Accessed: 2017-03-23 (cit. on p. 1).
- [3] J. Ferlay et al. “Cancer incidence and mortality worldwide: sources, methods and major patterns in GLOBOCAN 2012”. In: *International journal of cancer* 136.5 (2015), E359–E386 (cit. on p. 1).
- [4] H. Wang et al. “Global, regional, and national life expectancy, all-cause mortality, and cause-specific mortality for 249 causes of death, 1980–2015: a systematic analysis for the Global Burden of Disease Study 2015”. In: *The Lancet* 388.10053 (2016), pp. 1459–1544 (cit. on p. 1).
- [5] S Vatandoust, T. Price, and C. Karapetis. “Colorectal cancer: Metastases to a single organ.” In: *World journal of gastroenterology* 21.41 (2015), pp. 11767–11776 (cit. on p. 1).
- [6] D Hashim et al. “The global decrease in cancer mortality: trends and disparities”. In: *Annals of Oncology* 27.5 (2016), pp. 926–933 (cit. on p. 1).
- [7] G. C. Jayson et al. “Antiangiogenic therapy in oncology: current status and future directions”. In: *The Lancet* 388.10043 (2016), pp. 518–529 (cit. on pp. 1, 8).
- [8] S. H. Kim, A. Kamaya, and J. K. Willmann. “CT perfusion of the liver: principles and applications in oncology”. In: *Radiology* 272.2 (2014), pp. 322–344 (cit. on pp. 1, 2, 9, 13, 15, 20, 32, 36, 37, 39, 44).
- [9] R. García-Figueiras et al. “Imaging of Tumor Angiogenesis for RadiologistsPart 1: Biological and Technical Basis”. In: *Current problems in diagnostic radiology* 44.5 (2015), pp. 407–424 (cit. on pp. 2, 10, 11).

- [10] Y. Ohno et al. “Contrast-enhanced CT-and MRI-based perfusion assessment for pulmonary diseases: basics and clinical applications”. In: *Diagnostic and Interventional Radiology* 22.5 (2016), pp. 407–421 (cit. on pp. 2, 30).
- [11] P. Carmeliet and R. K. Jain. “Molecular mechanisms and clinical applications of angiogenesis”. In: *Nature* 473.7347 (2011), pp. 298–307 (cit. on p. 7).
- [12] K. Miller et al. “Paclitaxel plus bevacizumab versus paclitaxel alone for metastatic breast cancer”. In: *New England Journal of Medicine* 357.26 (2007), pp. 2666–2676 (cit. on pp. 7, 8).
- [13] K. Miles. “Tumour angiogenesis and its relation to contrast enhancement on computed tomography: a review”. In: *European journal of radiology* 30.3 (1999), pp. 198–205 (cit. on pp. 8, 12).
- [14] S. Goel et al. “Normalization of the vasculature for treatment of cancer and other diseases”. In: *Physiological reviews* 91.3 (2011), pp. 1071–1121 (cit. on pp. 8, 15).
- [15] R. A. Gatenby, O. Grove, and R. J. Gillies. “Quantitative imaging in cancer evolution and ecology”. In: *Radiology* 269.1 (2013), pp. 8–14 (cit. on pp. 8, 9).
- [16] W. van Elmpt et al. “Imaging techniques for tumour delineation and heterogeneity quantification of lung cancer: overview of current possibilities”. In: *Journal of thoracic disease* 6.4 (2013), pp. 319–327 (cit. on pp. 8, 11).
- [17] J. Ma and D. J. Waxman. “Combination of antiangiogenesis with chemotherapy for more effective cancer treatment”. In: *Molecular cancer therapeutics* 7.12 (2008), pp. 3670–3684 (cit. on p. 8).
- [18] S. Hong et al. “Efficacy and safety of angiogenesis inhibitors in advanced non-small cell lung cancer: a systematic review and meta-analysis”. In: *Journal of cancer research and clinical oncology* 141.5 (2015), pp. 909–921 (cit. on p. 8).
- [19] E. B. Garon et al. “Ramucirumab plus docetaxel versus placebo plus docetaxel for second-line treatment of stage IV non-small-cell lung cancer after disease progression on platinum-based therapy (REVEL): a multicentre, double-blind, randomised phase 3 trial”. In: *The Lancet* 384.9944 (2014), pp. 665–673 (cit. on p. 8).

- [20] J. M. Llovet et al. “Sorafenib in advanced hepatocellular carcinoma”. In: *New England journal of medicine* 359.4 (2008), pp. 378–390 (cit. on p. 8).
- [21] H.-C. Sun et al. “Postoperative interferon α treatment postponed recurrence and improved overall survival in patients after curative resection of HBV-related hepatocellular carcinoma: a randomized clinical trial”. In: *Journal of cancer research and clinical oncology* 132.7 (2006), pp. 458–465 (cit. on p. 8).
- [22] D. Cunningham et al. “Bevacizumab plus capecitabine versus capecitabine alone in elderly patients with previously untreated metastatic colorectal cancer (AVEX): an open-label, randomised phase 3 trial”. In: *The lancet oncology* 14.11 (2013), pp. 1077–1085 (cit. on p. 8).
- [23] E. Van Cutsem et al. “Addition of aflibercept to fluorouracil, leucovorin, and irinotecan improves survival in a phase III randomized trial in patients with metastatic colorectal cancer previously treated with an oxaliplatin-based regimen”. In: *Journal of Clinical Oncology* 30.28 (2012), pp. 3499–3506 (cit. on p. 8).
- [24] O. H Nielsen et al. “Anti-angiogenic drugs in the treatment of metastatic renal cell carcinoma: advances in clinical application”. In: *Current vascular pharmacology* 13.3 (2015), pp. 381–391 (cit. on p. 8).
- [25] B. Escudier et al. “Sorafenib in advanced clear-cell renal-cell carcinoma”. In: *New England Journal of Medicine* 356.2 (2007), pp. 125–134 (cit. on p. 8).
- [26] D. W. Miles et al. “Phase III study of bevacizumab plus docetaxel compared with placebo plus docetaxel for the first-line treatment of human epidermal growth factor receptor 2–negative metastatic breast cancer”. In: *Journal of Clinical Oncology* 28.20 (2010), pp. 3239–3247 (cit. on p. 8).
- [27] T. J. Perren et al. “A phase 3 trial of bevacizumab in ovarian cancer”. In: *New England Journal of Medicine* 365.26 (2011), pp. 2484–2496 (cit. on p. 8).
- [28] R. A. Burger et al. “Incorporation of bevacizumab in the primary treatment of ovarian cancer”. In: *New England Journal of Medicine* 365.26 (2011), pp. 2473–2483 (cit. on p. 8).

- [29] L. Gianni et al. “AVEREL: a randomized phase III Trial evaluating bevacizumab in combination with docetaxel and trastuzumab as first-line therapy for HER2-positive locally recurrent/metastatic breast cancer”. In: *Journal of Clinical Oncology* 31.14 (2013), pp. 1719–1725 (cit. on p. 8).
- [30] A. Carrato et al. “Fluorouracil, leucovorin, and irinotecan plus either sunitinib or placebo in metastatic colorectal cancer: a randomized, phase III trial”. In: *Journal of Clinical Oncology* 31.10 (2013), pp. 1341–1347 (cit. on p. 8).
- [31] C. J. Allegra et al. “Bevacizumab in stage II-III colon cancer: 5-year update of the National Surgical Adjuvant Breast and Bowel Project C-08 trial”. In: *Journal of Clinical Oncology* 31.3 (2013), pp. 359–364 (cit. on p. 8).
- [32] N. S. Vasudev and A. R. Reynolds. “Anti-angiogenic therapy for cancer: current progress, unresolved questions and future directions”. In: *Angiogenesis* 17.3 (2014), pp. 471–494 (cit. on p. 8).
- [33] R. K. Jain. “Antiangiogenesis strategies revisited: from starving tumors to alleviating hypoxia”. In: *Cancer cell* 26.5 (2014), pp. 605–622 (cit. on p. 8).
- [34] R. K. Jain. “Normalizing tumor microenvironment to treat cancer: bench to bedside to biomarkers”. In: *Journal of Clinical Oncology* 31.17 (2013), pp. 2205–2218 (cit. on p. 8).
- [35] J. Folkman. “Anti-angiogenesis: new concept for therapy of solid tumors”. In: *Annals of surgery* 175.3 (1972), pp. 409–416 (cit. on p. 8).
- [36] R. Gillies et al. “Causes and effects of heterogeneous perfusion in tumors”. In: *Neoplasia* 1.3 (1999), pp. 197–207 (cit. on pp. 8, 106).
- [37] Q. Qi et al. “Evaluation of CT Perfusion Biomarkers of Tumor Hypoxia”. In: *PloS one* 11.4 (2016), e0153569 (cit. on p. 8).
- [38] H. Choudhry, A. L. Harris, and A. McIntyre. “The tumour hypoxia induced non-coding transcriptome”. In: *Molecular aspects of medicine* 47 (2016), pp. 35–53 (cit. on p. 8).
- [39] R. S. Heist et al. “Improved tumor vascularization after anti-VEGF therapy with carboplatin and nab-paclitaxel associates with survival in lung cancer”. In: *Proceedings of the National Academy of Sciences* 112.5 (2015), pp. 1547–1552 (cit. on pp. 8, 35).

- [40] Y. Tsuchida and P. Therasse. “Response evaluation criteria in solid tumors (RECIST): new guidelines”. In: *Medical and pediatric oncology* 37.1 (2001), pp. 1–3 (cit. on p. 9).
- [41] E. Eisenhauer et al. “New response evaluation criteria in solid tumours: revised RECIST guideline (version 1.1)”. In: *European journal of cancer* 45.2 (2009), pp. 228–247 (cit. on p. 9).
- [42] W. H. Organization. *Chronicle of the world health organization*. Vol. 9. The Organization, 1955 (cit. on p. 9).
- [43] E. Coche. “Assessment of lung tumor response by perfusion CT”. In: *Journal of the Belgian Society of Radiology* 96.3 (2013), pp. 172–174 (cit. on p. 9).
- [44] J. M. Provenzale. “Imaging of angiogenesis: clinical techniques and novel imaging methods”. In: *American Journal of Roentgenology* 188.1 (2007), pp. 11–23 (cit. on p. 9).
- [45] E. S. of Radiology (ESR et al. “White paper on imaging biomarkers”. In: *Insights into imaging* 1.2 (2010), pp. 42–45 (cit. on pp. 9, 115).
- [46] C. Dazzi et al. “Prognostic and predictive value of intratumoral microvessels density in operable non-small-cell lung cancer”. In: *Lung cancer* 24.2 (1999), pp. 81–88 (cit. on p. 9).
- [47] K. A. Miles et al. “Application of CT in the investigation of angiogenesis in oncology”. In: *Academic radiology* 7.10 (2000), pp. 840–850 (cit. on pp. 9, 18, 21).
- [48] C. Cuenod et al. “Tumor angiogenesis: pathophysiology and implications for contrast-enhanced MRI and CT assessment”. In: *Abdominal imaging* 31.2 (2006), pp. 188–193 (cit. on p. 9).
- [49] R. García-Figueiras et al. “Advanced imaging of colorectal cancer: From anatomy to molecular imaging”. In: *Insights into imaging* 7.3 (2016), pp. 285–309 (cit. on pp. 9, 10).
- [50] A. B. Rosenkrantz et al. “Clinical utility of quantitative imaging”. In: *Academic radiology* 22.1 (2015), pp. 33–49 (cit. on p. 9).
- [51] K. Miles. “Functional computed tomography in oncology”. In: *European Journal of Cancer* 38.16 (2002), pp. 2079–2084 (cit. on pp. 9, 11).
- [52] G Petralia et al. “CT perfusion in solid-body tumours. Part I: technical issues”. In: *La radiologia medica* 115.6 (2010), pp. 843–857 (cit. on pp. 10, 14, 15, 21, 28, 40, 44, 47).

- [53] P. V. Pandharipande et al. “Perfusion imaging of the liver: current challenges and future goals”. In: *Radiology* 234.3 (2005), pp. 661–673 (cit. on p. 11).
- [54] K. Miles. “Perfusion CT for the assessment of tumour vascularity: which protocol?” In: *Br J Radiol* 76.1 (2003), S36–S42 (cit. on pp. 11, 12, 37, 38, 42).
- [55] K. Miles and R. Williams. “Warburg revisited: imaging tumour blood flow and metabolism”. In: *Cancer Imaging* 8.1 (2008), pp. 81–86 (cit. on p. 11).
- [56] A Uusaro, E Ruokonen, and J Takala. “Estimation of splanchnic blood flow by the Fick principle in man and problems in the use of indocyanine green”. In: *Cardiovascular research* 30.1 (1995), pp. 106–112 (cit. on p. 11).
- [57] L. Axel. “Cerebral blood flow determination by rapid-sequence computed tomography: theoretical analysis.” In: *Radiology* 137.3 (1980), pp. 679–686 (cit. on p. 11).
- [58] L. W. Goldman. “Principles of CT: multislice CT”. In: *Journal of nuclear medicine technology* 36.2 (2008), pp. 57–68 (cit. on p. 11).
- [59] L. W. Goldman. “Principles of CT and CT technology”. In: *Journal of nuclear medicine technology* 35.3 (2007), pp. 115–128 (cit. on p. 11).
- [60] G Petralia et al. “CT perfusion in oncology: how to do it”. In: *Cancer Imaging* 10.1 (2010), pp. 8–19 (cit. on pp. 12, 15, 44, 46).
- [61] G. Brix et al. “Tracer kinetic modelling of tumour angiogenesis based on dynamic contrast-enhanced CT and MRI measurements”. In: *European journal of nuclear medicine and molecular imaging* 37.1 (2010), pp. 30–51 (cit. on pp. 12, 14, 17–19, 21).
- [62] B. Romain et al. “Parameter estimation of perfusion models in dynamic contrast-enhanced imaging: a unified framework for model comparison”. In: *Medical Image Analysis* 35 (2017), pp. 360–374 (cit. on pp. 12, 24, 47).
- [63] K. Miles and M. Griffiths. “Perfusion CT: a worthwhile enhancement?” In: *Br J Radiol* 76.904 (2003), pp. 220–231 (cit. on pp. 12, 13, 37, 40, 171).

- [64] E. Klotz et al. “Technical prerequisites and imaging protocols for CT perfusion imaging in oncology”. In: *European journal of radiology* 84.12 (2015), pp. 2359–2367 (cit. on pp. 12, 37, 42, 116).
- [65] C. Leiva-Salinas, J. M. Provenzale, and M. Wintermark. “Responses to the 10 most frequently asked questions about perfusion CT”. In: *American Journal of Roentgenology* 196.1 (2011), pp. 53–60 (cit. on p. 13).
- [66] S. Nakano et al. “Perfusion evaluation of lung cancer: assessment using dual-input perfusion computed tomography”. In: *Journal of thoracic imaging* 28.4 (2013), pp. 253–262 (cit. on p. 13).
- [67] X. Yuan et al. “Lung cancer perfusion: can we measure pulmonary and bronchial circulation simultaneously?” In: *European radiology* 22.8 (2012), pp. 1665–1671 (cit. on p. 13).
- [68] C. S. Ng et al. “Effect of dual vascular input functions on CT perfusion parameter values and reproducibility in liver tumors and normal liver”. In: *Journal of computer assisted tomography* 36.4 (2012), pp. 388–393 (cit. on pp. 13, 14).
- [69] D. Ippolito et al. “Hepatocellular carcinoma in cirrhotic liver disease: functional computed tomography with perfusion imaging in the assessment of tumor vascularization”. In: *Academic radiology* 15.7 (2008), pp. 919–927 (cit. on p. 14).
- [70] C. S. Reiner et al. “Liver perfusion imaging in patients with primary and metastatic liver malignancy: prospective comparison between ^{99m}Tc -MAA spect and dynamic CT perfusion”. In: *Academic radiology* 19.5 (2012), pp. 613–621 (cit. on pp. 14, 32).
- [71] H. F. Yang et al. “Perfusion computed tomography evaluation of angiogenesis in liver cancer”. In: *European radiology* 20.6 (2010), pp. 1424–1430 (cit. on pp. 14, 31, 32).
- [72] Y. Ohno et al. “Dynamic contrast-enhanced perfusion area-detector CT assessed with various mathematical models: Its capability for therapeutic outcome prediction for non-small cell lung cancer patients with chemoradiotherapy as compared with that of FDG-PET/CT”. In: *European Journal of Radiology* 86 (2017), pp. 83–91 (cit. on pp. 14, 35).

- [73] Y. Ohno et al. “Dynamic contrast-enhanced perfusion area detector CT for non-small cell lung cancer patients: Influence of mathematical models on early prediction capabilities for treatment response and recurrence after chemoradiotherapy”. In: *European journal of radiology* 85.1 (2016), pp. 176–186 (cit. on pp. 14, 21, 35, 47).
- [74] W.-F. Lv et al. “CT Perfusion Imaging Can Predict Patients’ Survival and Early Response to Transarterial Chemo-Lipiodol Infusion for Liver Metastases from Colorectal Cancers”. In: *Korean journal of radiology* 16.4 (2015), pp. 810–820 (cit. on pp. 14, 35, 47).
- [75] G. Chen et al. “Computed tomography perfusion in evaluating the therapeutic effect of transarterial chemoembolization for hepatocellular carcinoma”. In: *World J Gastroenterol* 14.37 (2008), pp. 5738–5743 (cit. on p. 14).
- [76] X. Yuan et al. “Differentiation of malignant and benign pulmonary nodules with first-pass dual-input perfusion CT”. In: *European radiology* 23.9 (2013), pp. 2469–2474 (cit. on pp. 14, 20, 32, 104).
- [77] C. A. Cuenod et al. “Early changes in liver perfusion caused by occult metastases in rats: detection with quantitative CT”. In: *Radiology* 218.2 (2001), pp. 556–561 (cit. on pp. 15, 22).
- [78] R. Jain et al. “Quantitative estimation of permeability surface-area product in astroglial brain tumors using perfusion CT and correlation with histopathologic grade”. In: *American Journal of Neuroradiology* 29.4 (2008), pp. 694–700 (cit. on pp. 15, 16).
- [79] S. Bisdas et al. “Quantitative measurements of perfusion and permeability of oropharyngeal and oral cavity cancer, recurrent disease, and associated lymph nodes using first-pass contrast-enhanced computed tomography studies”. In: *Investigative radiology* 42.3 (2007), pp. 172–179 (cit. on pp. 15, 16).
- [80] A. Eilaghi et al. “Quantitative Perfusion and Permeability Biomarkers in Brain Cancer from Tomographic CT and MR Images”. In: *Biomarkers in Cancer* 8.Suppl 2 (2016), pp. 47–59 (cit. on p. 16).
- [81] R. García-Figueiras et al. “CT perfusion in oncologic imaging: a useful tool?” In: *American Journal of Roentgenology* 200.1 (2013), pp. 8–19 (cit. on pp. 16, 37, 38, 40, 170, 172).

- [82] S. Turco, H. Wijkstra, and M. Mischi. “Mathematical Models of Contrast Transport Kinetics for Cancer Diagnostic Imaging: A Review”. In: *IEEE Reviews in Biomedical Engineering* 9 (2016), pp. 121–147 (cit. on pp. 17, 28, 29, 32).
- [83] K. Miles et al. “Current status and guidelines for the assessment of tumour vascular support with dynamic contrast-enhanced computed tomography”. In: *European radiology* 22.7 (2012), pp. 1430–1441 (cit. on pp. 17, 36–40, 42, 43, 51, 77, 116, 134, 146–148).
- [84] P. Meier and K. L. Zierler. “On the theory of the indicator-dilution method for measurement of blood flow and volume”. In: *Journal of applied physiology* 6.12 (1954), pp. 731–744 (cit. on pp. 17, 22, 47).
- [85] K. L. Zierler. “Theoretical basis of indicator-dilution methods for measuring flow and volume”. In: *Circulation Research* 10.3 (1962), pp. 393–407 (cit. on p. 17).
- [86] T.-Y. Lee. “Functional CT: physiological models”. In: *Trends in biotechnology* 20.8 (2002), S3–S10 (cit. on pp. 18, 21, 22, 155, 170–172).
- [87] K. A. Miles, M. P. Hayball, and A. K. Dixon. “Functional images of hepatic perfusion obtained with dynamic CT.” In: *Radiology* 188.2 (1993), pp. 405–411 (cit. on pp. 19, 104).
- [88] M. J. Blomley et al. “Liver perfusion studied with ultrafast CT.” In: *Journal of computer assisted tomography* 19.3 (1995), pp. 424–433 (cit. on p. 19).
- [89] K. A. Miles, M. P. Hayball, and A. K. Dixon. “Functional imaging of changes in human intrarenal perfusion using quantitative dynamic computed tomography.” In: *Investigative radiology* 29.10 (1994), pp. 911–914 (cit. on p. 19).
- [90] K. Miles, M. Hayball, and A. Dixon. “Measurement of human pancreatic perfusion using dynamic computed tomography with perfusion imaging”. In: *The British journal of radiology* 68.809 (1995), pp. 471–475 (cit. on p. 19).
- [91] A. Cenic et al. “A CT method to measure hemodynamics in brain tumors: validation and application of cerebral blood flow maps”. In: *American Journal of Neuroradiology* 21.3 (2000), pp. 462–470 (cit. on p. 19).

- [92] J. H. Gillard et al. “Assessment of quantitative computed tomographic cerebral perfusion imaging with H₂ (15) O positron emission tomography”. In: *Neurological research* 22.5 (2000), pp. 457–464 (cit. on p. 19).
- [93] D. H. Lee et al. “Multiphasic Dynamic Computed Tomography Evaluation of Liver Tissue Perfusion Characteristics Using the Dual Maximum Slope Model in Patients With Cirrhosis and Hepatocellular Carcinoma: A Feasibility Study”. In: *Investigative radiology* 51.7 (2016), pp. 430–434 (cit. on p. 21).
- [94] M. A. Fischer et al. “Renal versus splenic maximum slope based perfusion CT modelling in patients with portal-hypertension”. In: *European radiology* (2016), pp. 1–7 (cit. on p. 21).
- [95] Z. Tan et al. “The primary study of low-dose pancreas perfusion by 640-slice helical CT: a whole-organ perfusion”. In: *SpringerPlus* 4.1 (2015), p. 192 (cit. on p. 21).
- [96] A. Cenic et al. “Dynamic CT measurement of cerebral blood flow: a validation study”. In: *American Journal of Neuroradiology* 20.1 (1999), pp. 63–73 (cit. on p. 22).
- [97] M. Wintermark et al. “Simultaneous measurement of regional cerebral blood flow by perfusion CT and stable xenon CT: a validation study”. In: *American journal of neuroradiology* 22.5 (2001), pp. 905–914 (cit. on p. 22).
- [98] A. Fieselmann et al. “Deconvolution-based CT and MR brain perfusion measurement: theoretical model revisited and practical implementation details”. In: *Journal of Biomedical Imaging* 2011 (2011) (cit. on pp. 22, 47).
- [99] F. Zanderigo et al. “Nonlinear stochastic regularization to characterize tissue residue function in bolus-tracking MRI: assessment and comparison with SVD, block-circulant SVD, and Tikhonov”. In: *IEEE Transactions on Biomedical Engineering* 56.5 (2009), pp. 1287–1297 (cit. on p. 22).
- [100] K. A. Rempp et al. “Quantification of regional cerebral blood flow and volume with dynamic susceptibility contrast-enhanced MR imaging.” In: *Radiology* 193.3 (1994), pp. 637–641 (cit. on p. 22).

- [101] L. Østergaard et al. “High resolution measurement of cerebral blood flow using intravascular tracer bolus passages. Part I: Mathematical approach and statistical analysis”. In: *Magnetic resonance in medicine* 36.5 (1996), pp. 715–725 (cit. on p. 22).
- [102] S. Malavasi. “Studio e sviluppo di algoritmi di elaborazione di immagini da TC per analisi perfusionali”. MA thesis. Italy: University of Bologna, 2012 (cit. on p. 22).
- [103] F. Calamante, D. G. Gadian, and A. Connelly. “Quantification of bolus-tracking MRI: Improved characterization of the tissue residue function using Tikhonov regularization”. In: *Magnetic resonance in medicine* 50.6 (2003), pp. 1237–1247 (cit. on p. 22).
- [104] L. Willats, A. Connelly, and F. Calamante. “Improved deconvolution of perfusion MRI data in the presence of bolus delay and dispersion”. In: *Magnetic resonance in medicine* 56.1 (2006), pp. 146–156 (cit. on p. 22).
- [105] O. Wu et al. “Tracer arrival timing-insensitive technique for estimating flow in MR perfusion-weighted imaging using singular value decomposition with a block-circulant deconvolution matrix”. In: *Magnetic resonance in medicine* 50.1 (2003), pp. 164–174 (cit. on pp. 22, 23).
- [106] K. Kudo et al. “Difference in Tracer Delay-induced Effect among Deconvolution Algorithms in CT Perfusion Analysis: Quantitative Evaluation with Digital Phantoms 1”. In: *Radiology* 251.1 (2009), pp. 241–249 (cit. on p. 23).
- [107] H.-J. Wittsack et al. “CT-perfusion imaging of the human brain: advanced deconvolution analysis using circulant singular value decomposition”. In: *Computerized Medical Imaging and Graphics* 32.1 (2008), pp. 67–77 (cit. on p. 23).
- [108] K Nie et al. “SU-FR-34: Quantitative Perfusion Measurement in Rectal Cancer Using Three Different Pharmacokinetic Models: Implications for Prospective Study Design”. In: *Medical Physics* 43.6 (2016), pp. 3380–3380 (cit. on p. 23).
- [109] S. Zongqiong et al. “CT perfusion imaging of the stomach: a quantitative analysis according to different degrees of adenocarcinoma cell differentiation”. In: *Clinical imaging* 40.3 (2016), pp. 558–562 (cit. on p. 23).

- [110] E. Ma et al. “ROI for outlining an entire tumor is a reliable approach for quantification of lung cancer tumor vascular parameters using CT perfusion”. In: *OncoTargets and therapy* 9 (2016), pp. 2377–2384 (cit. on pp. 23, 44).
- [111] M. Ingrisich and S. Sourbron. “Tracer-kinetic modeling of dynamic contrast-enhanced MRI and CT: a primer”. In: *Journal of pharmacokinetics and pharmacodynamics* 40.3 (2013), pp. 281–300 (cit. on pp. 24, 26, 36).
- [112] R. MATERNE et al. “Non-invasive quantification of liver perfusion with dynamic computed tomography and a dual-input one-compartmental model”. In: *Clinical Science* 99.6 (2000), pp. 517–525 (cit. on pp. 25, 171).
- [113] T. Kanda et al. “Hepatic computed tomography perfusion: comparison of maximum slope and dual-input single-compartment methods”. In: *Japanese journal of radiology* 28.10 (2010), pp. 714–719 (cit. on pp. 25, 42).
- [114] T. Kanda et al. “CT hepatic perfusion measurement: comparison of three analytic methods”. In: *European journal of radiology* 81.9 (2012), pp. 2075–2079 (cit. on pp. 25, 42).
- [115] G. Brix et al. “Regional blood flow, capillary permeability, and compartmental volumes: measurement with dynamic CT initial experience”. In: *Radiology* 210.1 (1999), pp. 269–276 (cit. on p. 26).
- [116] J. F. Kallehauge et al. “Comparison of linear and nonlinear implementation of the compartmental tissue uptake model for dynamic contrast-enhanced MRI”. In: *Magnetic Resonance in Medicine* (2016) (cit. on pp. 26, 29).
- [117] J. F. Kallehauge et al. “Tracer kinetic model selection for dynamic contrast-enhanced magnetic resonance imaging of locally advanced cervical cancer”. In: *Acta Oncologica* 53.8 (2014), pp. 1064–1072 (cit. on p. 26).
- [118] K. S. S. Lawrence and T.-Y. Lee. “An adiabatic approximation to the tissue homogeneity model for water exchange in the brain: I. Theoretical derivation”. In: *Journal of Cerebral Blood Flow & Metabolism* 18.12 (1998), pp. 1365–1377 (cit. on p. 26).

- [119] S. H. Lee et al. “Advanced Hepatocellular Carcinoma: Perfusion Computed Tomography–Based Kinetic Parameter as a Prognostic Biomarker for Prediction of Patient Survival”. In: *Journal of computer assisted tomography* 39.5 (2015), pp. 687–696 (cit. on pp. 28, 41).
- [120] H. B. Larsson et al. “Brain capillary transit time heterogeneity in healthy volunteers measured by dynamic contrast-enhanced T1-weighted perfusion MRI”. In: *Journal of Magnetic Resonance Imaging* (2016) (cit. on p. 28).
- [121] T. G. Purdie, E. Henderson, and T.-Y. Lee. “Functional CT imaging of angiogenesis in rabbit VX2 soft-tissue tumour”. In: *Physics in medicine and biology* 46.12 (2001), pp. 3161–3175 (cit. on p. 28).
- [122] C. S. Ng et al. “Effect on perfusion values of sampling interval of CT perfusion acquisition in neuroendocrine liver metastases and normal liver”. In: *Journal of computer assisted tomography* 39.3 (2015), pp. 373–382 (cit. on p. 28).
- [123] Y. Wang, B. P. Hobbs, and C. S. Ng. “CT perfusion characteristics identify metastatic sites in liver”. In: *Biomed Res Int* 120749 (2015) (cit. on pp. 28, 32).
- [124] P. S. Tofts et al. “Estimating kinetic parameters from dynamic contrast-enhanced T 1-weighted MRI of a diffusable tracer: standardized quantities and symbols”. In: *Journal of Magnetic Resonance Imaging* 10.3 (1999), pp. 223–232 (cit. on p. 29).
- [125] S. P. Sourbron and D. L. Buckley. “On the scope and interpretation of the Tofts models for DCE-MRI”. In: *Magnetic Resonance in Medicine* 66.3 (2011), pp. 735–745 (cit. on p. 29).
- [126] C. Coolens et al. “Feasibility of 4D perfusion CT imaging for the assessment of liver treatment response following SBRT and sorafenib”. In: *Advances in Radiation Oncology* 1.3 (2016), pp. 194–203 (cit. on pp. 29, 51).
- [127] G. H. Jajamovich et al. “DCE-MRI of hepatocellular carcinoma: perfusion quantification with Tofts model versus shutter-speed modelinitial experience”. In: *Magnetic Resonance Materials in Physics, Biology and Medicine* 29.1 (2016), pp. 49–58 (cit. on p. 29).

- [128] S. Leibfarth et al. “Analysis of pairwise correlations in multi-parametric PET/MR data for biological tumor characterization and treatment individualization strategies”. In: *European journal of nuclear medicine and molecular imaging* 43.7 (2016), pp. 1199–1208 (cit. on p. 29).
- [129] C. S. Patlak, R. G. Blasberg, and J. D. Fenstermacher. “Graphical evaluation of blood-to-brain transfer constants from multiple-time uptake data”. In: *Journal of Cerebral Blood Flow & Metabolism* 3.1 (1983), pp. 1–7 (cit. on p. 29).
- [130] C. S. Patlak and R. G. Blasberg. “Graphical evaluation of blood-to-brain transfer constants from multiple-time uptake data. Generalizations”. In: *Journal of Cerebral Blood Flow & Metabolism* 5.4 (1985), pp. 584–590 (cit. on p. 29).
- [131] Y. Sun et al. “Low-dose volume perfusion computed tomography (VPCT) for diagnosis of solitary pulmonary nodules”. In: *European journal of radiology* 85.6 (2016), pp. 1208–1218 (cit. on pp. 29, 37, 38).
- [132] M. Goetz et al. “Machine-learning based comparison of CT-perfusion maps and dual energy CT for pancreatic tumor detection”. In: *SPIE Medical Imaging*. International Society for Optics and Photonics. 2016, 97851R–97851R (cit. on p. 29).
- [133] A. K. Yadav et al. “Perfusion CT—Can it resolve the pancreatic carcinoma versus mass forming chronic pancreatitis conundrum?” In: *Pancreatology* 16.6 (2016), pp. 979–987 (cit. on pp. 29, 32, 33).
- [134] T. Koh et al. “A physiologic model of capillary-tissue exchange for dynamic contrast-enhanced imaging of tumor microcirculation”. In: *Ieee transactions on biomedical engineering* 50.2 (2003), pp. 159–167 (cit. on p. 29).
- [135] M. K. Kapanen, J. T. Halavaara, and A.-M. Häkkinen. “Open Four-Compartment Model in the Measurement of Liver Perfusion”. In: *Academic radiology* 12.12 (2005), pp. 1542–1550 (cit. on pp. 29, 171, 179).
- [136] R. García-Figueiras et al. “Imaging of Tumor Angiogenesis for Radiologists Part 2: Clinical Utility”. In: *Current problems in diagnostic radiology* 44.5 (2015), pp. 425–436 (cit. on p. 30).
- [137] Z. Sun et al. “Clinical Applications of Computed Tomography (CT) Perfusion Imaging in Gastric Cancer”. In: *Journal of Medical Imaging and Health Informatics* 5.8 (2015), pp. 1931–1935 (cit. on p. 30).

- [138] B. Griffith and R. Jain. “Perfusion imaging in neuro-oncology: basic techniques and clinical applications”. In: *Radiologic Clinics of North America* 53.3 (2015), pp. 497–511 (cit. on p. 30).
- [139] W. M. Thaiss et al. “Clinical applications for dual energy CT versus dynamic contrast enhanced CT in oncology”. In: *European journal of radiology* 84.12 (2015), pp. 2368–2379 (cit. on p. 30).
- [140] H. Kim et al. “Quantitative computed tomography imaging biomarkers in the diagnosis and management of lung cancer”. In: *Investigative radiology* 50.9 (2015), pp. 571–583 (cit. on p. 30).
- [141] V. Goh and D. Prezzi. “Perfusion CT: Technical Aspects”. In: Berlin, Heidelberg: Springer Berlin Heidelberg, pp. 1–9. DOI: 10.1007/174_2017_9. URL: http://dx.doi.org/10.1007/174_2017_9 (cit. on p. 30).
- [142] S. Zhou et al. “Correlations between computed tomography perfusion enhancement parameters and lymph node metastasis in non-small cell lung cancer”. In: *Int J Clin Exp Med* 9.7 (2016), pp. 12896–12903 (cit. on p. 31).
- [143] W. Thaiss et al. “VEGFR-2 expression in HCC, dysplastic and regenerative liver nodules, and correlation with pre-biopsy Dynamic Contrast Enhanced CT”. In: *European Journal of Radiology* 85.11 (2016), pp. 2036–2041 (cit. on pp. 31, 47).
- [144] M. Osimani et al. “Perfusion MDCT of prostate cancer: correlation of perfusion CT parameters and immunohistochemical markers of angiogenesis”. In: *American Journal of Roentgenology* 199.5 (2012), pp. 1042–1048 (cit. on p. 31).
- [145] C. S. Reiner et al. “Computed tomography perfusion imaging of renal cell carcinoma: systematic comparison with histopathological angiogenic and prognostic markers”. In: *Investigative radiology* 48.4 (2013), pp. 183–191 (cit. on pp. 31, 33).
- [146] L. Ash et al. “Head and Neck Squamous Cell Carcinoma: CT Perfusion Can Help Noninvasively Predict Intratumoral Microvessel Density”. In: *Radiology* 251.2 (2009), pp. 422–428 (cit. on p. 31).

- [147] A. Kambadakone et al. “CT perfusion as an imaging biomarker in monitoring response to neoadjuvant bevacizumab and radiation in soft-tissue sarcomas: comparison with tumor morphology, circulating and tumor biomarkers, and gene expression.” In: *AJR. American journal of roentgenology* 204.1 (2015), W11–W18 (cit. on pp. 31, 34, 35, 102).
- [148] Y. Li et al. “Peripheral lung carcinoma: correlation of angiogenesis and first-pass perfusion parameters of 64-detector row CT”. In: *Lung cancer* 61.1 (2008), pp. 44–53 (cit. on pp. 31, 33, 34).
- [149] D. Spira et al. “Assessment of tumor vascularity in lung cancer using volume perfusion CT (VPCT) with histopathologic comparison: a further step toward an individualized tumor characterization”. In: *Journal of computer assisted tomography* 37.1 (2013), pp. 15–21 (cit. on pp. 31, 33, 34, 47).
- [150] S.-H. Ma et al. “Peripheral lung cancer: relationship between multi-slice spiral CT perfusion imaging and tumor angiogenesis and cyclin D1 expression”. In: *Clinical imaging* 31.3 (2007), pp. 165–177 (cit. on p. 31).
- [151] S.-H. Ma et al. “Peripheral pulmonary nodules: relationship between multi-slice spiral CT perfusion imaging and tumor angiogenesis and VEGF expression”. In: *BMC cancer* 8.1 (2008), p. 1 (cit. on pp. 31, 32).
- [152] Y.-W. Chen et al. “Assessment of blood flow in hepatocellular carcinoma: correlations of computed tomography perfusion imaging and circulating angiogenic factors”. In: *International journal of molecular sciences* 14.9 (2013), pp. 17536–17552 (cit. on pp. 31, 77).
- [153] V. Goh et al. “Colorectal Tumor Vascularity: Quantitative Assessment with Multidetector CT Do Tumor Perfusion Measurements Reflect Angiogenesis?” In: *Radiology* 249.2 (2008), pp. 510–517 (cit. on p. 31).
- [154] H. Sun et al. “Assessment of tumor grade and angiogenesis in colorectal cancer: whole-volume perfusion CT”. In: *Academic radiology* 21.6 (2014), pp. 750–757 (cit. on pp. 31, 33).
- [155] S. Dighe et al. “Perfusion CT vascular parameters do not correlate with immunohistochemically derived microvessel density count in colorectal tumors”. In: *Radiology* 268.2 (2013), pp. 400–410 (cit. on pp. 31, 157).

- [156] N. Cullu et al. “Feasibility study of CT perfusion imaging for prostate carcinoma”. In: *European radiology* 24.9 (2014), pp. 2236–2244 (cit. on p. 32).
- [157] C. Chen et al. “Study of 320-slice dynamic volume CT perfusion in different pathologic types of kidney tumor: preliminary results”. In: *PloS one* 9.1 (2014), e85522 (cit. on pp. 32, 33).
- [158] V. Goh et al. “Differentiation between Diverticulitis and Colorectal Cancer: Quantitative CT Perfusion Measurements versus Morphologic CriteriaInitial Experience”. In: *Radiology* 242.2 (2007), pp. 456–462 (cit. on pp. 32, 33).
- [159] D. Ippolito et al. “Quantitative assessment of tumour associated neo-vascularisation in patients with liver cirrhosis and hepatocellular carcinoma: role of dynamic-CT perfusion imaging”. In: *European radiology* 22.4 (2012), pp. 803–811 (cit. on pp. 32, 72).
- [160] T. Lefort et al. “Correlation and agreement between contrast-enhanced ultrasonography and perfusion computed tomography for assessment of liver metastases from endocrine tumors: normalization enhances correlation”. In: *Ultrasound in medicine & biology* 38.6 (2012), pp. 953–961 (cit. on p. 32).
- [161] E. Frampas et al. “Advanced Hepatocellular Carcinoma: early evaluation of response to targeted therapy and prognostic value of Perfusion CT and Dynamic Contrast Enhanced-Ultrasound. Preliminary results”. In: *European journal of radiology* 82.5 (2013), e205–e211 (cit. on pp. 32, 35).
- [162] D. A. Lynch. *Chest Imaging, An Issue of Clinics in Chest Medicine*. Vol. 36. 2. Elsevier Health Sciences, 2015 (cit. on p. 32).
- [163] A. P. Reeves et al. “On measuring the change in size of pulmonary nodules”. In: *IEEE Trans. Med. Imaging* 25.4 (2006), pp. 435–450 (cit. on p. 32).
- [164] D. M. Xu et al. “Limited value of shape, margin and CT density in the discrimination between benign and malignant screen detected solid pulmonary nodules of the NELSON trial”. In: *European journal of radiology* 68.2 (2008), pp. 347–352 (cit. on p. 32).
- [165] I. Sitartchouk et al. “Computed tomography perfusion using first pass methods for lung nodule characterization”. In: *Investigative radiology* 43.6 (2008), pp. 349–358 (cit. on p. 32).

- [166] Y. Ohno et al. “Differentiation of malignant and benign pulmonary nodules with quantitative first-pass 320-detector Row perfusion CT versus FDG PET/CT”. In: *Radiology* 258.2 (2011), pp. 599–609 (cit. on p. 32).
- [167] F. Shan et al. “Differentiation between malignant and benign solitary pulmonary nodules: Use of volume first-pass perfusion and combined with routine computed tomography”. In: *European journal of radiology* 81.11 (2012), pp. 3598–3605 (cit. on pp. 32, 47).
- [168] Y Li et al. “First-pass perfusion imaging of solitary pulmonary nodules with 64-detector row CT: comparison of perfusion parameters of malignant and benign lesions”. In: *The British journal of radiology* 83 (2010), pp. 785–790 (cit. on pp. 32, 33).
- [169] K. Hayano et al. “Quantitative characterization of hepatocellular carcinoma and metastatic liver tumor by CT perfusion”. In: *Cancer Imaging* 13.4 (2013), pp. 512–519 (cit. on pp. 33, 47).
- [170] T. D. L. Nguyen-Kim et al. “Assessment of bronchial and pulmonary blood supply in non-small cell lung cancer subtypes using computed tomography perfusion”. In: *Investigative radiology* 50.3 (2015), pp. 179–186 (cit. on pp. 33, 34, 102).
- [171] F Fraioli et al. “Whole-tumour CT-perfusion of unresectable lung cancer for the monitoring of anti-angiogenetic chemotherapy effects”. In: *The British journal of radiology* 86.1029 (2013), p. 20120174 (cit. on pp. 33, 34, 104).
- [172] E. Łuczyńska et al. “Correlation between CT Perfusion and Clinico-Pathological Features in Prostate Cancer: A Prospective Study”. In: *Medical science monitor: international medical journal of experimental and clinical research* 21 (2015), pp. 153–162 (cit. on p. 33).
- [173] M. Nesteruk et al. “Tumor stage, tumor site and HPV dependent correlation of perfusion CT parameters and [18F]-FDG uptake in head and neck squamous cell carcinoma”. In: *Radiotherapy and Oncology* 117.1 (2015), pp. 125–131 (cit. on p. 33).
- [174] R Jain et al. “Glioma Angiogenesis and Perfusion Imaging: Understanding the Relationship between Tumor Blood Volume and Leakiness with Increasing Glioma Grade”. In: *American Journal of Neuroradiology* 36.11 (2015), pp. 2030–2035 (cit. on p. 33).

- [175] M DOnofrio et al. “Perfusion CT can predict tumoral grading of pancreatic adenocarcinoma”. In: *European journal of radiology* 82.2 (2013), pp. 227–233 (cit. on pp. 33, 104).
- [176] Y.-L. Zhang et al. “Utility of CT perfusion imaging for grading of clear cell renal cell carcinoma”. In: *Hereditary Genetics: Current Research* 1.105 (2012) (cit. on p. 34).
- [177] D. Prezzi, A. Khan, and V. Goh. “Perfusion CT imaging of treatment response in oncology”. In: *European journal of radiology* 84.12 (2015), pp. 2380–2385 (cit. on p. 34).
- [178] J. C. Yao et al. “Perfusion computed tomography as functional biomarker in randomized run-in study of bevacizumab and everolimus in well-differentiated neuroendocrine tumors”. In: *Pancreas* 44.2 (2015), pp. 190–197 (cit. on p. 34).
- [179] K. Hayano et al. “Tumor blood flow change measured by CT perfusion during chemoradiation therapy (CRT) for monitoring response and predicting survival in patients with esophageal cancer”. In: *Esophagus* 11.1 (2014), pp. 72–79 (cit. on pp. 34, 35).
- [180] M. R. Meijerink et al. “The use of perfusion CT for the evaluation of therapy combining AZD2171 with gefitinib in cancer patients”. In: *European radiology* 17.7 (2007), pp. 1700–1713 (cit. on p. 34).
- [181] T Jiang et al. “Monitoring response to antiangiogenic treatment and predicting outcomes in advanced hepatocellular carcinoma using image biomarkers, CT perfusion, tumor density, and tumor size (RECIST)”. In: *Investigative Radiology* 47 (2012), pp. 11–17 (cit. on pp. 34, 35).
- [182] J. S. Lind et al. “Dynamic contrast-enhanced CT in patients treated with sorafenib and erlotinib for non-small cell lung cancer: a new method of monitoring treatment?” In: *European radiology* 20.12 (2010), pp. 2890–2898 (cit. on pp. 34, 35).
- [183] F. Fraioli et al. “Whole-tumor perfusion CT in patients with advanced lung adenocarcinoma treated with conventional and antiangiogenetic chemotherapy: initial experience”. In: *Radiology* 259.2 (2011), pp. 574–582 (cit. on pp. 34, 35, 45, 104).
- [184] K. Hayano et al. “Perfusion CT can predict the response to chemoradiation therapy and survival in esophageal squamous cell carcinoma: initial clinical results”. In: *Oncology reports* 18.4 (2007), pp. 901–908 (cit. on p. 35).

- [185] S Bisdas et al. “Response and progression-free survival in oropharynx squamous cell carcinoma assessed by pretreatment perfusion CT: comparison with tumor volume measurements”. In: *American Journal of Neuroradiology* 30.4 (2009), pp. 793–799 (cit. on p. 35).
- [186] J. Wang et al. “Tumor response in patients with advanced non-small cell lung cancer: perfusion CT evaluation of chemotherapy and radiation therapy”. In: *American Journal of Roentgenology* 193.4 (2009), pp. 1090–1096 (cit. on pp. 35, 104).
- [187] N. Tacelli et al. “Perfusion CT allows prediction of therapy response in non-small cell lung cancer treated with conventional and anti-angiogenic chemotherapy”. In: *European radiology* 23.8 (2013), pp. 2127–2136 (cit. on pp. 35, 105).
- [188] T. S. Koh et al. “Primary colorectal cancer: use of kinetic modeling of dynamic contrast-enhanced CT data to predict clinical outcome”. In: *Radiology* 267.1 (2013), pp. 145–154 (cit. on pp. 35, 43).
- [189] K. Hayano et al. “Quantitative measurement of blood flow using perfusion CT for assessing clinicopathologic features and prognosis in patients with rectal cancer.” In: *Diseases of the Colon & Rectum* 52.9 (2009), pp. 1624–1629 (cit. on p. 35).
- [190] G. d’Assignies et al. “Pancreatic endocrine tumors: tumor blood flow assessed with perfusion CT reflects angiogenesis and correlates with prognostic factors”. In: *Radiology* 250.2 (2009), pp. 407–416 (cit. on p. 35).
- [191] J. J. S. Shankar et al. “Evaluation of perfusion CT in grading and prognostication of high-grade gliomas at diagnosis: a pilot study”. In: *American Journal of Roentgenology* 200.5 (2013), W504–W509 (cit. on p. 35).
- [192] K. Hayano et al. “Exploration of Imaging Biomarkers for Predicting Survival of Patients With Advanced Non-Small Cell Lung Cancer Treated With Antiangiogenic Chemotherapy”. In: *American Journal of Roentgenology* 206.5 (2016), pp. 987–993 (cit. on pp. 35, 44, 68, 104, 105).
- [193] X. S. Li et al. “Value of Whole-Tumor Dual-Input Perfusion CT in Predicting the Effect of Multiarterial Infusion Chemotherapy on Advanced Non-Small Cell Lung Cancer”. In: *American journal of roentgenology* 203.5 (2014), W497–W505 (cit. on pp. 35, 171, 172).

- [194] V. Goh et al. “Can perfusion CT assessment of primary colorectal adenocarcinoma blood flow at staging predict for subsequent metastatic disease? A pilot study”. In: *European radiology* 19.1 (2009), pp. 79–89 (cit. on p. 35).
- [195] Q. S. Ng and V. Goh. “Angiogenesis in non-small cell lung cancer: imaging with perfusion computed tomography”. In: *Journal of thoracic imaging* 25.2 (2010), pp. 142–150 (cit. on pp. 36, 40).
- [196] J. G. Korporaal et al. “Dynamic Contrast-enhanced CT for Prostate Cancer: Relationship between Image Noise, Voxel Size, and Repeatability”. In: *Radiology* 256.3 (2010), pp. 976–984 (cit. on p. 37).
- [197] C. S. Ng et al. “Effect of sampling frequency in perfusion values in CT perfusion of lung tumors”. In: *AJR. American journal of roentgenology* 200.2 (2013), W155–W162 (cit. on p. 38).
- [198] A. E. Othman et al. “Radiation dose reduction in perfusion CT imaging of the brain: a review of the literature”. In: *Journal of Neuroradiology* 43.1 (2016), pp. 1–5 (cit. on p. 38).
- [199] O. M. Topcuoğlu et al. “Reproducibility and variability of very low dose hepatic perfusion CT in metastatic liver disease”. In: *Diagn Interv Radiol* 22 (2016), pp. 495–500 (cit. on p. 38).
- [200] D. V. Sahani et al. “Advanced Hepatocellular Carcinoma: CT Perfusion of Liver and Tumor Tissue Initial Experience”. In: *Radiology* 243.3 (2007), pp. 736–743 (cit. on pp. 38, 44).
- [201] V. Goh et al. “Quantitative assessment of tissue perfusion using MDCT: comparison of colorectal cancer and skeletal muscle measurement reproducibility”. In: *American Journal of Roentgenology* 187.1 (2006), pp. 164–169 (cit. on pp. 38, 44).
- [202] Q.-S. Ng et al. “Lung Cancer Perfusion at Multi-Detector Row CT: Reproducibility of Whole Tumor Quantitative Measurements”. In: *Radiology* 239.2 (2006), pp. 547–553 (cit. on pp. 38, 44, 72, 104).
- [203] Q. S. Ng et al. “Quantitative assessment of lung cancer perfusion using MDCT: does measurement reproducibility improve with greater tumor volume coverage?” In: *American Journal of Roentgenology* 187.4 (2006), pp. 1079–1084 (cit. on pp. 38, 44, 45, 104).

- [204] C. S. Ng et al. “Reproducibility of CT perfusion parameters in liver tumors and normal liver”. In: *Radiology* 260.3 (2011), pp. 762–770 (cit. on pp. 39, 40, 72, 73, 76, 81).
- [205] C. S. Ng et al. “Reproducibility of perfusion parameters obtained from perfusion CT in lung tumors”. In: *American Journal of Roentgenology* 197.1 (2011), pp. 113–121 (cit. on pp. 39, 40, 72, 73, 104).
- [206] M Bellomi et al. “Perfusion CT in solid body-tumours part II. Clinical applications and future development”. In: *La radiologia medica* 115.6 (2010), pp. 858–874 (cit. on p. 39).
- [207] R. Goetti et al. “Quantitative perfusion analysis of malignant liver tumors: dynamic computed tomography and contrast-enhanced ultrasound”. In: *Investigative radiology* 47.1 (2012), pp. 18–24 (cit. on p. 40).
- [208] T. San Koh et al. “Dynamic contrast-enhanced CT imaging of hepatocellular carcinoma in cirrhosis: feasibility of a prolonged dual-phase imaging protocol with tracer kinetics modeling”. In: *European radiology* 19.5 (2009), pp. 1184–1196 (cit. on pp. 40, 72).
- [209] T. Koh et al. “Assessment of tumor blood flow distribution by dynamic contrast-enhanced CT”. In: *IEEE transactions on medical imaging* 32.8 (2013), pp. 1504–1514 (cit. on pp. 40, 65, 77).
- [210] N. K. Jensen et al. “Prediction and reduction of motion artifacts in free-breathing dynamic contrast enhanced CT perfusion imaging of primary and metastatic intrahepatic tumors”. In: *Academic radiology* 20.4 (2013), pp. 414–422 (cit. on pp. 40, 72, 78, 81, 104).
- [211] D. Muenzel et al. “Dynamic CT perfusion imaging of the myocardium: a technical note on improvement of image quality”. In: *PloS one* 8.10 (2013), e75263 (cit. on p. 41).
- [212] T. R. Bader et al. “Measurement of hepatic perfusion with dynamic computed tomography: assessment of normal values and comparison of two methods to compensate for motion artifacts”. In: *Investigative radiology* 35.9 (2000), pp. 539–547 (cit. on pp. 41, 51, 72).
- [213] M. Moreira et al. “A framework for cerebral CT perfusion imaging methods comparison”. In: *International Conference Image Analysis and Recognition*. Springer. 2010, pp. 141–150 (cit. on p. 41).

- [214] M. Romano et al. “Robustness to noise of arterial blood flow estimation methods in CT perfusion”. In: *BMC research notes* 7.1 (2014), p. 540 (cit. on p. 41).
- [215] M D’Antò et al. “Study of different Time Attenuation Curve processing in liver CT perfusion”. In: *Proceedings of the 10th IEEE International Conference on Information Technology and Applications in Biomedicine*. IEEE. 2010, pp. 1–4 (cit. on pp. 41, 51).
- [216] H. K. Thompson et al. “Indicator transit time considered as a gamma variate”. In: *Circ Res* 14.6 (1964), pp. 502–515 (cit. on p. 41).
- [217] M. D. Harpen and M. L. Lecklitner. “Derivation of gamma variate indicator dilution function from simple convective dispersion model of blood flow”. In: *Medical physics* 11.5 (1984), pp. 690–692 (cit. on p. 41).
- [218] C. A. Cuenod et al. “Deconvolution technique for measuring tissue perfusion by dynamic CT: application to normal and metastatic liver”. In: *Academic radiology* 9.1 (2002), S205–S211 (cit. on p. 41).
- [219] S. Goutelle et al. “The Hill equation: a review of its capabilities in pharmacological modelling”. In: *Fundamental & clinical pharmacology* 22.6 (2008), pp. 633–648 (cit. on pp. 41, 48).
- [220] S. H. Lee et al. “Use of tracer kinetic model-driven biomarkers for monitoring antiangiogenic therapy of hepatocellular carcinoma in first-pass perfusion CT”. In: *International MICCAI Workshop on Computational and Clinical Challenges in Abdominal Imaging*. Springer. 2013, pp. 270–279 (cit. on p. 43).
- [221] V. Goh, S. Halligan, and C. I. Bartram. “Quantitative Tumor Perfusion Assessment with Multidetector CT: Are Measurements from Two Commercial Software Packages Interchangeable?” In: *Radiology* 242.3 (2007), pp. 777–782 (cit. on p. 43).
- [222] V. Goh et al. “Commercial software upgrades may significantly alter Perfusion CT parameter values in colorectal cancer”. In: *European radiology* 21.4 (2011), pp. 744–749 (cit. on p. 43).
- [223] C. Cuenod and D Balvay. “Perfusion and vascular permeability: basic concepts and measurement in DCE-CT and DCE-MRI”. In: *Diagnostic and interventional imaging* 94.12 (2013), pp. 1187–1204 (cit. on p. 44).

- [224] C. S. Reiner et al. “Histogram analysis of CT perfusion of hepatocellular carcinoma for predicting response to transarterial radioembolization: value of tumor heterogeneity assessment”. In: *Cardiovascular and interventional radiology* 39.3 (2016), pp. 400–408 (cit. on pp. 44, 104).
- [225] F. Michallek and M. Dewey. “Fractal analysis in radiological and nuclear medicine perfusion imaging: a systematic review”. In: *European radiology* 24.1 (2014), pp. 60–69 (cit. on p. 44).
- [226] F. E. Lennon et al. “Lung cancer [mdash] a fractal viewpoint”. In: *Nature Reviews Clinical Oncology* 12.11 (2015), pp. 664–675 (cit. on p. 44).
- [227] S. Gordic et al. “Correlation between Dual-Energy and Perfusion CT in Patients with Hepatocellular Carcinoma”. In: *Radiology* (2016), pp. 78–87 (cit. on pp. 44, 104).
- [228] D. Ippolito et al. “Intraobserver and Interobserver Agreement in the Evaluation of Tumor Vascularization With Computed Tomography Perfusion in Cirrhotic Patients With Hepatocellular Carcinoma”. In: *Journal of computer assisted tomography* 40.1 (2016), pp. 152–159 (cit. on pp. 44, 104).
- [229] M. R. Meijerink et al. “Total-liver-volume perfusion CT using 3-D image fusion to improve detection and characterization of liver metastases”. In: *European radiology* 18.10 (2008), pp. 2345–2354 (cit. on pp. 45, 51, 86, 200).
- [230] A. Bevilacqua et al. “Quantitative Assessment of Effects of Motion Compensation for Liver and Lung Tumors in CT Perfusion”. In: *Academic radiology* 21.11 (2014), pp. 1416–1426 (cit. on pp. 46, 51, 56, 65, 91).
- [231] G. U. Yule. “On a method of investigating periodicities in disturbed series, with special reference to Wolfer’s sunspot numbers”. In: *Philosophical Transactions of the Royal Society of London. Series A, Containing Papers of a Mathematical or Physical Character* 226 (1927), pp. 267–298 (cit. on p. 46).
- [232] G. Walker. “On periodicity in series of related terms”. In: *Proceedings of the Royal Society of London. Series A, Containing Papers of a Mathematical and Physical Character* 131.818 (1931), pp. 518–532 (cit. on p. 46).

- [233] S. Wu et al. “Optimal metabolite curve fitting for kinetic modeling of 11C-WAY-100635”. In: *Journal of Nuclear Medicine* 48.6 (2007), pp. 926–931 (cit. on p. 48).
- [234] A. Gibaldi et al. “Effects of Guided Random Sampling of TCCs on Blood Flow Values in CT Perfusion Studies of Lung Tumors”. In: *Academic radiology* 22.1 (2015), pp. 58–69 (cit. on pp. 51, 55, 67).
- [235] A. Bevilacqua and S. Baiocco. “Automatic classification of lung tumour heterogeneity according to a visual-based score system in dynamic contrast enhanced CT sequences”. In: *International Journal of Modern Physics C* 27.10 (2016) (cit. on pp. 51, 59, 65).
- [236] A. Bevilacqua et al. “Automatic detection of misleading blood flow values in CT perfusion studies of lung cancer”. In: *Biomedical Signal Processing and Control* 26 (2016), pp. 109–116 (cit. on pp. 51, 57, 65, 102, 104).
- [237] A. Bevilacqua et al. “A novel approach for semi-quantitative assessment of reliability of blood flow values in DCE-CT perfusion”. In: *Biomedical Signal Processing and Control* 31 (2017), pp. 257–264 (cit. on pp. 51, 65, 67).
- [238] S. M. Lee et al. “Adaptive 4D volume perfusion CT of lung cancer: effects of computerized motion correction and the range of volume coverage on measurement reproducibility”. In: *American Journal of Roentgenology* 200.6 (2013), W603–W609 (cit. on pp. 51, 104).
- [239] A Chandler et al. “Validation of motion correction techniques for liver CT perfusion studies”. In: *The British Journal of Radiology* 85.1016 (2012), e514 (cit. on pp. 51, 72, 81).
- [240] R. Goetti et al. “Quantitative computed tomography liver perfusion imaging using dynamic spiral scanning with variable pitch: feasibility and initial results in patients with cancer metastases”. In: *Investigative radiology* 45.7 (2010), pp. 419–426 (cit. on pp. 51, 200).
- [241] A. M. Mendrik et al. “TIPS bilateral noise reduction in 4D CT perfusion scans produces high-quality cerebral blood flow maps”. In: *Physics in medicine and biology* 56.13 (2011), pp. 3857–3872 (cit. on p. 51).
- [242] M. Wintermark et al. “Using 80 kVp versus 120 kVp in perfusion CT measurement of regional cerebral blood flow”. In: *American journal of neuroradiology* 21.10 (2000), pp. 1881–1884 (cit. on p. 51).

- [243] D. Marin et al. “Low-tube-voltage, high-tube-current multidetector abdominal ct: improved image quality and decreased radiation dose with adaptive statistical iterative reconstruction algorithminitial clinical experience 1”. In: *Radiology* 254.1 (2009), pp. 145–153 (cit. on p. 51).
- [244] G. Upton and I. Cook. *A dictionary of statistics 3e*. Oxford university press, 2014 (cit. on p. 61).
- [245] G. Zack, W. Rogers, and S. Latt. “Automatic measurement of sister chromatid exchange frequency.” In: *Journal of Histochemistry & Cytochemistry* 25.7 (1977), pp. 741–753 (cit. on p. 62).
- [246] D. Balvay et al. “Mapping the Zonal Organization of Tumor Perfusion and Permeability in a Rat Glioma Model by Using Dynamic Contrast-enhanced Synchrotron Radiation CT 1”. In: *Radiology* 250.3 (2009), pp. 692–702 (cit. on p. 65).
- [247] C. E. Shannon and W. Weaver. *The mathematical theory of communication*. University of Illinois press, 2015 (cit. on p. 67).
- [248] C. E. Shannon. “A note on the concept of entropy”. In: *Bell System Tech. J* 27 (1948), pp. 379–423 (cit. on p. 67).
- [249] F. Davnall et al. “Assessment of tumor heterogeneity: an emerging imaging tool for clinical practice?” In: *Insights into imaging* 3.6 (2012), pp. 573–589 (cit. on pp. 68, 103).
- [250] M. G. Lubner et al. “CT textural analysis of hepatic metastatic colorectal cancer: pre-treatment tumor heterogeneity correlates with pathology and clinical outcomes”. In: *Abdominal imaging* 40.7 (2015), pp. 2331–2337 (cit. on p. 68).
- [251] C. Dennie et al. “Role of quantitative computed tomography texture analysis in the differentiation of primary lung cancer and granulomatous nodules”. In: *Quantitative Imaging in Medicine and Surgery* 6.1 (2016), pp. 6–15 (cit. on p. 68).
- [252] S.-X. Rao et al. “CT texture analysis in colorectal liver metastases: A better way than size and volume measurements to assess response to chemotherapy?” In: *United European gastroenterology journal* 4.2 (2016), pp. 257–263 (cit. on p. 68).
- [253] S. Malavasi et al. “Multislice Analysis of Blood Flow Values in CT Perfusion Studies of Lung Cancer”. In: *BioMed Research International* 2017 (2017) (cit. on p. 69).

- [254] A Nakashige et al. “Quantitative measurement of hepatic portal perfusion by multidetector row CT with compensation for respiratory misregistration.” In: *The British journal of radiology* 77.921 (2004), pp. 728–734 (cit. on pp. 72, 172).
- [255] A. Chandler et al. “Semiautomated motion correction of tumors in lung CT-perfusion studies”. In: *Academic radiology* 18.3 (2011), pp. 286–293 (cit. on pp. 72, 81).
- [256] J. F. Barrett and N. Keat. “Artifacts in CT: recognition and avoidance 1”. In: *Radiographics* 24.6 (2004), pp. 1679–1691 (cit. on pp. 73, 75).
- [257] F. E. Boas and D. Fleischmann. “CT artifacts: causes and reduction techniques”. In: *Imaging in Medicine* 4.2 (2012), pp. 229–240 (cit. on pp. 73, 74, 76).
- [258] R. Brooks and G Di Chiro. “Beam hardening in X-ray reconstructive tomography”. In: *Physics in Medicine and Biology* 21 (1976), pp. 390–398 (cit. on p. 74).
- [259] K. Erlandsson et al. “A review of partial volume correction techniques for emission tomography and their applications in neurology, cardiology and oncology”. In: *Physics in medicine and biology* 57.21 (2012), R119 (cit. on p. 74).
- [260] I. Mori et al. “Photon starvation artifacts of X-ray CT: their true cause and a solution”. In: *Radiological physics and technology* 6.1 (2013), pp. 130–141 (cit. on p. 75).
- [261] K. M. Andersson et al. “Metal artefact reduction in CT imaging of hip prostheses—an evaluation of commercial techniques provided by four vendors”. In: *The British journal of radiology* 88.1052 (2015), p. 20140473 (cit. on p. 76).
- [262] C Yuan et al. “SU-FI-08: CT Image Ring Artifact Reduction Based On Prior Image”. In: *Medical Physics* 43.6 (2016), pp. 3388–3388 (cit. on p. 76).
- [263] M. K. Fuld et al. “Pulmonary perfused blood volume with dual-energy CT as surrogate for pulmonary perfusion assessed with dynamic multi-detector CT”. In: *Radiology* 267.3 (2013), pp. 747–756 (cit. on p. 76).

- [264] M. W. Huellner et al. “Multiparametric PET/CT-perfusion does not add significant additional information for initial staging in lung cancer compared with standard PET/CT”. In: *EJNMMI Research* 4.1 (2014), pp. 1–13 (cit. on p. 76).
- [265] H. Wang and Y. Cao. “Correction of arterial input function in dynamic contrast-enhanced MRI of the liver”. In: *Journal of Magnetic Resonance Imaging* 36.2 (2012), pp. 411–421 (cit. on p. 77).
- [266] S. Kandel et al. “Comparison of free breathing versus breath-hold in perfusion imaging using dynamic volume CT”. In: *Insights into imaging* 3.4 (2012), pp. 323–328 (cit. on p. 86).
- [267] J. Zar. *Biostatistical Analysis*. Prentice Hall, 1999. ISBN: 9780130815422. URL: <https://books.google.it/books?id=edxqAAAAMAAJ> (cit. on pp. 95, 107).
- [268] A. Gherardi, S. Bravaccini, and A. Bevilacqua. “Computer assisted detection of regions of interest in histopathology using a hybrid supervised and unsupervised approach”. In: *SPIE Medical Imaging*. International Society for Optics and Photonics. 2013, 86760W–86760W (cit. on p. 95).
- [269] S. W. Harders et al. “Dynamic contrast-enhanced CT in suspected lung cancer: quantitative results”. In: *The British journal of radiology* 86.1031 (2013), p. 20130257 (cit. on p. 104).
- [270] M. A. Mazzei et al. “CT Perfusion: Technical Developments and Current and Future Applications”. In: *BioMed research international* 2015 (2015) (cit. on p. 104).
- [271] F. Shan et al. “First-pass CT perfusion in small peripheral lung cancers: effect of the temporal interval between scan acquisitions on the radiation dose and quantitative vascular parameters”. In: *Academic radiology* 20.8 (2013), pp. 972–979 (cit. on p. 104).
- [272] T. Win et al. “Tumor heterogeneity and permeability as measured on the CT component of PET/CT predict survival in patients with non-small cell lung cancer”. In: *Clin Cancer Res* 19.13 (2013), pp. 3591–3599 (cit. on p. 104).
- [273] D. Bohlsen et al. “First pass dual input volume CT-perfusion of lung lesions: The influence of the CT-value range settings on the perfusion values of benign and malignant entities”. In: *European journal of radiology* 85.6 (2016), pp. 1109–1114 (cit. on p. 104).

- [274] C. Altar. “The Biomarkers Consortium: on the critical path of drug discovery”. In: *Clinical Pharmacology & Therapeutics* 83.2 (2008), pp. 361–364 (cit. on p. 115).
- [275] D. J. Sargent et al. “Validation of novel imaging methodologies for use as cancer clinical trial end-points”. In: *European journal of cancer* 45.2 (2009), pp. 290–299 (cit. on pp. 115, 116).
- [276] J. M. Bernstein, J. J. Homer, and C. M. West. “Dynamic contrast-enhanced magnetic resonance imaging biomarkers in head and neck cancer: potential to guide treatment? A systematic review”. In: *Oral oncology* 50.10 (2014), pp. 963–970 (cit. on p. 116).
- [277] M. Intven et al. “Combined T2w volumetry, DW-MRI and DCE-MRI for response assessment after neo-adjuvant chemoradiation in locally advanced rectal cancer”. In: *Acta Oncologica* 54.10 (2015), pp. 1729–1736 (cit. on p. 116).
- [278] K. A. Miles et al. “Quantitative contrast-enhanced computed tomography: is there a need for system calibration?” In: *European radiology* 17.4 (2007), pp. 919–926 (cit. on pp. 116, 148).
- [279] M. Westerterp et al. “Quantification of FDG PET studies using standardised uptake values in multi-centre trials: effects of image reconstruction, resolution and ROI definition parameters”. In: *European journal of nuclear medicine and molecular imaging* 34.3 (2007), pp. 392–404 (cit. on p. 117).
- [280] P. Vera et al. “FDG PET during radiochemotherapy is predictive of outcome at 1 year in non-small-cell lung cancer patients: a prospective multicentre study (RTEP2)”. In: *European journal of nuclear medicine and molecular imaging* 41.6 (2014), pp. 1057–1065 (cit. on p. 117).
- [281] N. Lassau et al. “Standardization of dynamic contrast-enhanced ultrasound for the evaluation of antiangiogenic therapies: the French multicenter Support for Innovative and Expensive Techniques Study”. In: *Investigative radiology* 47.12 (2012), pp. 711–716 (cit. on p. 117).
- [282] B. Whitcher et al. “A Bayesian hierarchical model for DCE-MRI to evaluate treatment response in a phase II study in advanced squamous cell carcinoma of the head and neck”. In: *Magnetic Resonance Materials in Physics, Biology and Medicine* 24.2 (2011), pp. 85–96 (cit. on p. 117).
- [283] S. J. Swensen et al. “Lung Nodule Enhancement at CT: Multicenter Study 1”. In: *Radiology* 214.1 (2000), pp. 73–80 (cit. on p. 117).

- [284] M. Leach et al. “Imaging vascular function for early stage clinical trials using dynamic contrast-enhanced magnetic resonance imaging”. In: *European radiology* 22.7 (2012), pp. 1451–1464 (cit. on pp. 120, 121).
- [285] P. Mildenerger, M. Eichelberg, and E. Martin. “Introduction to the DICOM standard”. In: *European radiology* 12.4 (2002), pp. 920–927 (cit. on p. 120).
- [286] Y. X. Kitzing. “Picture Archiving and Communication System (PACS)”. In: *Imaging the ICU Patient*. Springer, 2014, pp. 73–75 (cit. on p. 121).
- [287] S. J. Rascovsky et al. “Informatics in radiology: use of CouchDB for document-based storage of DICOM objects”. In: *Radiographics* 32.3 (2012), pp. 913–927 (cit. on p. 121).
- [288] I. TSALAFOUTAS and S. METALLIDIS. “A method for calculating the dose length product from CT DICOM images”. In: *British journal of radiology* 84.999 (2011), pp. 236–243 (cit. on p. 122).
- [289] K. T. Bae. “Intravenous contrast medium administration and scan timing at CT: considerations and approaches”. In: *Radiology* 256.1 (2010), pp. 32–61 (cit. on p. 131).
- [290] A. Sundin. “Imaging of adrenal masses with emphasis on adrenocortical tumors”. In: *Theranostics* 2.5 (2012), pp. 516–22 (cit. on pp. 141, 185, 186).
- [291] M. Kapanen, J. Halavaara, and A.-M. Häkkinen. “Comparison of liver perfusion parameters studied with conventional extravascular and experimental intravascular CT contrast agents”. In: *Academic radiology* 14.8 (2007), pp. 951–958 (cit. on p. 171).
- [292] M. K. Kapanen, J. T. Halavaara, and A.-M. Häkkinen. “Assessment of vascular physiology of tumorous livers: comparison of two different methods”. In: *Academic radiology* 10.9 (2003), pp. 1021–1029 (cit. on p. 171).
- [293] A. A. Moss et al. “Hepatic tumors: magnetic resonance and CT appearance.” In: *Radiology* 150.1 (1984), pp. 141–147 (cit. on p. 171).
- [294] W. M. Thaiss et al. “Iodine concentration as a perfusion surrogate marker in oncology: Further elucidation of the underlying mechanisms using Volume Perfusion CT with 80 kVp”. In: *European radiology* (2015), pp. 1–8 (cit. on pp. 171, 179).

- [295] T. P. C. Yeung et al. “Improving quantitative CT perfusion parameter measurements using principal component analysis”. In: *Academic radiology* 21.5 (2014), pp. 624–632 (cit. on pp. 171, 179).
- [296] O. W. Hamer et al. “Fatty Liver: Imaging Patterns and Pitfalls 1”. In: *Radiographics* 26.6 (2006), pp. 1637–1653 (cit. on pp. 184, 188).
- [297] W. Krause. “Delivery of diagnostic agents in computed tomography”. In: *Advanced drug delivery reviews* 37.1 (1999), pp. 159–173 (cit. on pp. 185, 186).
- [298] S Kojima et al. “Increased density of the liver and amiodarone-associated phospholipidosis.” In: *Cardiology research and practice* 2009 (2008), pp. 598940–598940 (cit. on pp. 185, 186).
- [299] H. Oikawa et al. “Liver cirrhosis induced by long-term administration of a daily low dose of amiodarone: a case report.” In: *World journal of gastroenterology* 11.34 (2005), pp. 5394–5397 (cit. on pp. 185, 186).
- [300] R. Lamba et al. “CT Hounsfield numbers of soft tissues on unenhanced abdominal CT scans: variability between two different manufacturers MDCT scanners”. In: *American Journal of Roentgenology* 203.5 (2014), pp. 1013–1020 (cit. on pp. 185, 186).
- [301] J. Rahman et al. “Estimation of Range of Hounsfield Unit on CT for Different Grades of Fatty Infiltration of Liver Categorized Using Ultrasound”. In: *GJRA-Global Journala for Research Analysis* 4.6 (2015), pp. 337–340 (cit. on p. 188).
- [302] L. Wang et al. “Assessment of liver fibrosis in the early stages with perfusion CT”. In: *International journal of clinical and experimental medicine* 8.9 (2015), p. 15276 (cit. on p. 200).
- [303] M. G. Frederick et al. “Timing of parenchymal enhancement on dual-phase dynamic helical CT of the liver: how long does the hepatic arterial phase predominate?” In: *AJR. American journal of roentgenology* 166.6 (1996), pp. 1305–1310 (cit. on p. 200).
- [304] K. A. Miles et al. “Colorectal cancer: texture analysis of portal phase hepatic CT images as a potential marker of survival 1”. In: *Radiology* 250.2 (2009), pp. 444–452 (cit. on pp. 200, 210).

- [305] X. Wang et al. “Quantitative hepatic CT perfusion measurement: comparison of Couinaud’s hepatic segments with dual-source 128-slice CT”. In: *European journal of radiology* 82.2 (2013), pp. 220–226 (cit. on p. 210).

Acknowledgements

Many people contributed to the work of this Thesis and in general supported me in these years, helping me when I needed to be helped and being happy for me every time I reached a goal. It would be impossible for me to create a list including all names of people I would like to thank. Nevertheless, I want to spend a few words regarding some of you that have been really important for me in some parts of my life.

Prof. **Alessandro Bevilacqua**, we started working together in 2011 so it is a long time we know each other, but I have to admit it, if I reached this goal it is only thanks to you that saw my potentialities even before I knew I had some! You believed in me from beginning and you helped me to discover and to strengthen my capabilities day by day, without ever losing your patient. Thank you for what you taught me, in the research field and in life, helping me to become the person now I am.

Prof. **Giampaolo Gavelli**, thank you for your constant availability and support you gave me during this 3-years PhD. Your experienced suggestions and opinions have always been of fundamental importance during all my research activities.

Dott. **Domenico Barone**, thank you for the hard work we did together on lung tumours. Your deep experience joined together with your availability and kindness allowed me to carry out a great work and acquire a good knowledge of CT perfusion data on both lung and liver.

Prof. **Valèrie Vilgrain**, thank you for giving me the opportunity of working by your lab for several months. Having the opportunity of working at your Department has been a very instructive experience to me, also allowing me to deeply improve my knowledge of hepatic physiology. Moreover, your high professionalism and kindness, and your support have been of fundamental importance to carry out my research activities.

Prof. **Bernard Van Beers**, thank you for welcoming me in your research group, where I have had the opportunity to become aware of the dynamics of

a high level International research group.

Finally, I would like to thank some people that have a special place in my heart.

Cari **Mamma e Papà**, vi ringrazio per quanto mi avete dato in questi 30 anni. Il mio carattere tenace e solare mi hanno consentito di giungere fino a questo importante e prestigioso traguardo, ma questo lo devo anche a voi. Ogni abbraccio, incoraggiamento e anche rimprovero sono stati indispensabili a farmi diventare la donna che sono. Grazie.

Grazie a **tutta la mia famiglia**, zii, cugini, ma anche agli amici ed ai colleghi, che un po', parte della mia famiglia lo sono diventati! Grazie per aver riso, gioito e pianto con me ad ogni successo ed ad ogni caduta di questo lungo percorso. Grazie a chi mi ha offerto un sorriso o mi ha teso una mano nel momento del bisogno. Grazie a chi ha sempre creduto in me. Grazie a chi mi ha donato anche solo un'ora del proprio tempo ed ha camminato al mio fianco, condividendo sogni, speranze e desideri. Un caro saluto a tutti.

THESIS END

Silvia Malavasi

Biomedical Engineer

PhD in Bioengineering (2014-2016)

Master's degree in Biomedical Engineering (2012)

Bachelor's degree in Biomedical Engineering (2009)

E-mail: s.malavasi@unibo.it

Research group website: <http://cvg.deis.unibo.it>

Website: <http://people.unibo.it/it/s.malavasi>
(Curriculum Vitae available on the personal website)

Office address:

Via Toffano 2/2, IT-40125, Bologna, Italy

Home address:

Via Mascagni 4, IT-40141, Bologna, Italy